



Erosional control on alkalinity release in a changing Arctic

Dissertation

Von der Fakultät für Mathematik und Naturwissenschaften der Carl von Ossietzky
Universität Oldenburg zur Erlangung des Grades und Titels eines Doktors der Natur-
wissenschaften

"doctor rerum naturalium" (Dr. rer. nat.)

angenommene Dissertation

von Frau

Nele Lehmann

geboren am 08.12.1991 in Rotenburg (Wümme)

Oldenburg, Dezember 2022

Gutachter: Prof. Dr. Helmuth Thomas

Weiterer Gutachter: Prof. Dr. Thorsten Dittmar

Disputationsdatum: 16.03.2023

Abstract

Erosion is thought to be one of the controlling factors on terrestrial weathering of silicates and carbonates, and thus on CO₂ drawdown and alkalinity generation. Climate change is expected to significantly alter soil erosion rates. Because climate change is strongest in the Arctic, high-latitude systems bear the greatest potential for large and rapid changes in erosion. These may lead to changes in alkalinity generation that would have significant impacts on the carbon cycle. Yet, the occurrence, magnitude and timescale of the changes are poorly understood. To adequately examine the influence of changing erosion rates induced by a changing climate on alkalinity generation, it is first essential to determine the relation between alkalinity generation and erosion rate in an assumed steady state system prior to the onset of the change.

The overall aim of this thesis was to investigate the influence of erosion rate on terrestrial alkalinity generation. Specifically, the objectives were to (i) investigate whether erosion rate is a first-order controlling factor on terrestrial alkalinity generation at the global scale, (ii) identify the major weathering pathways and hydrological controls on alkalinity generation in an Arctic hillslope catchment in a degrading permafrost landscape, and (iii) quantify a possible change in erosion due to climate change for the same catchment. While the first objective was approached by compiling a global dataset pairing measured alkalinity concentrations with long-term catchment-wide average erosion rates, the other two objectives were addressed by conducting two case studies in the Gaskabohki headwater catchment on the hillside of Iskorasfjellet on the Finnmarksvidda in northern Norway.

First, an empirically-based model was developed from global (44°S to 51°N) riverine alkalinity data and ¹⁰Be-derived erosion rates, demonstrating that areal proportion of carbonate, mean annual temperature (MAT), erosion rate, catchment area and soil thickness are first-order controls on riverine alkalinity concentration at the global scale. A non-linear relation characterized erosion rate and terrestrial alkalinity generation, with alkalinity best modeled by a second-order polynomial of the erosion rate. Thereby, the optimum of the alkalinity-erosion rate function represents a regime of '*efficient erosion rate*' at slow to intermediate erosion rates. Furthermore, alkalinity generation was found to respond strongly to a change in MAT. The weathering flux to the ocean was predicted to be significantly altered by climate warming as early as the end of this century. Thereby, both direction and accentuation of the change in alkalinity fluxes strongly

depend on the evolution of climate, as shown by projected emissions scenarios, resulting in either a strengthening or a weakening of the weathering-liberated alkalinity flux, and thus of the oceanic CO₂ buffer.

Second, the analysis of total alkalinity (AT) and dissolved inorganic carbon (DIC) concentrations, as well as the stable isotope signature of the latter ($\delta^{13}\text{C-DIC}$) in conjunction with dissolved cation and anion loads, revealed that AT was almost entirely derived from weathering of minor carbonate occurrences in the silicate-dominated Gaskabohki headwater catchment in northern Norway. The riparian zone proved to be a hotspot area for AT generation and release due to its enhanced hydrological connectivity, while the contribution of the weathering load from the uphill catchment was limited by insufficient contact time of weathering agents and weatherable material. By using stable water isotopes, it was possible to explain temporal variations in AT concentrations following a precipitation event due to surface runoff.

Third, $^{239+240}\text{Pu}$ inventories from soil cores and in situ ^{10}Be concentrations from stream sediments were used to determine a current (post-1960) and a long-term (averaged over the last 243 kyr) erosion rate, respectively, for the Gaskabohki catchment. A spatially highly heterogeneous distribution of $^{239+240}\text{Pu}$ was found across the catchment, suggesting that the applicability of this tracer to determine catchment-wide average erosion rates may be limited to regions at lower latitudes. A site-based mean current erosion rate of $184 (\pm 114) \text{ mm kyr}^{-1}$ was determined. From the analysis of ^{10}Be concentrations, it was inferred that the Gaskabohki catchment and the additional catchments studied (2.8 to 7,255 km²) reflected inheritance, confirming the general agreement on cold-based, non-erosive Fennoscandian ice sheets over the central sector of Fennoscandia. Under the assumption of zero glacial erosion, long-term catchment-wide average interglacial denudation rates were determined to range from 11 mm kyr^{-1} in the headwater catchment to 25 mm kyr^{-1} in the larger catchments, with the observed trend likely due to an enhanced fluvial erosion in the larger catchments. Despite the uncertainties associated with both rates, erosion in the headwater catchment has very likely increased over the past ~60 years relative to a long-term interglacial baseline, as the difference between the two rates is about an order of magnitude. The elevated erosion was attributed to a combination of increased rainfall erosivity and the presence of erodible soils that are not yet stabilized due to a sparse vegetation cover.

This thesis substantially advanced the understanding of the alkalinity-erosion rate dependency, at the global scale and in a small basin in the Arctic.

Zusammenfassung

Es wird davon ausgegangen, dass Erosion einer der steuernden Faktoren für die terrestrische Verwitterung von Silikaten und Karbonaten, und damit für die CO₂-Bindung und die Alkalinitätsbildung, ist. Es wird erwartet, dass der Klimawandel die Bodenerosionsraten erheblich verändern wird. Da der Klimawandel in der Arktis am stärksten ist, haben arktische Systeme das größte Potenzial für erhebliche und schnelle Veränderungen der Erosion. Veränderte Erosionsraten aufgrund des Klimawandels können zu Veränderungen in der Alkalinitätsbildung führen, die sich erheblich auf den Kohlenstoffkreislauf auswirken würden. Auftreten, Ausmaß und Zeitskala dieser Veränderungen sind jedoch derzeit nur unzureichend geklärt. Um den Einfluss potenziell veränderter Erosionsraten, die durch den Klimawandel hervorgerufen werden, auf die Alkalinitätsbildung angemessen zu untersuchen, ist es zunächst wichtig, die Beziehungen in einem als stationär angenommenen System vor dem Einsetzen der Veränderung zu bestimmen.

Das übergeordnete Ziel dieser Arbeit war es, den Einfluss der Erosionsrate auf die terrestrische Alkalinitätsbildung zu untersuchen. Im Einzelnen ging es darum, (i) zu untersuchen, ob die Erosionsrate ein Kontrollfaktor erster Ordnung für die terrestrische Alkalinitätsbildung auf globaler Ebene ist, (ii) die wichtigsten Verwitterungspfade und hydrologischen Einflussfaktoren auf die Alkalinitätsbildung in einem arktischen Hangeinzugsgebiet in einer degradierenden Permafrostlandschaft zu identifizieren und (iii) eine mögliche Veränderung der Erosion aufgrund des Klimawandels für dasselbe Einzugsgebiet zu quantifizieren. Während das erste Ziel durch die Zusammenstellung eines globalen Datensatzes erreicht wurde, welcher gemessene Alkalinitätskonzentrationen mit langfristigen einzugsgebietsweiten Erosionsraten verbindet, wurden die beiden anderen Ziele durch die Durchführung von zwei Fallstudien im Gaskabohki-Einzugsgebiet am Hang des Iskorasfjellet auf der Finnmarksvidda-Hochebene in Nordnorwegen erreicht.

Erstens wurde ein empirisch basiertes Modell aus globalen (44°S bis 51°N) Daten über die Alkalinität von Flüssen und aus ¹⁰Be abgeleiteten Erosionsraten entwickelt. Mit diesem konnte nachgewiesen werden, dass der flächenmäßige Anteil von Karbonat, die mittlere Jahrestemperatur (MAT), die Erosionsrate, die Einzugsgebietsgröße und die Bodendicke einen Einfluss erster Ordnung auf die Alkalinitätskonzentration in Flüssen auf globaler Ebene darstellen. Dabei zeigte sich, dass Erosionsrate und terrestrische Alkalinitätsbildung durch eine nichtlineare Beziehung gekennzeichnet

sind, wobei die Alkalinität am besten durch ein Polynom zweiter Ordnung der Erosionsrate modelliert wird. Dabei stellte das Optimum der Alkalinitäts-Erosionsraten-Funktion ein Regime von "effizienten Erosionsraten" bei langsamen bis mittleren Erosionsraten dar. Außerdem wurde festgestellt, dass die Alkalinitätserzeugung stark auf eine Änderung der MAT reagiert. Es wurde vorhergesagt, dass sich der Verwitterungsfluss zum Ozean durch die Klimaerwärmung bereits Ende dieses Jahrhunderts erheblich verändern wird. Dabei hängen sowohl die Richtung als auch die Akzentuierung der Veränderung der Alkalinitätsflüsse stark von der Entwicklung des Klimas ab, beispielhaft dargestellt durch die prognostizierten Emissionsszenarien, die entweder zu einer zusätzlichen CO₂-Senke oder -Quelle führen.

Zweitens ergab die Analyse der Gesamtalkalinität (AT) und der Konzentrationen des gelösten anorganischen Kohlenstoffs (DIC) sowie der stabilen Isotopensignatur des letzteren ($\delta^{13}\text{C-DIC}$) in Verbindung mit den gelösten Kationen- und Anionenmengen, dass die AT fast vollständig aus der Verwitterung geringer Karbonatvorkommen im silikat-dominierten Gaskabohki-Einzugsgebiet stammt. Die Uferzone erwies sich aufgrund ihrer verbesserten hydrologischen Konnektivität als Hotspot für die AT-Bildung und -Freisetzung, während der Beitrag des Hangs durch die unzureichende Kontaktzeit von Säure und verwitterbarem Material begrenzt war. Durch die Verwendung stabiler Wasserisotope war es möglich, die zeitlichen Schwankungen der AT-Konzentrationen nach einem Niederschlagsereignis durch Oberflächenabfluss zu erklären.

Drittens wurden $^{239+240}\text{Pu}$ -Inventare aus Bodenkernen und in situ ^{10}Be -Konzentrationen aus Flusssedimenten verwendet, um eine aktuelle (nach 1960) bzw. eine langfristige (gemittelt über die letzten 243 kyr) Erosionsrate für das Gaskabohki-Einzugsgebiet zu bestimmen. Es wurde eine räumlich sehr heterogene Verteilung von $^{239+240}\text{Pu}$ im gesamten Einzugsgebiet festgestellt, was darauf hindeutet, dass die Anwendbarkeit dieses Tracers zur Bestimmung von einzugsgebietsweiten Erosionsraten auf Regionen in niedrigeren Breitengraden beschränkt sein könnte. Es wurde eine standortbezogene mittlere aktuelle Erosionsrate von 184 (\pm 114) mm kyr⁻¹ ermittelt. Aus der Analyse der ^{10}Be -Konzentrationen wurde gefolgert, dass das Gaskabohki-Einzugsgebiet und die weiteren untersuchten Einzugsgebiete (2,8 bis 7,255 km²) Vererbung widerspiegeln, was die allgemeine Übereinstimmung über kalt-basierte, nicht-erosive fennoskandische Eisschilde über dem zentralen Sektor Fennoskandiens bestätigt. Ausgehend von der Annahme, dass es keine glaziale Erosion gab, wurden

langfristige einzugsgebietsweite interglaziale Denudationsraten zwischen 11 mm kyr^{-1} im Gaskabohki-Einzugsgebiet und 25 mm kyr^{-1} in den größeren Einzugsgebieten ermittelt, wobei der beobachtete Trend wahrscheinlich auf eine verstärkte fluviale Erosion in den größeren Einzugsgebieten zurückzuführen ist. Trotz der Unsicherheiten, die mit beiden Raten verbunden sind, hat die Erosion im Gaskabohki-Einzugsgebiet in den letzten ~60 Jahren im Vergleich zu einer langfristigen interglazialen Ausgangslage sehr wahrscheinlich zugenommen, da der Unterschied zwischen den beiden Raten etwa eine Größenordnung beträgt. Die erhöhte Erosion wurde auf eine Kombination aus erhöhter Niederschlagserosivität und dem Vorhandensein erodierbarer Böden zurückgeführt, die aufgrund einer spärlichen Vegetationsdecke noch nicht stabilisiert sind.

Diese Arbeit hat das Verständnis der Abhängigkeit zwischen Alkalinität und Erosionsrate sowohl auf globaler Ebene als auch in einem kleinen Einzugsgebiet in der Arktis wesentlich erweitert.

Table of Contents

Abstract.....	i
Zusammenfassung.....	iii
1 Introduction	1
1.1 Accelerated climate change in the Arctic.....	3
1.1.1 Arctic amplification	3
1.1.2 Intensification of the Arctic freshwater cycle and its implications for alkalinity fluxes	4
1.2 Controlling factors on alkalinity generation.....	6
1.2.1 Availability of weatherable minerals	7
1.2.2 Availability of weathering agents	10
1.2.3 Generation of soluble products	11
1.2.4 Hydrological connectivity.....	12
1.3 Alkalinity generation at the global scale	14
1.4 Alkalinity generation in a changing Arctic.....	15
1.4.1 Degrading permafrost.....	15
1.5 Research questions.....	18
1.6 Thesis structure.....	19
1.7 Author contributions	20
2 Methods	21
2.1 Quantifying short- and long-term erosion rates	21
2.1.1 Short-term erosion rates derived from $^{239+240}\text{Pu}$	22
2.1.2 Long-term erosion rates derived from ^{10}Be	24
2.2 Measurements of hydrochemical parameters	29
2.2.1 AT and DIC	30
2.2.2 $\delta^{13}\text{C}$ -DIC, major elements, and stable water isotopes.....	31
3 Alkalinity responses to climate warming destabilize the Earth's thermostat.....	32
3.1 Introduction	32
3.2 First-order controls on riverine alkalinity.....	33
3.3 Global riverine alkalinity function.....	38

3.4	Sensitivity of alkalinity generation to MAT	39
3.5	Impact of climate change on the terrestrial alkalinity flux	41
3.6	Methods	47
3.6.1	Water sampling and measurements.....	47
3.6.2	Data requirements and sources	47
3.6.3	CO ₂ consumption of carbonate and silicate weathering at different timescales	49
3.6.4	¹⁰ Be-derived erosion rates.....	50
3.6.5	Model preparation	51
3.6.6	Global riverine alkalinity function.....	52
3.6.7	Calculation of change in alkalinity flux due to climate warming	54
3.7	Supplementary material	56
4	Alkalinity generation from carbonate weathering in a silicate-dominated headwater catchment at Iskorasfjellet, northern Norway.....	66
4.1	Introduction	67
4.2	Materials and methods.....	71
4.2.1	Study site	71
4.2.2	Water sampling	74
4.2.3	Hydrochemical analyses	75
4.2.4	Geospatial analyses	76
4.2.5	Modelling of soil respiration.....	76
4.3	Results and discussion.....	77
4.3.1	Weathering and alkalinity generation in the Gaskabohki catchment.....	77
4.3.2	Controlling factors on alkalinity across watershed scales....	92
4.4	Conclusions.....	97
5	²³⁹⁺²⁴⁰ Pu inventories from soil cores and in situ ¹⁰ Be concentrations from stream sediments at Iskorasfjellet, northern Norway: Implications for current and long-term erosion	100
5.1	Introduction	101
5.2	Materials and methods.....	104

5.2.1	Gaskabohki catchment at Iskorasfjellet on the Finnmarksvidda	105
5.2.2	Larger catchments on the Finnmarksvidda	107
5.2.3	Geospatial analyses	108
5.2.4	Current erosion rates using $^{239+240}\text{Pu}$	109
5.2.5	Long-term denudation rates using in situ ^{10}Be	112
5.3	Results	114
5.3.1	$^{239+240}\text{Pu}$ in soils.....	114
5.3.2	In situ ^{10}Be in stream sediments.....	121
5.4	Discussion.....	133
5.4.1	Current erosion rates using $^{239+240}\text{Pu}$	133
5.4.2	Increased adsorption of Pu by fine earth fraction	135
5.4.3	Long-term denudation rates using in situ ^{10}Be	139
5.4.4	Uncertainties in determining interglacial denudation rates	140
5.4.5	Comparison of current and long-term erosion rates in the Gaskabohki catchment.....	141
5.5	Conclusions.....	142
5.6	Supplementary material	144
6	Conclusions	147
6.1	Answers to research questions	147
6.2	Outlook.....	151
	Acronyms	x
	Bibliography	xii
	Acknowledgements	xlvi
	Eidesstaatliche Erklärung.....	xlviii

1 Introduction

CO₂ drawdown and alkalinity generation by terrestrial silicate weathering is thought to be an integral part of the Earth's carbon cycle by counteracting solid-Earth CO₂ degassing from volcanism, metamorphism, and diagenesis over millions of years (Fig. 1-1a). Silicate weathering and thus CO₂ consumption increases in a warmer and wetter climate caused by elevated CO₂ levels, i.e., the atmospheric greenhouse effect, constituting a negative feedback (Walker et al., 1981; Berner et al., 1983). It is therefore considered to be ultimately responsible for the Earth's continuous habitability by stabilizing surface temperatures and keeping water in liquid form over the past 3.5 billion years, despite a large increase in solar luminosity (Kasting and Catling, 2003).

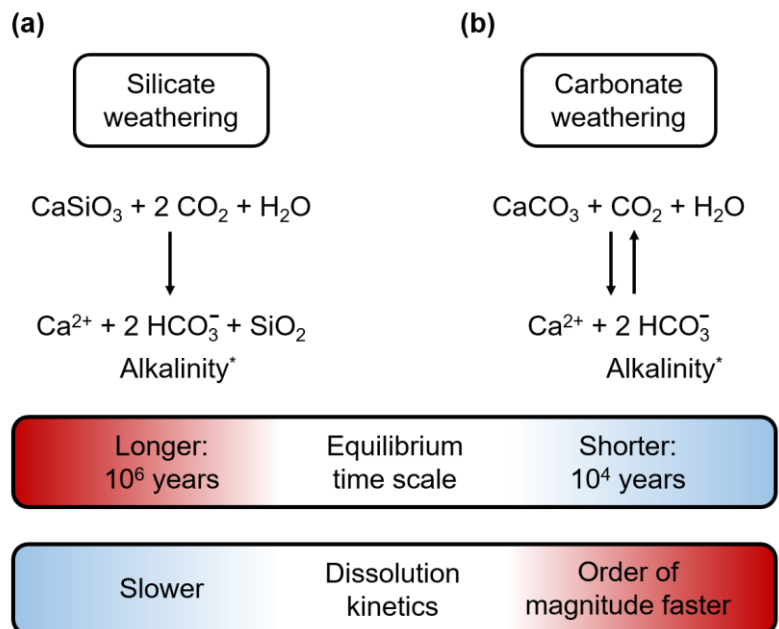


Fig. 1-1: Comparison of silicate and carbonate weathering. (a) Silicate weathering consumes two equivalents of CO₂. It is in equilibrium with solid-Earth CO₂ degassing at timescales of 10⁶ years. It shows slower dissolution kinetics than carbonate weathering. (b) Carbonate weathering consumes one equivalent of CO₂. It is in equilibrium with marine calcification at timescales of 10⁴ years. Compared to silicate weathering, its dissolution kinetics are several orders of magnitude faster. *At pH 7-9, alkalinity concentration is approximately equal to the bicarbonate (HCO₃⁻) concentration (Stumm and Morgan, 1981).

The sequestered CO₂ is transported in the form of alkalinity, or acid-neutralizing capacity, to the ocean, where the alkalinity is about 2.3 mmol kg⁻¹ (Jiang et al., 2019). There, it is precipitated as calcium carbonate due to supersaturation with respect to calcium carbonate (back reaction in Fig. 1-1b) and removed to the sediments, and thus returned to the lithosphere.

This so-called 'weathering thermostat' was originally thought to be at steady state since pre-industrial times (Walker et al., 1981; Berner et al., 1983). However, a global study by Goll et al. (2014) recently reported increased CO₂ consumption due to climate-driven changes in chemical weathering since 1850.

In addition to silicate weathering, alkalinity is also generated by carbonate weathering (Fig. 1-1b). However, while weathering of divalent cation silicates consumes two equivalents of CO₂, carbonate weathering consumes only one. Therefore, beyond the calcium carbonate compensation time (~10,000 yr; Zeebe and Westbroek, 2003), in which about one equivalent of CO₂ is released back into the atmosphere, only silicate weathering acts as a long-term sink for atmospheric CO₂, while carbonate weathering acts CO₂-neutral (Berner et al., 1983). Compared to silicate rocks, however, carbonate rocks are weathered more rapidly, and their dissolution kinetics are several orders of magnitude faster (Lasaga, 1984; Stallard and Edmond, 1987). This allows carbonate weathering to be more responsive to rapid environmental changes, such as during contemporary climate change. Global estimates (Gaillardet et al., 1999; Amiotte Suchet et al., 2003; Hartmann et al., 2009) attribute 49-63% of current CO₂ consumption by terrestrial weathering to silicate rocks, the remainder to carbonate rocks.

Environmental changes occurring over shorter timescales than calcium carbonate compensation, e.g., changes in temperature, hydrology, vegetation, erosion and atmospheric CO₂ content, have the potential to shift carbonate weathering away from its steady state, thereby altering the Earth's carbon cycle (Calmels et al., 2014). It is therefore **essential to assess the short- and long-term anthropogenic, climatic and geologic drivers of alkalinity fluxes.**

Riverine alkalinity

Total alkalinity (AT) was defined for seawater samples by Dickson (1981) as the number of moles of hydrogen ions equal to the excess of proton acceptors (bases formed from weak acids such as bicarbonate, carbonate, borate, or hydroxide) over proton donors in 1 kg of sample. This entails that alkalinity measures the ability of a water to neutralize acid. In fresh water, AT is mainly composed of bicarbonate (HCO₃⁻) and carbonate (CO₃²⁻), i.e., carbonate alkalinity. At pH values between 7 and 9, the alkalinity concentration is approximately equal to the HCO₃⁻ concentration (~95% of the carbon in the water is in the form of HCO₃⁻), as the equilibrium between HCO₃⁻ and CO₃²⁻ in this pH range is strongly in favor of HCO₃⁻

(Stumm and Morgan, 1981; Schroeder, 2002). Compared to carbonate alkalinity, dissolved inorganic carbon (DIC) also includes CO_2^* (the sum of dissolved CO_2 and H_2CO_3), and thus DIC is composed of CO_2^* , HCO_3^- and CO_3^{2-} , with the relative proportion of the DIC species depending on alkalinity and environmental conditions such as temperature.

1.1 Accelerated climate change in the Arctic

Climate change is particularly strong in the Arctic, as evidenced in the annually averaged near-surface air temperature, which increased by 0.71°C per decade from 1979 to 2021, nearly four times faster than the global average (Rantanen et al., 2022). This phenomenon is known as Arctic amplification. Polar warming has occurred in all seasons except boreal summer, with the warming being greatest in the fall and winter (Previdi et al., 2021). In addition to temperature, total annual precipitation increased by 24% from 1971 to 2019 (AMAP, 2022), and overall ‘greening’ of the Arctic tundra has taken place, which reflects enhanced plant growth and productivity (Osborne et al., 2018).

1.1.1 Arctic amplification

The Arctic carbon cycle is expected to undergo significant changes associated with the loss of sea ice, thawing of permafrost, and other physical changes in the Arctic environment due to climate warming. These changes can affect atmospheric concentrations of the well-mixed greenhouse gases CO_2 and methane, and thus global climate forcing by these gases (Previdi et al., 2021). Further, increased ice melt, the cause for projected global sea level rise, along with projected increases in high-latitude precipitation and ocean warming, are expected to weaken the ocean’s meridional overturning circulation (IPCC, 2013). This in turn has implications for regional climate change and global ocean heat and carbon uptake.

Although, overall, the most important climate forcing during the industrial age is the increase in atmospheric CO_2 levels, it is debated whether direct radiative forcing from CO_2 or subsequent climate system responses to this forcing are responsible for Arctic amplification (Previdi et al., 2021). There is general agreement in the literature that the underlying physical mechanisms contributing positively to Arctic amplifications are temperature feedbacks, surface albedo feedbacks, and atmospheric and oceanic poleward energy transport (PET) changes (Previdi et al., 2021). In a warming Arctic, as sea ice and snow cover diminish, the surface albedo, or reflectivity, decreases and more of the incoming solar radiation is absorbed by the Earth

system. Arctic climate is affected by changes in PET that are influenced by warming anomalies outside the Arctic. In contrast, the influence of direct CO₂ forcing on Arctic amplification remains unclear. Model simulations suggest that when the current climate state changes, e.g., the meridional temperature gradient significantly weakens, Arctic amplification itself becomes less pronounced (Merlis and Henry, 2018; Lutsko and Popp, 2018).

In contrast to the Arctic, its Southern Hemisphere counterpart, the Antarctic, shows a much weaker climate response, which has been attributed to the large heat uptake over the Southern Ocean (Flato and Boer, 2001). Further, the Antarctic was found to have a weaker climate response due to its weaker intrinsic sensitivity to both greenhouse gas forcing and the state of the ocean (Singh et al., 2018).

Because climate is changing most dramatically in the Arctic, alkalinity generation has the potential to change most rapidly there (Beaulieu et al., 2012). In addition to the stronger climate response, the Arctic generally has a greater weathering potential than the Antarctic given that only 0.44% of Antarctica's area is ice-free (Brooks et al., 2019), and in these ice-free areas, prevailing aridity limits denudation and solute fluxes (Nezat et al., 2001). The Antarctic Ice Sheet, which covers most of the continent, shows a cation denudation rate that is about two orders of magnitude lower than the average of glaciers in a global compilation (Li et al., 2022).

1.1.2 Intensification of the Arctic freshwater cycle and its implications for alkalinity fluxes

Climate change has led to an intensification of the entire Arctic freshwater cycle, i.e., the movement of freshwater between the Arctic's atmosphere, land and ocean compartments has been increasing (Rawlins et al., 2010; Zhang et al., 2013). The freshwater system of the Arctic plays a key role in storing and transporting sediments and solutes to the Arctic Ocean (McGuire et al., 2009; Wegner et al., 2015). This crucial role is also reflected at the global scale: For although the Arctic Ocean accounts for only about 1% of the total global ocean volume, it receives more than 10% of the world's total river discharge (Holmes et al., 2012). The volume of freshwater exported from the eight major Arctic rivers to the Arctic Ocean increased by 7.8% between 1971 and 2019 (AMAP, 2022). An increased net ratio of precipitation minus evaporation is projected, resulting in increased freshwater flux from the land surface to the Arctic Ocean, which is projected to be 30% above current levels by 2100 under representative concentration pathway (RCP) 4.5 (Haine et al., 2015; Meredith et al., 2019).

While Arctic change in the six largest Arctic river basins (Fig. 1-2) has been well documented by the “Arctic Great Rivers Observatory” initiative since 2003 (McClelland et al., 2008), **hydrological datasets for smaller Arctic catchments are scarce** (Speetjens et al., 2022). The larger catchments drain a vast land area encompassing different land cover types and varying permafrost extent. These factors, together with the tremendous difference in catchment area, impact flow pathways and residence time of water differently than in smaller catchments, which could result in significantly different biogeochemical fluxes in larger and smaller catchments to the Arctic Ocean (Holmes et al., 2012). Based on observations in western Siberia, small rivers are anticipated to experience the greatest change in DIC concentrations with climate warming (Pokrovsky et al., 2015).

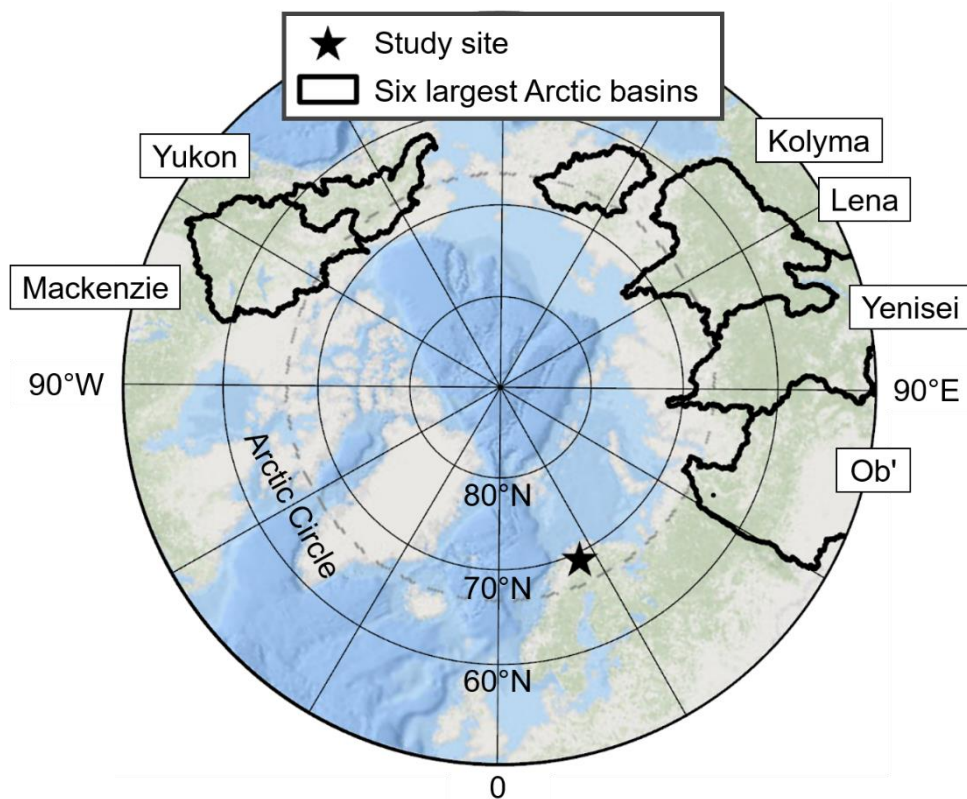


Fig. 1-2: The six largest Arctic drainage basins: Mackenzie, Yukon, Kolyma, Lena, Yenisei, and Ob'. The star indicates the location of the Iskoras sampling site in northern Norway where samples were collected for the studies presented in Chapters 4 and 5. The watersheds were derived from GRDC (2020). Background map from Esri, HERE, Garmin, GEBCO, NOAA, NGDC, and other contributors (ESRI, 2022).

Drake et al. (2018) recently reported a 185% and 135% increase in alkalinity flux between 1974 and 2015 in the largest (by discharge) Arctic river, the Yenisei, and the third largest Arctic river, the Ob', respectively, demonstrating that contemporary climate change in the Arctic is concomitant with

increased weathering and alkalinity generation. Their findings were based on the above-mentioned “Arctic Great Rivers Observatory” datasets (Drake et al., 2018). Alkalinity flux represents the product of alkalinity concentration and discharge. While the increase in alkalinity flux in the Yenisei River was driven by both increasing alkalinity concentration and increasing discharge, the increase in alkalinity flux in the Ob' River resulted only from an increase in alkalinity concentration, as discharge has not changed (Drake et al., 2018). From this, it can be inferred that weathering and alkalinity generation in these two catchments has indeed increased, rather than merely the flushing of solutes in a presumably transport-limited system (see section 1.2.4). On the other hand, a considerably smaller increase in alkalinity flux of 12.5% was observed in the Mackenzie River, the largest contributor of freshwater and DIC flux from the North American continent to the Arctic Ocean, from 1973-2012 (Tank et al., 2016). Here, alkalinity flux increased only during the winter months, mainly due to increasing discharge and secondarily due to concentration (Tank et al., 2016).

Despite its importance, the **transport and transformation of carbon is one of the least understood components of the carbon cycle** (Winnick et al., 2017). Changes in alkalinity flux are primarily due to **changes in the transport rate or in the weathering rate. Disentangling these two main factors, and quantifying each of them, is important for predicting a change in alkalinity flux due to climate change in the future.** Likewise, Drake et al. (2018) advocated a **better understanding of the drivers of the observed increasing alkalinity export and future projections of its magnitude**, as these are crucial to studying carbon sequestration in the terrestrial environment of the Arctic as well as the vulnerability of the Arctic Ocean to acidification (Shadwick et al., 2013).

1.2 Controlling factors on alkalinity generation

To adequately investigate the influence of changing environmental conditions due to climate change on alkalinity generation and thus on CO₂ draw-down, the relationships in an assumed steady state system prior to the onset of change must first be established. To do so, suitable tracers capturing the influence of the respective parameter on alkalinity generation at a reasonable time scale should be identified.

For a given mineral type, the general controls on chemical weathering are the availability of weatherable minerals, mainly provided by physical weathering of regolith, and the supply of weathering agents, i.e., acids

(Raymond and Hamilton, 2018). Further, to generate the soluble weathering products, favorable conditions such as high temperatures, abundant moisture and high contact of mineral surfaces with water should prevail. Lastly, the hydrological transport of these solutes out of the weathering zone is another controlling factor (Raymond and Hamilton, 2018).

1.2.1 Availability of weatherable minerals

The long-term balance between the input and output of minerals and their dissolution products in the weathering zone controls the availability of weatherable minerals, resulting in soils with varying degrees of weathering, from 'fresh' to highly weathered soils (White and Brantley, 2003; Raymond and Hamilton, 2018). The weathering zone has also been termed the 'critical zone' (CZ) or the 'critical zone reactor' whose thickness is determined by the advance of the weathering front by mechanical and chemical processes on the one hand, and mass loss by denudation on the other hand (Fig. 1-3; Anderson et al., 2007). Fresh soils are the result of short residence times within the CZ, driven by faster erosion rates. Those soils are thought to produce higher chemical weathering solute yields due to greater accessibility of weatherable minerals and enhanced mechanical breakdown of rock (Anderson et al., 2002; Riebe et al., 2004; Waldbauer and Chamberlain, 2005; Anderson et al., 2007). Mechanical weathering and physical erosion are driven by stress gradients which fracture and displace material (Anderson et al., 2007). Gravitational stress, phase transformations (such as ice growth, salt precipitation, oxidation or hydration of minerals), or biologic agents (roots and burrowing animals) can induce these stress gradients (Anderson et al., 2007).

However, the positive effect of faster erosion rates on chemical weathering does not appear to hold universally, but only up to a certain threshold, in supply-limited environments. As erosion rates increase, the potential increase in weathering rate due to exposure of fresher materials is compensated by the decrease in total volume of exposed minerals due to thinner regolith (Millot et al., 2002; West et al., 2005; Gabet and Mudd, 2009). The numerical model of Ferrier and Kirchner (2008) suggests that the chemical denudation rate approaches zero in two cases: First, when the physical erosion rate approaches zero because soluble minerals become depleted in the soil, and second, when the physical erosion rate approaches the maximum soil production rate because soil thickness approaches zero. Therefore, an intermediate physical erosion rate results in optimum chemical weathering rates (Ferrier and Kirchner, 2008).

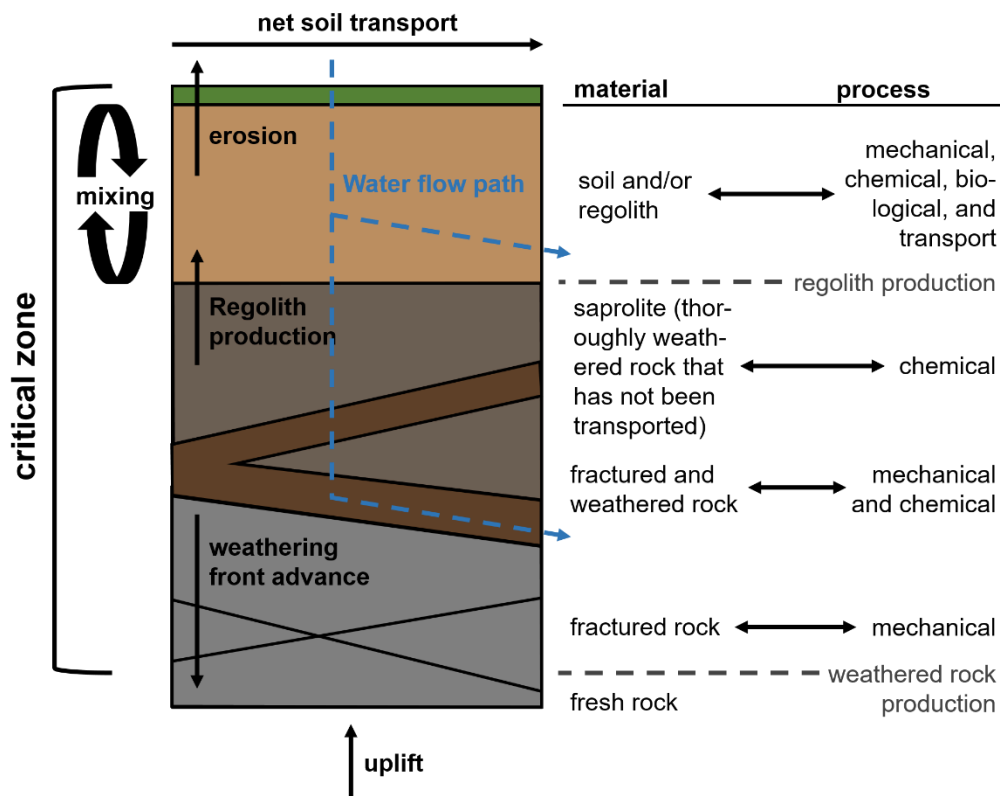


Fig. 1-3: Conceptual model of the critical zone at the Earth's surface. The thickness of the critical zone is determined by the advance of the weathering front by mechanical and chemical processes as well as by mass loss due to erosion. Mixing in the soil and/or regolith can be initiated by bio- and cryoturbation. When infiltration of water occurs below the water table, soil waters become groundwaters (Berner and Berner, 2012). Soil: material with horizons; regolith: disaggregated, transportable material; figure adapted from Anderson et al. (2007).

Fracturing below the CZ, driven by tectonic processes, is an important factor in the advance of the weathering front (Anderson et al., 2007). The rate and geometry of active tectonic faulting is thought to promote physical denudation, and in turn, chemical denudation (Hovius and Blanckenburg, 2007). In addition to rock fracturing, faulting can also initiate a drop in river base level that causes incision of the drainage network. This can lead to a mechanical (enhancement of soil erosion and rates of physical denudation and sediment production) and/or to a chemical chain (development of new groundwater flow paths, resulting in stronger dilution and less saturation of soil pore water which in turn enhances rates of mineral dissolution, ultimately leading to higher chemical weathering and soil production rates; Hovius and Blanckenburg, 2007; Anderson et al., 2007).

Typical supply-limited landscapes are the highly weathered ancient landscapes of the humid tropics and subtropics (Raymond and Hamilton,

2018), such as large parts of the Amazon lowland basin, where new minerals for weathering are derived only from the gradual degradation of the underlying regolith, resulting in thick saprolite (Stallard and Edmond, 1983). Unlike soils, saprolites retain the texture of the rock. Very thick saprolites prevent water from reaching the weathering front, resulting in decreased weathering rates (Berner and Berner, 2012). The absence of recent tectonic forcing prevents high denudation rates in these geologically old landscapes (Anderson et al., 2007). Other cratonic landscapes, such as the Canadian, Siberian and African Shield, also show a directly proportional relation between the weathering rate of silicate cations and physical erosion rate (West et al., 2005).

The counterpart to these old, stable landscapes are young, recently deglaciated terrains where fine-grained glacial debris is readily available for rapid chemical weathering (Raymond and Hamilton, 2018) or mountainous areas with steep slopes and sufficient rainfall, where rapid erosion regularly evacuates the soil and exposes fresh bedrock for further weathering (Berner and Berner, 2012). Generally, such young surfaces consisting of highly erodible sediments are associated with high erosion rates (Musso et al., 2020). The chemical weathering rates in these landscapes are controlled rather kinetically (kinetic-limited) by factors such as temperature, availability of moisture, and contact time of mineral surfaces with water (see section 1.2.3). In many settings, an intermediate weathering situation is reached, in which the CZ thickness is constant and the production of weathered rock is equal to its loss due to erosion, which is known as steady state weathering (Berner and Berner, 2012).

Because the weathering regime threshold that determines whether supply or kinetic limitations prevail is itself a function of kinetic factors, such as temperature and runoff, a change in climate can affect this threshold. **Understanding the time scale of adjustment in the weathering regime to a change in climate is critical for comprehending the response of the weathering system to climatic disturbances** (West et al., 2005).

Tracing long-term erosion rates

A valuable tracer for long-term (10^2 - 10^5 years) catchment-wide average erosion rates in steady state systems is the terrestrial (in situ) cosmogenic nuclide ^{10}Be in river sediments (Brown et al., 1995; Blanckenburg, 2005). While conventional sediment-yield measurements can often substantially underestimate long-term average erosion rates (Kirchner et al., 2001), ^{10}Be -derived erosion rates also capture infrequent high-magnitude events due to their longer observation windows (Blanckenburg, 2005; West et al.,

2005). Furthermore, they are relatively robust to short-term changes (Blanckenburg, 2005). However, the ^{10}Be approach requires that the landscape has achieved steady state with respect to the gradual removal of quartz. Another caveat is that the ^{10}Be -derived erosion rates consider the entire mass loss (chemical and detritus), i.e., total denudation. However, Dixon and Blanckenburg (2012) found that globally physical erosion accounts for about 50-90% of total denudation. The observation window of ^{10}Be -derived denudation rates is a function of the denudation rate itself (Lal, 1991; Blanckenburg, 2005). While rapidly eroding catchments show very short averaging time scales of about 10^2 years, slowly eroding ones are characterized by averaging time scales of 10^4 - 10^5 years.

In situ ^{10}Be is produced by interaction with secondary cosmic rays in quartz in the uppermost layer of the Earth's surface (Gosse and Phillips, 2001). Briefly, the method for determining ^{10}Be -derived denudation rates is based on a characteristic production depth scale of about 1 m. The measured ^{10}Be concentration records an integrated denudation history as the material passes through this depth interval (Blanckenburg, 2005). This means that material that erodes slowly is exposed to cosmic rays for a longer time within the production window than material that is removed rapidly. Hence, denudation rates are inversely related to ^{10}Be concentrations under steady state conditions. Measurement of the ^{10}Be concentration in river sediment at the outlet of a catchment allows one to average total denudation rates over both the whole basin area and long time periods.

1.2.2 Availability of weathering agents

Weathering rates are limited by the availability of weathering agents, i.e., acidic fluids, as they drive the dissolution reaction by supplying protons. The protons replace cations on mineral surfaces, thus bringing about disintegration of the minerals (Berner and Berner, 2012). The main source for terrestrial weathering is carbonic acid (H_2CO_3), a weak acid, which partly dissociates into a proton and bicarbonate. Carbonic acid is formed by the combination of water with CO_2 , which mostly comes from the atmosphere or from soil respiration, i.e., the oxidation of organic matter by microbes (Berner and Berner, 2012).

Other acids driving weathering reactions are weak organic acids (carboxylic acids) from vegetation and strong inorganic acids, mainly sulfuric (H_2SO_4) and nitric (HNO_3) acid, derived from the oxidation of sulfides and ammonium, respectively (Raymond and Hamilton, 2018). Human activities have resulted in the addition of excess acid to soils, which includes sulfuric

and nitric acid from acid rain and sulfuric acid from mining of coal or metallic sulfides (Berner and Berner, 2012).

Tracing availability and differentiating weathering agents

Weathering agents can be traced by examining the composition of anion loads in river or groundwater samples. While weathering reactions with carbonic acid produce bicarbonate ions, those with sulfuric and nitric acid generate sulfate and nitrate ions, respectively. To gain further insight, these anion compositions can be combined with the stable isotope composition of DIC, $\delta^{13}\text{C-DIC}$ (see section 4 or, e.g., Li et al., 2010). These measurements represent a snapshot of the current state. To obtain an impression of the average weathering situation, the occurrence of different weathering agents should be monitored over several years to several decades, capturing all seasons, as soil respiration is greater during the summer months (Jones and Mulholland, 1998; Watts et al., 2022). Hydrochemical data from decade-long studies or monitoring programs are accessible through global compilations, such as the GLORICH database (Hartmann et al., 2019).

For a general assessment of the availability of weathering agent in the form of carbonic acid in a certain region or at the global scale, soil partial pressure of CO_2 ($p\text{CO}_2$) at the weathering front is estimated (Zeng et al., 2022). Process-based or empirical models approximate $p\text{CO}_2$ by using evapotranspiration (Brook et al., 1983), net primary productivity (Gwiazda and Broecker, 1994; Godd ris et al., 2010) and soil volumetric water content (Romero-Mujalli et al., 2019b). Lastly, at a local scale, $p\text{CO}_2$ can also be measured directly in soil and groundwater (Marx et al., 2017a).

1.2.3 Generation of soluble products

The reaction rate depends on a combination of parameters, such as pH, temperature, the degree of solution undersaturation with respect to the mineral to be dissolved, and concentrations of dissolved reacting species, and soil hydrology (Berner and Berner, 2012).

Temperature is a strong modulator on reaction rate due to its effect on reaction kinetics and solubility. It has a non-linear positive effect on reaction rate following the Arrhenius law (White and Blum, 1995). Unlike silicate minerals, carbonate minerals are less soluble at higher temperatures (Raymond and Hamilton, 2018).

Weathering is controlled by the saturation state of water in the CZ (Anderson et al., 2007). Insufficient moisture in soils can cause weathering to essentially cease, e.g., soil solutions in small soil pores between rainfalls can come to equilibrium with the minerals undergoing dissolution. Therefore, a continuous influx of fresh water is required to sustain dissolution reactions, e.g., by new precipitation flushing out these soil pores (Berner and Berner, 2012). Finally, sufficient residence time of water in contact with minerals, which facilitates wetting of mineral surfaces and allows time for reaction, and a large mineral surface area promote weathering (Raymond and Hamilton, 2018).

Tracing controlling factors on reaction kinetics

Climate data, such as annual mean air temperature (MAT) and annual mean precipitation (MAP), are widely available, either locally from records at individual weather stations or spatially interpolated from global datasets, such as the WorldClim database (Fick and Hijmans, 2017). To investigate the influence of these climate variables on alkalinity generation, a record over a period of several years to several decades would be appropriate.

Besides field studies, functional relations of weathering rates and mechanisms to important variables such as temperature, pH or the degree of solution undersaturation with respect to the mineral to be dissolved are examined in laboratory experiments. However, these experiments often cannot reproduce field conditions as flow paths and wetting and drying of mineral surfaces differ strongly from laboratory studies in which suspended particles are continuously exposed to a highly undersaturated, agitated solution (Berner and Berner, 2012)

1.2.4 Hydrological connectivity

The transport of solutes out of the CZ into rivers is governed by gradients in hydraulic conductivity. These gradients are controlled by porosity, pore size, and water content. While infiltration and percolation of precipitation brings water to the weathering zone, evapotranspiration removes water from soils to the depth at which plant roots occur (Raymond and Hamilton, 2018).

Generally, water flow rate decreases with CZ depth (Anderson et al., 2007). At low rates of water throughput (long water residence times in the CZ), solute fluxes to the fluvial system become transport-limited. On the other hand, a high water throughput (short water residence times in the CZ) should in principal promote a higher solute flux to the river system. However, as the contact time of mineral surfaces with water is reduced,

decreasing the reaction time, solute fluxes to the river system become reaction-limited (Raymond and Hamilton, 2018). Based on his studies of weathering rates in granitic sediments, Maher (2010) proposed that most weathering systems are transport-limited because typical hydrologic fluxes at the Earth's surface are slow. From this predominance of transport-limited weathering, he further deduced that chemical weathering rates depend more strongly on fluid flow, pH, and mineral solubility than on mineral surface area and mineral kinetics (Maher, 2010).

Finally, at the catchment scale, hillslopes may connect to the stream only during certain precipitation events or seasons. Hydrological connectivity can be achieved either through surface (overland) or subsurface flow (Blume and van Meerveld, 2015). In many areas in a temperate climate, subsurface stormflow is the main runoff generation mechanism on hillslopes after the development of saturation above a less permeable layer, such as at the soil-bedrock interface (Weiler et al., 2006; Blume and van Meerveld, 2015). Under high antecedent soil moisture conditions, transient water tables form (Weiler et al., 2006), connecting solute-charged groundwater with the river system. In settings with frozen soils, however, water infiltration is limited and surface runoff is the predominant mechanism for generating runoff (Johnsson and Lundin, 1991).

When the hillslope catchment is saturated, caused by a long rainfall event, water is transmitted rapidly, via preferential flowpaths, from the hillslopes through the riparian zone to the stream. In contrast, during dry conditions, the hillslope contribution to runoff is limited (Camporese et al., 2014).

Tracing the hydrological transport of solutes to rivers

A simplistic approach to monitoring the transport efficiency of weathering products from the CZ to rivers at the catchment scale is to compare solute concentrations in soil and groundwater, ideally performing multiple measurements along a transect perpendicular to the channel (González-Pinzón et al., 2015; Coch et al., 2020), with concentrations in rivers.

Hydrological connectivity on a broader scope can be tracked by performing soil moisture analyses, shallow water table measurements, or by deploying surface runoff and subsurface sensors, among other methods (Bracken et al., 2013). However, hydrological connectivity has been interpreted and measured differently between research groups (Bracken et al., 2013).

1.3 Alkalinity generation at the global scale

Although it is widely accepted that **rock type and river discharge are the two most dominant factors controlling global alkalinity fluxes to the ocean, it has proven difficult to quantify the impact of other first-order controlling factors** (Amiotte Suchet and Probst, 1993; Amiotte Suchet and Probst, 1995; Hartmann, 2009; Hartmann et al., 2009; Lechuga-Crespo et al., 2020). **Particularly challenging remains the separation of climatic and erosional influences.**

While there is general agreement that **physical erosion rate and soil acidity** are first-order controls in addition to catchment lithology and river discharge, it is **challenging to precisely quantify these controls at regional to global scales, and records that are both spatially diverse and temporally comprehensive remain scarce** (Calmels et al., 2014; Romero-Mujalli et al., 2019a). Quantifying the influence of soil $p\text{CO}_2$ on alkalinity generation has been attempted with various models that approximate soil $p\text{CO}_2$, e.g., based on net primary production, yet no single model by itself appears to perform well at the global scale (Zeng et al., 2022). As a proxy for physical erosion rate, suspended matter flux and land cover (Hartmann, 2009), a soil shielding term based on empirical findings that different soil types are associated with different degrees of reduction in weathering rate (Hartmann et al., 2014), or regolith thickness (Lechuga-Crespo et al., 2020) have been used. **A global assessment including actual measurements of physical erosion rates is still missing.**

The influence of temperature on weathering at the global scale has been long debated (Hartmann et al., 2009; Lechuga-Crespo et al., 2020), although two recent global studies reveal optimal carbonate weathering in temperate climates (Gaillardet et al., 2019; Romero-Mujalli et al., 2019a).

While regional studies show that physical erosion can enhance weathering, at least for low to moderate erosion rates, i.e., in supply-limited systems (West et al., 2005; Blanckenburg, 2005; Lyons, 2005; Jacobson and Blum, 2003; Millot et al., 2002), **no such relationship between physical erosion and alkalinity flux has been identified at the global scale** (Hartmann, 2009; Hartmann et al., 2009; Lechuga-Crespo et al., 2020).

1.4 Alkalinity generation in a changing Arctic

In northern high latitudes, carbonate weathering is expected to increase in the future, and with it the carbon-sink function, as soil $p\text{CO}_2$ and temperature increase (Zeng et al., 2022). Although direct causes could not be conclusively determined, a dramatic increase in alkalinity flux (134-185%) was recorded in two of the largest Arctic rivers from 1974 to 2015, in parallel with Arctic amplification (Drake et al., 2018). Potential drivers of this increase may have been higher temperatures, increased precipitation, permafrost thaw, changes to hydrologic flow paths, shifts in vegetation, and decreased acid deposition from industrial activity (Drake et al., 2018).

As discussed in section 1.2.3, elevated temperatures and precipitation are drivers of increased weathering and alkalinity generation because they directly affect reaction kinetics and moisture conditions. Higher plants, such as trees, are thought to accelerate weathering compared to barren ground or that inhabited by mosses and lichens because, amongst others, their roots release organic acids and allow for greater moisture retention (Berner et al., 2003; Berner and Berner, 2012).

Because analyses to date suggest that the sensitivity of the Arctic carbon cycle is highly uncertain for the remainder of the 21st century, there is a **pressing need to collect data on observations of carbon dynamics in regional studies and link them to the processes that are likely to drive those** (McGuire et al., 2009).

1.4.1 Degrading permafrost

Permafrost or perennially frozen ground is any soil, regolith, or bedrock that remains below 0°C for two or more consecutive years regardless of its moisture content or lithology (Muller and Geological Survey, 1945). Approximately 15% of exposed land in the Northern Hemisphere is covered by permafrost (Obu et al., 2018). Based on its areal extent, permafrost is subdivided into four categories: continuous (> 90%), discontinuous (50-90%), sporadic (10-50%), and isolated patches (< 10%; Brown et al., 1997). While the typical permafrost thickness is 100-800 m for continuous permafrost, it is only 10-50 m for sporadic permafrost (Anisimov, 2005). The uppermost part of the permafrost thaws seasonally even in the most severe climatic regimes. The thickness of this so-called active layer ranges from several centimeters to a few meters (Dixon, 2013). The thickness of the active layer is controlled principally by air temperature, but is also influenced by snow cover, vegetation, and the thickness of organic matter

(Dixon, 2013). The seasonal thawing of the active layer drives ground disturbances in permafrost terrains, such as ground settling, frost heave, solifluction, detachment slides, and retrogressive thaw slumps (Dixon, 2013).

Permafrost is currently thawing rapidly across the Arctic (Biskaborn et al., 2019). It has warmed by 2-3°C since the 1970s and the active layer thickness has increased at many sites since the 1990s (AMAP, 2022). By the end of this century, Arctic near-surface permafrost is projected to decrease by 2-66% and 30-90% under RCP2.6 and RCP8.5, respectively, essentially leading to widespread disappearance (Meredith et al., 2019).

Since **most of the scientific work about permafrost thaw in the Arctic has focused on the exposure of ancient organic carbon stored in permafrost**, which releases large amounts of greenhouse gases into the atmosphere after microbial degradation and thus represents a positive feedback process in climate change (e.g., Schuur et al., 2015; Natali et al., 2021), **less has been published on the release of dissolved inorganic carbon or alkalinity** (Tank et al., 2012; Dornblaser and Striegl, 2015; Pokrovsky et al., 2015; Lehn et al., 2017; Zolkos et al., 2020). In general, permafrost thaw is anticipated to promote weathering (Frey and McClelland, 2009) by causing the Arctic terrestrial freshwater system to improve its connectivity between surface waters and deeper groundwater pathways (Striegl et al., 2005; Walvoord and Striegl, 2007). It may ultimately move from a surface water-dominated to a groundwater-dominated system (Frey and McClelland, 2009). Thawed soils allow for longer residence times of infiltrating surface water, thereby facilitating more contact with unweathered mineral surfaces and additional mixing with mineral-rich groundwater, resulting in higher alkalinity fluxes (Drake et al., 2018).

In contrast to fast Arctic coastal erosion with rates of up to 25 m yr⁻¹ (Jones et al., 2009; Günther et al., 2015) and rapid erosional responses to abrupt thaw processes of ice-rich permafrost further inland, such as thermokarst (Kirkby, 1995; Osterkamp et al., 2009; Toniolo et al., 2009; Rowland et al., 2010; Lamoureux et al., 2014; Olefeldt et al., 2016), **quantifications of potentially enhanced erosion rates due to gradual permafrost thaw in Arctic regions, where permafrost degradation is already well advanced, are missing**. Gradual permafrost thaw is considered a so-called press disturbance, which unfolds its effects at larger spatial and longer temporal scales (decades to centuries) than the so-called pulse disturbances (Collins et al., 2007; Grosse et al., 2011). However, when a certain threshold is reached, a press disturbance could trigger pulse disturbances,

e.g., widespread top-down permafrost thaw could initiate increased soil erosion (Grosse et al., 2011).

Tracing short-term erosion rates

An emerging tracer for current erosion rates are the anthropogenic radionuclides ^{239}Pu and ^{240}Pu . These so-called fallout radionuclides (FRNs) were distributed globally mainly by nuclear weapons fabrication and testing in the 1950s to 1960s (Alewell et al., 2014). Therefore, they provide a current erosion rate averaged over the last 60-70 years. After reaching the Earth's surface, Pu is strongly adsorbed to the fine earth fraction in the topsoil, which makes it suitable as a soil distribution tracer (Loba et al., 2022). Soil distribution rates are calculated by comparing the total FRN inventory per unit area of a reference site, which is assumed to have experienced neither erosion nor deposition since fallout, with the one of the site of interest. When the inventory of the study site is lower (higher) than the one of the reference site, the study site experienced erosion (deposition) since fallout (Alewell et al., 2017).

Compared to the established soil erosion tracer ^{137}Cs , the only recently introduced Pu isotopes offer the advantage of a longer half-life (24,110 years for ^{239}Pu and 6,561 years for ^{240}Pu) and a homogeneous spatial distribution (Loba et al., 2022). Because ^{137}Cs has a short half-life of 30 years, about 70% of its global fallout has already disappeared through radioactive decay (Xu et al., 2015). Furthermore, as most of the fallout ^{137}Cs originates from the 1986 Chernobyl incident and not nuclear weapons fabrication and testing, its deposition was rather heterogeneous in Europe (Loba et al., 2022). The **employment of the relatively new soil erosion tracer $^{239+240}\text{Pu}$** in tundra landscapes has been limited to alpine sites (Portes et al., 2018; Zollinger et al., 2015) and has **not previously been applied in high latitude regions** (Loba et al., 2022).

1.5 Research questions

The overall aim of this thesis is to investigate the influence of erosion rate on terrestrial alkalinity generation. This is examined firstly at the global scale, and secondly, in the context of accelerated climate change, in a case study of an Arctic headwater catchment in northern Norway, where permafrost degradation is already well advanced. Furthermore, for the same catchment, the weathering pathways are investigated responsible for alkalinity generation and the influence of environmental forcing on alkalinity release. With this thesis, I will address the following research questions:

- 1) Is erosion rate a controlling factor on terrestrial alkalinity generation at the global scale?
 - If so, what are the dependencies between erosion rate and terrestrial alkalinity generation?

I will attempt to answer these questions by compiling and evaluating a global dataset that pairs measured alkalinity concentrations with ^{10}Be -derived catchment-wide average erosion rates.

- 2) What is the influence of environmental forcing on alkalinity release in a small Arctic headwater catchment in a degrading permafrost landscape during fall? In particular:
 - Is the primary pathway for alkalinity generation the weathering of silicate minerals?
 - How is alkalinity release hydrologically controlled in this hillside catchment underlain by sporadic permafrost?

I will attempt to answer these questions by analyzing hydrochemical data, such as AT, DIC, cation and anion loads, and stable isotope signatures of DIC and H_2O , from water samples collected in the fall of 2020 in the headwater catchment of interest.

- 3) Has the erosion rate in a small Arctic headwater catchment in a degrading permafrost landscape increased in the last few decades due to contemporary climate change?

I will attempt to answer this question by comparing a long-term pre-industrial erosion rate with a short-term current erosion rate by combining different tracers. In particular, I will quantify the long-term erosion rate using ^{10}Be concentrations in stream sediments and the short-term erosion rate using $^{239+240}\text{Pu}$ inventories in soil cores.

1.6 Thesis structure

This thesis includes an Introduction (Chapter 1), a description of the methods (Chapter 2), three original research papers that are currently under review or revision for publication in international peer-reviewed journals or close to submission (Chapters 3, 4 and 5), and a Conclusion (Chapter 6).

The study in Chapter 3 identifies first-order controlling factors on alkalinity generation at the global scale and shows that the weathering flux to the ocean will be significantly altered by climate warming as early as the end of this century. This study combines global riverine alkalinity data with consistent erosion rate measurements to develop an empirically-based model. The study in Chapter 4 identifies the weathering pathways responsible for alkalinity generation in a small Arctic catchment in northern Norway mainly dominated by silicate minerals and underlain by sporadic permafrost during fall 2020, and explains temporal variations in AT concentrations following a precipitation event. The study in Chapter 5 quantifies a long-term pre-industrial erosion rate derived from ^{10}Be concentrations in stream sediments and a short-term current erosion rate derived from $^{239+240}\text{Pu}$ inventories in soil cores of the same catchment as in Chapter 4.

- **Chapter 3.** Lehmann, N., Stacke, T., Lehmann, S., Lantuit, H., Gosse, J., Mears, C., Hartmann, J., Thomas, H. Alkalinity responses to climate warming destabilize the Earth's thermostat. Manuscript under revision in *Nature Communications* (Manuscript ID: NCOMMS-22-22577A).
- **Chapter 4.** Lehmann, N., Lantuit, H., Böttcher, M. E., Hartmann, J., Eulenburg, A., Thomas, H. Manuscript under review in *Biogeosciences*. A preprint is available at <https://doi.org/10.5194/bg-2022-205>.
- **Chapter 5.** Lehmann, N., Stübner, K., Lantuit, H., Gosse, J., Fiener, P., Ketterer, M., Lachner, J., Rugel, G., Zimmermann, T., Pröfrock, D., Thomas, H. $^{239+240}\text{Pu}$ inventories from soil cores and in situ ^{10}Be concentrations from stream sediments at Iskorasfjellet, northern Norway: Implications for current and long-term erosion.

The following datasets were published in a scientific data repository as follows:

- Lehmann, N., Thomas, H. (2021): Alkalinity and DIC data in water samples from the Alps and Germany collected in 2020. PANGAEA, <https://doi.org/10.1594/PANGAEA.939660>

- Lehmann, N., Mears, C., Thomas, H. (2022): ^{10}Be erosion rates and riverine alkalinity concentration globally. PANGAEA, dataset in review, <https://doi.pangaea.de/10.1594/PANGAEA.940522>

1.7 Author contributions

Chapter 3.

N. Lehmann, H. Thomas and J. Gosse designed the study. **N. Lehmann** and S. Lehmann participated in sample collection. **N. Lehmann** measured the DIC concentration in the collected samples. **N. Lehmann** and C. Mears built the dataset. **N. Lehmann** analyzed the data. **N. Lehmann** and S. Lehmann developed the model. T. Stacke provided the data (simulated discharge and temperature data) for analyzing the effect of climate warming. **N. Lehmann** wrote the draft with the help of H. Thomas, H. Lantuit, J. Gosse and T. Stacke, and with input from all other co-authors.

Chapter 4.

N. Lehmann, H. Lantuit and H. Thomas designed the study. **N. Lehmann** led the field research and coordinated laboratory analyses. **N. Lehmann** measured DIC concentration. A. Eulenburg measured cation and anion concentrations. M. E. Böttcher and J. Hartmann contributed (isotope) analytical measurements and data interpretation. **N. Lehmann** wrote the draft with the help of H. Thomas, H. Lantuit and M. E. Böttcher, and with input from all other co-authors.

Chapter 5.

N. Lehmann, J. Gosse, H. Lantuit and H. Thomas designed the study. **N. Lehmann** led the field research and coordinated laboratory analyses. **N. Lehmann** prepared the ^{10}Be AMS targets with the help of K. Stübner. J. Lachner and G. Rugel conducted the ^{10}Be AMS measurement and data evaluation. M. Ketterer prepared the $^{239+240}\text{Pu}$ samples and measured them using ICP-MS. T. Zimmermann and D. Pröfrock provided multi-element data from ICP-MS measurements. **N. Lehmann** wrote the draft with the help of H. Thomas, H. Lantuit, K. Stübner and P. Fiener, and with input from all other co-authors.

2 Methods

2.1 Quantifying short- and long-term erosion rates

To assess a potential change in erosion rate due to on-going climate change, both a current and a long-term, pre-industrial erosion rate must be determined. Suitable methods to capture the erosion rate of the last decades and up to the last hundreds of thousands of years are the FRN $^{239+240}\text{Pu}$ and the terrestrial cosmogenic nuclide ^{10}Be , respectively. To determine the concentration of the respective tracer, both methods follow a similar procedure of sampling, physical preparation, chemical extraction and measurement.

In terms of processing times and costs, each method has its advantages and disadvantages. As the erosional behavior was to be averaged over a small headwater catchment, 83 soil cores were taken according to a grid scheme and 10 additional cores, which served as a reference, were taken for $^{239+240}\text{Pu}$ analysis. This resulted in a long processing time both in the field and in the laboratory to prepare each increment for chemical extraction of the target element (Fig. 2-1a).

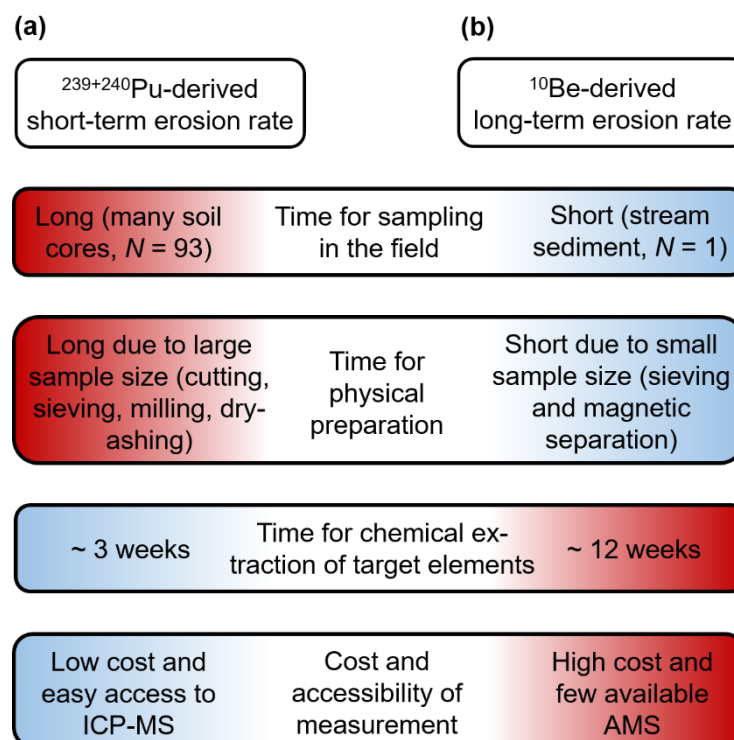


Fig. 2-1: Comparison of time for sampling, physical preparation and chemical extraction, and cost and accessibility of measurement technique between (a) $^{239+240}\text{Pu}$ and (b) in situ ^{10}Be . The time for chemical extraction of in situ ^{10}Be can be reduced when

the original material contains a higher quartz content. The chemical preparation of a 'pure' quartz sample takes about 2-3 weeks.

In contrast, the effort to take a sample for ^{10}Be analysis, i.e., collecting about 2 kg of stream sediment, is very small. Furthermore, the river sediment sample taken at the outlet of the catchment integrates over the entire catchment, so that if the erosion rate of only one catchment is to be determined, the effort for the physical preparation preceding the chemical extraction remains within reasonable limits (Fig. 2-1b). In my case, however, the chemical extraction of in situ ^{10}Be required a comparatively long time (~12 weeks) because the original stream sediment grains were not pure quartz, but contained a relatively high amount of impurities that I had to remove. The chemical preparation of a 'pure' quartz sample takes about 2-3 weeks. This is approximately the amount of time it takes to chemically prepare the $^{239+240}\text{Pu}$ samples. Finally, since the introduction of measurement by inductively coupled plasma mass spectrometry (ICP-MS; Eroglu et al., 1998; Muramatsu et al., 2001; Ketterer et al., 2002), measuring $^{239+240}\text{Pu}$ is much less expensive and easily accessible. In contrast, the measurement of ^{10}Be by accelerator mass spectrometry (AMS) is both costly and more difficult to access, as there are only 80 AMS facilities worldwide (Merchel et al., 2012). In the following, the procedure for each method, from sampling to measurement, is presented.

2.1.1 Short-term erosion rates derived from $^{239+240}\text{Pu}$

While I participated in the on-site sampling and coordinated the entire procedure leading up to the measurement, I was supported in the physical preparation, chemical extraction, and measurement. Nevertheless, in the following I will briefly outline the main steps.

To cover the entire catchment area, 83 soil cores were extracted in a grid sampling scheme (distance to the next sampling points ~100 m). Additionally, 10 reference soil cores on two flat hilltops adjacent to the catchment were taken assuming that these represent soil profiles without erosion or deposition. Cores were taken with a mechanical corer (diameter = 5 cm) to the depth where a gravel layer or bedrock was encountered. The sampled material was stored in inner liner tubes and brought back to the laboratory, where we performed subsampling and further processing (Fig. 2-2).

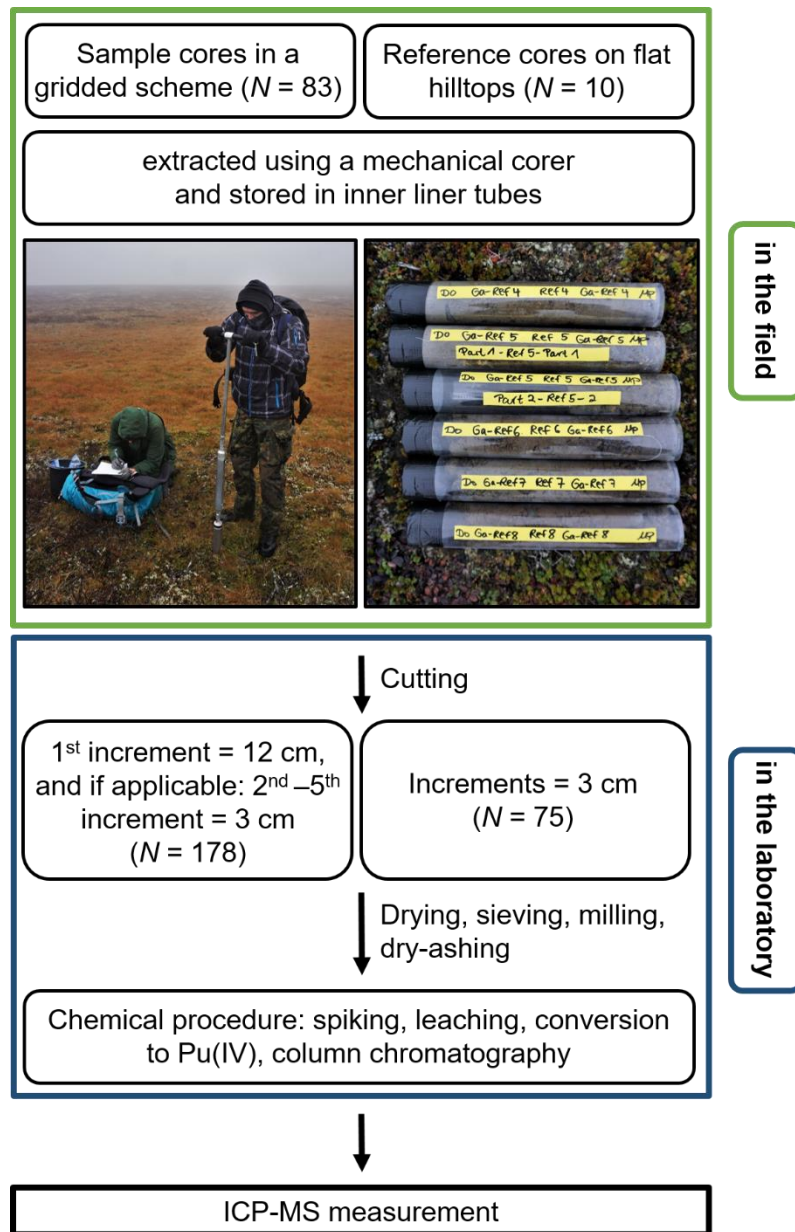


Fig. 2-2: Overview of the method for $^{239+240}\text{Pu}$ – from sampling in the field to ICP-MS measurement. A distinction is made between sample and reference cores.

In the laboratory at Helmholtz-Zentrum Hereon, the reference cores (mean soil core length = 25 cm) were cut in increments of 3 cm, resulting in a total of 75 subsamples. In contrast, the first increment of the sample cores (mean soil core length = 14 cm) was 12 cm. For core lengths greater than 12 cm, the remaining core was cut into shorter increments of 3 cm, resulting in a total of 178 subsamples (Fig. 2-2). After cutting, the samples were air-dried and manually sieved to 2 mm. The fine earth fraction (< 2 mm) was then milled and dry-ashed to remove any organic matter.

In the framework of a master thesis (Rohrweber, 2022), the chemical preparation and measurement was attempted to be optimized at Helmholtz-

Zentrum Hereon. However, time was insufficient to complete this optimization, which meant that my samples could not be measured at Hereon. The dry-ashed samples were instead sent to the Trace Element Analysis Center at Northern Arizona University, USA, where they were chemically prepared by Michael Ketterer according to an adapted version of the protocol presented by him and colleagues in Ketterer et al. (2004), and were subsequently measured. The chemical procedure was as follows: Each sample was spiked with a ^{242}Pu tracer solution, leached with 8 M HNO_3 , and membrane-filtered at 0.45 μm and rinsed with water. Then, $\text{FeSO}_4 \cdot 7\text{H}_2\text{O}$ and NaNO_2 were added in the form of concentrated aqueous solutions to convert Pu to the Pu(IV) oxidation state. After the conversion to Pu(IV) was complete, TEVA resin was added to the sample solutions. After the sample-resin mixtures were homogenized, the resin was collected using a plastic column with a glass wool plug. After discarding the pass-through sample solution, the resin columns were rinsed with the following sequence to remove matrix elements, U and Th: i) 2 M HNO_3 ; ii) 9 M HCl ; and iii) 2 M HNO_3 . Finally, Pu was eluted with the following sequence: i) H_2O ; ii) 0.05 M ammonium oxalate; and iii) H_2O .

Activities of $^{239+240}\text{Pu}$ (in Bq kg^{-1}) were measured using a quadrupole ICP-MS system. The masses of ^{239}Pu and ^{240}Pu in the samples were converted into the summed activity $^{239+240}\text{Pu}$. A detection limit of 0.01 Bq kg^{-1} $^{239+240}\text{Pu}$ was estimated for a sample of nominal mass of 10 g.

2.1.2 Long-term erosion rates derived from ^{10}Be

After collecting the samples in the field and sieving them in the laboratory at Helmholtz-Zentrum Hereon, I performed the physical and chemical processing under the guidance of Silke Merchel and Konstanze Stübner at Helmholtz-Zentrum Dresden-Rossendorf (HZDR). The prepared samples were measured by the Ion Beam Centre (IBC) team at the AMS facility at HZDR in the framework of the GATE project. A GATE proposal can be used to request free beam time at the IBC. Even though I only used the ^{10}Be concentration in the stream sediment at the outlet of the Gaskabohki catchment for comparison with the Pu-derived short-term erosion rate, I processed seven other samples and one processing blank in parallel (batch of $N = 9$). By determining concentrations in the other seven samples, I was able to better evaluate the general long-term erosion behavior in the area studied in northern Norway. One processing blank was added to monitor any possible unwanted contributions, such as contamination between samples in the chemistry laboratory and during measurement, and from any chemical products and target preparation materials used. In the

following, I will explain the individual steps in physical and chemical processing and give a brief introduction to AMS at the end.

Physical and chemical preparation of samples for in situ ^{10}Be AMS measurement

Since the production rate of in situ ^{10}Be is very low, even long exposure quartz samples have very low in situ ^{10}Be concentrations of sub-ppq (sub parts per quadrillion, $< 10^{-15}$; Hunt et al., 2008; Merchel et al., 2012). Enrichment by up to a factor of 10^6 is required to allow analysis of typical 1 mg targets (Merchel et al., 2012). In addition, the removal of elements interfering with the AMS measurement that are commonly found in quartz, such as Ti and Fe, the retardation of the isobar ^{10}B , and the complete separation of Be and Al are essential for the successful preparation of AMS targets from sediment samples (Hunt et al., 2008; Binnie et al., 2015).

The samples were dry-sieved and the 400-630 μm fraction was further processed. To enrich the quartz grains from the polymineral samples, first a magnetic separation was performed using a Frantz magnetic separator. The principle is based on separating the magnetic grains from the non-magnetic quartz-containing grains (Fig. 2-3). After one round of leaching with HCl (32%) and H_2SiF_6 (35%) in a mixing ratio of 1:3, the samples were visually found to remain contaminated, so a density separation using sodium polytungstate in water at densities of 2.70 g cm^{-3} was performed second. With this method, grains that have a density higher than 2.7 g cm^{-3} sink down into the funnel and are thus removed. Grains with a density lower than 2.7 g cm^{-3} , on the other hand, remain at the top of the funnel. This is the case for grains containing mainly quartz, since quartz has a density of 2.65 g cm^{-3} (Fig. 2-3). Presumably, this step unfortunately did not quantitatively remove the feldspars that are abundant in the sampling area, as they have a similar density to quartz, e.g., plagioclase (Na, Ca) feldspars have a density of 2.62 to 2.76 g cm^{-3} (Kohl and Nishiizumi, 1992).

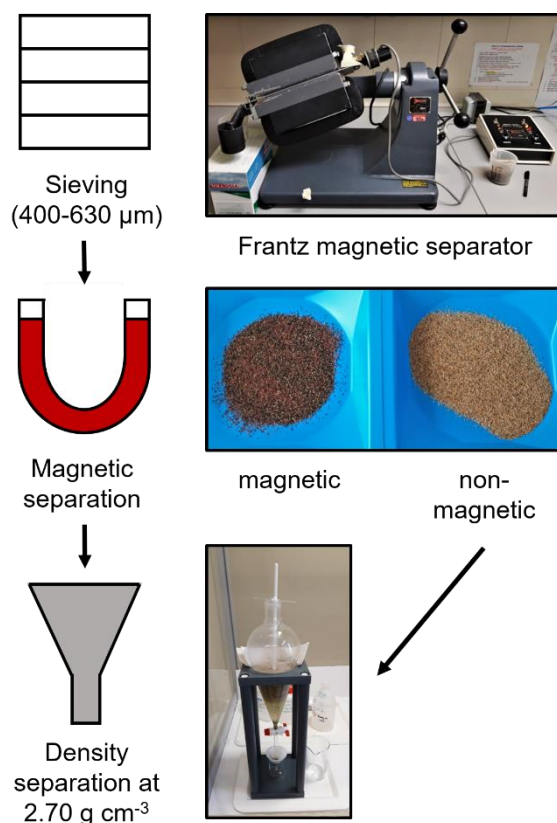


Fig. 2-3: Steps for separating grains containing quartz from grains not containing quartz. After sieving, quartz grains are separated on the basis of their magnetic properties (quartz is non-magnetic) and their density (quartz has a density of 2.65 g cm⁻³).

To further remove residual non-quartz minerals, we leached the samples several times with acid solutions of different concentrations (Fig. 2-4): starting with solutions of HCl (32%) and H₂SiF₆ (35%) in different mixing ratios (1:3 to 1:1; Merchel et al., 2019) and finally with diluted HF (2%). After each leaching step, the samples were thoroughly washed with H₂O and examined under the microscope to check the progress of the purification. This was repeated until the samples were found to be quartz pure under the microscope. This was subsequently verified by ICP-MS measurement. Here, the concentration of Al is of particular interest. It is important that much of the Al initially present in the sample has been removed by this step (concentration of Al < 100 ppm) as Al was found to depress ⁹Be³⁺ beam currents beyond the effects of dilution which impacts the quality of the AMS ¹⁰Be measurement (Hunt et al., 2008). Continuing with higher aluminum concentrations at this stage may cause the column capacity to be overloaded with Al at a later stage, which may lead to Be eluting too early, along with Al and other elements (Binnie et al., 2015).

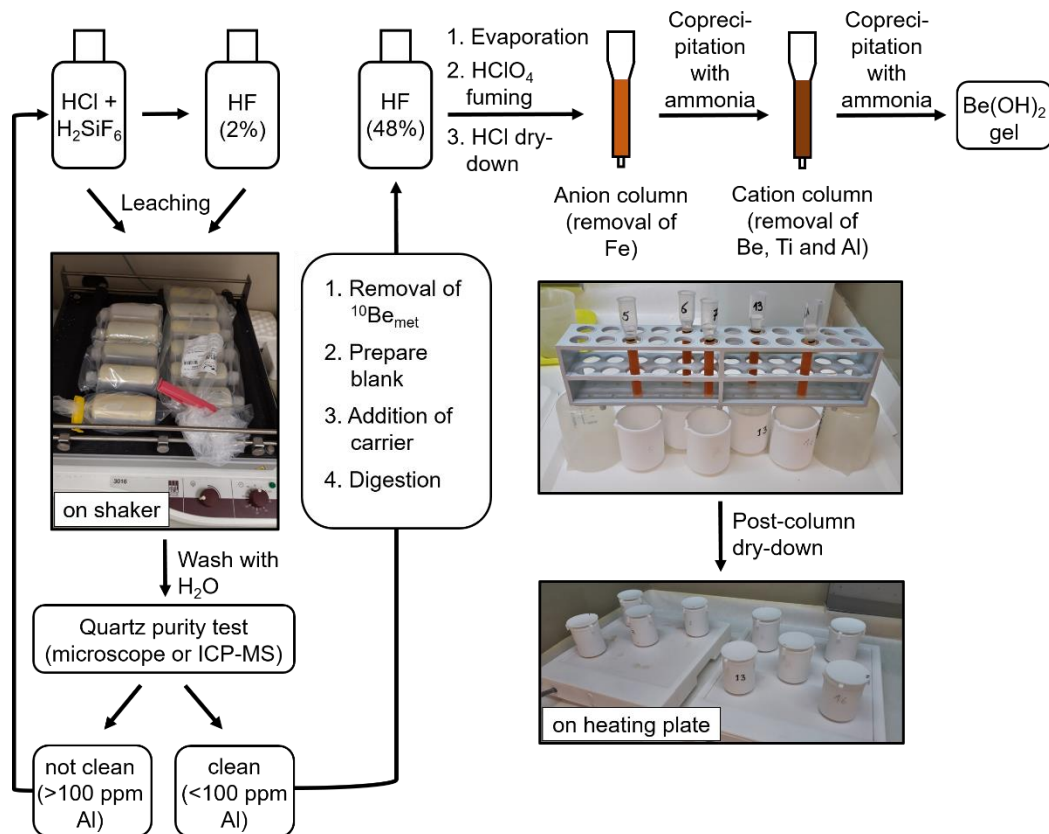


Fig. 2-4: Steps for the chemical purification of in situ ^{10}Be . After several rounds of leaching, until a sufficiently low Al concentration is reached, meteoric ^{10}Be is removed, the ^9Be carrier is added, and the material is completely digested by the addition of HF (48%). After anion and cation exchange columns and selective coprecipitation with ammonia solution, the $\text{Be}(\text{OH})_2$ gel is obtained.

After a sufficiently low Al concentration was detected by ICP-MS, meteoric ^{10}Be was dissolved from the surface of the grains by the addition of HF (48%). Meteoric ^{10}Be is produced by cosmic rays in the atmosphere and brought to the Earth's surface by wet and dry deposition where it is readily adsorbed onto mineral surfaces (Blanckenburg et al., 2012). It is several orders of magnitude more concentrated than its in situ counterpart. Enough HF (48%) was added so that about 30% of the total material should have dissolved. Thereby, the minerals at the surface of the grains react most rapidly, so that it can be assumed that the meteoric Be has been quantitatively removed. Subsequently, $\sim 300 \mu\text{g}$ of ^9Be carrier was added to about 20 g of sample and all the material was digested in HF. Following the evaporation of remaining HF, samples were fumed with perchloric acid (HClO_4) to break up and drive off fluoride compounds (Ochs and Ivy-Ochs, 1997; Corbett et al., 2016). The samples were then fumed with HCl to convert them to the chloride form.

First, Fe was removed by anion exchange column chromatography, since Fe forms anionic complexes when dissolved in HCl, but Be does not. Accordingly, Be was eluted with the first column volume of HCl, while the Fe anionic complex was retained by the column. Second, after coprecipitation with ammonia solution, the samples were redissolved in HCl and B, Ti, and Al were removed by cation exchange column chromatography. Trivalent cations such as Al bind most strongly to the cation column material and are retained. While monovalent cations are eluted first from the column with 1 M HCl, Be is collected in a second fraction not before several column volumes. Trivalent cations are only rinsed from the column with 4.5 M HCl. After coprecipitation with ammonia solution, the $\text{Be}(\text{OH})_2$ gel is obtained. After washing the gel twice, it was dehydrated on a hot plate and converted to BeO in a furnace at 900°C (Fig. 2-5).

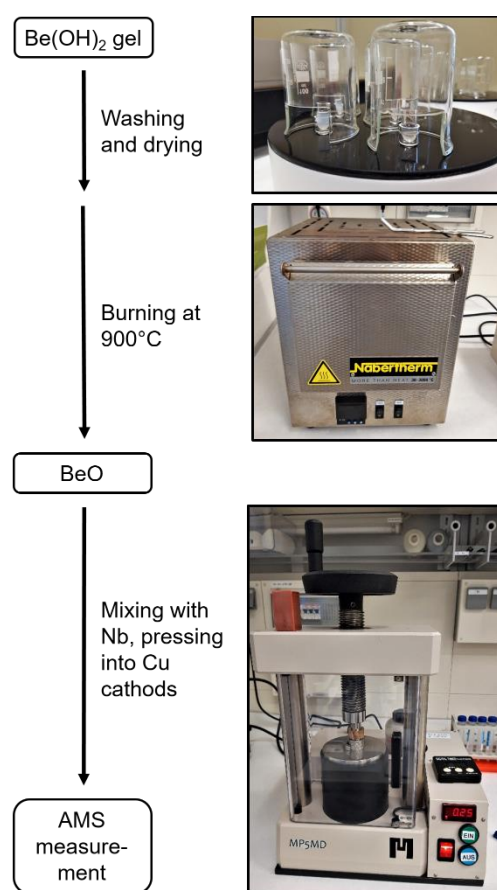


Fig. 2-5: Conversion of the $\text{Be}(\text{OH})_2$ gel to BeO and AMS target preparation. The AMS target represents a Cu cathode into which the BeO mixed with Nb is pressed.

The resulting BeO was mixed with Nb (with about four times the mass of BeO) and pressed into Cu cathodes which are placed in the AMS. Originally, BeO had been mixed with Ag, but mixing with Nb resulted in increased ${}^9\text{Be}^{3+}$ beam currents (Hunt et al., 2006; Merchel et al., 2008).

AMS measurement

AMS is used to measure the extremely small number of rare cosmogenic nuclides relative to a stable reference isotope that is present in known quantities, e.g., $^{10}\text{Be}/^9\text{Be}$ (Blanckenburg, 2005). Isotope ratios as low as 10^{-16} can be detected (Akhmadaliev et al., 2013). The major advantage of AMS over conventional mass spectrometry (MS) is the efficient suppression of interfering signals from molecular ions and isobars. This is mainly due to the higher energy to which the ions are accelerated: MeV instead of keV. The AMS provides much lower detection limits (about 10^6 atoms or 10^{-8} Bq) than MS (Merchel et al., 2012).

A basic AMS setup consists of the following parts: In the ion source, by bombardment with Cs^+ ions, single negative elemental or molecular ions, such as BeO^- , are generated and extracted from the sample targets (Merchel et al., 2012). The negative ions with the desired energy, mass and charge are selected by electrostatic and magnetic analyzers and shot into the tandem accelerator where they are accelerated to the positively charged high voltage terminal, where a "stripper" (foil and/or gas) is located. This both removes electrons from the electron shell, resulting in a charge reversal to multiple positive ions, and breaks all molecular bonds (Merchel et al., 2012). The now positively charged atomic ions (Be^{2+}) are accelerated to the other end of the tandem, which is at ground potential. The ion beam leaving the accelerator consists of different ion species with different charge states and energies (Merchel et al., 2012). An analyzing magnet at the high-energy part of the AMS separates the ions according to their momentum-to-charge ratio, acting as a second mass separator. Additionally, an electrostatic analyzer separates the ions according to their energy-to-charge ratio. Both analyzers serve to further reduce the background (Merchel et al., 2012). The detector system is adapted to the specific requirements: Mostly gas ionization detectors are used for counting the radioactive isotopes, whereas the macroscopic current of the stable isotopes is measured via so-called Faraday cups. From this, the characteristic ratio of radioactive to stable isotope is determined (Merchel et al., 2012).

2.2 Measurements of hydrochemical parameters

For the studies in Chapters 3 and 4, I collected water samples for AT and DIC analysis. In addition, for chapter 4, I also took water samples for the analysis of $\delta^{13}\text{C}$ -DIC, major elements, and stable water isotopes ($\delta^{18}\text{OH}_2\text{O}$ and $\delta^2\text{H}$ - H_2O). The different types of hydrochemical samples and their

preservation techniques are shown in Tab. 2-1. At every sampling location, water temperature, electrical conductivity and turbidity were measured in situ.

Tab. 2-1: Sample volume, specification of filtration and preservation techniques of sampled hydrochemical parameters.

Parameter	Sample volume (mL)	Filtered (0.45 μm)	Preservation
AT and DIC	300	no	added 300 μL of HgCl_2 solution (sat.), no headspace, stored cool and dark
$\delta^{13}\text{C}$ -DIC	12	yes	added 10 μL of HgCl_2 solution (sat.), no headspace, stored cool and dark
cations	50	yes	added 50 μL of HNO_3 (conc.) + stored cool and dark
anions	15	yes	stored cool and dark
stable water isotopes	2	yes	stored cool and dark

2.2.1 AT and DIC

AT was analyzed by performing an automated, potentiometric titration with 0.02 M HCl at the University of Hamburg. The recovery was $\geq 99\%$. A Marianda VINDTA 3C (Versatile Instrument for the Determination of Titration Alkalinity) was used to determine the DIC concentration by coulometric titration at Helmholtz-Zentrum Hereon. The method is based on acidifying the sample and measuring the CO_2 generated. The CO_2 reacts with a component in a solution and this solution is then back-titrated to its initial state with electric current, i.e., coulometry (Mintrop, 2016). The precision was $\pm 2 \mu\text{mol L}^{-1}$ (Shadwick et al., 2011). AT and DIC measurements were calibrated against certified reference materials (CRMs) provided by Andrew Dickson (Scripps Institution of Oceanography). Providing AT, DIC and water temperature, pH and $p\text{CO}_2$ were calculated using the program CO2SYS (Pierrot et al., 2011) with the freshwater equilibrium constants from Millero (1979).

2.2.2 $\delta^{13}\text{C}$ -DIC, major elements, and stable water isotopes

Isotope measurements were conducted at Leibniz Institute for Baltic Sea Research Warnemünde (IOW). $\delta^{13}\text{C}$ -DIC was measured by means of continuous-flow isotope-ratio-monitoring mass spectrometry (CF-irmMS) following the procedure described by Winde et al. (2014). The precision of $\delta^{13}\text{C}$ -DIC analysis was better than $\pm 0.1\text{‰}$. Results are given versus the VPDB standard. Stable water isotopes ($\delta^{18}\text{O}$ -H₂O and $\delta^2\text{H}$ -H₂O) were measured by means of cavity ring-down spectroscopy (CRDS). International besides in-house standards were used to scale the water isotope measurements (Böttcher and Schmiedinger, 2021). Stable isotope results had a precision of better than $\pm 0.06\text{‰}$ for oxygen and $\pm 0.3\text{‰}$ for hydrogen isotopes.

Major elements were measured at Alfred Wegener Institute, Helmholtz Centre for Polar and Marine Research Potsdam. Multi-element composition (Al, Ba, Ca, Fe, K, Mg, Mn, Na, P, Si, Sr) was analyzed by means of inductively coupled plasma optical emission spectrometry (ICP-OES). Anion concentrations (Br^- , Cl^- , F^- , NO_3^- , SO_4^{2-}) were determined by means of ion chromatography (IC). The precision for multi-element and anion analyses was $\pm 10\%$.

3 Alkalinity responses to climate warming destabilize the Earth's thermostat

Alkalinity generation from rock weathering modulates the Earth's climate at geological time scales (Berner et al., 1983). Although it is widely accepted that rock type is a dominant factor controlling alkalinity generation globally, it has proven difficult to quantify the impact of other first-order controlling factors (Amiotte Suchet and Probst, 1993; Amiotte Suchet and Probst, 1995; Hartmann, 2009; Hartmann et al., 2009; Lechuga-Crespo et al., 2020). Particularly challenging remains the separation of climatic and erosional influences. Here, we use global riverine alkalinity data paired with consistent erosion rate measurements to develop an empirically-based model demonstrating that areal proportion of carbonate, mean annual temperature, erosion rate, catchment area and soil thickness are first-order controls on riverine alkalinity concentration. We show that the weathering flux to the ocean will be significantly altered by climate warming as early as the end of this century, up to 68% depending on the environmental conditions, constituting a sudden feedback of ocean CO₂ sequestration to climate. While we anticipate that climate warming under a low-emissions scenario will induce a reduction in terrestrial alkalinity flux from mid-latitudes (-1.6 t(bicarbonate) a⁻¹ km⁻²) until the end of the century, resulting in a reduction in CO₂ sequestration, we expect an increase (+0.5 t(bicarbonate) a⁻¹ km⁻²) under a high-emissions scenario, yielding an additional CO₂ sink.

3.1 Introduction

Weathering-derived alkalinity fluxes to the ocean are a key component of the Earth's carbon cycle (Berner et al., 1983). Weathering of both carbonate and silicate rocks consumes atmospheric/soil CO₂ and increases the alkalinity of the ocean. Carbonate and silicate weathering is thought to be in equilibrium with marine calcification at long timescales (~10 ka; Zeebe and Westbroek, 2003), yet it has the potential to alter alkalinity, and thus the carbon cycle, over millennial and shorter timescales. Beyond the calcium carbonate compensation time, only silicate weathering acts as a long-term sink for atmospheric CO₂, while carbonate weathering acts CO₂-neutral (Berner et al., 1983).

Compared to silicate rocks, carbonate rocks are weathered more rapidly and their dissolution kinetics are up to three orders of magnitude faster (Stallard and Edmond, 1987; Erlanger et al., 2021). This allows carbonate weathering to be more responsive to rapid environmental changes, like

acid rain and anthropogenic increases in groundwater CO₂ levels (Li et al., 2008; Macpherson et al., 2008). Environmental changes occurring over shorter timescales than calcium carbonate compensation (< 10 ka; Zeebe and Westbroek, 2003), e.g., changes in temperature, hydrology, vegetation and atmospheric CO₂ content, have the potential to shift carbonate weathering away from its steady state, thereby altering the Earth's carbon cycle (Calmels et al., 2014). It is therefore essential to assess the short-term and long-term anthropogenic, climatic and geologic drivers of global alkalinity fluxes. Terrestrial river discharge and watershed lithology are recognized as the two most dominant factors controlling global alkalinity fluxes to the ocean (Amiotte Suchet and Probst, 1993; Amiotte Suchet and Probst, 1995; Hartmann, 2009; Hartmann et al., 2009; Lechuga-Crespo et al., 2020). Acidity, which is mostly supplied from atmospheric and soil CO₂, and the rate of physical erosion, also exert first-order controls on global alkalinity fluxes. The influence of temperature at the global scale has been long debated (Hartmann et al., 2009; Lechuga-Crespo et al., 2020), although two recent global studies reveal optimal weathering in temperate climates (Gaillardet et al., 2019; Romero-Mujalli et al., 2019a). It remains challenging, however, to precisely quantify these controls (e.g., soil CO₂ content) at regional to global scales, and records that are both spatially diverse and temporally comprehensive remain scarce (Calmels et al., 2014; Romero-Mujalli et al., 2019a). While regional studies show that physical erosion can enhance weathering, at least for low to moderate erosion rates (supply-limitation; Millot et al., 2002; Jacobson and Blum, 2003; West et al., 2005; Blanckenburg, 2005; Lyons, 2005), no such relationship between physical erosion and alkalinity flux has been identified at the global scale (Hartmann, 2009; Hartmann et al., 2009).

Here, we combine riverine alkalinity measurements with in situ ¹⁰Be-derived erosion rates from multi-lithological catchments across different climate zones to reveal the impact of physical erosion on alkalinity generation in the global context. We then quantify the impact of two future climate scenarios, represented by two shared socio-economic pathways (SSPs), on the riverine alkalinity flux.

3.2 First-order controls on riverine alkalinity

We compiled data from 233 sampling locations on six continents ranging from 44°S to 51°N, for which both alkalinity and ¹⁰Be erosion rate measurements were available (Fig. 3-1a). To overcome the ramifications of runoff and alkalinity concentration (i.e., dilution by 'pure' water or evaporation),

we use runoff-normalized alkalinity as the ratio of observed alkalinity in a given river sample to the mean annual runoff of that river. We sought to characterize alkalinity in a volume-independent manner and therefore considered alkalinity concentration per unit runoff. In the following, we will first highlight the relationships of erosion rate, areal carbonate proportion and mean annual temperature (MAT) with runoff-normalized alkalinity that we can derive from our dataset. Then we will show the results of how our empirically-based modeling approach represents these relationships. We employed a generalized linear model (GLM) allowing us to establish linear relationships between runoff-normalized alkalinity and the various predictor variables, even though their actual relationship may not be linear. This allowed for a readily understandable interpretation. In addition to erosion rate, areal carbonate proportion and MAT, our model analyzes normalized alkalinity as a function of catchment area and soil thickness (see sections 3.6.5 and 3.6.6).

Catchments with both low ($< 10 \text{ mm ka}^{-1}$) and high ($> 1000 \text{ mm ka}^{-1}$) erosion rates produce little alkalinity, independent of carbonate and MAT. Where erosion rates are very slow, i.e., less than $\sim 10 \text{ mm ka}^{-1}$, we suggest that the stream dissolved load is too low for alkalinity production. Similarly, catchments that erode rapidly ($> 1000 \text{ mm ka}^{-1}$) produce little alkalinity because they appear to be equilibrium-limited, i.e., limited by acid availability (see below for further explanation). At slow to intermediate erosion rates ($\sim 10\text{-}1000 \text{ mm ka}^{-1}$, gray-shaded box, Fig. 3-1b), we identify a regime of '*efficient erosion rate*' which induces the highest normalized alkalinity concentrations. A study in tropical Taiwan (Bufe et al., 2021) confirms the increase in carbonate weathering as a function of erosion rate for an erosional gradient similar to our study. However, discrepancies appear at high erosion rates, where we obtain decreasing alkalinities. We attribute this to a high degree of pyrite weathering in the studied area in Taiwan according to the authors, which would result in higher groundwater acidity and thus higher solubility of carbonates in their study.

Within the *efficient erosion rate regime*, normalized alkalinity peaks at erosion rates of $\sim 100 \text{ mm ka}^{-1}$ and is governed by the areal proportion of carbonate and MAT in the catchment. Our global dataset indicates that areal carbonate proportion has a first-order positive effect on normalized alkalinity concentration. The highest normalized alkalinity concentrations are only found in catchments with carbonate present, while in catchments without carbonate, weathering produces only low amounts of alkalinity (Fig. 3-1b and c, Extended Data Fig. 3-1).

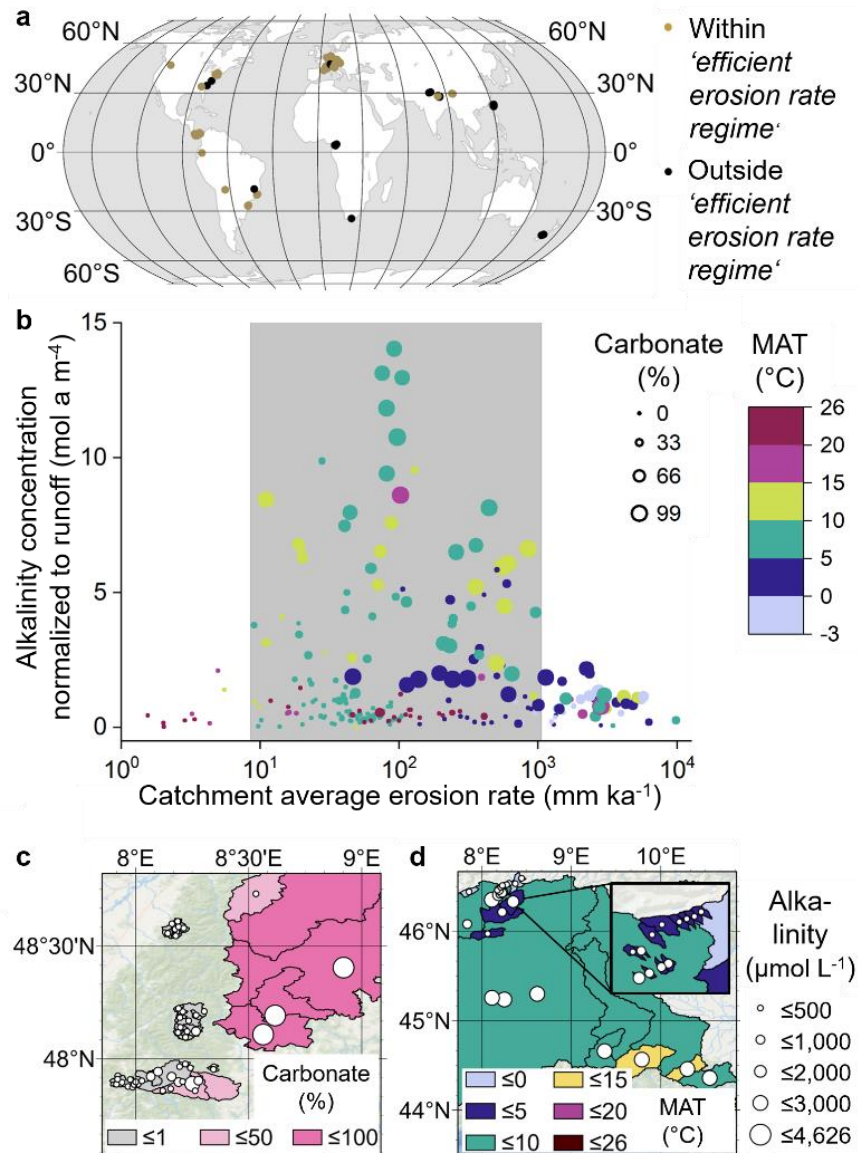


Fig. 3-1: Erosion rate, areal carbonate proportion and temperature are first-order controls on catchment-scale alkalinity concentrations. (a) World map with sampling locations. Catchments within the limits of the *efficient erosion rate regime*, characterized by erosion rates of $\sim 10\text{--}1000\text{ mm ka}^{-1}$ (see Fig. 3-1b), are highlighted. (b) High runoff-normalized alkalinity concentrations are found in the *efficient erosion rate regime* (gray-shaded box). A high proportion of areal carbonate and a temperate climate (MAT: $5\text{--}15^\circ\text{C}$) promote high alkalinity concentrations, as shown in the excerpts for selected European catchments: (c) Black Forest, Germany, where a high areal proportion of carbonate is associated with high riverine alkalinity; and (d) Switzerland and northern Italy, where catchments with MATs of $5\text{--}15^\circ\text{C}$ show high alkalinity concentrations. MAT: mean annual temperature.

Our model results show that weathering from carbonate rocks dominates alkalinity generation globally. This predominance of carbonate was also recognized by another study (Amiotte Suchet and Probst, 1995), in which

the flux of CO₂ consumed by weathering in carbonate watersheds was determined to be 17 times higher than in plutonic and metamorphic watersheds, which reveal the lowest flux. Our results also indicate that, when other influential parameters (e.g., erosion rate and MAT) are ideally set (i.e., within the *efficient erosion rate regime*, ~10–1000 mm ka⁻¹, and MAT ~10°C), catchments dominated by rock types other than carbonate (areal carbonate proportion ≤ 50%) still produce high amounts of alkalinity (normalized alkalinity concentration ~2.5-10.0 mol a m⁻⁴, third quartile of normalized alkalinity concentration and alkalinity concentration in our dataset ~2.1 mol a m⁻⁴ and ~2010 μmol L⁻¹, respectively; Fig. 3-1b, Extended Data Fig. 3-1).

In addition to erosion rate and areal carbonate proportion, we identify MAT as a first-order control on riverine alkalinity generation globally. A temperate climate (5-15°C) promotes extensive carbonate weathering (Fig. 3-1b and d). This is supported by our model, where normalized alkalinity concentration shows a maximum in the range of 7.5-15.0°C (Extended Data Fig. 3-2b). Similar conclusions have been drawn by other authors (Romero-Mujalli et al., 2019a; Gaillardet et al., 2019), who found the highest carbonate weathering rates to be in temperate climates. Romero-Mujalli et al. (2019a) describe the temperature dependency of alkalinity by a Gaussian function, with an optimum at 11°C. Furthermore, they attribute the increase in alkalinity concentration until 11°C MAT to an increase in soil–rock CO₂ content supplied by elevated ecosystem respiration. Above 11°C, the effect of decreased carbonate mineral solubility with increasing temperature causes alkalinity concentration to again decrease. Our results confirm that temperature, in addition to influencing kinetics and solubility, is an important driver of acid availability.

Colder MATs (< 5°C) generally hinder weathering and are associated with low normalized alkalinity concentrations, even when both the areal carbonate proportion is high (> 80%) and the erosion rate lies within the *efficient erosion rate regime* (Fig. 3-1b and d). We attribute this to reduced ecosystem respiration and, hence, to lower acid availability. In addition, weathering may be limited at low temperatures due to reduced reaction rates according to the Arrhenius equation. In contrast, higher MATs (> 15°C) can produce high normalized alkalinity concentrations, but only in watersheds that are both within the *efficient erosion rate regime* and have a high areal carbonate proportion. However, these conditions are rarely encountered, since warmer climate zones are normally associated with only a small areal carbonate proportion (Extended Data Fig. 3-3). This is

observed in our global dataset, where the vast majority of catchments with higher MAT ($> 15^{\circ}\text{C}$) have a relatively low areal carbonate proportion (Fig. 3-1b). We propose that normalized alkalinity concentration decreases at MATs greater than $\sim 12.5^{\circ}\text{C}$ and reaches its minimum at $\sim 22.5^{\circ}\text{C}$. We relate the decreasing trend in alkalinity to the generally semi-arid conditions associated with this temperature regime globally. This is supported by prior work (Schoonejans et al., 2016) demonstrating that water availability limits chemical and physical weathering processes in dry environmental conditions. Overall, we suggest that the MAT covariate in our model is representative of the availability of soil acid and water, and that the ideal conditions for weathering-liberated alkalinity are met in temperate catchments with high areal carbonate proportion, within the *efficient erosion rate regime*.

Beyond peak alkalinities, at intermediate to high erosion rates ($> 100 \text{ mm ka}^{-1}$), a general decrease in acid availability in both ground and river water correlates with a decrease in riverine alkalinity, consistent with prior work in Western Europe (Erlanger et al., 2021; Calmels et al., 2014). In regions in the Jura mountains undergoing extensive carbonate weathering, Calmels et al. (2014) found that soil CO_2 content decreases with altitude. The authors propose that this is linked to a change in vegetation (above 800 m above mean sea level (amsl)), climate, and soil properties. Indeed, our global dataset reveals, first, a positive correlation between erosion rate and altitude ($R^2 = 0.5$) and, second, that catchments with a mean elevation of at least 1500 m amsl are characterized by an erosion rate $> 100 \text{ mm ka}^{-1}$ (Extended Data Fig. 3-4a). There is also a positive correlation between erosion rate and mean slope gradient, which is representative of relief ($R^2 = 0.7$; Extended Data Fig. 3-4b). This suggests that denudation causes soil CO_2 to decrease with elevation and relief. Taking a different approach, Erlanger et al. (2021) found that in the Northern Apennine Mountains of Italy, precipitation of secondary calcium carbonate from supersaturated rivers led to the loss of 20-90% of dissolved Ca^{2+} from carbonate-rich catchments. The supersaturation is a result of degassing of excess river CO_2 through equilibration with atmospheric CO_2 partial pressure. Turbulent flow aids this degassing process. We propose that a reduction in alkalinity concentration may be found in the rapidly eroding catchments in our dataset because they are associated with steep slopes (as mentioned above, erosion rate and mean slope gradient are positively correlated), which in turn are responsible for turbulent flow in rivers. It seems that morphology, and not directly erosion rate, is mainly responsible

for turbulent flow and thus CO₂ degassing. However, morphology and erosion rate are closely linked. In catchments with high erosion rates, extreme flow events can transport large boulders into the riverbed, which in turn cause turbulent flow.

3.3 Global riverine alkalinity function

From an iterative model and a variable selection process, we developed a generalized linear model to describe normalized alkalinity concentration. In addition to erosion rate, areal carbonate proportion and MAT, we included catchment area, calculated as 2D area, and soil thickness (depth to bedrock; Shangguan et al., 2017) as covariates (see sections 3.6.5 and 3.6.6). Normalized alkalinity concentration increases continuously for both catchment area and soil thickness (Extended Data Fig. 3-2c and d). Firstly, it is possible that larger catchment areas, which tend to capture more precipitation, provide a greater power for lateral planation or incision. In fact, the stream power law as derived by Moss et al. (1980) is commonly expressed as erosion rate $E = kA^m S^n$, which substitutes catchment area, A , for water discharge Q_w ($Q_w = kA^m$; *c.f.* Sklar and Dietrich, 1998). However, the stream power law applies more to the stream processes of incision which generates suspended, bed, and dissolved loads. As riverine alkalinity corresponds directly to the dissolved load, there are likely other factors that can manifest spatial scaling. A larger watershed may also provide opportunities to include areas of steeper slopes, giving more energy for incision and slope wash (the S in the above stream power law). However, larger catchments have a higher potential for sediment storage and greater land surface areas of low relief (e.g., Willenbring et al., 2013) which provide a greater opportunity for weathering and soil development. It is this increase in chemical weathering on flatter and finer-grained unconsolidated landforms that likely contributes a first-order link between dissolved load and catchment area. Other authors (Hartmann et al., 2009) found that alluvial sediments in small, steep Japanese basins are relatively poorly weathered in comparison to larger basins in other regions, possibly where sediment storage and shallower slopes increase weathering efficiency.

Secondly, beyond peak weathering rates at an optimum soil thickness, chemical weathering is thought to decrease due to an ineffective interaction between water and fresh mineral surfaces (Stallard, 1995). In wet regions, chemical weathering is usually extensive, but the leached bedrock has not been physically moved downslope and soil production rates are often slow (Heimsath et al., 2020). Soil production is generally driven by

stochastic bioturbation (e.g., penetration of roots), which produces well-mixed and mobile soil layers (Roering et al., 2002; Roering et al., 2010). The disturbance frequency is governed by soil thickness, and soil production rates are thought to generally decrease non-linearly with increasing soil thickness (Heimsath et al., 1997, 2001). We acknowledge the divergent feedbacks between chemical weathering, biotic processes, and soil production and transport processes. However, we cannot observe this trend in our dataset (Extended Data Fig. 3-5). Except for the four data points with the highest soil thicknesses (> 21m) in our dataset, which show low normalized alkalinity concentrations, we detect a continuous increase of normalized alkalinity concentration with increasing soil thickness. In future studies, it would be beneficial to include catchments with higher soil thicknesses (> 25m) to investigate whether decreasing weathering can be detected above a certain soil thickness.

3.4 Sensitivity of alkalinity generation to MAT

We employed our model to assess how MAT affects normalized alkalinity concentrations in different climatic zones (Fig. 3-2). For this sensitivity test, we applied global mean values for the remaining covariates: erosion rate, areal carbonate proportion, catchment area and soil thickness. As shown in Extended Data Fig. 3-2b, the expression of the normalized alkalinity – MAT function is (partly) altered by varying the values of the other covariates. The general dependency of the function, as shown in Fig. 3-2a, however, is not changed.

For the temperature range of 0-20°C, MAT exerts a strong to intermediate influence on normalized alkalinity concentration in our model. At high latitude, in subarctic or alpine climates (< 2.5°C), our model predicts an increase in normalized alkalinity concentration with decreasing MAT. We relate this enhanced carbonate weathering to glacial and periglacial erosion. A study investigating the geochemistry of rivers draining the New Zealand Alps (Jacobson et al., 2003) found that glaciated watersheds contain ~25% more Sr²⁺ from carbonate weathering than non-glaciated ones. In our dataset, normalized alkalinity increases with the areal extent of permanent snow and ice cover (for all catchments with permanent snow and ice cover > 1%; Extended Data Fig. 3-6). This correlation can be explained by enhanced weathering at the margins of the glaciers, where meltwaters interact with atmospheric CO₂ and fine-grained glacial debris (Ludwig et al., 1998). For non-glaciated catchments with an MAT around 5°C at ~60-45°N, normalized alkalinity concentration is relatively small owing to lower

acid availability (annual soil respiration decreases with latitude; Warner et al., 2019). In temperate climates ($\sim 12.5^\circ\text{C}$) at $\sim 45\text{-}35^\circ\text{N}$, both water and soil acid are abundant, resulting in an increase in normalized alkalinity concentration. In (semi-)arid climates ($> 15^\circ\text{C}$), at $\sim 35\text{-}25^\circ\text{N}$, weathering is limited by water supply, resulting in the lowest normalized alkalinity concentration. Finally, our model predicts an increase in normalized alkalinity concentration for warmer climates ($> 22.5^\circ\text{C}$). We attribute this increase to elevated reaction rates according to the Arrhenius law.

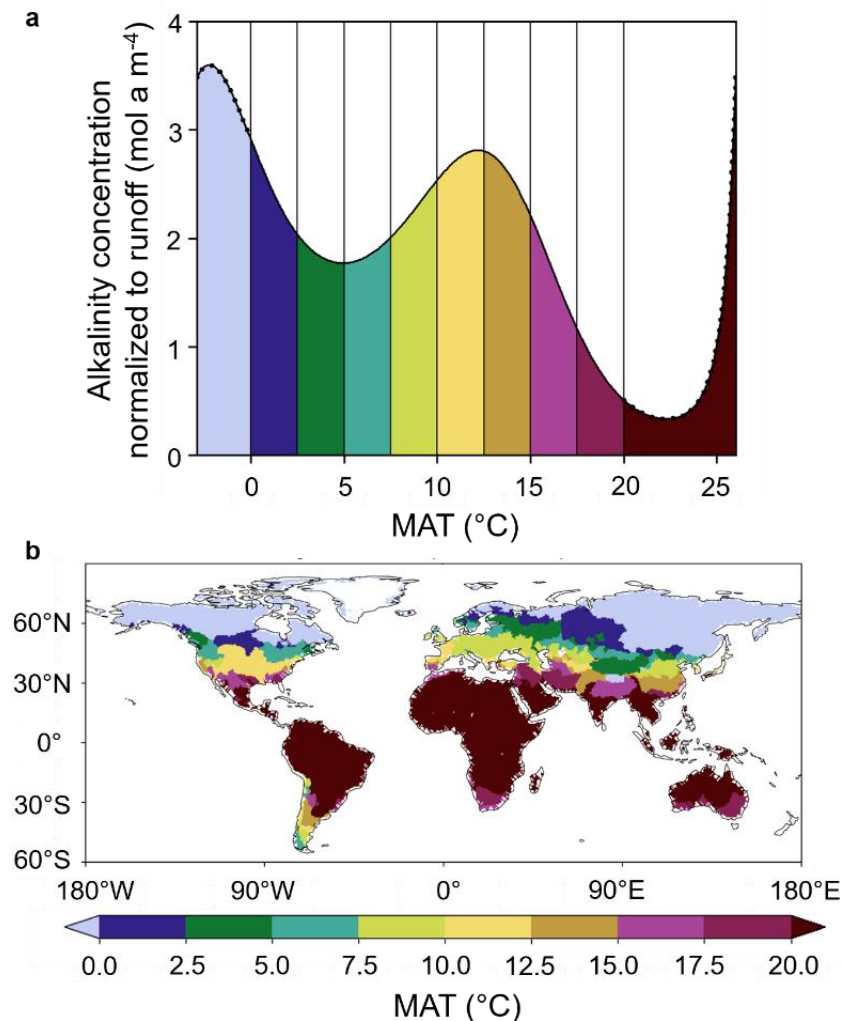


Fig. 3-2: Runoff normalized alkalinity concentration in catchments with different MAT. (a) The fitted line shows the model output as a function of MAT; the line is dotted for $\text{MAT} < 0^\circ\text{C}$ and $\geq 20^\circ\text{C}$, indicating the minor influence of MAT on normalized alkalinity concentration for these temperatures. The other covariates are kept constant (mean global coverage by carbonates ($sc + sm$) = 22%; Hartmann and Moosdorf, 2012), erosion rate = 100 mm ka^{-1} , catchment area = 1000 km^2 , soil thickness = 15 m). (b) MAT of catchments globally, derived from data provided by the ISIMIP project (Lange and Büchner,

2021) based on the GFDL-ESM4 Model (Krasting, J. P. et al., 2018). See also Extended Data Fig. 3-2b.

Our model predicts high and very high normalized alkalinity concentrations for polar ($< 0^{\circ}\text{C}$) and tropical ($> 25^{\circ}\text{C}$) regions, respectively (dotted line in Fig. 3-2a). While our dataset covers a broad temperature range [$-2.9, 26.9^{\circ}\text{C}$], we restrict our quantitative interpretation of the influence of MAT on normalized alkalinity concentration to a more narrow temperature range of $0.0\text{-}20.0^{\circ}\text{C}$. Outside this range, (i) we would perform an out-of-sample prediction regarding the areal carbonate proportion and (ii) the implicit constancy of the erosion rate covariate (erosion rate = 100 mm ka^{-1}) appears unrealistic for these regions. Our global dataset reveals that catchments with high MAT ($> 20^{\circ}\text{C}$) have a low areal carbonate proportion (mean = 2.8%; Extended Data Fig. 3-7). In fact, our dataset does not contain any catchments that show both high temperatures ($> 20^{\circ}\text{C}$) and high areal carbonate proportion ($> 40\%$). However, some catchments in warm areas ($> 20^{\circ}\text{C}$) to which we apply our model function in our global assessment also have high carbonate contents (up to 100%). For the catchments with low MAT ($< 0^{\circ}\text{C}$) in our dataset, the assumption of an erosion rate of 100 mm ka^{-1} is untenable, as the mean erosion rate for this temperature regime is $\sim 2600\text{ mm ka}^{-1}$, with almost all observations falling above the *efficient erosion rate regime* (Extended Data Fig. 3-8). Therefore, in the following, we will limit our quantitative assessment of the effect of MAT changes on alkalinity to the temperature range of $0.0\text{-}20.0^{\circ}\text{C}$.

3.5 Impact of climate change on the terrestrial alkalinity flux

Global surface temperatures are projected to increase over the next decades under all emissions scenarios (IPCC, 2021), as shown for two shared socio-economic pathways (SSPs), a low (SSP1-2.6) and a high (SSP5-8.5) emissions scenario (Fig. 3-3a and b, respectively). SSPs are future narratives that combine projections of atmospheric greenhouse gas concentrations with socio-economic developments in a consistent way. Examples for these developments are population growth, climate change mitigation strategies and economic relations between countries. The SSPs 1-2.6 and 5-8.5 are of special interest because they provide pathways for either reaching the 2-degree target or living in a world that remains reliant on fossil resources. Using these pre-defined scenarios enables us to capture the broadest range of possible feedbacks between climate change and alkalinity.

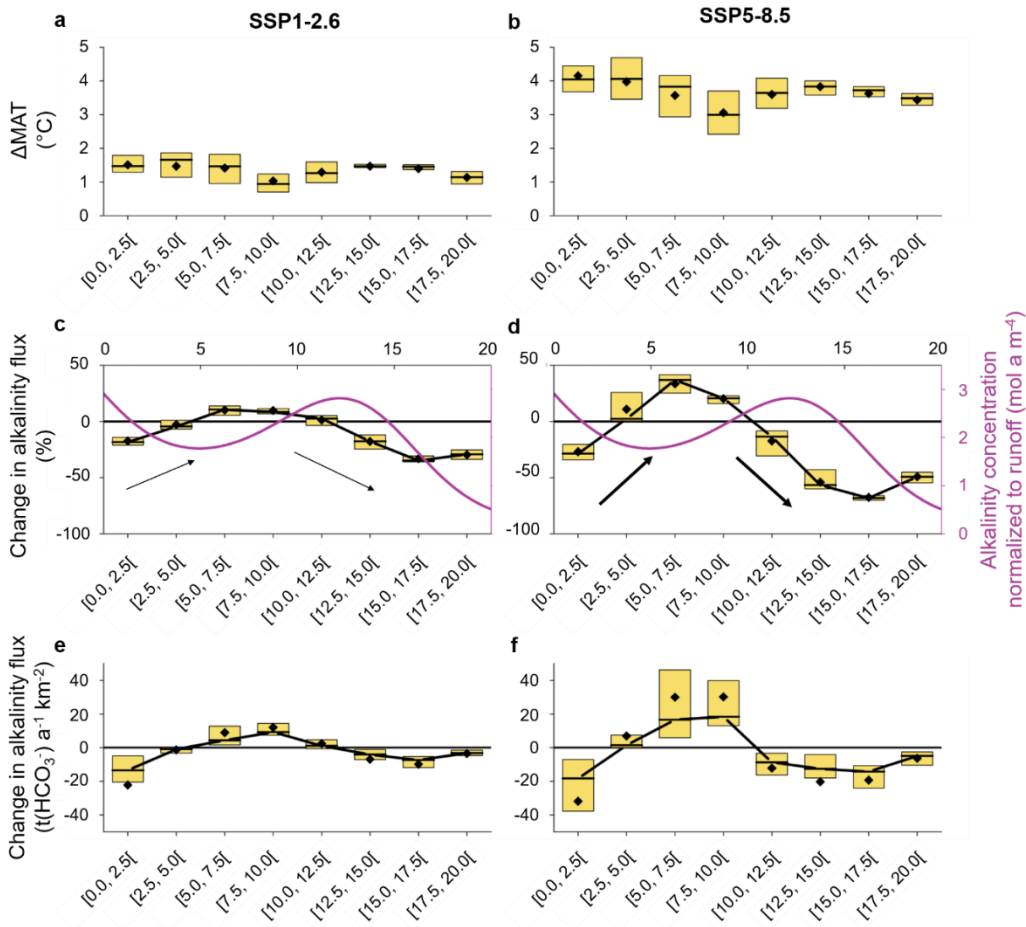


Fig. 3-3: Alkalinity flux impacted by increased temperatures. Simulated historical data (1980–2009) are contrasted with simulated future data affected by climate warming according to (a, c, e) a low (SSP1-2.6) emissions scenario and (b, d, f) a high (SSP5-8.5) emissions scenario (2070–2099). (a, b) Difference in MAT; (c, d) Relative change in alkalinity flux due to change in MAT. The schematic evolution of runoff normalized alkalinity concentration according to our model (Fig. 3-2a) is shown for a better understanding. Thick arrows indicate that weathering responds more drastically to more rapidly rising temperatures than to less rapidly rising temperatures, indicated by the thin arrows; and (e, f) Absolute change in alkalinity flux due to change in MAT. For the calculation of the absolute alkalinity flux as specific mass flux, a molar mass of 61.02 g mol^{-1} for bicarbonate (HCO_3^-) was used, as at pH 7-9, the alkalinity concentration is approximately equal to the bicarbonate concentration (Dreybrodt, 1988; Schroeder, 2002). Boxes indicate 0.25 and 0.75 quantiles and black diamonds show the arithmetic mean. Temperature projections are provided by the ISIMIP project (Lange and Büchner, 2021) based on the GFDL-ESM4 data (Krasting, J. P. et al., 2018). River discharge was simulated using the HydroPy global hydrology model (Stacke and Hagemann, 2021).

Temperature, as shown by our model, has the potential to greatly change alkalinity generation globally. We upscaled our model for normalized alkalinity concentration to the mid-latitudes (corresponding to the temperature range of $0.0\text{-}20.0^{\circ}\text{C}$) to study the effect of increasing MAT on alkalinity flux

(alkalinity concentration multiplied by mean annual river discharge). Our results show that the alkalinity flux decreases by up to 68% in the current MAT range of 15.0-17.5°C. With MATs increasing, on average, by 1.4 and 3.6°C within this temperature band until the end of this century in the low and high emissions scenarios, respectively, normalized alkalinity concentration is projected to be shifted towards its minimum at ~22.5°C (refer to the schematic evolution of normalized alkalinity concentration in Fig. 3-3c and d). This results in a reduction of alkalinity flux by 33 and 68%, respectively. We propose this decrease is due to future aridification, which is projected to be especially pronounced in the Mediterranean, southwestern South America and western North America (IPCC, 2021). A rise in MAT within the 12.5-15.0°C band is also anticipated to cause a decrease in alkalinity flux for both emissions scenarios, since alkalinity generation will depart from its optimal climatic conditions (high water and acid availability). We attribute this effect to the concomitant decrease in solubility of carbonates. Further, in the 17.5-20.0°C band, under both emission scenarios, the alkalinity flux is expected to decrease as it is pushed toward its minimum value around 22.5°C. While we expect a further decrease in alkalinity flux for the temperature band 10.0-12.5°C under SSP5-8.5, a small increase is seen under SSP1-2.6. Given the small increase in MAT expected in the latter (1.0°C), the majority of the catchments remains in the optimal weathering range. In contrast, MAT under the SSP5-8.5 scenario will increase by 3.0°C, pushing these catchments outside of their optimal weathering conditions. Finally, our model predicts a reduction in alkalinity flux for the temperature range of 0.0-2.5°C under both emissions scenarios. This could be explained by a reduction in glacial cover, and thus the erosive force, in these regions. However, we would also expect a significantly large surface area of fine-grained matrix to be exposed in these scenarios, which should in contrast cause weathering to increase. This contrast may be attributed to the fact that our dataset currently contains no known Arctic erosion rates, meaning that, our model input data for this temperature band are not from the Arctic, but rather from high-altitude catchments like the Himalayas (Fig. 3-1a). Accordingly, we recommend that focus on erosion rate and alkalinity measurement in high-latitude catchments worldwide is now needed to enhance understanding of the direct impact of the on-going rapid deglaciation on carbonate weathering.

We expect the alkalinity flux in catchments with historical MATs in the range of 5.0-10.0°C to increase with advancing climate warming under both emissions scenarios. We attribute this to a greater acid availability

from soil respiration, which increases with climate warming (Bond-Lamberty and Thomson, 2010). In both scenarios, alkalinity generation is pushed from its local minimum at $\sim 5^{\circ}\text{C}$ towards the local maximum at $\sim 12.5^{\circ}\text{C}$. Based on data from 60 large rivers, Meybeck (1979) determined the highest alkalinity flux in temperate, very humid regions to be $72.3 \text{ t}(\text{bicarbonate}) \text{ a}^{-1} \text{ km}^{-2}$. We expect the highest absolute increase in alkalinity flux of $30.1 \text{ t}(\text{bicarbonate}) \text{ a}^{-1} \text{ km}^{-2}$ for the historical temperature band $7.5\text{-}10.0^{\circ}\text{C}$ under scenario SSP5-8.5 (Fig. 3-3f) and attribute this to a shift towards a more temperate and humid climate with sufficient acid availability and favorable carbonate solubility. For the temperature band $2.5\text{-}5.0^{\circ}\text{C}$, the change in alkalinity flux is dependent on the emissions scenario: Under SSP1-2.6, the catchments are moved further to the minimum weathering zone and a reduction in alkalinity flux of 3% is expected. In contrast, the temperature increase under SSP5-8.5 is far greater and allows for a transition out of the minimum weathering zone, resulting in a gain in terrestrial alkalinity flux of 11%. This is supported by prior findings of increased bicarbonate flux due to climate warming for the period 1961-2004 in eight rivers in Iceland (Gislason et al., 2009).

Our results show that carbonate weathering will respond to temperature changes as long as moisture availability is constant or sufficient. Weathering reacts more extremely to stronger rising temperatures under the high emissions scenario compared to the low emissions one (refer to the thick and thin arrows in Fig. 3-3d and c, respectively). Because the size of our dataset was limited by the number of consistent erosion rates available, we could not cover the full range in model parameters (very low and very high values) that occur at mid-latitudes. The catchments that showed extreme values that were not covered by our model training dataset were excluded from the calculations of alkalinity flux changes in mid-latitudes (see section 3.6.7). The resulting bias might lead to an overestimation of the flux changes. The exclusion of all catchments with a mean annual runoff $< 150 \text{ mm a}^{-1}$ probably also omits relatively water-scarce catchments, in which weathering is generally lower. In addition, the erosion rate of 100 mm ka^{-1} assumed for all catchments is within the *efficient erosion rate regime*, which has the potential to produce high amounts of alkalinity. In the following, our calculations of absolute change in alkalinity flux in mid-latitudes thus represent a good first estimate, but should be viewed with some caution because the model training dataset represented the crucial, yet not the full range of mid-latitude catchments.

In both scenarios, we expect the greatest increase in alkalinity flux in Central Europe and Central Asia, following a latitudinal band at $\sim 45^\circ\text{N}$ (predicted for the world's largest basins which are characterized by a historical MAT of $0.0\text{-}20.0^\circ\text{C}$, illustrated in Fig. 3-4a and b). While the main part of the USA is projected to have no significant change in alkalinity flux under scenario SSP1-2.6, in SSP5-8.5 a lower flux is anticipated. A reduced alkalinity flux is mainly associated with regions north of 60°N and south of 30°N .

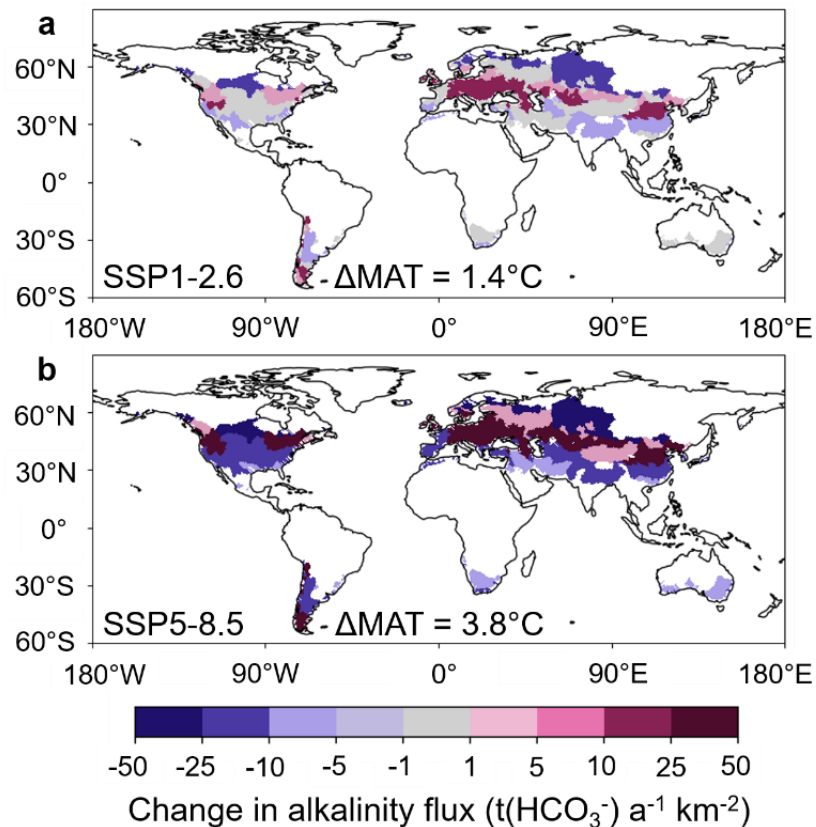


Fig. 3-4: Projected change in alkalinity flux due to climate warming. Colors indicate the projected absolute change in alkalinity flux of catchments per temperature band for the historical temperature range of $0.0\text{-}20.0^\circ\text{C}$, globally, under scenarios (a) SSP1-2.6 and (b) SSP5-8.5. The mean change in MAT (ΔMAT) under SSP1-2.6 and SSP5-8.5 until the year 2100 are projected to be 1.4 and 3.8°C , respectively. Catchment areas in white were excluded from the analysis, since their historical MATs were lower or higher than the temperature range of $0.0\text{-}20.0^\circ\text{C}$. For the calculation of the absolute alkalinity flux as specific mass flux, a molar mass of 61.02 g mol^{-1} for bicarbonate (HCO_3^-) was used, as at pH 7-9, the alkalinity concentration is approximately equal to the bicarbonate concentration (Dreybrodt, 1988; Schroeder, 2002).

We show that the mid-latitude ($0.0\text{-}20.0^\circ\text{C}$) alkalinity flux would decrease, on average, by $1.6 \text{ t}(\text{bicarbonate}) \text{a}^{-1} \text{km}^{-2}$ in SSP1-2.6 and increase, on average, by $0.5 \text{ t}(\text{bicarbonate}) \text{a}^{-1} \text{km}^{-2}$ in SSP5-8.5. We here assume that

the change in terrestrial alkalinity flux is solely due to a change in alkalinity concentration. However, we did not take into account the combined climate change-induced impacts on weathering and freshwater discharge, as currently we insufficiently understand how the product of discharge and concentration responds to climate change (see Extended Data Fig. 3-9 and Extended Data Fig. 3-10). Considering a mean global bicarbonate flux to the ocean of $19.4 \text{ t a}^{-1} \text{ km}^{-2}$ (Meybeck, 1979), our results imply a reduction of the global alkalinity flux of $\sim 8\%$ under SSP1-2.6, or an increase of $\sim 3\%$ under SSP5-8.5 due to the projected change in mid-latitudes.

If we attribute this decrease/increase in riverine alkalinity flux solely to carbonate weathering, we can expect an increase/drawdown of atmospheric CO_2 of the same magnitude for mid-latitudes until the end of the century (assuming CO_2 to be the dominant source of acidity and half of the bicarbonate equivalents originating from CO_2). Thus, under SSP1-2.6, reduced carbonate weathering in mid-latitudes due to climate warming leads to a reduction in CO_2 sequestration ($\Delta = +0.3 \text{ tC a}^{-1} \text{ km}^{-2}$). In contrast, we expect an increase in carbonate weathering under SSP5-8.5, resulting in an additional short-term CO_2 sink ($\Delta = -0.1 \text{ tC a}^{-1} \text{ km}^{-2}$). Globally, chemical weathering currently drives CO_2 consumption of $\sim 2 \text{ tC a}^{-1} \text{ km}^{-2}$ (Hartmann et al., 2009). Our values for a projected change in CO_2 release and consumption due to climate warming in mid-latitudes would affect this rate by $\sim 15\%$ and $\sim 5\%$, respectively. In terms of global anthropogenic emissions per year (34.9 GtCO_2 in 2021; Liu et al., 2022), the change we predict in CO_2 uptake or release is small. Under SSP5-8.5, an increase in carbonate weathering offsets $\sim 0.05\%$ of anthropogenic emissions. We note that the change predicted by us refers only to the catchments with historical MAT of $0.0\text{--}20.0^\circ\text{C}$, so that the magnitude of the change could be larger if all catchments globally were taken into account; especially considering that some of the alkalinity hotspots are located in areas with historical MAT $> 20.0^\circ\text{C}$. Moreover, it is a slow process that, as we show, is nevertheless influenced. This unfolds its effect over time and not via speed.

Our analysis of the first global dataset on catchment alkalinity and erosion reveals that catchment average erosion rate is a first-order non-linear control on alkalinity generation globally. Both the direction and degree of climate change-driven alteration of alkalinity fluxes depend on how strongly climate parameters will change in the future. To predict weathering rates at a global scale more precisely, we advocate for an expansion of ^{10}Be

erosion rate data where applicable, particularly in areas of under-represented areal carbonate proportion, temperature ranges and soil thicknesses.

3.6 Methods

3.6.1 Water sampling and measurements

We collected 111 water samples for analysis of total alkalinity (AT) and dissolved inorganic carbon (DIC) during two sampling campaigns, one in Germany in May 2020 and another in Switzerland, Italy and Austria in June/July 2020. We collected the river water directly into 300-mL BOD bottles, added 300 μ L of saturated mercury chloride solution and sealed the bottles with ground-glass stoppers, Apiezon type M grease and plastic caps (no-headspace). The bottles were stored in the dark at ambient temperature. We used a Marianda VINDTA 3C (Versatile Instrument for the Determination of Titration Alkalinity) to determine the DIC concentration by coulometric titration (Shadwick et al., 2011). We analyzed the AT concentration by performing a potentiometric titration using a Metrohm 888 Titrando with an Aquatrode pH probe. We calibrated both instruments against certified reference materials (CRMs) provided by Andrew Dickson (Scripps Institution of Oceanography). We recorded in situ water temperature and electrical conductivity using a WTW Multi3430 with IDS TetraCon 925 and turbidity using a HACH 2100Qis. All measurements are reported at <https://doi.pangaea.de/10.1594/PANGAEA.939660>.

3.6.2 Data requirements and sources

Since we wanted to build our analysis on a uniform set of ^{10}Be erosion rates, we first extracted all locations of available ^{10}Be erosion rate measurements from the OCTOPUS database (Codilean et al., 2018). (We note that there are other works not included in the OCTOPUS database.) We then assigned available alkalinity data in compliance with the following conditions: (i) The location of the alkalinity measurement should be in the same river as that of the erosion rate; ideally, the sampling locations of both measurements are identical. (ii) If the ideal condition of identical locations cannot be fulfilled, the location of the alkalinity measurement needs to be downstream of the erosion rate one so that the potential effects of an erosional event are captured in the alkalinity signal. (iii) The distance between the two locations should not exceed 25 current kilometers. (iv) One should try to exclude alkalinity locations that allow the inflow of tributaries larger than 10 current kilometers downstream of the erosion rate location.

We made exceptions to these conditions for larger rivers (e.g., Maas or Neckar). We examined each location individually using QGIS 3.10.0.

For 111 of the 233 total erosion rate locations used in our analysis, we generated our own alkalinity data. We selected these sites because the respective catchments showed a large range in areal carbonate proportion, MAT and erosion rate, enhancing the diversity of our dataset. We ensured that there were no dams in the immediate vicinity of the sampling sites upstream (proportion of the catchment area affected by dams < 50%). In our dataset, 19 catchments are characterized by an areal proportion affected by dams of $\geq 10\%$. We performed a sensitivity test for normalized alkalinity concentration examining the influence of dams by removing all catchments characterized by an areal proportion affected by dams of $\geq 10\%$ from the training dataset and running the GLM with the same set of covariates as in model M5. The resulting model function was similar to the original one of model M5 (comparison of both model function is shown in Extended Data Fig. 3-11). After looking through the GLORICH database (Hartmann et al., 2019), we obtained 76 further alkalinity measurement locations which met the above defined requirements. We obtained the remaining 46 alkalinity values from individual published manuscripts or on request from government agencies. All original sources are listed at <https://doi.pangaea.de/10.1594/PANGAEA.940522>.

In addition to direct measurements of AT, we also accepted bicarbonate concentrations as alkalinity values. Alkalinity in rivers is approximately equal to the concentration of bicarbonate (Dreybrodt, 1988; Schroeder, 2002). We were able to confirm this by calculating the concentrations of bicarbonate, carbonate and hydroxide using the program CO2SYS (Pierrot et al., 2011) for the samples from our sampling campaigns 2020. We used the measured values for AT, DIC, salinity and water temperature together with the CO₂ constants from Millero (1979). The average proportion of bicarbonate in total alkalinity is $98 \pm 4\%$ (Extended Data Fig. 3-12).

Our dataset comprises erosion rates spanning four orders of magnitude ($2\text{-}9829 \text{ mm ka}^{-1}$) and alkalinity covering a large range ($4\text{-}4626 \text{ }\mu\text{mol L}^{-1}$). The alkalinity data include both single and time-series measurements (1-3940 measurements per location). For locations with multiple measurements (bi-monthly to monthly measurements, sometimes decades-long studies), the mean was calculated, while locations with single measurements were regarded as mean annual values. The seasonal bias introduced by this simplification is tolerable, as, with a few exceptions, it is low

compared to the entire range of alkalinity concentrations in our study (Extended Data Fig. 3-13). To circumvent the problem of concentration/dilution, we used normalized alkalinity concentration (alkalinity concentration divided by mean annual runoff) and excluded all observations with a mean annual runoff lower than 150 mm a⁻¹.

We combined the point sampling measurements of erosion rate and alkalinity concentration with the spatial description of runoff, lithology, temperature, precipitation, permanent snow and ice cover, forest cover, soil thickness and area affected by dams, of the respective catchment upstream from the erosion rate measurement location. We used the basin outlines from the OCTOPUS database (Codilean et al., 2018) to compute the catchments' mean values using QGIS 3.10.0. We calculated mean annual runoff from the 0.5° x 0.5° raster in the UNH/GRDC Composite Runoff Fields V1.0 (Fekete et al., 2002) to normalize the alkalinity measurements (alkalinity concentration divided by mean annual runoff). We determined the lithological coverage of the basins from the global lithological map database GLiM (Hartmann and Moosdorf, 2012) by calculating the area of the individual rock classes as a percentage of the total catchment area. We combined two main classes ("sc" = "carbonate sedimentary rocks" with carbonate rocks being dominant; "sm" = "mixed sedimentary rocks" with carbonate being mentioned) and one subclass ("mtpu" = "metamorphics" with minor carbonate occurrences) indicative of carbonate presence into one class (Hartmann and Moosdorf, 2012). We computed the annual mean air temperature (MAT) and the annual mean precipitation (MAP), based on climate data for 1970-2000, from the 10' x 10' raster of the WorldClim 2.1 database (Fick and Hijmans, 2017). We extracted the areal proportion of permanent snow and ice as well as of forest cover from the 300 m x 300 m raster of the GlobCover 2009 land cover map (Arino et al., 2012). We took soil thickness, defined as the depth from the surface to the bedrock, from the 1 km x 1 km raster of the DTB (Global Depth to Bedrock) dataset (Shangguan et al., 2017). We calculated the proportion of the watershed affected by dams using the global vector file from GOODD (GIObal geOreferenced Database of Dams; Mulligan et al., 2020). All data are summarized at <https://doi.pangaea.de/10.1594/PANGAEA.940522>.

3.6.3 CO₂ consumption of carbonate and silicate weathering at different timescales

At pH 7-9, the alkalinity concentration is approximately equal to the bicarbonate ion concentration (~95% of the carbon in the water is in the form of bicarbonate ions), as the equilibrium between dissolved CO₂, bicarbonate

and carbonate in this pH range is strongly in favor of bicarbonate (Dreybrodt, 1988; Schroeder, 2002). While weathering of divalent cation silicates consumes two equivalents of CO₂, carbonate weathering consumes just one. Once in solution, the produced ions are transported via rivers to the ocean, where the bicarbonate ions can also dissociate into carbonate ions, depending on the buffer capacity of the ocean, i.e., oceanic alkalinity. In supersaturated waters with respect to calcium carbonate, such as at the ocean surface, the bicarbonate ions can react with calcium ions and about one equivalent of CO₂ is released into the atmosphere. The carbonate ions can be directly precipitated as calcium carbonate. Consequently, beyond the calcium carbonate compensation time (~10 ka; Zeebe and Westbroek, 2003), only silicate weathering acts as a long-term sink for atmospheric CO₂ and carbonate weathering acts CO₂-neutral (Berner et al., 1983). Terrestrial carbonate weathering initiated by volcanogenic or anthropogenic sulfuric acid instead of CO₂ also leads to CO₂ released to the atmosphere (Calmels et al., 2007; Torres et al., 2016; Bufe et al., 2021).

3.6.4 ¹⁰Be-derived erosion rates

Among other approaches, terrestrial erosion rates over scales of centuries to millennia are now frequently obtained from paleo-sediment flux measurements and terrestrial cosmogenic nuclides (Blanckenburg, 2005; Codilean et al., 2018). However, no approach is ideal. Conventional sediment-yield measurements can substantially underestimate long-term average erosion rates (Kirchner et al., 2001). The analysis of cosmogenic nuclides, such as ¹⁰Be, in river sediment at the outlet of a catchment allows one to average total denudation rates over both the whole basin area and long time periods (10²-10⁵ a), also capturing infrequent high-magnitude events (West et al., 2005; Blanckenburg, 2005). However, the ¹⁰Be approach requires that the landscape has achieved steady state with respect to the gradual removal of quartz, with predictable ¹⁰Be concentrations from quartz-bearing soils throughout a catchment (such as, e.g., a recently deglaciated catchment has not achieved). Where adequate appreciation for the assumptions and caveats of the sampling approach are considered, total erosion rates from cosmogenic nuclides can reproduce sediment-yield derived erosion rates for the same catchment (Dixon and Blanckenburg, 2012; Derakhshan-Babaei et al., 2020). A significant caveat is that the ¹⁰Be-derived catchment erosion rate (a mass loss rate generally expressed in units of mm ka⁻¹) has a relatively long observation window (centuries to tens of thousands of years, for very fast and very slow eroding

catchments, respectively) whereas active stream sediment discharge calculated for example from suspended load measurements are averaged over hour to decadal windows. Another caveat is that the ^{10}Be -derived erosion rates consider the entire mass loss (chemical and detritus) whereas dissolved loads are not always measured for streams gauged for suspended load. The best correspondence between ^{10}Be and alkalinity would therefore be in a relatively flat stable catchment where chemical erosion dominates, and soil mass-depth is uniform over many millennia.

The averaging time scale of ^{10}Be -derived erosion rates is a function of the erosion rate itself (Blanckenburg, 2005). We calculated the averaging time scales for the erosion rates used in our study by dividing the average cosmic ray absorption depth scale in soils (~ 1000 mm) by the erosion rate (Extended Data Fig. 3-14). While rapidly eroding catchments show the shortest averaging time scales of $\sim 10^2$ a, slowly eroding ones are characterized by averaging time scales of 10^4 - 10^5 a. To test whether the long-term averaged ^{10}Be -derived erosion rates were related to the alkalinity signal, as proposed by our model, rather than a potential short-term disturbance in erosion rate, such as the construction of a dam, we included the proportion of the watershed affected by dams as a variable in the model. In our dataset, 20% of all catchments contained at least one dam. An areal proportion of the watershed affected by dams of at least 10% were found in 8% of all data points. The variable proved to be significant but did not change the general trend in normalized alkalinity as a function of ^{10}Be -derived erosion rate. Furthermore, another global study (Chen et al., 2022) determined short-term erosion rates (estimated from suspended sediment yield) to be only 1.4 times as high as long-term erosion rates (estimated from ^{10}Be concentrations) in temperate climates. Accordingly, we assume that the set of ^{10}Be -derived erosion rates used in our study represents the erosional behavior of a watershed well and that a potential temporal disjunction between ^{10}Be -derived erosion rate and alkalinity concentration has no decisive impact on the investigated relationships.

3.6.5 Model preparation

We carried out the statistical analysis by using the packages “stats” (R Core Team, 2020) for generalized linear models (GLMs) and “mgcv” (Wood, 2011) for generalized additive models (GAMs) in *R* (R Core Team, 2020). While determining the predictor variables for modelling normalized riverine alkalinity, we achieved the best model results by using a GAM.

We used GAM methodology to employ a fully data-driven approach to get a first impression of the general functional relationships of the independent variables to normalized alkalinity concentration. In our GAM specification, all covariates were included as smooth functions. We then fitted a GLM with polynomial functions of different degree based on the findings of our GAM results, accepting a lower model fit of the GLM when compared to the GAM, for the following three reasons: (i) Some functions, which have been proven to demonstrate a linear relation (e.g., weathering and areal carbonate proportion; Amiotte Suchet and Probst, 1995), showed ‘wiggleness’ (lack of smoothness). Therefore, we restricted them by forcing a linear relation. The scientifically inexplicable ‘wiggleness’ is most likely caused by our sample size. (ii) We wanted to ensure a better comparability with the coefficients of previous studies (Hartmann, 2009; Lechuga-Crespo et al., 2020) and thus used polynomial functions for the remaining variables. (iii) The leave-one-out cross-validation revealed a higher mean squared prediction error for the GAM than for models M4 and M5, suggesting that the GAM may overfit.

For the model and variable selection process, we used Akaike and Bayesian information criteria (AIC and BIC) and residual sum of squares (RSS). From this iterative process, we extracted five different models (M1-M5). While in the first model (M1) only the areal carbonate proportion is included as a predictor variable, our final model (M5) comprises five covariates. We used the GAM as reference (Extended Data Tab. 3-1).

Since normalized alkalinity concentration is a non-negative continuous response variable, we used a natural logarithm as the link function (Fahrmeir et al., 2013). We tested the robustness of our model fit by performing a leave-one-out cross-validation, in which only a certain part of the data (number of observations - 1) is set to fit the model, while the remaining part (1 observation) is used to test the model.

3.6.6 Global riverine alkalinity function

As expected and published elsewhere (Amiotte Suchet and Probst, 1993; Amiotte Suchet and Probst, 1995; Hartmann, 2009; Hartmann et al., 2009; Lechuga-Crespo et al., 2020), we identified lithology as the dominant control on alkalinity production (M1, Extended Data Tab. 3-1). We decided to use carbonate (sum of “sc”, “sm” and “mtpu”; Hartmann and Moosdorf, 2012) as the only lithological predictor variable for normalized alkalinity. The remaining rock types were not significant predictors (as revealed when considered in model M5, at a significance-level of 0.05), with the exception

of “intermediate plutonic rocks” (p-value = 0.007). As the latter lithology only covers 0.4% of the terrestrial Earth (Hartmann and Moosdorf, 2012) and its inclusion improved the model score only minimally, we only incorporated carbonate into our models.

The discrepancy between observations and fitted model values was substantially reduced by adding MAT as a covariate (M2). To model the effect of MAT, we used a third (M2-M4) and a fifth (M5) degree polynomial function. To test whether the fifth degree polynomial representation of MAT (M5) describes normalized alkalinity concentration better than the third degree one (M3 and M4) in different climatic zones presented in our dataset, we divided our observations into temperature bands (5°C steps) and determined the individual RSS. For all temperature bands, model M5 shows lower RSS than models M3 and M4 (Extended Data Tab. 3-2). Although the leave-one-out cross-validation for model M4 yielded an overall lower mean squared prediction error, we chose M5 as our final model because the leave-one-out cross-validation revealed a lower or similar mean squared prediction error for all individual temperature bands examined, with the exception of the temperature band [15°C, 20°C). Accordingly, M5 performed better than M4 at the outer parts of our temperature range.

Model performance was further improved by adding (the natural logarithm of) physical erosion rate to the model (M3), revealing for the first time on a global level that physical erosion rate is also a first-order control on riverine alkalinity. Modelled normalized alkalinity as a function of erosion rate increases steeply until the *efficient erosion rate regime* is reached and then smoothly decreases again (Extended Data Fig. 3-2a).

We recognized that (the natural logarithm of) catchment area, calculated as 2D area, and soil thickness (depth to bedrock; Shangguan et al., 2017), are two additional important predictor variables for normalized alkalinity concentration and these are considered in model M4 and our final model, M5.

Normalized alkalinity concentration in model M5 is calculated with the following equation:

$$\begin{aligned} \text{Normalized alkalinity concentration} = & \\ & \exp [- 1.163 \\ & + 0.01867 (\text{areal carbonate proportion}) \\ & - 0.1504 (\text{MAT}) \\ & - 0.009028 (\text{MAT})^2 \end{aligned}$$

$$\begin{aligned}
&+ 0.005944 (\text{MAT})^3 \\
&- 0.0004681 (\text{MAT})^4 \\
&+ 0.00001007 (\text{MAT})^5 \\
&+ 0.2873 (\ln(\text{erosion rate})) \\
&- 0.05615 (\ln(\text{erosion rate}))^2 \\
&+ 0.1342(\ln(\text{catchment area})) \\
&+ 0.05078(\text{soil thickness}) \\
&]
\end{aligned}$$

We did not include runoff as a predictor variable for normalized alkalinity, since we defined normalized alkalinity as alkalinity concentration per unit of runoff. The inclusion of runoff in the model would result in auto-correlation, which we need to avoid. We also examined other variables such as areal proportion of snow and ice cover, vegetation (as areal proportion of forest cover), and MAP for their effects on normalized alkalinity. The first two were not significant when added to our final model M5. Precipitation was significant, but we decided not to include it into our final model because it only slightly improved the model score and there was a high degree of multi-collinearity (MAP and MAT showed a high correlation), which we wanted to avoid.

The model results with all covariates and coefficients are shown in the *R* script, which is provided at <https://github.com/nelelehmann/Alkalinity-responses-to-climate-warming-destabilise-the-Earth-s-thermostat/>.

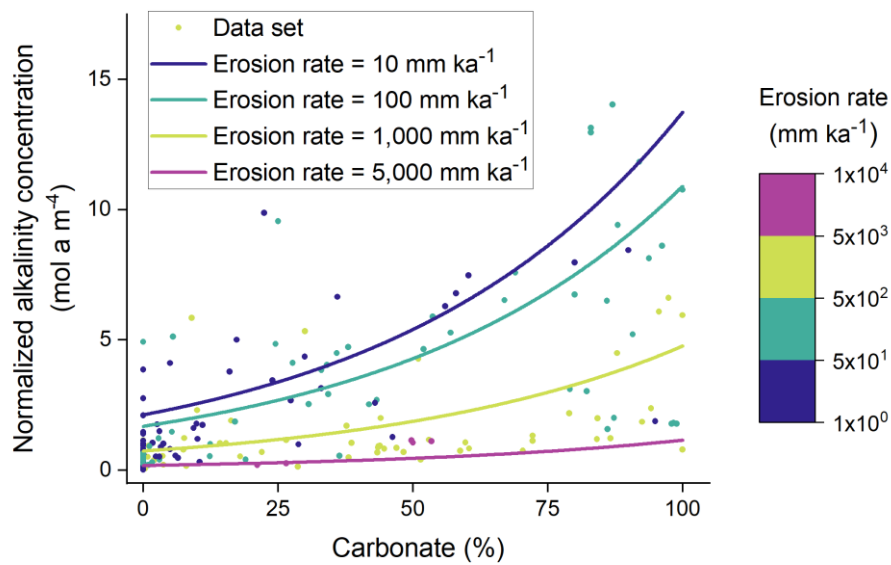
3.6.7 Calculation of change in alkalinity flux due to climate warming

We calculated the terrestrial alkalinity flux on a catchment basis for catchments with historical (1980-2009) MAT of 0.0-20.0°C. Global temperature fields for historical and future (2070-2099) periods were provided by ISIMIP (Lange and Büchner, 2021), based on scenario simulations conducted with the GFDL-ESM4 for the CMIP6 project (Eyring et al., 2016). Together with atmospheric fields from the same source (precipitation, radiation, humidity and wind), we could run the global hydrological model HydroPy (Stacke and Hagemann, 2021) to generate runoff and river discharge data. We compared historical with future data affected by climate warming according to a low (SSP1-2.6) and a high (SSP5-8.5) emissions scenario (SSP: shared socio-economic pathway). In contrast to MAT, we kept the other covariates in model M5 constant. Since no global map for ¹⁰Be erosion

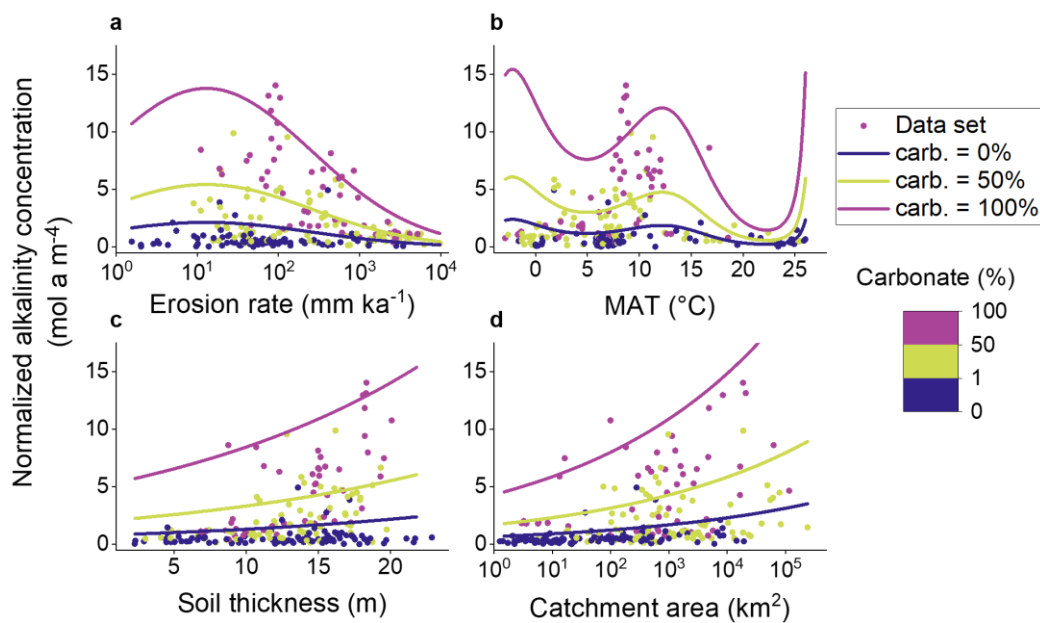
rates exists, we assumed an erosion rate of 100 mm ka^{-1} for all catchments. Further, we excluded all catchments whose values (in runoff, catchment area, soil thickness) are not covered by our calibration data (i.e., runoff $< 150 \text{ mm a}^{-1}$, catchment area $> 239,000 \text{ km}^2$, soil thickness $< 2.29 \text{ m}$ and $> 22.85 \text{ m}$). Even though the largest 105 catchments are not included in the calculations due to this data filter, we applied an extrapolation to the entire land surface area for the temperature range of $0.0\text{-}20.0^\circ\text{C}$, because the most important controlling factors (areal carbonate proportion, MAT and erosion rate) were not affected.

First, we fed our final model M5 with historical and future temperatures to yield estimates for historical and future normalized alkalinity, respectively. Second, we multiplied these with mean annual runoff (historical data: 1980-2009), which yielded alkalinity concentration. To assess only the effect of temperature change on alkalinity flux, we kept the discharge constant over time and multiplied both the historical and the future alkalinity concentration by historical mean annual discharge.

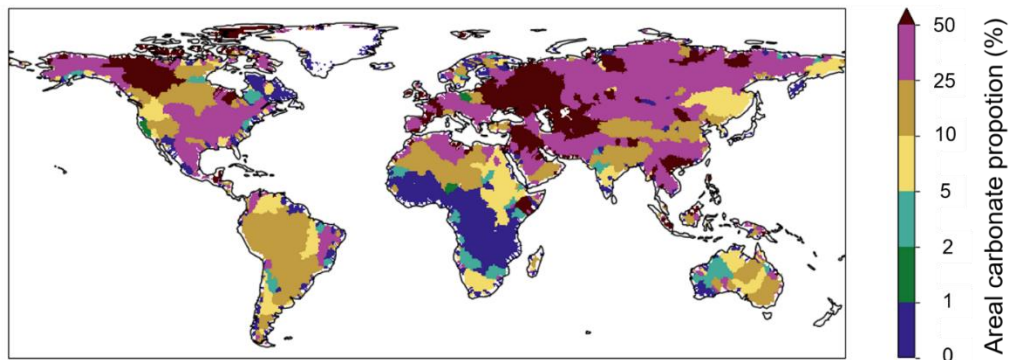
3.7 Supplementary material



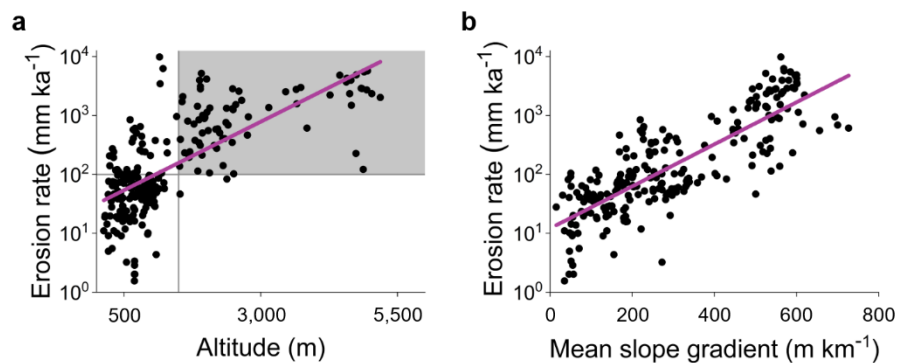
Extended Data Fig. 3-1: Normalized alkalinity concentration in relation to areal carbonate proportion. Dots are observations. The fitted lines show the model outputs of our final model M5 for different erosion rates. The other covariates are kept constant (MAT = 10°C, catchment area = 1000 km², soil thickness = 15 m).



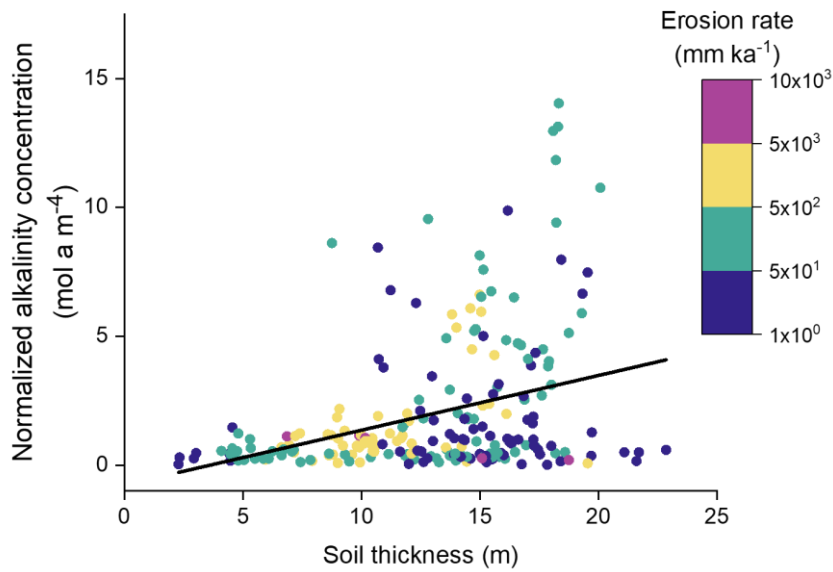
Extended Data Fig. 3-2: Normalized alkalinity concentration controlled by (a) erosion rate, (b) MAT, (c) soil thickness and (d) catchment area. Dots are observations. The fitted lines show the model outputs of our final model M5 for different areal carbonate proportions. The other covariates are kept constant (MAT = 10°C, catchment area = 1000 km², soil thickness = 15 m, erosion rate = 100 mm ka⁻¹).



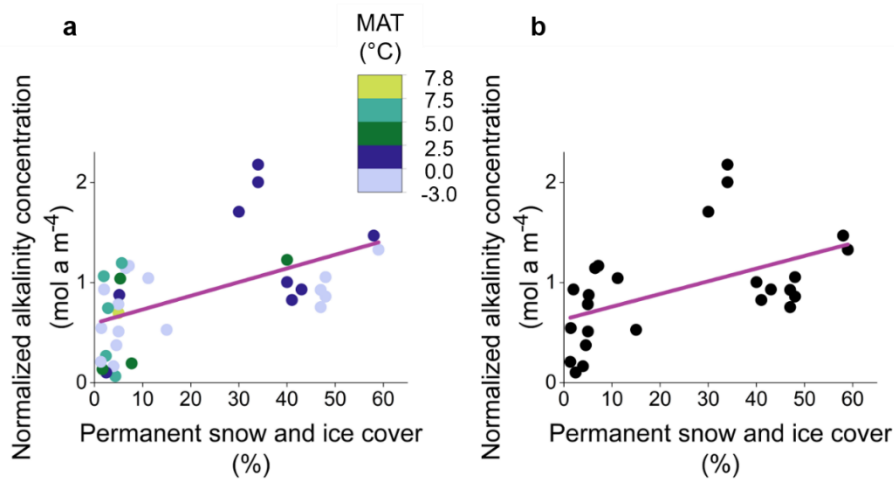
Extended Data Fig. 3-3: Global carbonate extent. The colors indicate the catchment average areal carbonate proportion of the world's major catchments. Areal carbonate proportion was calculated as the sum of the rock types "sc" and "sm" from the GLiM database (Hartmann and Moosdorf, 2012).



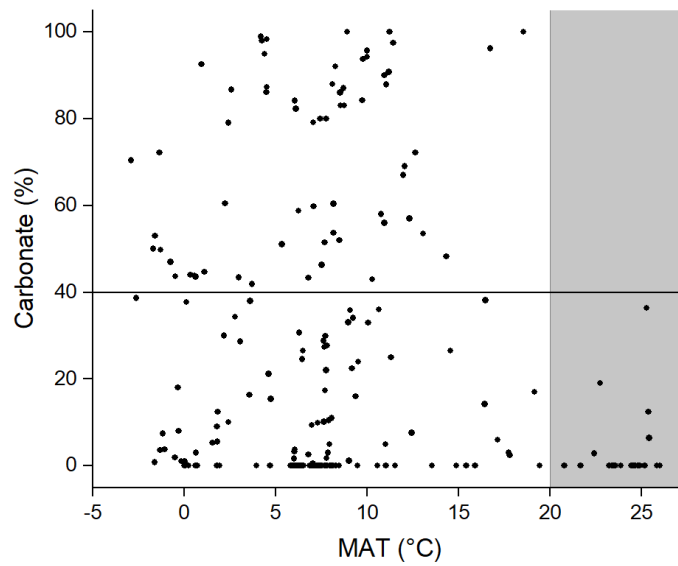
Extended Data Fig. 3-4: Erosion rate and topography. Erosion rate increases with both (a) altitude ($R^2 = 0.5$; p -value $< 2.2 \times 10^{-16}$) and (b) mean slope gradient ($R^2 = 0.7$; p -value $< 2.2 \times 10^{-16}$). (a) At mean altitudes > 1500 m amsl, catchments show intermediate to high erosion rate (gray-shaded box: erosion rate > 100 mm ka^{-1}). (b) A high mean slope gradient promotes high erosion rates. The values for mean slope gradient were extracted from the OCTOPUS database (Codilean et al., 2018). Note: Although the reported R^2 refer to the linear regression of erosion rate and (a) altitude and (b) mean slope gradient, respectively, here the erosion rate is plotted on a logarithmic axis, indicating a non-linear relation.



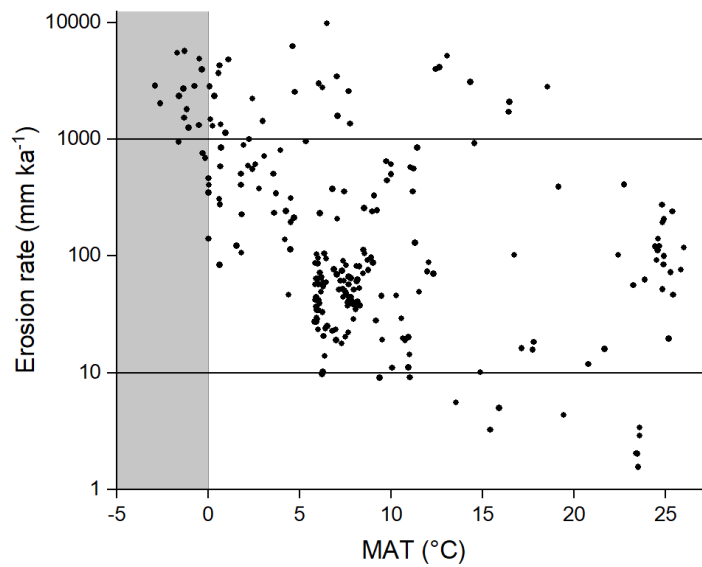
Extended Data Fig. 3-5: Normalized alkalinity concentration increases with soil thickness. Normalized alkalinity concentration increases linearly with soil thickness ($R^2 = 0.1$; p -value = 6.2×10^{-8}). Colors indicate erosion rate.



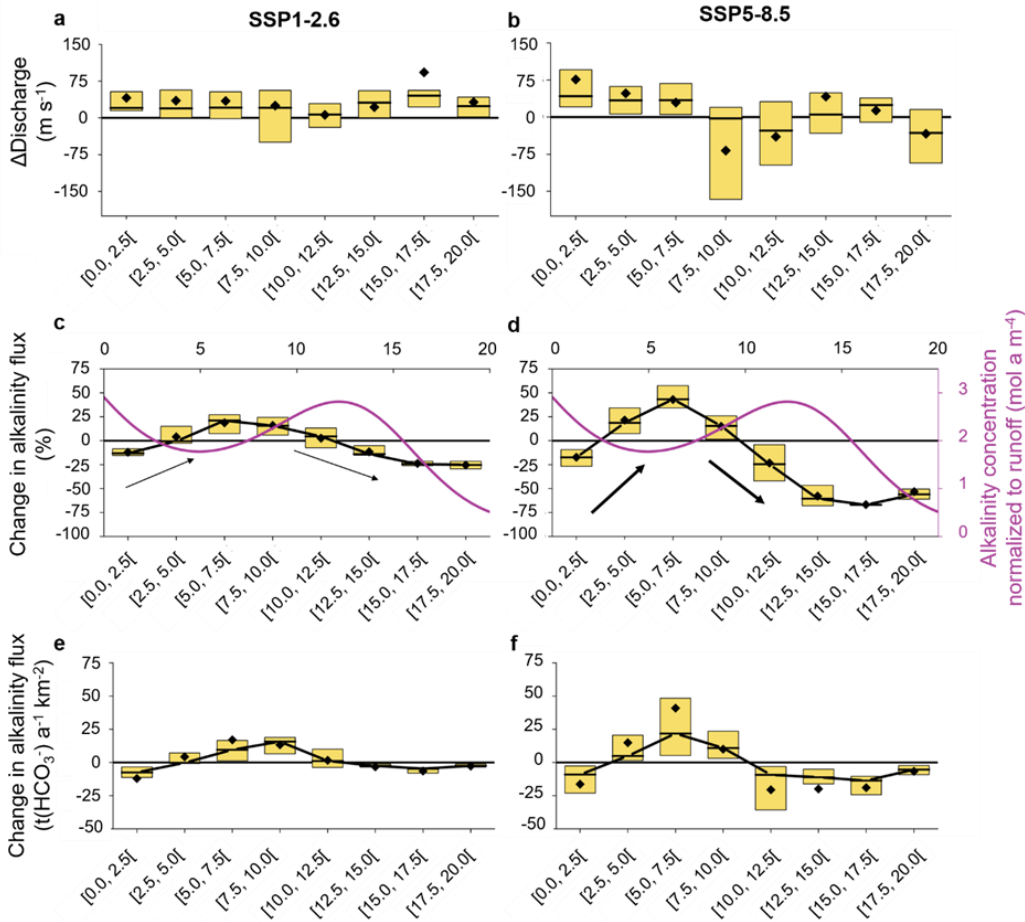
Extended Data Fig. 3-6: Normalized alkalinity concentration and permanent snow and ice cover. (a) Normalized alkalinity concentration increases linearly with permanent snow and ice cover for all catchments with permanent snow and ice cover > 1% ($R^2 = 0.3$; p -value = 0.0011). Colors indicate mean annual temperature (MAT). (b) Normalized alkalinity concentration increases linearly with permanent snow and ice cover for all catchments with permanent snow and ice cover > 1% and MAT < 2.5 °C ($R^2 = 0.3$).



Extended Data Fig. 3-7: Areal carbonate proportion in relation to MAT. In catchments with a warm climate (gray-shaded box: MAT > 20°C), the proportion of areal carbonate is generally low and does not exceed 40%.

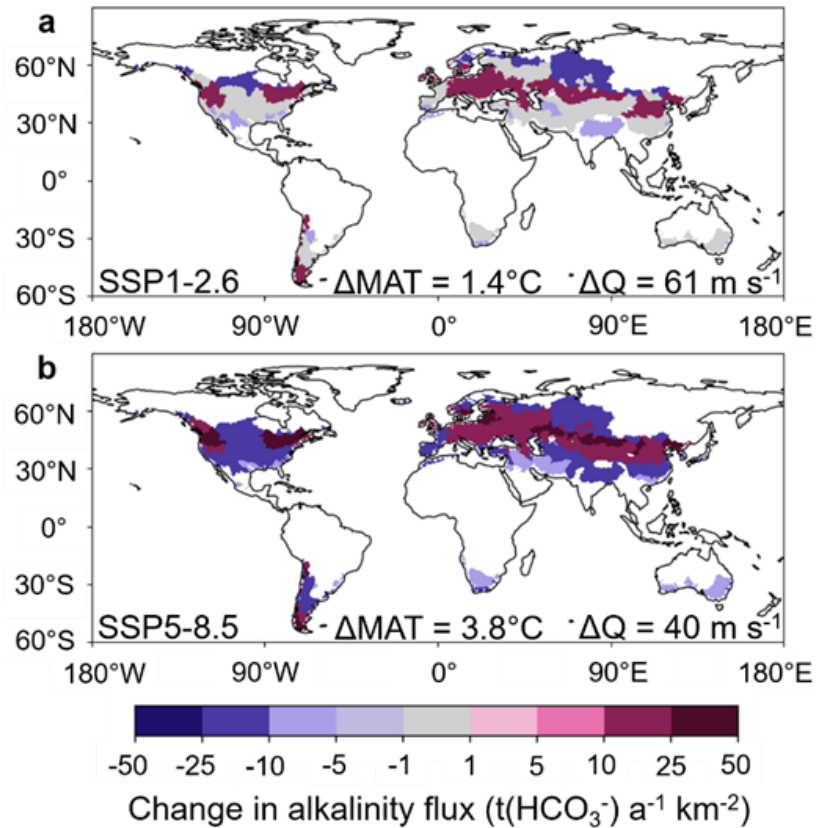


Extended Data Fig. 3-8: Correlation of erosion rate with MAT. Catchments with low MAT show only high erosion rates. Within the gray-shaded box (MAT < 0°C), erosion rates are very high, with almost all observations lying outside the *efficient erosion rate regime* (> 1000 mm ka⁻¹).

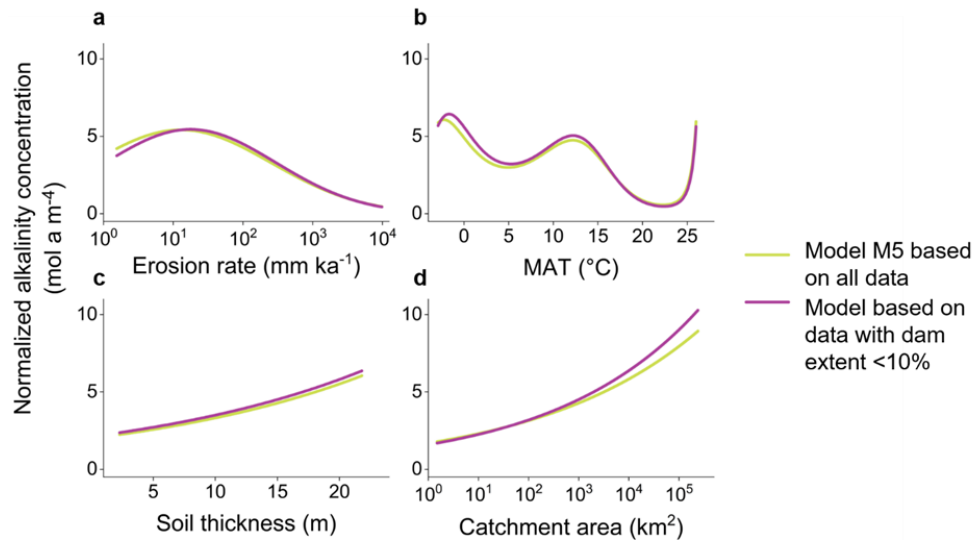


Extended Data Fig. 3-9: Alkalinity flux impacted by both changed alkalinity concentration and changed river discharge. The combined influence of alkalinity concentration and river discharge changes on the alkalinity flux is shown. In contrast, Fig. 3-3 shows the sole influence of the alkalinity concentration on the alkalinity flux (discharge is kept constant), since we cannot distinguish the individual influences of the two parameters within the combined signal. However, this cause attribution was the main focus of this paper. Simulated historical data (1980-2009) are contrasted with simulated future data affected by climate change according to (a, c, e) a low (SSP1-2.6) emissions scenario and (b, d, f) a high (SSP5-8.5) emissions scenario (2070-2099). (a, b) Difference in discharge (The difference in MAT can be seen in Fig. 3-3a and b.); (c, d) Relative change in alkalinity flux due to change in both MAT and discharge. The schematic evolution of runoff normalized alkalinity concentration according to our model (from Fig. 3-2a) is shown for a better understanding. Thick arrows indicate that weathering responds more drastically to more rapidly changing temperature and discharge than to less rapidly changing temperature and discharge, indicated by the thin arrows; and (e, f) Absolute change in alkalinity flux due to change in both MAT and discharge. In contrast to Fig. 3-3, the discharge was not kept constant in this calculation, but instead the way it changes due to climate change was taken into account. For the calculation of the absolute alkalinity flux as specific mass flux, a molar mass of 61.02 g mol^{-1} for bicarbonate (HCO_3^-) was used, as at pH 7-9, the alkalinity concentration is approximately equal to the bicarbonate concentration (Dreybrodt, 1988; Schroeder, 2002). Boxes indicate 0.25 and 0.75 quantiles and black diamonds show the arithmetic mean. Temperature projections are provided by the ISIMIP

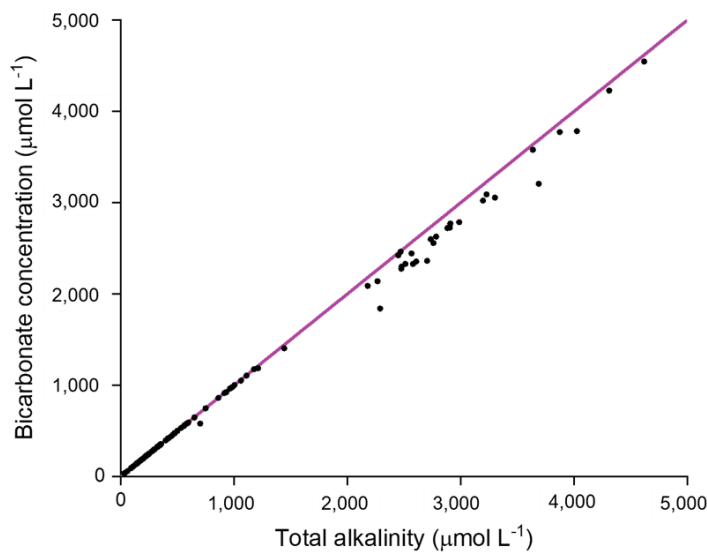
project (Lange and Büchner, 2021) based on the GFDL-ESM4 data (Krasting, J. P. et al., 2018). Discharge was simulated using the HydroPy global hydrology model (Stacke and Hagemann, 2021).



Extended Data Fig. 3-10: Projected change in alkalinity flux due to increased temperatures and changed river discharge. The combined influence of alkalinity concentration and river discharge changes on the alkalinity flux is shown. In contrast, Fig. 3-4 shows the sole influence of the alkalinity concentration on the alkalinity flux (discharge is kept constant), since we cannot distinguish the individual influences of the two parameters within the combined signal. However, this cause attribution was the main focus of this paper. Colors indicate the projected absolute change in alkalinity flux of catchments per temperature band for the historical temperature range of 0.0-20.0°C, globally, under scenarios (a) SSP1-2.6 and (b) SSP5-8.5. The mean change in MAT (ΔMAT) under SSP1-2.6 and SSP5-8.5 until the year of 2100 are projected to be 1.4 and 3.8°C, respectively. In contrast to Fig. 3-4, the discharge was not kept constant in this calculation, but instead the way it changes due to climate change was taken into account. The mean change in discharge (ΔQ) under SSP1-2.6 and SSP5-8.5 until the year of 2100 are projected to be 61 and 40 m s⁻¹, respectively. Catchment areas in white were excluded from the analysis, since their historical MATs were lower or higher than the temperature range of 0.0-20.0°C. For the calculation of the absolute alkalinity flux as specific mass flux, a molar mass of 61.02 g mol⁻¹ for bicarbonate (HCO₃⁻) was used, as at pH 7-9, the alkalinity concentration is approximately equal to the bicarbonate concentration (Dreybrodt, 1988; Schroeder, 2002).

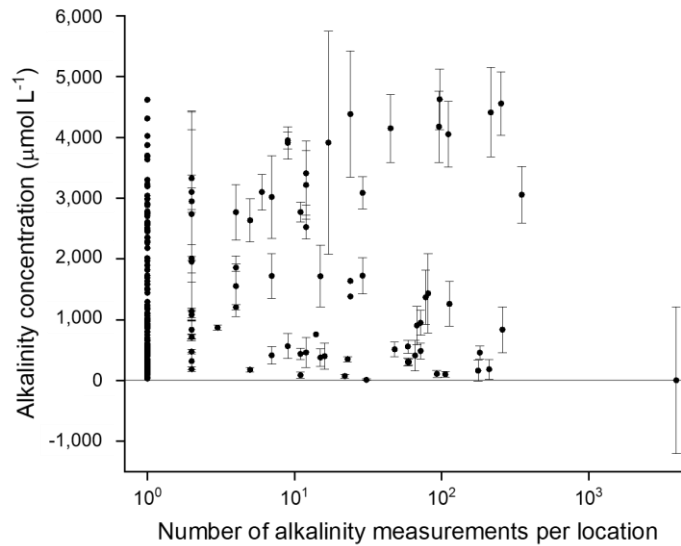


Extended Data Fig. 3-11: Influence of areal proportion affected by dams on alkalinity generation. The model function of M5 (based on complete training dataset, yellow line) is compared to a model function which is based on only the data with catchments that are characterized by an areal proportion affected by dams of < 10% (purple line). Normalized alkalinity concentration as a function of (a) erosion rate, (b) MAT, (c) soil thickness and (d) catchment area. The other covariates are kept constant (MAT = 10°C, catchment area = 1000 km², soil thickness = 15 m, erosion rate = 100 mm ka⁻¹).

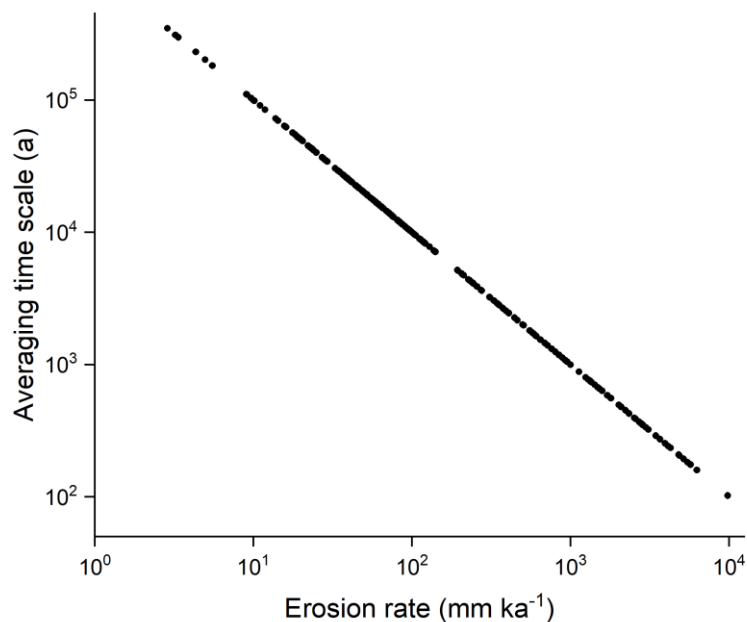


Extended Data Fig. 3-12: Bicarbonate concentration vs. total alkalinity concentration. Bicarbonate concentrations were calculated from total alkalinity and dissolved inorganic carbon for all samples taken during our sampling campaigns 2020. The data show

almost equal proportions (1:1), with a greater variation at higher total alkalinity concentrations ($> 2000 \mu\text{mol L}^{-1}$), which can be explained by an increase in the proportion of carbonate ion concentration.



Extended Data Fig. 3-13: Alkalinity concentration, its standard deviation and the number of alkalinity measurements per location.



Extended Data Fig. 3-14: Time scales over which ^{10}Be -derived erosion rates integrate. Assumed absorption depth scale $\sim 1000 \text{ mm}$.

Extended Data Tab. 3-1: Comparison of model fit for normalized alkalinity concentration. All models (M1-M5) are generalized linear models (GLMs) with a natural logarithm as the link function. The model performance of a generalized additive model (GAM), also having a natural logarithm as the link function, but incorporating all covariates as smooth functions, is given as a reference. AIC: Akaike Information Criterion, BIC: Bayesian Information Criterion, RSS: residual sum of squares, Ad. R²: adjusted R², pol. = polynomial.

	Covariates	AIC	BIC	RSS	Ad. R ²
M1	areal carbonate proportion	1024	1034	1077	0.342
M2	areal carbonate proportion	956	977	785	0.519
	MAT (3 rd degree pol.)				
M3	areal carbonate proportion	868	895	527	0.680
	MAT (3 rd degree pol.)				
	ln(erosion rate) (2 nd degree pol.)				
M4	areal carbonate proportion	794	829	378	0.763
	MAT (3 rd degree pol.)				
	ln(erosion rate) (2 nd degree pol.)				
	soil thickness				
	ln(area)				
M5	areal carbonate proportion	789	831	364	0.768
	MAT (5 th degree pol.)				
	ln(erosion rate) (2 nd degree pol.)				
	soil thickness				
	ln(area)				
GAM	areal carbonate proportion	709	824	214	0.849
	MAT				
	ln(erosion rate)				
	soil thickness				
	ln(area)				

Extended Data Tab. 3-2: Comparison of model performance for different temperature bands. RSS: residual sum of squares.

Temperature band (°C)	Number of observations	RSS (M3)	RSS (M4)	RSS (M5)
[-3,0)	16	11.3	3.1	1.4
[0,5)	45	206.6	136.7	124.8
[5,10)	106	1586.9	1342.9	1293.5
[10,15)	27	639.5	486.1	469.2
[15,20)	11	165.2	133.1	125.3
[20,27)	27	9.4	10.6	9.3

4 Alkalinity generation from carbonate weathering in a silicate-dominated headwater catchment at Iskorasfjellet, northern Norway

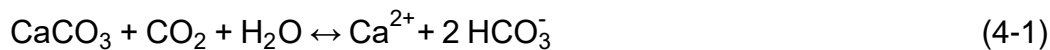
The weathering rate of carbonate minerals is several orders of magnitude higher than for silicate minerals. Therefore, small amounts of carbonate minerals have the potential to control the dissolved weathering loads in silicate-dominated catchments. Both weathering processes produce alkalinity under the consumption of CO₂. Given that only alkalinity generation from silicate weathering is thought to be a long-term sink for CO₂, a misattributed weathering source could lead to incorrect conclusions about long- and short-term CO₂ fixation. In this study, we aimed to identify the weathering sources responsible for alkalinity generation and CO₂ fixation across watershed scales in a degrading permafrost landscape in northern Norway, 68.7-70.5°N, and at a temporal scale, in a subarctic headwater catchment on the mountainside of Iskorasfjellet, characterized by sporadic permafrost and underlain mainly by silicates as the alkalinity-bearing lithology. By analyzing total alkalinity (AT) and dissolved inorganic carbon (DIC) concentrations, as well as the stable isotope signature of the latter ($\delta^{13}\text{C-DIC}$) in conjunction with dissolved cation and anion loads, we found that AT was almost entirely derived from weathering of the sparse carbonate minerals. We propose that in the headwater catchment, the riparian zone is a hotspot area of AT generation and release due to its enhanced hydrological connectivity, and that the weathering load contribution from the uphill catchment is limited by insufficient contact time of weathering agent and weatherable material. By using stable water isotopes, it was possible to explain temporal variations in AT concentrations following a precipitation event due to surface runoff. In addition to carbonic acid, sulfuric acid, probably originating from pyrite oxidation, is shown to be a potential corrosive reactant. An increased proportion of sulfuric acid as a potential weathering agent may have resulted in a decrease in AT. Therefore, carbonate weathering in the studied area should be considered not only as a short-term CO₂ sink, but also as a potential CO₂ source. Finally, we found that AT increased with decreasing permafrost probability, and attributed this relation to an increased water storage capacity associated with increasing contact of weathering agent and rock surfaces, and enhanced microbial activity. As both soil respiration and permafrost thaw are expected to increase with climate change, increasing the availability of weathering agent in the

form of CO₂ and water storage capacity, respectively, we suggest that future weathering rates and alkalinity generation will increase concomitantly in the study area.

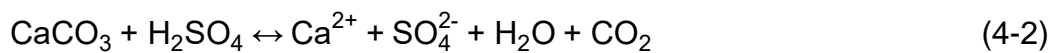
4.1 Introduction

Weathering of silicate rocks is thought to be the long-term sink (millions of years) for atmospheric CO₂ (Berner et al., 1983; Garrels and Berner, 1983). While alkalinity generation from weathering of calcium-silicates contributes to the long-term drawdown of CO₂ via the precipitation of carbonates in the ocean and thus the return of carbon to the lithosphere, the alkalinity generation from weathering of carbonate rocks does not have such an impact on these timescales. Carbonate weathering is thought to be in equilibrium with marine calcification over shorter time-scales (~10,000 years; Zeebe and Westbroek, 2003). Global estimates (Gaillet et al., 1999; Amiotte Suchet et al., 2003; Hartmann et al., 2009) attribute 49-63% of CO₂ consumption by terrestrial weathering to silicate rocks, the remainder to carbonate rocks. These studies rely on lithological maps and bulk river chemistry data used to infer whether CO₂ consumption is due to silicate or carbonate weathering. However, some case and regional studies (Blum et al., 1998; White et al., 1999; Jacobson et al., 2002; Jacobson et al., 2003; Oliver et al., 2003; White et al., 2005; Moore et al., 2013; Jacobson et al., 2015) indicate that the global calculations relying on bulk river chemistry data may overestimate silicate weathering. Hartmann (2009) pointed out that interpretation of the molar ratio of Ca²⁺/Na⁺ may lead to incorrect attribution of CO₂ drawdown to silicate weathering in predominantly silicate areas, which should instead be attributed to the weathering of accessory carbonate minerals. He calculated trace carbonate contribution for igneous rocks and silicate sediments, and applied the developed method globally (Hartmann et al., 2009). Especially silicate-dominated regions which are physically active or show early stages of weathering (e.g., during and following periods of glaciation and tectonism) show high weathering loads of accessory carbonate minerals (White et al., 1999; Jacobson et al., 2002; Jacobson et al., 2003; Oliver et al., 2003; White et al., 2005; Moore et al., 2013; Jacobson et al., 2015). The weathering rate of carbonates is several orders of magnitude faster than the one of silicates (Lasaga, 1984; Stallard and Edmond, 1987; Jacobson et al., 2003), thus dissolved inorganic carbon (DIC) is often controlled by carbonates (Liu et al., 2018).

DIC is composed of CO_2^* (i.e., the sum of dissolved CO_2 and H_2CO_3), HCO_3^- and CO_3^{2-} , with the relative proportion of the DIC species depending on alkalinity and environmental conditions such as temperature. In fresh water, total alkalinity (AT), or acid-neutralizing capacity, is mainly composed of carbonate alkalinity (i.e., HCO_3^- and CO_3^{2-}). At pH values between 7 and 9, the alkalinity concentration is approximately equal to the HCO_3^- concentration (~95% of the carbon in the water is in the form of HCO_3^-), as the equilibrium between CO_2^* , HCO_3^- and CO_3^{2-} in this pH range is strongly in favor of HCO_3^- (Stumm and Morgan, 1981). Alkalinity in the form of HCO_3^- is produced from the weathering of carbonate minerals (shown here for calcite) under the consumption of one equivalent of atmospheric and/or soil CO_2 as follows:

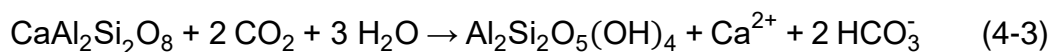


Assuming that the weathering agent is not carbonic acid, but other inorganic acids such as sulfuric and nitric acid, carbonate weathering (shown here for calcite weathering with sulfuric acid) releases CO_2 , thereby increasing the DIC concentration, but not contributing to alkalinity generation (Berner and Berner, 1987; Marx et al., 2017a; Liu et al., 2018):



Sulfuric acid can be generated from the dissolution of sulfate-containing minerals, such as gypsum, or the oxidation of sulfide minerals, such as pyrite. Furthermore, both sulfuric and nitric acid can be brought into the soil via acid rain. Finally, nitric acid can also be produced from the oxidation of ammonium fertilizers (Li et al., 2010; Marx et al., 2017a).

While in carbonic acid induced carbonate weathering only one of the two equivalents of HCO_3^- is derived from atmospheric and/or soil CO_2 , in silicate weathering all HCO_3^- originates from CO_2 (shown here for anorthite weathering, one of the three major types of feldspar):



When silicates are weathered by non-carbon based acids, neither DIC nor AT is generated (shown here for anorthite weathering with sulfuric acid):



A valuable tool to distinguish between the sources of DIC in streams is the stable isotope composition of DIC, $\delta^{13}\text{C}\text{-DIC}$ (Deines et al., 1974; Böttcher, 1999), which varies across a wide range, typically from +5‰ to -35‰ (Campeau et al., 2017). In addition to the above mentioned geogenic

sources, DIC is also governed by biogenic sources, CO₂ evasion, and in-stream processes (Kempe, 1982; Campeau et al., 2017). Biogenic DIC originates from autotrophic respiration or organic matter mineralization. In regions dominated by C₃ plant vegetation, this biogenic DIC has a typical $\delta^{13}\text{C}$ value of about -27‰ (O'Leary, 1988). When measured in soil solution, this value typically increases by 1-4‰, as dissolution and gas exchange across the soil-atmosphere interphase take place (Cerling et al., 1991; Davidson, 1995; Amundson et al., 1998). When carbonate minerals, which have a typical $\delta^{13}\text{C}$ value of about 0‰ (Hoefs, 1973; Land, 1980), are weathered by soil respired dissolved CO₂ (about -24‰), the final DIC is at saturation with carbonate minerals and is characterized by an isotopic composition of about -12‰, considering evolution under conditions closed with reference to a CO₂ gas phase in C₃ vegetation-dominated catchments (Deines et al., 1974). C₄-type of vegetation leads to shift towards heavier stable isotope values (Deines et al., 1974). When the weathering takes place by other inorganic acids, the resulting $\delta^{13}\text{C}$ -DIC can even turn more positive (Schaefer and Usdowski, 1987, 1992; Michaelis, 1992) and reach under extreme conditions the $\delta^{13}\text{C}$ value of carbonate minerals of about 0‰ (Lehn et al., 2017). The actual isotope composition of DIC depends also on the boundary conditions (presence of biogenic CO₂) during the groundwater evolution (Deines et al., 1974; Schaefer and Usdowski, 1987, 1992; Böttcher, 1999). DIC generated from carbonic acid induced silicate weathering has a typical $\delta^{13}\text{C}$ value of about -24‰, as soil CO₂ is the dominant source for DIC (Lehn et al., 2017; Purkamo et al., 2022) and fractionation between the aqueous and gas phase is small at low pH values (Deines et al., 1974).

When CO₂ is degassed from the stream due to supersaturation, which is especially prominent in headwater catchments (Michaelis et al., 1985; Marx et al., 2017a), the remaining stream water DIC is enriched in ¹³C. Equilibrium exchange fractionation between stream DIC and atmospheric CO₂, which has a typical $\delta^{13}\text{C}$ value of about -8‰ (Troler et al., 1996), has the same effect on stream $\delta^{13}\text{C}$ -DIC as CO₂ outgassing (Michaelis et al., 1985; Liu and Han, 2020).

Finally, the $\delta^{13}\text{C}$ -DIC values on flowing surface waters may also be influenced by in situ biogeochemical processes such as biological respiration, DOC photo-oxidation, photosynthesis, mixing with groundwaters, and anaerobic metabolism (Campeau et al., 2017).

The general controls on chemical weathering are the availability of weatherable minerals, mainly provided by physical weathering of regolith, and

the supply of weathering agents, i.e., acids (Raymond and Hamilton, 2018). Further, to generate the soluble weathering products, favorable conditions such as high temperatures, abundant moisture and high contact of mineral surfaces with water should prevail. Lastly, the hydrological transport of these solutes out of the weathering zone is another controlling factor (Raymond and Hamilton, 2018).

Feedback between the Earth's carbon cycle and terrestrial weathering was originally thought to be slow, and CO₂ consumption by terrestrial weathering to be at steady state since pre-industrial times (Walker et al., 1981; Berner et al., 1983). However, a global study (Goll et al., 2014) reported increased CO₂ consumption since 1850, and regional studies (Raymond et al., 2008; Li et al., 2008; Gislason et al., 2009; Drake et al., 2018; Macpherson et al., 2019) found an increase in riverine alkalinity over the last decades and related this to changes in temperature, precipitation, vegetation, availability of acids, liming, or hydrologic flow conditions. Thawing permafrost in cold regions was assumed, too; thereby advocating for a possibly rapid (decadal) feedback between climate and land-use change and riverine alkalinity generation upon terrestrial weathering. Especially carbonate weathering was found to be very responsive to contemporary environmental changes (Michaelis, 1992; Zeng et al., 2019). Besides the tropical region, northern high latitudes are expected in the future to experience enhanced carbonate weathering and thus a higher carbon-sink function due to increased soil CO₂ partial pressures and temperatures (Zeng et al., 2022). The aquifers and soils of Fennoscandia, however, are mainly composed of non-carbonate rocks (O'Nions et al., 1970; Hartmann and Moosdorf, 2012; Zeng et al., 2022), and therefore, a response in terms of CO₂ sequestration through weathering on environmental changes might be expected to be slow (Moosdorf et al., 2011).

Climate change is particularly accelerated in the Arctic, as reflected in the annually averaged near-surface air temperature, which increased by 0.71°C per decade from 1979 to 2021, nearly four times faster than the global average (Rantanen et al., 2022). This rapid warming simultaneously affects permafrost, hydrology and surface vegetation, with all of these processes having the potential to alter the generation of alkalinity (Drake et al., 2018). Permafrost thaw causes the Arctic terrestrial freshwater system to increase its connectivity between surface waters and deeper groundwater pathways (Striegl et al., 2005; Walvoord and Striegl, 2007) and may ultimately move from a surface water-dominated to a groundwater-dominated system (Frey and McClelland, 2009). Thawed soils allow for longer

residence times of infiltrating surface water, thereby facilitating more contact with unweathered mineral surfaces and additional mixing with mineral-rich groundwater, resulting in higher alkalinity fluxes (Drake et al., 2018). So far, studies about fast feedback between alkalinity generation from rock weathering and climate change in northern high latitudes have investigated the impact of a varying glacial cover (Gislason et al., 2009) or retrogressive thaw slumps (Zolkos et al., 2020) or focused on large Arctic river systems (Drake et al., 2018) and on subcatchments of the circumboreal (Tank et al., 2012). An in-depth study of the weathering processes in catchments of the silicate-rich Fennoscandian Shield in northern Norway, potentially influenced by a changing climate, which could lead to an enhanced alkalinity generation, is still missing.

Our aim in the present study is to identify the weathering pathways responsible for alkalinity generation in a small subarctic catchment on the mountainside of Iskorasfjellet in northern Norway mainly dominated by silicate minerals and characterized by sporadic permafrost during early fall of 2020. In particular, we aimed at distinguishing between different weathering agents (dissolved CO₂ vs. other acids) and different source minerals (silicate vs. carbonate) under different environmental forcing, thereby analyzing the potential for CO₂ drawdown. In addition to the detailed analysis of the Gaskabohki watershed at Iskorasfjellet, we extended the investigation of controlling factors on alkalinity generation to several other catchments, some of which stretch as far as the Barents Sea with varying extent of permafrost, in order to establish broader implications and evaluate how climate change might provide feedback for CO₂ sequestration in this subarctic region.

4.2 Materials and methods

4.2.1 Study site

The Gaskabohki watershed (catchment area = 0.7 km²) is a headwater catchment located on the mountain slope of Iskorasfjellet, Karasjok Municipality, northern Norway (Fig. 4-1). Iskorasfjellet is situated inland on the Finnmarksvidda plateau (300-500 m above mean sea level (amsl)), with local peaks rising above 600 m amsl), which borders Finland to the south and east. The Finnmarksvidda plateau was completely ice-covered during the Pleistocene glaciations. Due to glacial activity, ground-moraine, glaci-ofluvial, and glaciolacustrine sediments were accumulated on the surface geology (Sollid et al., 1973). Iskorasfjellet was deglaciated ~10,900-

10,800 cal. yr BP (Stroeven et al., 2016). The Gaskabohki catchment is underlain by quartzite and arkose, in places with layers of different shales (NGU, 2022a). Therefore, the alkalinity-bearing lithology is dominated by feldspar, with minor contribution of calcite within the shales. Just before the outlet, however, a small area of partly calcareous quartz feldspar shale (0.5% areal proportion of the entire catchment area) underlies the catchment. This area coincides with a wider riparian zone (Fig. 4-1d). Besides the main channel, drainage gullies are present which were dried out at the time of sampling in the fall.

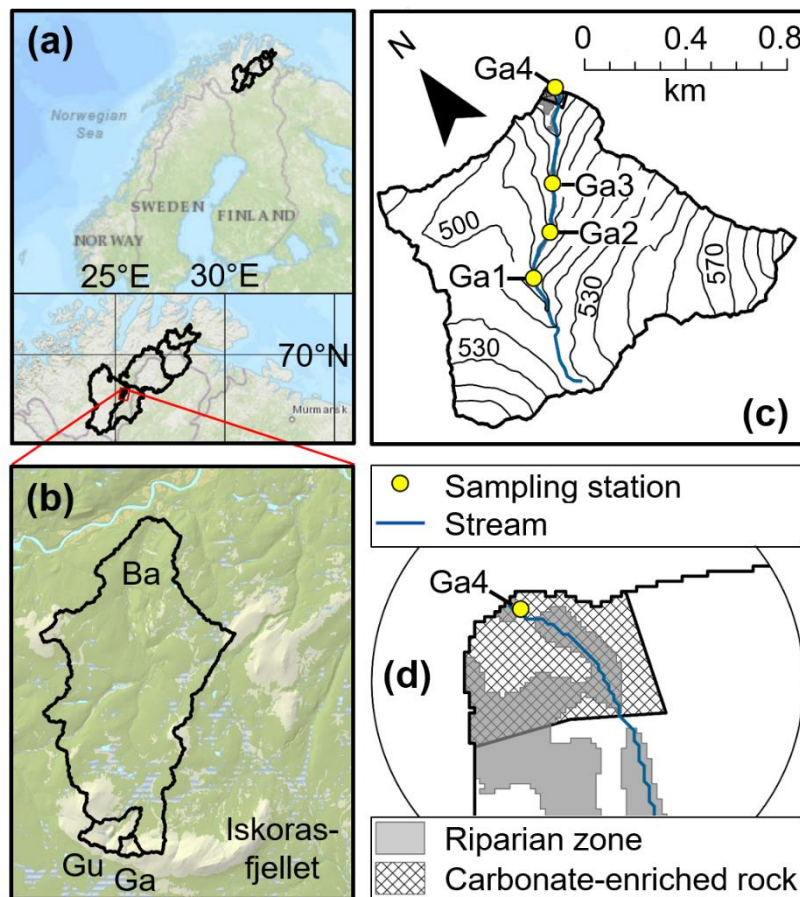


Fig. 4-1: Study area. (a) Location of all studied basins in Fennoscandia. Background map from Esri, HERE, Garmin, FAO, NOAA, USGS (ESRI, 2022). (b) Zoom on the study area at Iskorasfjellet with the Bahkiljohka (Ba), Guovzilbohki (Gu) and Gaskabohki (Ga) catchments. Background map is the ArcGis web map “Topografisk Norgeskart” (ESRI, 2022). (c) Zoom on the Gaskabohki headwater catchment with sampling stations Ga1 to Ga4 (Gaskabohki 1 to Gaskabohki 4). Contour interval = 10 m. (d) Zoom on the outlet of the Gaskabohki catchment with the wider riparian zone overlapping with an area of partly calcareous quartz feldspar shale (carbonate-enriched rock).

From the top of the mountain at 644 m amsl., the landscape slopes down (~3% slope) to the Iskoras peat plateau at ~380 m amsl. The peat began

to form around 9,800 cal. year BP in the form of wet fens, which were prevalent during most of the Holocene. Dry surface conditions associated with permafrost peat plateau aggradation developed around 950-100 cal. year BP, probably caused by the Little Ice Age cooling (Kjellman et al., 2018).

The Iskoras peat plateau is enclosed by the Bahkiljohka catchment (catchment area = 78 km²), which is underlain by an increased proportion of partly calcareous quartz feldspar shale (up to 34% of areal carbonate extent; NGU, 2022a) when compared to the Gaskabohki catchment (0.5%). From Iskorasfjellet, the sampling area stretches out further northeast, following the larger rivers Karasjohka and Tanaelva, until the Tanafjord. While the Bahkiljohka catchment is characterized by isolated patches of permafrost (catchment average permafrost probability = 0.04), the Gaskabohki watershed as well as the rest of the studied area show sporadic permafrost (catchment average permafrost probability = 0.10-0.17; Obu et al., 2018). Tundra vegetation (e.g., lichen crusts, *Betula* shrubs and *Empetrum nigrum* ssp. *hermaphroditum*) dominates at Iskorasfjellet. Below an elevation of ~570 m amsl, mountain birch (*Betula pubescens* ssp. *czerepanovii*) forest is also present.

The climate of Finnmarksvidda is continental. For the last six years (September 2014 to August 2020, longest continuous record at Iskorasfjellet), the mean summer (June-July-August) and winter (December-January-February) air temperatures were 8.7°C and -9.3°C, respectively (measured at the meteorological station at Iskorasfjellet, 591 m amsl, SN97710; Seklima, 2020). Compared to the air temperature normal (1961-1990), temperatures increased by 0.2°C and 4.2°C, respectively. Mean monthly precipitation sums during the summer and winter for the last six years were 66 mm and 38 mm, which correspond to 117% and 237% of the monthly precipitation sums of the climate normal, respectively. The annual precipitation averaged over the last six years, from September 2017 to August 2020, was 492 mm (measured at the meteorological station in Karasjok, 131 m amsl, SN97251, 20 km from Iskorasfjellet; Seklima, 2020). The mean daily snow depth during the snow season (October to May) was 29 cm (measured at the meteorological station at Iskorasfjellet, 591 m amsl, SN97710; Seklima, 2020).

During the sampling campaign in fall 2020, a precipitation sum of 7 mm was measured, which is about half of what was recorded over the same period averaged over the six years prior to sampling (Seklima, 2020). Thus, the fall of 2020 was comparatively dry. There was no snowfall and

the mean daily air temperature averaged over the sampling period was 3.9°C, which is ~2.7°C higher than during the same fall period 2014-2019 (Seklima, 2020).

4.2.2 Water sampling

From September 22nd to October 6th 2020, we collected water samples daily from the outlet of the Gaskabohki catchment (Ga) to investigate how DIC and AT may change under different environmental forcing (changing precipitation and temperature). We further sampled weekly (3x) at three stations upstream of the outlet to track the changes of the carbonate system with distance from the spring. Besides this temporal examination, we also expanded the investigation spatially, by collecting water samples from seven further catchments. These catchments included the Guovzilbohki headwater catchment (Gu), which shows similar topographic properties as the adjacent Gaskabohki watershed, but a higher carbonate-to-silicate bedrock ratio; the Bahkiljohka catchment (Ba) which is characterized by the lowest permafrost probability; and five larger catchments (catchment area = 4,900-15,000 km²). In that way, we were able to investigate further controlling factors (catchment area, roughness, permafrost probability, peatland cover, EVI (mean enhanced vegetation index), and bedrock lithology) on alkalinity generation.

At all sampling sites, we collected water samples for DIC and AT, $\delta^{13}\text{C}$ -DIC, major elements, and stable water isotopes ($\delta^{18}\text{O}$ -H₂O and $\delta^2\text{H}$ -H₂O). For DIC and AT analysis, we collected the river water directly into 300-mL BOD bottles, added 300 μL of saturated mercury chloride solution and sealed the bottles with ground-glass stoppers, Apiezon type M grease and plastic caps (no-headspace). For $\delta^{13}\text{C}$ -DIC analysis, the solution was membrane-filtered (0.45 μm pore widths) into 12-mL glass vials, 10 μL of saturated mercury chloride solution were added, and the vials were sealed with a septum without headspace. For cation measurements, we filtered the surface water (0.45 μm pore widths) into 50 mL acid-washed tubes and acidified the samples with 50 μL of concentrated trace metal-grade HNO₃. For anion measurements, we filtered (0.45 μm pore widths) the samples into 15 mL tubes, from which we later took an aliquot (~1.5 mL) for stable water isotope analysis. All samples were stored in the dark at ambient temperature (~1-10°C). We measured stream temperature and electric conductivity using a precalibrated WTW Multi3430 with IDS TetraCon 925, and turbidity using a precalibrated HACH 2100Qis. Finally, at the outlet of the Gaskabohki catchment, we performed a discharge measurement once a day, at the same time as taking the water samples, by recording stream

velocity using a Marsh-McBirney Model 2000 Flo-Mate portable flow meter at increments equal to ~10% of the stream width. By measuring the corresponding stream depth, we were able to calculate stream discharge from the product of stream velocity and cross-sectional area.

4.2.3 Hydrochemical analyses

We analyzed the AT concentration by performing a potentiometric titration using a Metrohm 888 Titrando with an Aquatrode pH probe. The recovery was $\geq 99\%$. We used a Marianda VINDTA 3C (Versatile Instrument for the Determination of Titration Alkalinity) to determine the DIC concentration by coulometric titration. The precision was $\pm 2 \mu\text{mol L}^{-1}$ (Shadwick et al., 2011). AT and DIC measurements were calibrated against certified reference materials (CRMs) provided by Andrew Dickson (Scripps Institution of Oceanography). We calculated pH and $p\text{CO}_2$ by using the program CO2SYS (Pierrot et al., 2011), providing AT, DIC and water temperature, and using the freshwater equilibrium constants from Millero (1979). $\delta^{13}\text{C}$ -DIC were measured by means of continuous-flow isotope-ratio-monitoring mass spectrometry (CF-irmMS) using a Finnigan MAT 253 gas mass spectrometer coupled to a gas bench (GasBench II, Thermo Fisher Scientific) via a ConFlo IV continuous flow interface following the procedure described by Winde et al. (2014). Precision of $\delta^{13}\text{C}$ -DIC analysis was better than $\pm 0.1\text{‰}$. Results are given versus the VPDB standard. Stable water isotopes ($\delta^{18}\text{O}$ -H₂O and $\delta^2\text{H}$ -H₂O) were measured by means of cavity ring-down spectroscopy (CRDS) using a Picarro L2140-I system. International besides in-house standards were used to scale the water isotope measurements (Böttcher and Schmiedinger, 2021). Stable isotope results are given in the conventional δ -notation versus the VSMOW standard and had a precision of better than $\pm 0.06\text{‰}$ for oxygen and $\pm 0.3\text{‰}$ for hydrogen isotopes (Böttcher and Schmiedinger, 2021). All stable isotope data given in '‰' are equivalent to 'mUr' (milli Urey; Brand and Coplen, 2012). Multi-element composition (Al, Ba, Ca, Fe, K, Mg, Mn, Na, P, Si, Sr) was analyzed by inductively coupled plasma optical emission spectrometry (ICP-OES) using a Perkin Elmer Optima 8300DV spectrometer. We determined anion concentrations (Br^- , Cl^- , F^- , NO_3^- , SO_4^{2-}) using a Thermo Fisher Scientific Dionex ICS-2100 ion chromatograph. The precision for multi-element and anion analyses was $\pm 10\%$. The complete hydrochemical dataset will be available through PANGAEA.

4.2.4 Geospatial analyses

We delineated stream networks and watershed areas using the SAGA-GIS modules “Channel Network and Drainage Basins” and “Upslope Area” (Conrad et al., 2015) in QGIS 3.22.2 (QGIS.org, 2022) from the gridded digital elevation model ArcticDEM (Porter et al., 2018) and used ArcGIS Pro 2.8.0 (ESRI, 2022) to create the maps. While we used the full resolution model (2 m) for the two small headwater catchments Gaskabohki and Guovzilbohki, we used the 32 m-resolution one for the larger watersheds.

We calculated the catchments’ mean values of terrain roughness, permafrost probability, peatland cover, enhanced vegetation index (EVI) and bedrock lithology. We computed terrain roughness, which is indicative of the potential for physical erosion (Riley et al., 1999), by using the GDAL tool “Roughness” (Rouault et al., 2022). We determined permafrost probability by using the Northern Hemisphere permafrost map based on TTOP (temperature at the top of the permafrost) modelling for 2000-2016 at 1 km² scale, which performs well in sparsely vegetated tundra regions and mountains (Obu et al., 2018), reflecting our study region. We determined the areal proportion of peatland cover, including mires, from the peatland map of Europe (Tanneberger et al., 2017). EVI can serve as a proxy for vegetation productivity (Huete et al., 2002). We used the EVI of the MODIS vegetation index (VI) products, which is based on MODIS data with a resolution of 250 m from October 6th 2020 (Didan et al., 2015). We determined the lithological coverage of the smaller basins (Gaskabohki, Guovzilbohki and Bahkiljohka) from the Norwegian bedrock map “Berggrunn N250” (NGU, 2022a) by calculating the area of the individual rock types (e.g., quartzite) as a percentage of the total catchment area. For the comparison with the larger catchments, we used the global lithological map database GLiM, which contains 16 lithological classes (Hartmann and Moosdorf, 2012).

We determined the riparian zone in the Gaskabohki catchment by first calculating the slope per 2 x 2 m DEM cell and then, starting from the streambed, identifying all cells belonging to the riparian zone that had a slope less than 10° (gradient of 1 : 5.7).

4.2.5 Modelling of soil respiration

We used the streamCO₂-DEGAS model by Polsenaere and Abril (2012) to calculate initial soil *p*CO₂. The model first simulates the decrease in *p*CO₂ and increase in δ¹³C-DIC that occur along the stream watercourse during degassing, starting from an assumed initial soil *p*CO₂ and ending at the in

situ $p\text{CO}_2$ or $\delta^{13}\text{C}\text{-DIC}$. Subsequently, soil $p\text{CO}_2$ is adjusted until $p\text{CO}_2$ and $\delta^{13}\text{C}\text{-DIC}$ simultaneously reach the in situ measured values. Soil organic matter isotopic composition and the isotopic fractionation of CO_2 in the soil due to selective molecular diffusion of the gas through the soil pores are considered. The model is applicable for small, unproductive streams (assumption of insignificant primary production in the aquatic system) with acidic pH (4.6-7.2) and demands the input variables of AT, $\delta^{13}\text{C}\text{-DIC}$, $p\text{CO}_2$, and stream temperature (Polsenaere and Abril, 2012). We assumed a proportion of non-carbon based acid induced alkalinity generation of 0.2 and a proportion of in-stream respiration of 0.

4.3 Results and discussion

4.3.1 Weathering and alkalinity generation in the Gaskabohki catchment

During the study period of fall 2020, the Gaskabohki catchment showed a mean AT concentration (\pm standard deviation) of $125 (\pm 5) \mu\text{mol L}^{-1}$ and a mean DIC concentration of $148 (\pm 21) \mu\text{mol L}^{-1}$. As the Gaskabohki catchment is mainly underlain by quartzite and arkose, thus the alkalinity-bearing mineral being feldspar, it is reasonable that the measured AT concentration exactly matches the concentration that Meybeck (1987) found for catchments draining pure silicate bedrock.

Carbonic-acid induced carbonate weathering dominates alkalinity generation

The mean sum of major cation concentrations (Na^+ , K^+ , Ca^{2+} , Mg^{2+}) in the Gaskabohki stream was $120 (\pm 4) \mu\text{mol L}^{-1}$. This is consistent with the lower range found for rivers of the Canadian Shield in the Grenville Province which are characterized by a similar catchment geology (Millot et al., 2002). The average $\text{Ca}^{2+}/\text{Na}^+$ and $\text{Mg}^{2+}/\text{Na}^+$ molar ratios in the Gaskabohki stream were $0.74 (\pm 0.05)$ and $0.49 (\pm 0.02)$, respectively. These values are consistent with the ones found by Meybeck (1986) for quartz sand and sandstone watersheds, and slightly higher than the ones calculated by Gaillardet et al. (1999) for the global silicate end-member. As we did not correct our data for precipitation due to the lack of rainwater composition data at the study site, these molar ratios are likely underestimated. Therefore, the weathering load would move closer to the carbonate end-member. In our dataset, the highest $\text{Ca}^{2+}/\text{Na}^+$ molar ratios (up to 0.83) are associated with both the highest AT and the highest electrical conductivity values, indicating enhanced carbonate weathering. Considering that our

ionic concentrations are not corrected for rainwater input, these elevated $\text{Ca}^{2+}/\text{Na}^{+}$ molar ratios, if corrected, should approach the molar ratio ($\text{Ca}^{2+}/\text{Na}^{+} > 1$) reported by Oliva et al. (2004) for a weathering load that is extensively influenced by trace minerals such as calcite in high elevation systems draining granitic environments.

The DIC system of the Gaskabohki catchment is neither completely kinetically- (mineral weathering reactions) nor completely equilibrium- (mixing with atmospheric and biotic CO_2) controlled. It is controlled both by HCO_3^- production from carbonate weathering and by the CO_2 pool in the soil (Fig. 4-2a).

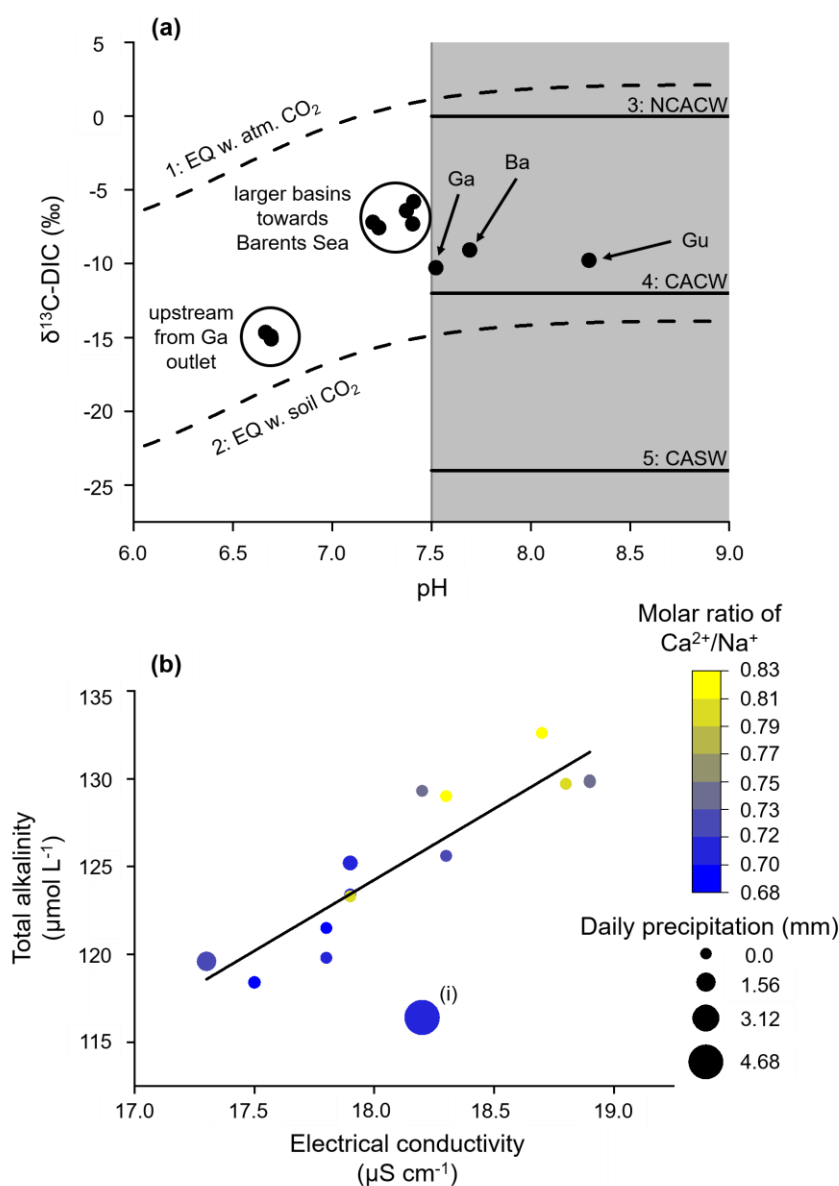


Fig. 4-2: Equilibrium- vs. – kinetically-controlled systems. (a) If the pH of the stream water is below 7.5, then the DIC system is equilibrium-controlled, meaning that the stream

DIC is in equilibrium with a large pool of either atmospheric (1) or soil (2) CO₂. The δ¹³C-DIC values (dashed lines) were calculated based on the temperature-dependent fractionation factors that partition the carbon isotopes among the DIC species (Zhang et al., 1995). If the pH is above 7.5, the DIC system is kinetically-controlled and three weathering pathways can be identified. Depending on the δ¹³C-DIC value, the DIC originates from (3) NCACW (non-carbon based acid induced carbonate weathering), (4) CACW (carbonic acid induced carbonate weathering), (5) CASW (carbonic acid induced silicate weathering). Ga: Gaskabohki catchment; Gu: Guovzilbohki catchment; Ba: Bahkiljohka catchment. The figure was adjusted from Lehn et al. (2017). **(b)** AT as a function of electrical conductivity for the Gaskabohki catchment. The linear increase of AT with electrical conductivity indicates that mineral weathering is a major control in this catchment (y-intercept = -21.2 μmol L⁻¹, slope coefficient = 8.1). (i) We excluded this data point from the linear regression, as it shows the highest δ¹⁸O-H₂O value, thus indicating the highest proportion of surface water.

While the DIC system mainly consists of HCO₃⁻ ions (~83 (± 7) %), CO₂^{*} plays a minor role (~16 (± 9) %) and CO₃²⁻ ions (~1 (± 3) %) are negligible. We found that AT increases linearly with electric conductivity (adjusted R² = 0.81), suggesting that the Gaskabohki catchment is mainly controlled by mineral weathering (Fig. 4-2b). We excluded the measurement with the highest daily precipitation sum of 4.7 mm (4.3 mm within 3 h) from the linear regression (Fig. 4-2b, (i)), because this measurement showed a distinctly higher δ¹⁸O-H₂O value when compared to the other measurements, thus indicating the highest proportion of surface water. Furthermore, it also showed a distinctly higher turbidity. As mineral weathering in headwater catchments is generally associated with groundwater inputs (Shin et al., 2011), we thought this exclusion reasonable. Other authors (Hill and Neal, 1997) explained decreases in AT associated with increases in electric conductivity with enhanced soil- and surface-derived components, such as nutrients and organic acids. We can also observe this in our dataset, where we detected a nitrate signal in the samples that were taken during a day with rainfall or on up to four days that followed, before falling under the detection limit, indicating a hysteresis effect (Fig. 4-3).

We assumed the δ¹³C-DIC endmember for carbonic acid induced carbonate weathering to be at about -12‰, as the vegetation at Iskorasfjellet is of C3 type characterized by a δ¹³C value of about -27‰ (Kjellman et al., 2018). With the diffusive fractionation in low temperature waters, such as during fall in this subarctic region, causing a positive shift of about 3‰, the δ¹³C value of the CO₂ pool would be about -24‰ (Deines et al., 1974; Michaelis et al., 1985; Zhang et al., 1995; Lehn et al., 2017). When dissolving carbonate minerals with a δ¹³C value of about 0‰, the resulting δ¹³C-DIC would thus be about -12‰. If the weathering agent is a non-carbon based

acid, the $\delta^{13}\text{C}$ -DIC endmember for carbonate weathering will be about 0‰. As the mean $\delta^{13}\text{C}$ -DIC of the Gaskabohki catchment was $-10.3 (\pm 1.3) \text{‰}$, we attribute the alkalinity generation in the basin entirely to the dissolution of accessory carbonate rock by carbonic acid generated from soil respiration. We suggest that the small deviation from the carbonic acid induced carbonate weathering $\delta^{13}\text{C}$ -DIC endmember of -12‰ to slightly less negative values is caused by a small contribution from non-carbon based acid induced carbonate weathering. We believe, that the primary weathering agent of silicate minerals were non-carbon based acids, with no generation of DIC and AT.

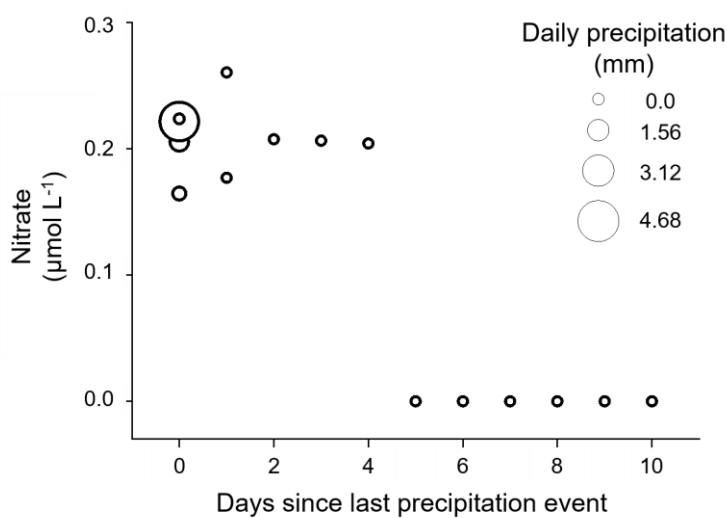


Fig. 4-3: A nitrate signal is associated with a precipitation event and the days that follow. On the fifth day after the last precipitation event, we could not detect any more nitrate.

Carbonate weathering by sulfuric acid decreases alkalinity concentration

During the study period, AT was positively correlated with the concentration sum of Ca^{2+} and Mg^{2+} (adjusted $R^2 = 0.57$, Fig. 4-4a), which further confirms that alkalinity is produced from carbonate weathering alone. For one equivalent of a divalent cation, we found about two equivalents of alkalinity in our samples, as would be expected from carbonic acid induced carbonate weathering (see equation (4-1)). AT concentrations that fall below the regression line are associated with a high molar ratio of $\text{SO}_4^{2-}/\text{AT}$. We explain this with Ca^{2+} and Mg^{2+} originating from carbonate minerals that were dissolved by sulfuric acid. Thus, no AT, but SO_4^{2-} was generated. An indicator of the presence of sulfuric acid in the Gaskabohki catchment

is that we observed a negative alkalinity concentration at a theoretical electrical conductivity of 0 (according to the linear regression in Fig. 4-2b, y-intercept = $-21.2 \mu\text{mol L}^{-1}$). We believe that sulfuric acid balances this negative alkalinity in the Gaskabohki catchment. Sulfuric acid could be generated from the oxidation of pyrite or be a remnant of acid rain. Minor occurrences of pyrite are present in the upper parts of the Palaeoproterozoic bedrock of the Fennoscandian Shield (Sandström and Tullborg, 2009). As our study area is situated on the Karasjok Greenstone Belt, which forms the westernmost unit in a Palaeoproterozoic tectonic belt (Braathen and Davidsen, 2000), the generation of sulfuric acid by the oxidation of pyrite is a reasonable explanation. Even though acid rain deposition has decreased considerably since the end of the last century in northern Norway (Aas et al., 2021), the recovery from acid rain in deeper soil horizons may be highly delayed (Berger et al., 2016; Marx et al., 2017b). This delayed soil acidification was also observed in southern Sweden, where the B2 horizon did not reach its most acidic conditions until 2013, almost 25 years after the sulfur deposition began to decline (McGivney et al., 2019). Our studied area could be influenced by legacy acid rain distributed area-wide from coal burning or, under the assumption of long-distance transport of pollutants, by the emissions of SO_2 from the smelters in Nikel and Zapoljarnij on the Kola Peninsula in Russia (linear distance between these two sites and Iskorasfjellet: ~ 200 km). A study in the Tibetan Plateau by Yuanrong et al. (2021) found that the sulfate concentration in glacial and permafrost streams was elevated compared to streams in other landscapes and explained this by condensed storage of acid deposition from long-distance transport during lower temperatures and a release during higher temperatures. Since the main wind directions on the Kola Peninsula in Russia are to the south and to the north (Chekushin et al., 1998) and the Russian smelters are located east of Iskorasfjellet, the sulfuric acid could presumably originate from pyrite oxidation and legacy acid rain from coal burning.

The $\delta^{13}\text{C}$ -DIC signal also reflects that two different weathering agents in the Gaskabohki catchment dissolve carbonate minerals. It shows a value of about -12‰ typical of carbonic acid induced carbonate weathering at a low molar ratio of $\text{SO}_4^{2-}/\text{AT}$ (Fig. 4-4b). As the ratio increases, so does the $\delta^{13}\text{C}$ -DIC, suggesting an increased proportion of sulfuric acid as the weathering agent of carbonate minerals. We found that a logistic function better fit the data than a linear regression (adjusted $R^2 = 0.78$ and 0.68 , respectively), suggesting a change in weathering pathways. Therefore, regarding the CO_2 budget impacted by terrestrial weathering, the catchment can

switch from a complete CO₂ sink to a partial CO₂ source. Since the δ¹³C-DIC depends on the molar ratio of SO₄²⁻/AT and shows no correlation to discharge (Pearson correlation coefficient $r = 0.02$, not significant at $p < 0.01$), indicative of turbulence, we assume that the influence of CO₂ outgassing along the stream on the δ¹³C-DIC signal at the catchment outlet can be ignored.

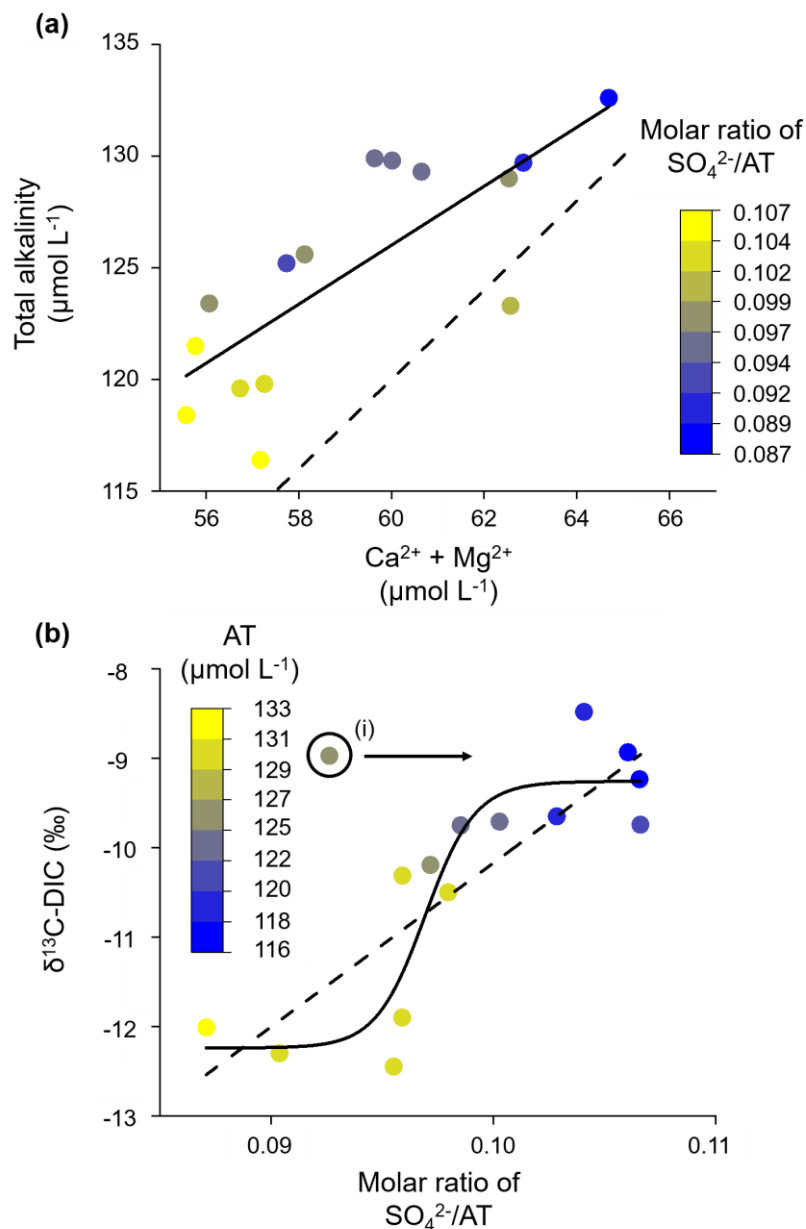


Fig. 4-4: Alkalinity generation from carbonic acid induced carbonate weathering. (a) AT increases linearly with the concentration sum of Ca²⁺ and Mg²⁺. At a constant concentration of divalent cations, AT decreases with increasing molar ratio of SO₄²⁻/AT, indicating an increased proportion of carbonate weathering induced by sulfuric acid (release of divalent cations with no generation of alkalinity). Solid line: linear regression (y-intercept = 46.8 μmol L⁻¹, slope coefficient = 1.3); dashed line: representing the typical molar ratio

of carbonic acid induced carbonate weathering of $\text{AT}/(\text{Ca}^{2+} + \text{Mg}^{2+})$ of 2:1. (b) $\delta^{13}\text{C}\text{-DIC}$ increases with the molar ratio of $\text{SO}_4^{2-}/\text{AT}$. The logistic fit (solid line) yielded a higher adjusted R^2 than the linear regression fit (dashed line: y-intercept = -28.5‰ , slope coefficient = 183.3), suggesting that a changeover of weathering pathways explains the $\delta^{13}\text{C}\text{-DIC}$ signal better than a linear relationship. (i) We excluded this data point from both model fits, because it has a high pH, likely resulting from in-stream photosynthesis.

We excluded the point with the highest pH (pH = 9.6) from both data fits, which was characterized by a high $\delta^{13}\text{C}\text{-DIC}$ value and a low molar ratio of $\text{SO}_4^{2-}/\text{AT}$ (see (i) in Fig. 4-4b), as it most likely experienced in-stream photosynthesis which would have lowered the $\text{SO}_4^{2-}/\text{AT}$ molar ratio that was present when initially released into the stream. It is reasonable to assume photosynthesis, because we collected this sample during the afternoon on a day with a long sunshine duration, which would be ideal conditions for photosynthesis (Fig. 4-5). In addition, the Gaskabohki stream experiences no or only minimal canopy shading. Therefore, it is likely that in-stream photosynthesis during the course of the day consumed most of the CO_2 that was initially produced in the soil and released into the stream, increasing the pH and alkalinity.

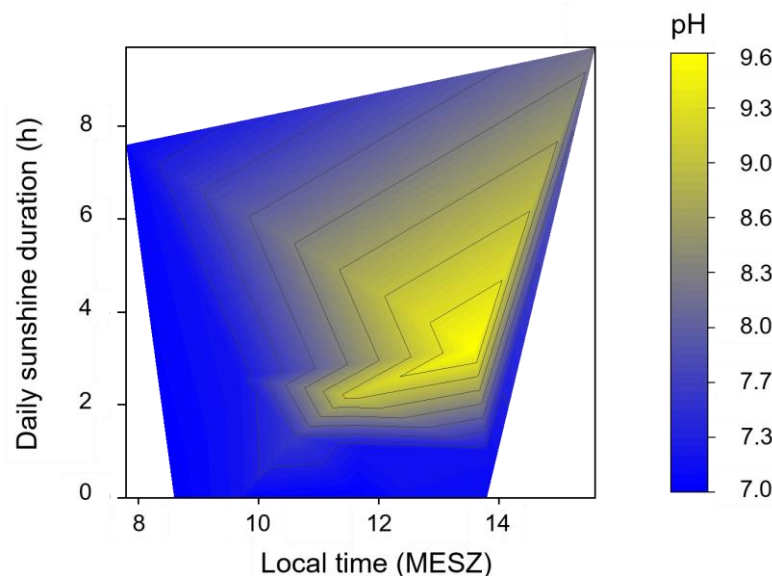


Fig. 4-5: Heatmap showing the pH for different sampling times and sunshine durations. A high pH was measured in samples that were taken in the afternoon on a day with

a high sunshine duration, indicating in-stream photosynthesis. The pH of samples that were collected in the morning were not affected by a high sunshine duration.

Carbonate-dominated riparian zone controls alkalinity signal

We propose that the AT signal is driven by preferential contribution from two different groundwater sources dominated by different weathering processes: (i) The first source is governed by carbonate minerals being dissolved almost exclusively by carbonic acid, which results in high AT concentrations and a low $\delta^{13}\text{C-DIC}$ value of about -12‰ . (ii) The second source is governed by an increased proportion of sulfuric acid induced carbonate weathering in which no AT, but CO_2 and sulfate are produced and $\delta^{13}\text{C-DIC}$ is shifted to higher values of about -9‰ (Fig. 4-4b). Samples that show an intermediate $\delta^{13}\text{C-DIC}$ signal of about -11 to -9.5‰ represent a mixing of sources. We suggest that the first source (i) is situated in a wider riparian zone, ~ 1 km downstream of the spring and thus close to the catchment outlet, representing a hotspot of alkalinity release and the second source (ii) is stretched out upslope over the remainder of the catchment, representing $\sim 99\%$ of the entire catchment area.

While almost the entire catchment is underlain by silicates with only accessory calcite from shale as the alkalinity-bearing lithology, the downstream riparian zone coincides with bedrock of partly calcareous quartz feldspar shale. Therefore, the downstream riparian zone bears a greater potential for carbonate weathering. In addition to its advantageous lithological properties, we propose that the downstream riparian zone, if undisturbed, dominates the alkalinity concentration of the Gaskabohki catchment due to an enhanced hydrological connectivity. Increased soil moisture and shallower water tables near the stream enable both the transport of weathering agent, in the form of soil respired CO_2 , to the weatherable material and the transport of weathered products from the groundwater to the stream. That the downstream riparian zone is mainly responsible for the alkalinity signal is also reflected in Fig. 4-2a: While the samples of the three upstream sampling stations, which are characterized by a narrow riparian zone, are equilibrium-controlled and show a low mean $\text{HCO}_3^-/\text{CO}_2$ molar ratio of 1.3-1.4, the samples from the catchment outlet, which includes the larger downstream riparian zone, are kinetically controlled and show a higher mean $\text{HCO}_3^-/\text{CO}_2$ molar ratio of 4.9, indicating enhanced alkalinity generation. Li et al. (2013) also recognized that in the dry season the land cover in the riparian zone much better explained the major elements in the river than the land cover over the entire catchment.

Precipitation event temporarily reduces control of the riparian zone

We found that a larger precipitation event on the fourth day of sampling caused a drastic decrease in AT at the outlet of the catchment, reducing AT to $116 \mu\text{mol L}^{-1}$, the minimum value during our sampling campaign (Fig. 4-6a, 'day 0' corresponds to the day of the precipitation event).

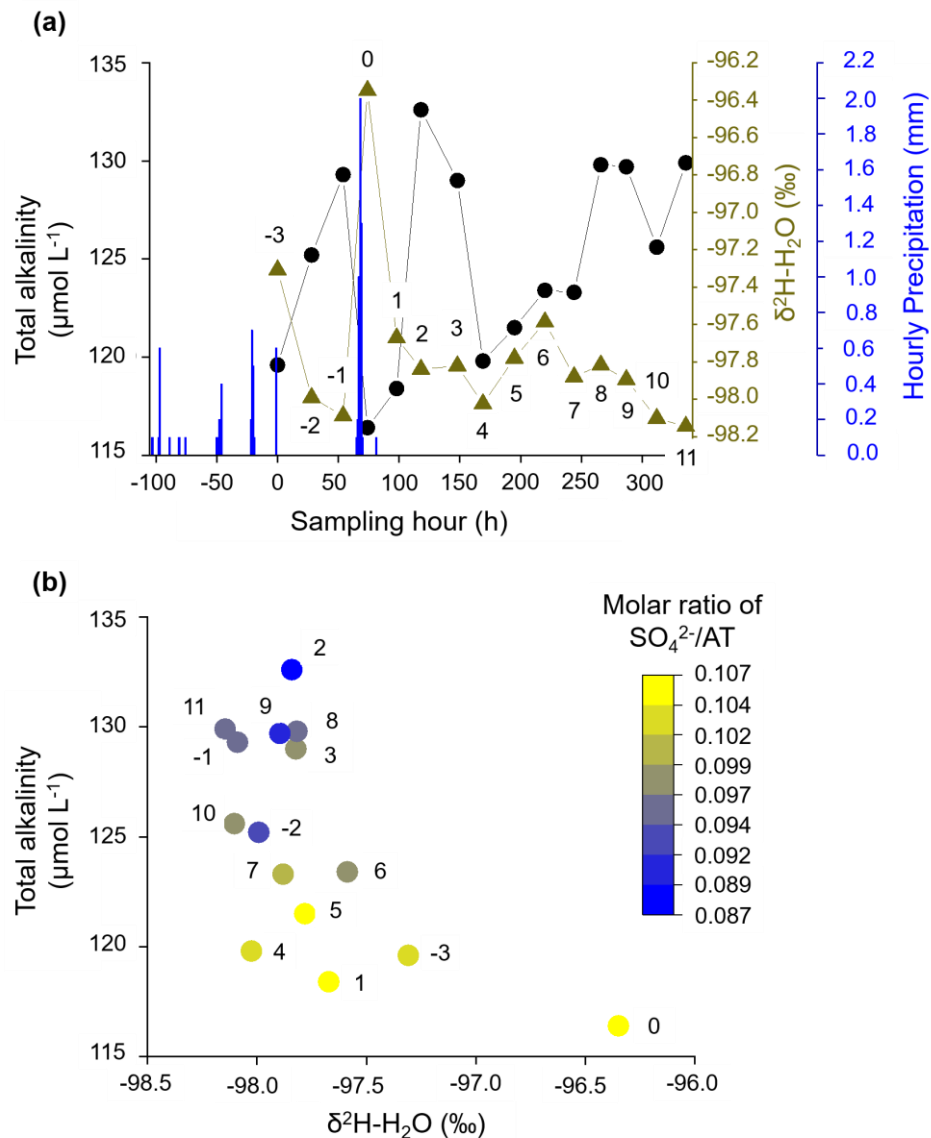


Fig. 4-6: Alkalinity concentration is influenced by precipitation. (a) Variation of AT, $\delta^2\text{H-H}_2\text{O}$ and hourly precipitation over the course of the sampling campaign. (b) AT decreases with increasing $\delta^2\text{H-H}_2\text{O}$, i.e., increasing contribution from surface water. At constant $\delta^2\text{H-H}_2\text{O}$, AT decreases with increasing molar ratio of $\text{SO}_4^{2-}/\text{AT}$, indicating an increased contribution from the uphill catchment to the weathering load. Numbers next to

data points show the number of days before (negative values) and after (positive values) the major rain event (0).

We explain this with a high proportion of surface water from precipitation which diluted the AT signal. This dilution effect can also be observed for the entire dataset when plotting AT as a function of $\delta^2\text{H-H}_2\text{O}$: AT generally decreased with increasing $\delta^2\text{H-H}_2\text{O}$ (Fig. 4-6b). When surface water mixes with the alkalinity-charged groundwater, the AT concentration measured in the stream is reduced.

On the second day after the rain event ('day 2'), the AT concentration increased considerably up to $133 \mu\text{mol L}^{-1}$, the maximum value in our time series. This coincided with a minimum molar ratio of $\text{SO}_4^{2-}/\text{AT}$, indicating that groundwater from the downstream riparian zone is maximally distributed to the stream water without being diluted by other sources. Petrone et al. (2007) also found that saturated riparian soils and precipitation mainly influence the storm chemistry for a low-permafrost watershed.

After a fast initial surface water response to the precipitation event ('days 0 and 1'), alkalinity-charged groundwater from the downstream riparian zone dominated the stream water signal ('days 2 and 3'). Consequently, we describe the catchment storage-discharge relationship as a clockwise loop with streamflow responding faster than groundwater. On the fourth day after the precipitation event ('day 4'), the AT concentration is reduced once more to $120 \mu\text{mol L}^{-1}$. However, when compared to the last drop in the AT signal directly after the precipitation event ('day 0'), this decrease cannot be explained with dilution from direct surface water, as the $\delta^2\text{H-H}_2\text{O}$ stayed on a low level. We rather attribute this decrease in AT to an increased contribution from uphill groundwater flow, which is dominated by an increased proportion of sulfuric acid-induced carbonate weathering, as the molar ratio of $\text{SO}_4^{2-}/\text{AT}$ is high. The $\delta^2\text{H-H}_2\text{O}$ signal slightly increased again ('day 4-6'), indicating a delayed contribution from new water of the precipitation event. We suggest that some of the precipitation did not go directly to runoff, but infiltrated the soil of the uphill catchment, mixed with old water and created delayed runoff ('day 5 and 6'). Similarly, in a study about an Arctic watershed in northern Alaska, McNamara et al. (1997) reported that with on-going thawing season, the storage capacity of the watershed increased, and in conjunction with this, that more new water entered the soil and mixed with old water, as opposed to going directly to runoff. Furthermore, this delayed contribution of uphill groundwater to the stream signal is related to generally larger time scales for subsurface pro-

cesses. Myrabø (1997) and Camporese et al. (2014) found a similar hysteresis in the catchment storage-discharge relationship. For a riparian zone located in a deeply incised glacial till valley in Indiana, USA, Vidon (2012) reported a quick rise of the water table near the stream and a concomitant decrease in hillslope water contributions to the stream during a storm event. In general, shallower water tables, which characterize riparian zones, frequently respond much more strongly to water infiltration than deeper water tables (Meyboom, 1967). Moreover, for most storms, Vidon (2012) observed the development of a water table down valley gradient. In our study, during the next days after the second decrease in AT ('days 5-8'), the AT signal slowly recovered, which coincided with a decrease in the molar ratio of $\text{SO}_4^{2-}/\text{AT}$, i.e., a declining influence from the uphill catchment (Fig. 4-6b).

In conclusion, we identify the downstream riparian zone and the hillslope as two key catchment units that collect and transfer water to the stream, as was shown by other authors before (McGlynn and Seibert, 2003; McGlynn and McDonnell, 2003a, 2003b). Usually, in headwater catchments, hillslopes are assumed to be the main contributor to streamflow (Seibert et al., 2009; McGuire and McDonnell, 2010; Vidon, 2012). In our dataset, however, we observed that the riparian zone responded more quickly to the precipitation event, probably due to higher antecedent soil moisture and a shallower groundwater table. The stable water isotope composition of all our stream water samples only slightly deviates from the regional and global meteoric water lines (Fig. 4-7), indicating that the groundwater contribution to stream water most likely originated from shallow groundwater. The average isotopic composition of local precipitation closely reflects the isotopic compositions of shallow groundwater (Fritz et al., 1987). The fall of 2020 was comparatively dry, which may have resulted in particularly pronounced decoupling of uphill groundwater from the stream.

On the three days prior to the major precipitation event ('days -3 to -1'), AT showed an increasing trend, while $\delta^2\text{H-H}_2\text{O}$ was decreasing. Even though the rainfall intensity on the first day of sampling was not as high as on the fourth day, a contribution of surface water was evident in the $\delta^2\text{H-H}_2\text{O}$ signal. Therefore, AT was comparatively low at the beginning of sampling, which is due to a longer, albeit less intense, rain period on a few days prior to the first day of sampling, and thus dilution by surface water. This longer rain period most likely also activated the release of soil-stored nitrate into the stream, which lasted until the fourth day after the last day with rainfall

(Fig. 4-3). This agrees with observations of Dingman (1971) over a small subarctic catchment with discontinuous permafrost in Alaska, where he found that streamflow recessions are dominated by a combination of tunnel flow under moss-covered parts of the basin and typical groundwater flow through the moss and soils.

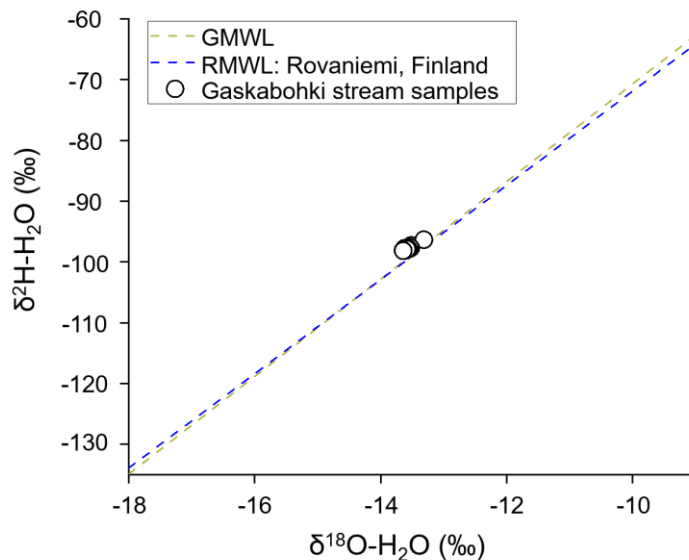


Fig. 4-7: Stable water isotope composition. The stable water isotope compositions of the Gaskabohki stream water samples plot closely to the global (GMWL) and regional (RMWL) meteoric water line. RMWL line (y-intercept = 5.6‰, slope coefficient = 7.7) is based on monthly integrated samples collected between January 2004 and December 2019 at the GNIP (Global Network of Isotopes in Precipitation) station in Rovaniemi, Finland (International Atomic Energy Agency).

Silicate weathering with minor alkalinity generation

We suggest that the products from silicate weathering are released together with the products originating from carbonate weathering by an increased proportion of sulfuric acid from the groundwater of the catchment upstream from the carbonate hotspot riparian zone. Except for this downstream riparian zone, the entire catchment is underlain by silicates with only accessory calcite from shale as the alkalinity-bearing lithology. Based on the $\delta^{13}\text{C-DIC}$ signal, silicate bedrock is dissolved by sulfuric acid alone, with no generation of DIC. However, some excess alkalinity remains when balancing AT with divalent cations (see dashed line in Fig. 4-4a, representing the typical molar ratio of carbonic acid induced carbonate weathering of $\text{AT}/(\text{Ca}^{2+} + \text{Mg}^{2+})$ of 2:1). Therefore, we assume that silicate rocks are also weathered by carbonic acid to a small extent. However, when car-

bonic acid becomes available through soil respiration, it preferentially reacts with the accessory carbonate minerals due to faster dissolution kinetics. Weathering of silicate rocks in the Gaskabohki catchment contributes only minimally to CO₂ fixation. Interestingly, theoretical alkalinity production through carbonate weathering (dashed line) deviates most from actual production (solid line) at low concentration sums of Ca²⁺ and Mg²⁺ and high molar ratios of SO₄²⁻/AT. These are the data points that we associate with increased groundwater contribution from the uphill catchment area, where silicate rock clearly dominates the composition of underlying bedrock over accessory carbonate from shales.

In the previous section ('Carbonate weathering by sulfuric acid decreases alkalinity concentration'), we used the molar ratio of SO₄²⁻/AT as an indicator for the solute contribution from the uphill catchment to the stream water signal at the catchment outlet. This molar ratio is positively correlated with the molar ratio of Na/(Ca²⁺ + Mg²⁺) (adjusted R² = 0.72), indicating that SO₄²⁻/AT can also be used as a tracer for solute contributions from uphill silicate weathering (Fig. 4-8a). When the silicate cationic load increases in relation to the carbonate cationic load (Na/(Ca²⁺ + Mg²⁺)), AT linearly decreases (adjusted R² = 0.65, Fig. 4-8b). As silicate bedrock is weathered by sulfuric acid, Na⁺ and SO₄²⁻ are the main weathered products from silicate weathering in the groundwater in the uphill catchment, with no generation of AT.

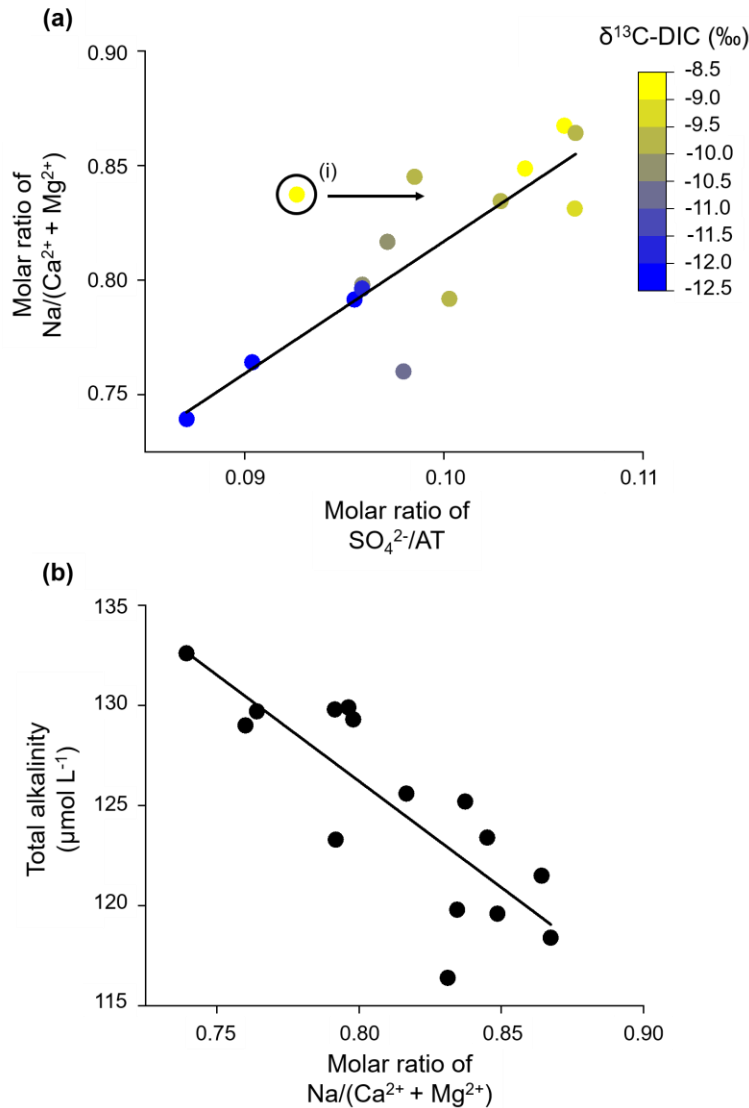


Fig. 4-8: Uphill silicate weathering. (a) Molar ratio of $\text{Na}/(\text{Ca}^{2+} + \text{Mg}^{2+})$ increases linearly with the molar ratio of $\text{SO}_4^{2-}/\text{AT}$, indicating that the uphill silicate cation load behaves similar to the weathering load originating from sulfuric acid induced carbonate weathering. (i) We excluded this data point from the linear regression (y-intercept = 0.24, slope coefficient = 5.8), because it has a high pH, likely resulting from in-stream photosynthesis. (b) AT decreases linearly with the molar ratio of $\text{Na}/(\text{Ca}^{2+} + \text{Mg}^{2+})$, indicating that AT is only minimally released from the weathering of the abundant silicate bedrock. Instead, sulfuric acid acts as the main weathering agent; linear regression: y-intercept = $211.1 \mu\text{mol L}^{-1}$, slope coefficient = -106.1.

Availability of weathering agent

The Gaskabohki stream was on average undersaturated with CO_2 ($p\text{CO}_2 = 371 (\pm 219)$ ppm) with respect to atmospheric $p\text{CO}_2$, but reached a maximum $p\text{CO}_2$ of 651 ppm. By investigating a global compilation of streams

and rivers, Marx et al. (2017a) found that catchments with areas up to 500 km² show consistently high maximum $p\text{CO}_2$ values of ~80,000 ppm. The maximum value we measured during the sampling period in fall 2020 was two orders of magnitude lower. This discrepancy can be explained by the fact that soil respiration in this subarctic region is generally lower compared to the global average, as annual soil respiration decreases with latitude (Warner et al., 2019). Furthermore, with decreased temperatures in the fall, soil respiration was reduced when compared to the summer, during which soil respiration is highly elevated. In a study about CO_2 supersaturation in a temperate hardwood-forested catchment, soil $p\text{CO}_2$ was modelled between 907 ppm in winter and 35,313 ppm in summer. (Jones and Mulholland, 1998). Another study about soil respiration in permafrost-affected tundra and boreal ecosystems in Alaska and Northwest Canada also recognized the summertime as the main driver of annual soil respiration and calculated that summer months contributed to 58% of the regional soil respiration, winter months contributed to 15%, and the shoulder months contributed to 27% (Watts et al., 2021).

As the mean pH at the 'Gaskabohki 1' sampling station, located ~700 m upstream from the outlet and ~400 m downstream of the spring, was 6.7 (± 0.0) and thus DIC was present in the form of CO_2^* from respiration of terrestrial organic matter and HCO_3^- from rock weathering, we were able to model the initial CO_2 released from soils to surface waters according to the stream CO_2 -DEGAS model by Polsenaere and Abril (2012). We then used this modelled upstream soil $p\text{CO}_2$ as a proxy for the entire Gaskabohki catchment, to which the stream CO_2 -DEGAS model could not be applied, as the mean pH at the outlet was 7.5 (± 0.8), hence most of DIC was only in the form of HCO_3^- . With a mean modelled soil $p\text{CO}_2$ of 2009 (± 471) ppm during fall 2020, the Gaskabohki catchment is characterized by a rather low soil respiration signal when compared to a basin with similar catchment characteristics, but with an annual average temperature of 5.5°C, situated in northern Czech Republic, which showed a modelled soil $p\text{CO}_2$ of 1828-94,454 ppm during fall 2014 (Marx et al., 2018). Our mean modelled soil $p\text{CO}_2$ was likely lower due to lower temperatures and less rainfall.

These comparatively low values might explain why the abundant silicate bedrock is almost exclusively weathered by sulfuric acid instead of carbonic acid from soil respiration. When carbonic acid is available, it mainly reacts with the accessory carbonate in the shale layers due to more favorable reaction conditions. We propose that only in the riparian zone along

the channel, where soil moisture is highest, soil-respired CO₂ is efficiently transported down to the weathering zone.

When looking at individual $p\text{CO}_2$ values in the stream at the 'Gaskabohki 1' sampling station, we recognized that a precipitation event caused the highest $p\text{CO}_2$ and when no rain fell, a higher temperature resulted in a higher $p\text{CO}_2$. We explain this finding with precipitation causing an increased connectivity of CO₂-rich soil solutions with the stream, comparable to the increased washout that we observed for soil-stored nitrate (Fig. 4-3), and higher temperatures causing increased soil respiration.

We propose that the in situ weathering rates of carbonate minerals by carbonic acid are moderately activated in the fall due to relatively low CO₂ levels. We suggest that these rates are highest during the summertime, when soil respiration is most activated by elevated temperatures. During that time, groundwater concentrations of alkalinity from carbonic acid induced carbonate weathering should be highest. Therefore, we propose that the riparian zone with its efficient transport of soil CO₂ to the weathering zone and its shallow groundwater table is mainly responsible for maintaining high AT concentrations in the Gaskabohki stream.

4.3.2 Controlling factors on alkalinity across watershed scales

No rain fell on the two days on which we extended the sampling to the further catchments up to the Tanafjord. In addition, no precipitation was detected up to seven days before. Thus, a dilution effect, which could be more pronounced in some catchments than others, did not need to be considered. Accordingly, we compared the alkalinity concentration without further normalization and an unconstrained investigation of the factors influencing alkalinity production should be granted.

Decreasing permafrost probability enhances hydrological connectivity

First, we will compare the three catchments, which are all situated on the mountainside of Iskorasfjellet: Gaskabohki, Bahkiljohka and Guovzilbohki. Compared to the Gaskabohki catchment, the Bahkiljohka catchment shows a higher stream water pH, therefore plotting further to the right in Fig. 4-2a, moving more to the site of the end-members for kinetically-controlled mineral weathering reactions. The Bahkiljohka catchment shows a larger catchment area and a lower permafrost probability than the Gaskabohki catchment (Tab. 4-1). Even more dominated by kinetically-controlled

mineral weathering reactions, however, is the Guovzilbohki catchment. This watershed is a headwater catchment, like the Gaskabohki catchment. In contrast to the Gaskabohki catchment, whose bedrock area is only 0.5% partly calcareous quartz feldspar shale, however, about half (54%) of the Guovzilbohki watershed is underlain by this carbonate-enriched bedrock. The Bahkiljohka catchment is characterized by an intermediate proportion (35%) of carbonate-containing lithology. Even though the areal carbonate extent in the Bahkiljohka catchment is not as high as in the Guovzilbohki catchment, it shows the highest AT concentration of $586 \mu\text{mol L}^{-1}$ (Fig. 4-9a). We assume that if a certain level of carbonate-containing lithology is present in the catchment, catchment area and permafrost probability control alkalinity generation. This is evident when AT measured in all the catchments studied is plotted as a function of permafrost probability (Fig. 4-9b). AT linearly decreases with permafrost probability (adjusted $R^2 = 0.28$). Decreases in HCO_3^- flux with increasing permafrost probability was also observed by Tank et al. (2012) for catchment across the circum-boreal realm. While permafrost probability, lithology and catchment area are first- and second-order controlling factor on alkalinity concentration, terrain roughness, EVI and peat cover seem to play a subordinate role in our dataset. However, we found that AT generally decreases with increasing terrain roughness and decreasing peat cover, with the Bahkiljohka catchment being an outlier in both correlations. Finally, we recognized a high degree of multi-collinearity between permafrost probability and EVI (adjusted R^2 when plotting EVI as a function of permafrost probability = 0.63).

Tab. 4-1: Various catchment properties of the sampled streams and rivers. ¹mt: metamorphics (“wide variety of rocks from shales to gneiss, from amphibolite to quartzite”), ²vb: basalt-type rocks, ³pa: plutonic rocks containing quartz, ⁴sm: mixed sedimentary rocks (“carbonate is mentioned but not dominant”), ⁵sc: carbonate sedimentary rocks (Hartmann and Moosdorf, 2012).

	Catchment area (km ²)	Stream length (km)	Roughness	Permafrost probability	Areal proportion of peatland	EVI	Areal proportion of main lithology classes				
							mt ¹	vb ²	pa ³	sm ⁴	sc ⁵
Gaskabohki 1	0.2	0.4	25.5	0.13	0.00	0.29	1.00	0.00	0.00	0.00	0.0
Gaskabohki 2	0.2	0.6	25.8	0.13	0.00	0.29	1.00	0.00	0.00	0.00	0.0
Gaskabohki 3	0.4	0.8	27.8	0.13	0.00	0.28	1.00	0.00	0.00	0.00	0.0
Gaskabohki 4 (outlet)	0.7	1.1	27.7	0.13	0.00	0.28	1.00	0.00	0.00	0.00	0.0
Guovzilbohki	2.8	3.6	25.3	0.10	0.00	0.30	1.00	0.00	0.00	0.00	0.0
Bahkiljohka	78	20	19.8	0.04	0.06	0.30	0.76	0.16	0.00	0.06	0.0
Karasjohka 1	4,909	162	11.5	0.17	0.16	0.27	0.69	0.10	0.08	0.11	0.0
Karasjohka 2	7,255	187	12.9	0.14	0.18	0.28	0.67	0.16	0.06	0.08	0.0
Karasjohka 3	11,614	297	15.9	0.14	0.15	0.27	0.76	0.11	0.04	0.06	0.4
Tanaelva 1	14,085	357	15.8	0.13	0.15	0.27	0.69	0.11	0.10	0.07	0.5
Tanaelva 2	15,156	384	15.9	0.13	0.14	0.28	0.65	0.10	0.10	0.12	0.3

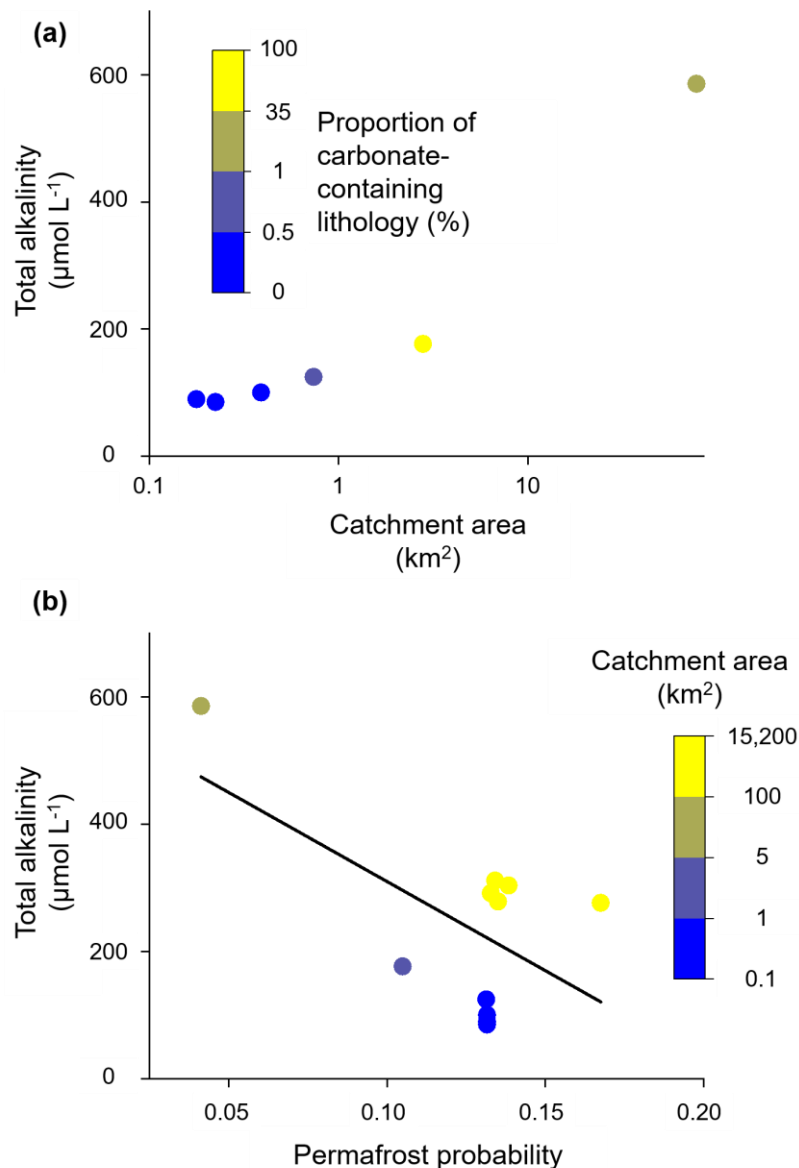


Fig. 4-9: Controlling factors on alkalinity concentration across watershed scales.

(a) At Iskorasfjellet, AT increases with catchment area and the proportion of carbonate-containing lithology. (b) At a larger spatial scale, AT is controlled by permafrost probability, with a low permafrost probability being associated with a high AT concentration. At a similar permafrost probability, a larger catchment area yields a higher AT concentration; linear regression: y-intercept = $590.0 \mu\text{mol L}^{-1}$, slope coefficient = -2800.6 .

As discussed in section 4.3.1 in detail for the Gaskabohki catchment, it seems that alkalinity generation is limited by the contact of weathering agent (CO_2 from soil respiration) with weatherable material as well as the transport of the weathered products out of the weathering zone into the stream. In the Gaskabohki catchment, the saturated riparian zone facilitates this hydrological transport. In the Bahkiljohka catchment, which

shows the highest AT concentration, the low permafrost probability is most likely responsible for enhanced hydrological connectivity. In another study about the effects of permafrost loss on discharge from a wetland-dominated, discontinuous permafrost basin, Stone et al. (2019) reported that total annual discharge from the channel fen decreased by 2.5% for every 10% decrease in permafrost area due to increased surface storage capacity, reduced run-off efficiency, and increased landscape evapotranspiration.

At constant permafrost probability and thus similar hydrological conditions, AT increases with catchment area. From the in-depth study of the Gaskabohki catchment, we found that a precipitation event resulted in the highest turbidity values, which we associate with increased sediment supply to the stream. Therefore, intense precipitation events have the potential to activate the fluvial transport of mineral substrate downstream. This new material together with the surface water most likely leave the headwaters quickly. In the larger rivers downstream, however, this material can undergo several weathering cycles, increasing alkalinity. From decade-long hydrometeorological and biogeochemical observations of catchments in the High Arctic, Beel et al. (2021) deduced that increased late summer rainfall enhanced terrestrial-aquatic connectivity for dissolved and particulate material fluxes. Zolkos et al. (2020) showed that this particulate material, in their study on retrogressive thaw slumps, can rapidly weather during fluvial transport within runoff.

The DIC systems of the three small subcatchments situated within the Gaskabohki headwater catchment and the five larger catchments that drain into the Barents Sea are equilibrium-controlled (Fig. 4-2a). However, while the DIC species of the three small catchments mix with biotic CO₂, the DIC species of the five larger basins are rather in exchange with atmospheric CO₂. For undisturbed headwater catchments on the Peel Plateau in Canada, Zolkos et al. (2020) also reported that stream chemistry reflected CO₂ from soil respiration processes.

Alkalinity generation from carbonate weathering – from Iskorasfjellet to the Tanafjord

As we found in the section ‘Carbonate weathering by sulfuric acid decreases alkalinity concentration’ for the Gaskabohki catchment on the temporal scale, AT also linearly increases on the spatial scale with the concentration sum of Ca²⁺ and Mg²⁺ (adjusted R² = 0.98, Fig. 4-10a). Therefore, we propose that alkalinity is produced from carbonate weathering by carbonic acid in all basins that we studied – from Iskorasfjellet to the

Tanafjord. While the Gaskabohki and Guovzilbohki headwater catchments with the two smallest concentration sums of Ca^{2+} and Mg^{2+} show the characteristic molar ratio of $\text{AT}/(\text{Ca}^{2+} + \text{Mg}^{2+})$ of 2:1, indicative for carbonate weathering by carbonic acid (see dashed line in Fig. 4-10a), the larger catchments show a reduced molar ratio. This decrease coincides with an increase in the molar ratio of $\text{SO}_4^{2-}/\text{AT}$, suggesting that the carbonate minerals are increasingly dissolved by sulfuric acid. In addition to the Gaskabohki catchment, sulfuric acid appears to be present in the other basins, because at a theoretical electrical conductivity of 0, the linear regression of AT as a function of electrical conductivity suggests a negative alkalinity (y-intercept = $-16.9 \mu\text{mol L}^{-1}$, adjusted $R^2 = 0.99$, Fig. 4-10b). Therefore, we assume that some of the divalent cations originate from sulfuric acid induced carbonate weathering, with no generation of AT, but CO_2 and SO_4^{2-} . Thus, carbonate weathering in the studied region does not only consume CO_2 , but also releases CO_2 , albeit to a lesser extent. Carbonic acid induced silicate weathering does not appear to contribute to alkalinity generation and thus to CO_2 sequestration (Fig. 4-2a), although silicate bedrock is generally more abundant in the study area than carbonate bedrock according to lithological maps (Tab. 4-1).

4.4 Conclusions

In the present study is shown that weathering of accessory carbonate dominates the alkalinity generation in a mainly silicate-dominated subarctic headwater catchment in Northern Norway. The vast Fennoscandian Shield is generally underlain by silicates as the alkalinity-bearing rock type. An area of $\sim 20,000 \text{ km}^2$ of the Fennoscandian Shield, however, is classified as metamorphic rocks with minor carbonate occurrences (Hartmann and Moosdorf, 2012), the same geology that dominates the Gaskabohki catchment. When transferring our results about the Gaskabohki catchment to the Fennoscandian Shield, we propose that alkalinity dynamics in this area are also drastically influenced by carbonate minerals, even though their occurrence may be low. Further, we have found that alkalinity generation by carbonate weathering greatly decreases when the proportion of sulfuric acid as the weathering agent increases. This was particularly evident in the larger catchments towards the Tanafjord.

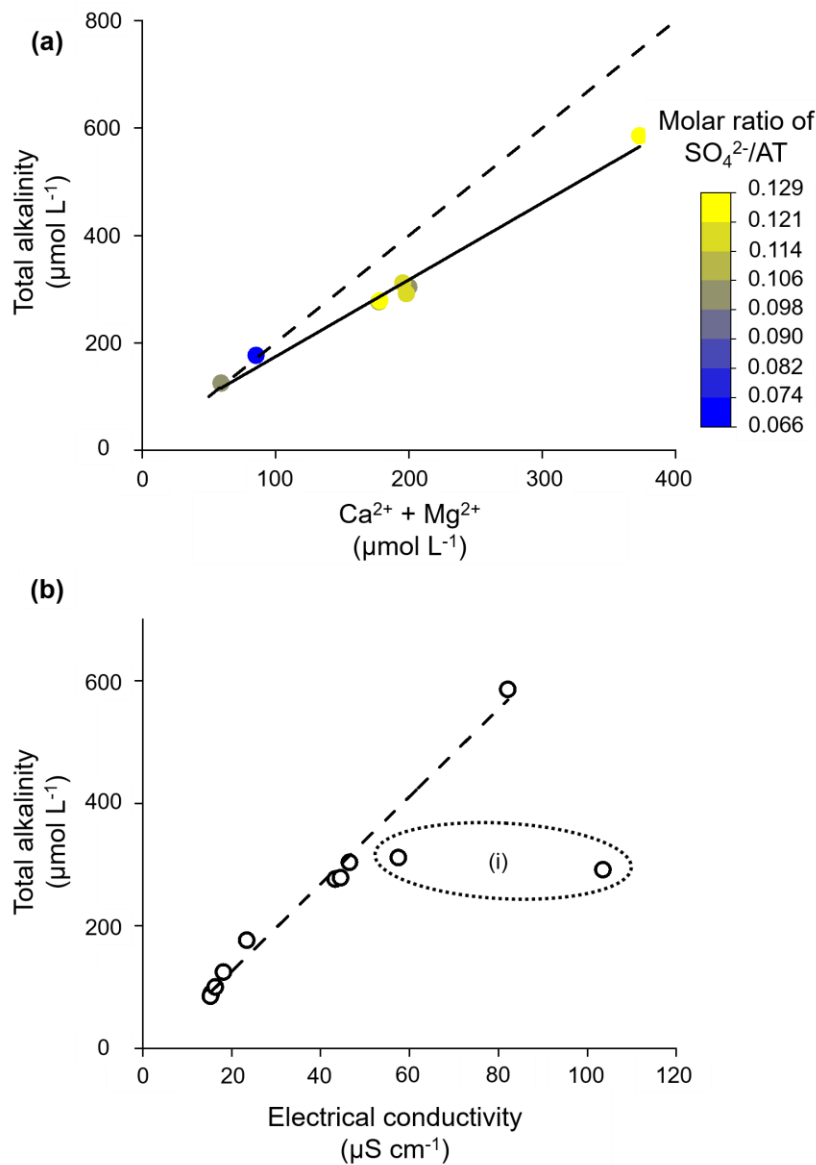


Fig. 4-10: Alkalinity generation from carbonate weathering across watershed scales. (a) AT increases linearly with the concentration sum of Ca^{2+} and Mg^{2+} . Solid line: linear regression (y-intercept = $31.1 \mu\text{mol L}^{-1}$, slope coefficient = 1.4); dashed line: representing the typical molar ratio of carbonic acid induced carbonate weathering of $\text{AT}/(\text{Ca}^{2+} + \text{Mg}^{2+})$ of 2:1. (b) AT increases linearly with electrical conductivity. (i) Dotted ellipse: We excluded these two data points from the linear regression (dashed line: y-intercept = $-19.9 \mu\text{mol L}^{-1}$, slope coefficient = 7.1), as they are characterized by distinctly higher Na^+ and Cl^- concentrations, indicating an influence from the salty fjord and seawater close by.

For the Gaskabohki headwater catchment, we identified the downstream riparian zone characterized by a carbonate-enriched lithology, as the main contributor to alkalinity in the stream. This riparian zone appears to facilitate both the transport of soil-respired CO_2 to the weathering zone and the transport of weathered products to the channel. When undisturbed, high

alkalinity concentrations ($\sim 130 \mu\text{mol L}^{-1}$) are maintained by the inflow of alkalinity-charged groundwater from the downstream riparian zone. However, after a precipitation event, the alkalinity concentration in the stream was reduced twice due to dilution: 1) immediately after the rain event, alkalinity was diluted by new surface water, and 2) after 4 to 7 days after the rain event, the signal was diluted again by a delayed contribution of uphill groundwater to the stream that contained reduced amounts of alkalinity.

Weathering of silicate rocks by carbonic acid, and hence long-term CO_2 sequestration, seems to be limited by insufficient contact between the weathering agent (CO_2^*) and the mineral surface. We expect silicate weathering rates to increase in the Gaskabohki headwater catchment due to climate change in the future, as both the permafrost extent is declining and the annual precipitation is increasing. These two trends will increase the water storage capacity, thereby increasing the contact time of weathering agent and weatherable material. McNamara et al. (1997) suggested that as the thickness of the active layer in permafrost increases, not only will the hydrological response of streams to precipitation inputs be attenuated due to greater water storage capacity, but also root and heterotrophic respiration will increase as it occurs almost exclusively in this thawed layer. Therefore, we expect the availability of weathering agent in the form of carbonic acid to increase.

In conclusion, we expect an increase in alkalinity generation from carbonic acid induced silicate weathering in the Gaskabohki catchment in the future, although we believe the feedback to be slow, as silicate weathering rates are several orders of magnitude slower than carbonate weathering rates. We also propose that carbonic acid induced carbonate weathering is likely to increase. We suppose that alkalinity generation from carbonate weathering is responding faster to a changing climate. We believe that parts of the Fennoscandian Shield will experience a rapid weathering response of accessory carbonate minerals to climate change in the future, resulting in elevated alkalinity levels. Future long-term studies that include more seasons and groundwater sampling are required to confirm this hypothesis.

5 $^{239+240}\text{Pu}$ inventories from soil cores and in situ ^{10}Be concentrations from stream sediments at Iskorasfjellet, northern Norway: Implications for current and long-term erosion

It is currently unclear how erosion in a gradually degrading permafrost landscape will respond to the strong environmental forcing of a rapidly changing Arctic. Changes in critical parameters such as temperature, permafrost, hydrology, vegetation, and precipitation can strongly influence erosion; yet, projections of direction and magnitude are limited given the sometimes complex interactions among them. In this study, we used $^{239+240}\text{Pu}$ inventories from soil cores and in situ ^{10}Be concentrations from stream sediments to determine a current (post-1960) and a long-term (averaged over the last 243 kyr) erosion rate, respectively, of a subarctic headwater catchment on the mountainside of Iskorasfjellet, northern Norway, underlain by sporadic permafrost. In addition to the comparative study of current and long-term erosion of the headwater catchment at Iskorasfjellet, we extended our sampling area to four larger catchments (2.8 to 7,255 km²) on the Finnmarksvidda plateau of the Fennoscandian Shield, where we collected stream sediments for ^{10}Be analysis.

We found a spatially highly heterogeneous distribution of $^{239+240}\text{Pu}$ across the headwater catchment, suggesting that the applicability of this tracer for determining catchment-wide average erosion rates may be limited to regions at lower latitudes. We determined a site-based mean current erosion rate of 184 (\pm 114) mm kyr⁻¹. From the analysis of ^{10}Be concentrations, we deduced that all catchments reflected inheritance, confirming the general agreement on cold-based, non-erosive Fennoscandian ice sheets over the central sector of Fennoscandia. Under the assumption of zero glacial erosion, we calculated long-term catchment-wide average interglacial denudation rates ranging from 11 mm kyr⁻¹ in the headwater catchment to 25 mm kyr⁻¹ in the larger catchments, and attributed the observed trend to an enhanced fluvial erosion in the larger catchments. Despite the uncertainties associated with both rates, we concluded that erosion in the headwater catchment has very likely increased over the past ~60 years relative to a long-term interglacial baseline because the difference between the two rates is about an order of magnitude. We suggest that the elevated erosion

is likely due to a combination of increased rainfall erosivity and the presence of erodible soils that are not yet stabilized due to a sparse vegetation cover.

5.1 Introduction

Physical erosion of rocks is thought to be one of the main controlling factors on chemical weathering (Anderson et al., 2007). Silicate weathering, resulting in alkalinity generation and the long-term drawdown of CO₂, is enhanced by physical erosion, at least in supply-limited environments at low to moderate erosion rates (Millot et al., 2002; West et al., 2005; Gabet, 2007; Ferrier and Kirchner, 2008). Climate change is expected to significantly impact soil erosion rates (Nearing et al., 2004; Borrelli et al., 2020). By exposing a larger amount of fresh minerals to weathering agents, increased physical erosion has the potential to facilitate rapid feedback between terrestrial weathering and the Earth's carbon cycle, a process usually thought to have been at steady state since pre-industrial times (Walker et al., 1981; Berner et al., 1983).

Because climate change is greater in the Arctic, erosion rates are expected to change most rapidly there. This amplified change is evidenced in the annually averaged near-surface air temperature, which increased by 0.71°C per decade from 1979 to 2021, nearly four times faster than the global average (Rantanen et al., 2022), and in total annual precipitation, which increased by 24% from 1971 to 2019 (AMAP, 2022). Both increased precipitation amounts and intensities are the most direct and important controlling factors on erosional changes, and in simulation studies, the ratio of erosion increase to annual precipitation increase was calculated to 1.7 (Nearing et al., 2004).

Currently, northern latitude systems with sporadic permafrost (< 50% coverage), such as catchments on the Finnmarksvidda plateau in northern Norway, a low-relief plain of moderate altitude (300-500 m above mean sea level (amsl)), are responding to climate change with rapid permafrost thaw. Under all climate scenarios, permafrost is predicted to completely vanish from the Finnmarksvidda as early as between 2041 and 2060 (Karjalainen et al., 2018). In contrast to abrupt thaw processes of ice-rich permafrost such as thermokarst, resulting in rapid responses of increased erosion (Kirkby, 1995; Osterkamp et al., 2009; Toniolo et al., 2009; Rowland et al., 2010; Lamoureux et al., 2014; Olefeldt et al., 2016), quantifications of potentially enhanced erosion rates due to gradual permafrost thaw in arctic, non-alpine regions, where permafrost degradation is already well

advanced, are missing. Gradual permafrost thaw is considered a so-called press disturbance, which unfolds its effects on larger spatial and longer temporal scales (decades to centuries) than the so-called pulse disturbances (Collins et al., 2007; Grosse et al., 2011). However, when a certain threshold is reached, a press disturbance could trigger pulse disturbances, e.g., widespread top-down permafrost thaw could initiate increased soil erosion (Grosse et al., 2011).

In addition to precipitation and permafrost, other climatic and environmental parameters, such as temperature, vegetation, and hydrology, and the interactions between them, can have divergent feedbacks on the erosion rate in this rapidly changing environment. The sedimentary record of an Arctic lake in Alaska associated with a small watershed underlain by continuous permafrost revealed that while temperature and vegetation proxies are first-order controlling factors on erosion rate, other proxies such as mass wasting and hydrologic conditions play a subordinate role (Shelef et al., 2022).

A valuable tracer for current (post-1960) erosion rates are the anthropogenic radionuclides $^{239+240}\text{Pu}$. These so-called fallout radionuclides (FRNs) were distributed globally mainly by nuclear weapons fabrication and testing in the 1950s to 1960s (Alewell et al., 2014). Therefore, they provide a current erosion rate averaged over the last 60-70 years. After reaching the Earth's surface, Pu is strongly adsorbed to the fine earth fraction in the topsoil, which makes it suitable as a soil distribution tracer (Loba et al., 2022). Soil distribution rates are calculated by comparing the total FRN inventory per unit area of a reference site, which is assumed to have experienced neither erosion nor deposition since fallout, with the one of the site of interest. When the inventory of the study site is lower (higher) than the one of the reference site, the study site experienced erosion (deposition) since fallout (Alewell et al., 2017). The employment of the relatively new soil erosion tracer $^{239+240}\text{Pu}$ in tundra landscapes has been limited to alpine sites (Portes et al., 2018; Zollinger et al., 2015) and has not previously been applied in high latitude regions (Loba et al., 2022).

To assess a potential change in erosion rate due to on-going climate change, a long-term, pre-industrial erosion rate must first be established. Total denudation rates over both the whole basin area and long time periods (10^2 - 10^5 yr) are now frequently obtained from terrestrial (in situ) cosmogenic nuclides such as ^{10}Be in river sediments (Brown et al., 1995; Blanckenburg, 2005; Codilean et al., 2018). In situ ^{10}Be is produced by

interaction with cosmic rays in quartz, with the production decreasing exponentially with depth in the top few meters of the Earth's surface (Gosse and Phillips, 2001). Because ^{10}Be accumulates when material moves towards the surface by the removal of overlying material, in situ cosmogenic nuclides always record the total rate of removal of mass (combined effect of physical erosion and chemical weathering) and thus measure denudation rate. The ^{10}Be concentration N (atoms g^{-1}) of well-mixed stream sediment sampled at the outlet of a catchment is inversely related to the average denudation rate D (cm yr^{-1}) of that catchment following Lal (1991):

$$N = \frac{P}{\lambda + \mu D} \quad (5-1)$$

where P is the local cosmogenic radionuclide production rate (atoms $\text{g}^{-1} \text{yr}^{-1}$), λ is the radioactive decay constant (yr^{-1}), and μ is the absorption coefficient (cm^{-1}) in the target with $\mu = \rho/\Lambda$, where ρ is the average density of the material (g cm^{-3}), and Λ is the exponential production attenuation length (g cm^{-2}). However, the method requires that the landscape has achieved steady state with respect to the gradual removal of quartz, i.e., ^{10}Be production equals ^{10}Be loss through erosion (and radioactive decay). The averaging time scale of ^{10}Be -derived denudation rates is a function of the denudation rate itself, where the average cosmic ray absorption depth scale, e.g., ~ 100 cm in soils or ~ 60 cm in bedrock, is divided by the denudation rate (Lal, 1991; Blanckenburg, 2005).

Slowly eroding landscapes, such as the low-relief Finnmarksvidda plateau on the Fennoscandian Shield, can have averaging time scales of up to 10^5 yr (Blanckenburg, 2005). Therefore, the eroding surface of the Finnmarksvidda has most likely not reached steady state since its deglaciation about 11,000 yr BP (Stroeven et al., 2016). Furthermore, as Finnmarksvidda is thought to have been covered by non-erosive, cold-based ice of the Fennoscandian ice sheet during the last Weichselian glaciation (Kleman et al., 1997), subglacial erosion may not have effectively removed the cosmogenic inventory originating from previous exposure during the preceding interstadial(s)/interglacial(s). In fact, Jansen et al. (2019) found that $> 85\%$ of blockfields and tors in Fennoscandia contain ^{10}Be inheritance, indicating that erosion was at least in some patches not very effective during the last glaciation(s). Thus, equation (5-1), which assumes steady state, needs to be modified considering a complex exposure (^{10}Be production and ^{10}Be loss due to subaerial erosion and decay) and shielding (no ^{10}Be production, only ^{10}Be loss due to decay and possibly subglacial erosion) history, modified after Fabel and Harbor (1999):

$$N_{\text{complex}} = \frac{P}{\lambda + \mu D} \left((1 - e^{-(\lambda + \mu D_S) \sum_{i=1}^n T_{\text{pre},i}}) (e^{-(\lambda + \mu D_G) \sum_{i=1}^n T_{\text{burial},i}}) + (1 - e^{-(\lambda + \mu D_S) \sum_{i=1}^n T_{\text{post},i}}) \right) \quad (5-2)$$

where N_{complex} (atoms g^{-1}) is the ^{10}Be concentration in the sample after a complex exposure and shielding history, D_S and D_G are the subaerial and subglacial denudation rate (cm yr^{-1}), respectively, and T_{pre} , T_{burial} , and T_{post} are the pre-burial (interglacial/interstadial before the i^{th} stadial), burial (glaciated during i^{th} stadial) and post-burial (deglaciated, Holocene) times (yr), respectively.

Our aim in the present study is to assess whether erosion in the subarctic Gaskabohki headwater catchment on the mountainside of Iskorasfjellet in northern Norway has increased in the last decades due to contemporary climate change, potentially providing feedback for CO_2 sequestration through increased chemical weathering of silicates. In particular, we aimed at determining a current (post-1960) erosion rate using $^{239+240}\text{Pu}$ and a long-term, pre-industrial erosion rate using in situ ^{10}Be . In addition to the detailed analysis of the Gaskabohki watershed at Iskorasfjellet, we extended the investigation of the long-term erosion rates influenced by several extensions and retreats of ice sheets to four larger catchments also situated on the Finnmarksvidda plateau.

5.2 Materials and methods

To compare a current with a long-term erosion rate of a small watershed in a degrading permafrost landscape at the mountainside of Iskorasfjellet in northern Norway (Fig. 5-1), we extracted soil cores in a grid sampling scheme for $^{239+240}\text{Pu}$ measurements and collected stream sediment at the outlet of the catchment for in situ ^{10}Be analysis, respectively.

In addition to the foremost goal of determining a watershed-wide current erosion rate, we chose a uniform grid to sample Pu because we wanted to examine how Pu was distributed throughout the watershed, which is characterized by degrading sporadic permafrost. This allowed us to better evaluate potential caveats associated with typical Arctic conditions to the applicability of $^{239+240}\text{Pu}$ as a soil distribution tracer. In addition to the detailed study of the small Gaskabohki catchment, we extended our sampling area to four larger catchments on the Fennoscandian Shield (Fig. 5-1a and b) to investigate whether long-term rates in this comparatively stable region are similar or markedly different. These catchments vary in size from 2.8

to 7,255 km² whereas lithology, land cover, and permafrost extent are relatively uniform throughout the study area. For these basins, we collected river sediment samples at the catchments' outlets to analyze long-term erosion from ¹⁰Be concentrations.

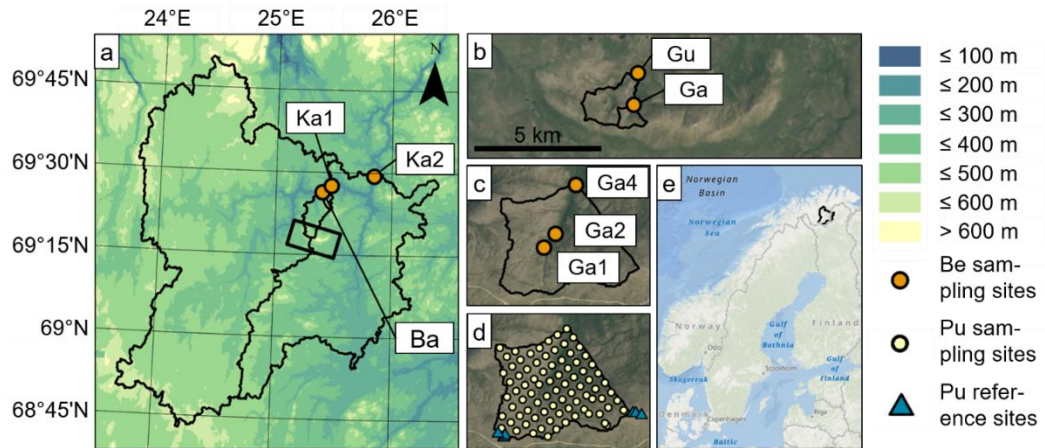


Fig. 5-1: Study area. (a) The three larger catchments: Karasjohka 2 (Ka2), Karasjohka 1 (Ka1) and Bahkiljohka (Ba) and the locations of their outlets, where we collected stream sediments for ¹⁰Be analysis (orange circles). The black rectangle shows the location of the Iskorasfjellet ridge, which is magnified in panel (b). Colors indicate the altitude in m above mean sea level (amsl), with the darkest blue color representing more developed river systems. (b) Zoom on the Iskorasfjellet ridge. The two smaller headwater catchments, Guovzilbohki (Gu) and Gaskabohki (Ga), are partially situated on the ridge. Zoom on the Gaskabohki headwater catchment with (c) the Be sampling sites along the stream and (d) the Pu grid sampling scheme. Here, the yellow circles denote Pu sampling sites and the blue triangles denote Pu reference sites on flat hills adjacent to the watershed. (e) Location of the study area in northern Norway in Fennoscandia shown by the outline of the largest catchment, Karasjohka 2. Background maps in (b), (c) and (d) from the Norwegian Mapping Authority (2022) and in (e) from Esri, GEBCO, DeLorme, NaturalVue, National Land Survey of Finland, HERE, Garmin, FAO, NOAA, USGS (ESRI, 2022).

5.2.1 Gaskabohki catchment at Iskorasfjellet on the Finnmarksvidda

The Gaskabohki watershed (catchment area = 0.7 km²) is a headwater catchment on the north-facing slope of Iskorasfjellet in Karasjok municipality in northern Norway (Fig. 5-1b). The north-facing side of the Iskorasfjellet ridge consists of micaceous quartzite (Nilsen, 1986). The ridge is ~10 km long and ~1.5 km wide with a highest elevation of 644 m amsl and a west-northwest/east-southeast orientation. Iskorasfjellet lies inland on the rolling (wavy, low relief) Finnmarksvidda plateau (300-500 m amsl), with local peaks over 600 m amsl, which borders Finland to the south and east. The Finnmarksvidda was completely covered by the Fennoscandian ice sheet during the last glaciation (Olsen et al., 2013). In addition to being covered

by the Fennoscandian ice sheet with an ice dome zone over Finland during the last stadial, the Finnmarksvidda was also covered by the Scandinavian ice sheets which grew from the mountainous area of northwest Sweden and from centers along the Caledonian mountain range in Norway during the Middle and Early Weichselian (Olsen, 1988; Olsen et al., 2013). While in early stages of the Weichselian glaciations the ice movement was directed towards the east/north-east in our study area, in the later stages it changed towards the north (Olsen, 1988). Its surface today is covered by thick Quaternary deposits (maximum thickness > 50 m, and average thickness estimated to ~6 m), consisting of till beds, interstadial and interglacial deposits, and paleosols (Olsen et al., 2013). Various soil types are present on the Finnmarksvidda: podzols with a thin to medium bleached layer, swamp soils, lithosols, rankerlike soils and brown earths (Lag, 1983).

Iskorasfjellet was deglaciated ~10,900-10,800 yr BP (Stroeven et al., 2016) and the Gaskabohki watershed is completely covered with moraine material of varying thickness (NGU, 2022b). The Gaskabohki catchment is mainly underlain by quartzite and arkose, in places with layers of different shales (NGU, 2022a) and shows sporadic permafrost (permafrost probability = 0.13; Obu et al., 2018). Permafrost probability is defined as the fraction of ensemble members ($N = 200$ for each 1 km^2 grid cell) with a mean annual ground temperature of 0°C or lower (Obu et al., 2018). Two boreholes that were drilled at Iskorasfjellet at 585 m amsl in the summers of 2007 and 2008 and which penetrated into the bedrock below the Quaternary sediment cover revealed that the active layer was more than 10 m and 7 m deep, respectively (Christiansen et al., 2010). The active layer is the top layer above the permafrost, which thaws in summer and refreezes in winter. Since then, permafrost temperatures at 10 m and 20 m depth increased at a rate of 0.5°C and 0.1°C per decade, respectively (Isaksen et al., 2022). Tundra vegetation (e.g., lichen crusts, *Betula* shrubs and *Empetrum nigrum* ssp. *hermaphroditum*) dominates at Iskorasfjellet. Vegetation density generally increases with decreasing elevation in the watershed (CLC, 2018). Below an elevation of ~570 m amsl, mountain birch (*Betula pubescens* ssp. *czerepanovii*) forest is also present. Besides the main channel, melt water channels are present (NGU, 2022b) which were dried out at the time of sampling in the fall.

The climate of Finnmarksvidda is continental. For the last six years (September 2014 to August 2020, longest continuous record at Iskorasfjellet), the mean summer (June-July-August) and winter (December-January-February) air temperatures were 8.7°C and -9.3°C , respectively (measured

at the meteorological station at Iskorasfjellet, 591 m amsl, SN97710; Seklima, 2020). Compared to the air temperature normal (1961-1990), temperatures increased by 0.2°C and 4.2°C, respectively. Mean monthly precipitation sums during the summer and winter for the last six years were 66 mm and 38 mm, which correspond to 117% and 237% of the monthly precipitation sums of the climate normal, respectively. The annual precipitation averaged over the last six years, from September 2017 to August 2020, was 492 mm (measured at the meteorological station in Karasjok, 131 m amsl, SN97251, 20 km from Iskorasfjellet; Seklima, 2020). The mean daily snow depth during the snow season (October to May) was 29 cm (measured at the meteorological station at Iskorasfjellet, 591 m amsl, SN97710; Seklima, 2020).

5.2.2 Larger catchments on the Finnmarksvidda

Adjacent to the Gaskabohki watershed on the hillslope of Iskorasfjellet lies the Guovzilbohki headwater catchment (Fig. 5-1b) which is characterized by a slightly larger catchment area (2.8 km²) and a higher abundance of minor carbonate occurrences (NGU, 2022a), but also shows sporadic permafrost (permafrost probability = 0.10; Obu et al., 2018). In contrast to the Gaskabohki watershed, the Guovzilbohki watershed is prone to landslides, as evidenced by loose mass deposits in a relatively steep valley (slope ~25°; NGU, 2022b). This valley coincides with a fault/fracture zone (Nilsen, 1986). The Guovzilbohki stream cuts through these deposits upstream following the fault. Further downstream, along the fault, the stream parallels an esker (~2000 m long).

The Bahkiljohka catchment (78 km²) encloses the Gaskabohki and Guovzilbohki headwater catchments. From the top of the catchment at 548 m amsl, the watercourse descends to the Iskoras peat plateau at ~380 m amsl. The peat began to form around 9,800 year BP (Kjellman et al., 2018) in the form of wet fens, which were prevalent during most of the Holocene. Dry surface conditions associated with permafrost peat plateau aggradation developed around 950-100 year BP, probably caused by the Little Ice Age cooling (Kjellman et al., 2018). The Bahkiljohka stream, like the Guovzilbohki stream which eventually becomes the Bahkiljohka stream, follows the main fault, which ends about halfway downstream, and then follows a band of amphibolite and metagabbro (Nilsen, 1986). However, mica schist and metasandstone are the two main rock types that dominate the basin (NGU, 2022a). The Bahkiljohka catchment is characterized by isolated patches of permafrost (permafrost probability = 0.04; Obu et al., 2018). While the Gaskabohki and Guovzilbohki headwater

catchments are predominantly sparsely vegetated, the Bahkiljohka catchment has the highest areal forest cover (0.82; CLC, 2018).

Finally, the two largest catchments, Karasjohka 1 (4,909 km²) and Karasjohka 2 (7,255 km²), are predominantly underlain by granitic gneiss, granodiorite and amphibole gneiss (NGU, 2022a). The Karasjohka 1 basin is enclosed by the larger Karasjohka 2 basin (Fig. 5-1a). They show sporadic permafrost (permafrost probability = 0.17 and 0.14, respectively; Obu et al., 2018) and the highest coverage of peat bogs (0.14 and 0.13, respectively) and water bodies (0.04 and 0.03, respectively; CLC, 2018). Otherwise, they are primarily covered by till. What distinguishes these two larger catchments from the smaller catchments associated with Iskorasfjellet is that they comprise longer eskers as well as many ablation ($N \sim 250$) and some end moraines ($N \sim 90$; NGU, 2022b). The Karasjohka River joins the Tanaelva River, which eventually drains into the Barents Sea via the Tanafjord.

5.2.3 Geospatial analyses

We delineated stream networks and watershed areas using the SAGA-GIS modules “Channel Network and Drainage Basins” and “Upslope Area” (Conrad et al., 2015) in QGIS 3.22.2 (QGIS.org, 2022) from the gridded digital elevation model ArcticDEM with 2 m and 32 m-resolution (Porter et al., 2018) for the detailed study of the Gaskabohki catchment and the analysis of the larger catchments, respectively. We used ArcGIS Pro 2.8.0 (ESRI, 2022) to create the maps. We determined the type of land cover using the CORINE Land Cover map, which has an accuracy of more than 100 m (CLC, 2018). To determine topographic characteristics such as slope, stream power index (SPI), and topographic position index (TPI) in the Gaskabohki catchment, we resampled the 2 m DEM to a 10 m DEM to ensure that a Pu sampling station is properly described, since the accuracy of the GPS we used was about 3 m. SPI is calculated based on slope and specific catchment area and indicates potential flow erosion (Conrad et al., 2015). TPI compares the elevation of the DEM cell of interest with the mean elevation of eight cells surrounding it (QGIS.org, 2022). As we chose a cell size of 10 m, the TPI in our analysis corresponds to microtopographic features. We georeferenced aerial photos (1:10,000) from the Norwegian Mapping Authority (2022) to obtain a multiband raster dataset with a resolution of 2 m. We were then able to extract red (R), green (G), and blue (B) raster band values, respectively. From this data, we determined the excess green index ($ExGI = 2G - (R + B)$), which indicates the extent of vegetation (Larrinaga and Brotons, 2019).

To identify landscape indicators of glacial erosion and non-erosion, we used a combination of field observations and GIS-mapping of topographical, hydrological and weathering data, following the approach presented by Ebert et al. (2015) for an area on the Fennoscandian Shield south of our study area. We examined the distribution of bedrock exposure, sediment thickness, glacially streamlined features, and the geometries of the drainage networks. We assigned values of -1 and +1 to the landscape indicators of glacial erosion and non-erosion, respectively. We used three-dimensional views provided by the online features of the Norwegian Mapping Authority (2022) and Bing, and in the case of the Gaskabohki headwater catchment, which we sampled in detail, we also used data from ground-truthing.

5.2.4 Current erosion rates using $^{239+240}\text{Pu}$

During September/October 2020, we extracted 83 soil cores in a grid sampling scheme (distance to the next sampling points ~100 m) to cover the entire Gaskabohki catchment area. Additionally, 10 reference soil cores on two flat hilltops adjacent to the catchment were taken assuming that these represent soil profiles without erosion or deposition (Fig. 5-1d). We used a mechanical corer (diameter = 5 cm) and sampled until we reached a gravel layer or bedrock. The sampled material was stored in inner liner tubes and brought back to the laboratory, where we performed subsampling and further processing.

The reference soil cores (mean soil core length = 25 cm) were cut in increments of 3 cm, resulting in a total of 75 subsamples. In contrast, the first increment of the sample soil cores (mean soil core length = 14 cm) was 12 cm. For core lengths greater than 12 cm, the remaining core was cut into shorter increments of 3 cm, resulting in a total of 178 subsamples. After cutting and air-drying, the samples were manually sieved to 2 mm. The fine earth fraction (< 2 mm) was then milled with a Retsch PM 400 planetary ball mill and dry-ashed at 440°C for 7 h to remove any organic matter.

The chemical procedures were adapted from those reported in Ketterer et al. (2004). Each sample was spiked with 26.7 pg (0.00390 Bq) of a Pu-242 tracer solution in 5 M HNO₃ (NIST 4334i) and leached with 30 mL of an 8 M HNO₃ solution at 75-80°C for 20 h with occasional shaking. Following leaching, the samples were membrane-filtered at 0.45 µm and rinsed with water until the solutions recovered had final volumes of 50-60 mL. Thereafter, 100 mg of FeSO₄·7H₂O and 1.0 g of NaNO₂ were added in the forms of concentrated aqueous solutions to convert Pu to the Pu(IV) oxidation

state. After allowing the generated NO₂ (g) to escape and permitting the completion of conversion to Pu(IV), we added 150 mg of TEVA resin to the sample solutions. The sample-resin mixtures were agitated on a mechanical shaker for 30 min and the resin was collected using a plastic column (V = 23 mL) with glass wool plug. After discarding the passthrough sample solution, the resin columns were rinsed with the following sequence to remove matrix elements, U and Th: i) 2 x 11 mL of 2 M HNO₃; ii) 5 mL of 9 M HCl; and iii) 5 mL of 2 M HNO₃. Finally, Pu was eluted with the following sequence: i) 0.5 mL H₂O; ii) 0.5 mL of 0.05 M ammonium oxalate; and iii) 0.5 mL H₂O.

Activities of ²³⁹⁺²⁴⁰Pu (in Bq kg⁻¹) were measured using a Thermo X2 quadrupole ICP-MS system equipped with an ESI Scientific Apex HF sample introduction system located at Northern Arizona University. The masses of ²³⁹Pu and ²⁴⁰Pu in the samples were converted into the summed activity ²³⁹⁺²⁴⁰Pu. A detection limit of 0.01 Bq kg⁻¹ ²³⁹⁺²⁴⁰Pu was estimated for a sample of nominal mass of 10 g. Data quality was evaluated through the analysis of blanks (Pu-devoid sandstone), control samples of known ²³⁹⁺²⁴⁰Pu activities (IAEA-447, Moss Soil) and duplicates.

We calculated soil redistribution (erosion or deposition) rates using the FRN conversion model MODERN (Modelling Deposition and Erosion rates with RadioNuclides; Arata et al., 2016). We chose this model because it reproduces the measured depth distributions of ²³⁹⁺²⁴⁰Pu isotopes at the reference sites without making assumptions or generalizations about the shape of the depth distribution. By overlapping the total inventory (Bq m⁻²) of each sampling site, *Inv*, with the depth profile of the reference site, which is modeled as a step function *g(x)* and which returns a value *Inv(inc)* for each increment *inc*, the intersection point *x** (cm) along the soil profile where the values match is found (Fig. 5-2; Arata et al., 2016).

The model thereby targets the level *x** from *x** to *x* + d*, with *d* being the total increment of depth (cm; Arata et al., 2016):

$$\int_{x^*}^{x^*+d} g(x)dx = Inv \quad (5-3)$$

To match higher inventories of deposition sites, so many simulated layers are added on top of the measured reference depth profile until the program finds solutions for these sites as well. In our case, we had to add one simulated layer and assumed that on average the deposition material originated from the top 3 cm of eroded soil (by setting the inventory of the simulated deposition layer equal to the one of the top 3 cm of the reference profile). The cumulated total inventory of the reference site, including these

new simulated layers, is described by the integral function S (Arata et al., 2016) as follows:

$$S(x) = \int_x^{x+d} g(x') dx' \quad (5-4)$$

The function S can then be solved through the primitive function G of the distribution function $g(x)$ as follows:

$$S(x) = G(x+d) - G(x) \quad (5-5)$$

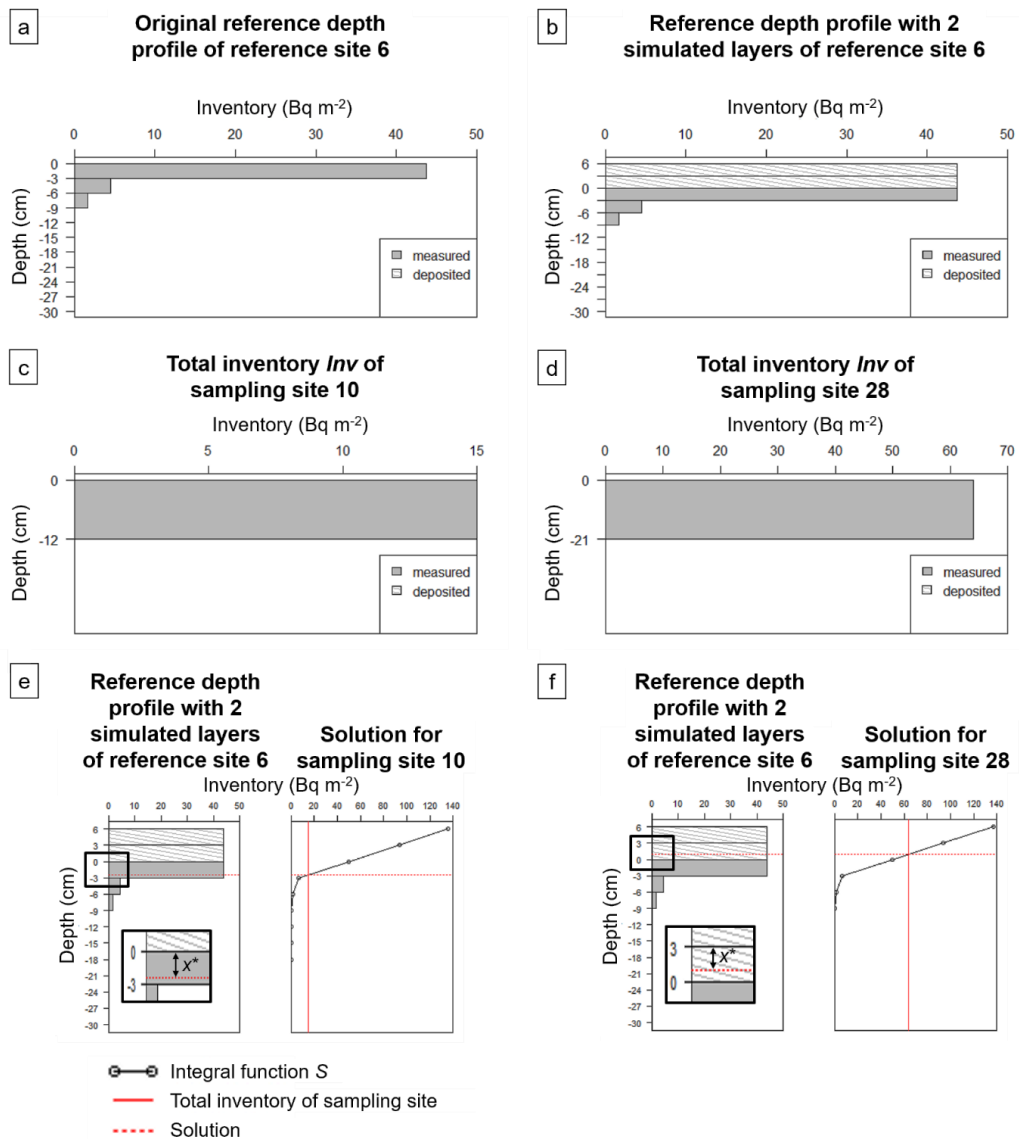


Fig. 5-2: Concept of MODERN. (a) Original reference depth profile shown exemplarily for reference site 6. (b) Reference depth profile of reference site 6 adjusted by adding two simulated layers on top. Total inventories of sampling sites 10 (c) and 28 (d). Note the different axis labels. MODERN compares the area covered by the depth profile of reference site 6 with the area of the total inventory of sampling site 10 (e) or 28 (f). MODERN

superimposes the two areas until finding the intersection point x^* where the two areas match. In case of sampling site 10, this intersection point is negative, indicating erosion, and in case of sampling site 28, it is positive, indicating deposition. The graphs were extracted from the freely available MODERN version in *R*.

Finally, soil redistribution rates Y (in $\text{t ha}^{-1} \text{yr}^{-1}$) can be calculated as follows:

$$Y = 10 \cdot \frac{x^* \cdot xm}{d(t_1 - t_0)} \quad (5-6)$$

where xm is the mass depth (kg m^{-2}) of the sampling site, and t_1 is the sampling year (yr, here: 2020), and t_0 (yr, here: 1963) is the reference year. We used the freely available MODERN version in *R* (Chiaradia et al., 2016).

5.2.5 Long-term denudation rates using in situ ^{10}Be

We sampled stream sediment at the outlet of the catchments in September/October 2020. The sediment was dry-sieved and the 400-630 μm fraction was further processed for in situ cosmogenic ^{10}Be concentration determination. To enrich the quartz grains from the polymineral samples, we performed first a magnetic separation using a Frantz magnetic separator and second a density separation using sodium polytungstate in water at densities of 2.70 g cm^{-3} . To further remove residual non-quartz minerals, we leached the samples several times with acid solutions of different concentrations: starting with solutions of HCl (32%) and H_2SiF_6 (35%) in different mixing ratios (1:3 to 1:1; Merchel et al., 2019) and finally with diluted HF (2%). We dissolved meteoric ^{10}Be from the surface of the grains by the addition of HF (48%). One processing blank was added to monitor any possible unwanted contributions, such as contamination between samples in the chemistry laboratory and during measurement, and from any chemical products and target preparation materials used. We added $\sim 315 \mu\text{g}$ of ^9Be carrier (“Phenakite EA”, $\sim 140 \mu\text{g}$ solution with a ^9Be concentration of $2246 \pm 11 \mu\text{g g}^{-1}$; Merchel et al., 2008) to $\sim 20 \text{ g}$ of sample. Following anion and cation exchange columns and selective coprecipitation with ammonia solution (25%; Merchel and Herpers, 1999), the resulting $\text{Be}(\text{OH})_2$ gel was dehydrated on a hot plate overnight. The $\text{Be}(\text{OH})_2$ was converted to BeO at 900°C for 2 h. The resulting BeO was mixed with Nb (about 4x the mass of BeO) and pressed into Cu cathodes. The $^{10}\text{Be}/^9\text{Be}$ ratios of each sample and the blank were determined at the Dresden Accelerator Mass Spectrometry (DREAMS) facility (Rugel et al., 2016). Results were quantified

versus the in-house standard SMD-Be-12 ($^{10}\text{Be}/^9\text{Be} = 1.704 \pm 0.030 \times 10^{-12}$; Akhmadaliev et al., 2013).

For the calculation of denudation rates based on equation (5-2), we used a Scandinavian ^{10}Be spallogenic sea-level high-latitude (SLHL) production rate of $4.12 \pm 0.11 \text{ atoms g}^{-1} \text{ yr}^{-1}$ (Stroeven et al., 2015), a decay constant of $5.00 \pm 0.06 \times 10^{-7} \text{ yr}^{-1}$ (Chmeleff et al., 2010; Korschinek et al., 2010), and a production attenuation length of 150 g cm^{-2} . We used an average density of the surface material of 2.1 g cm^{-3} since this corresponds to the mean bulk dry density of all soil cores collected at the Pu sampling sites (Fig. 1d). We scaled the production rate for altitude using the scaling factors proposed by Stone (2000) and assumed the fractions of production by spallation and muon capture equal to 0.974 and 0.026, respectively. Unless explicitly stated otherwise, ^{10}Be -derived denudation rates are reported without correction for shielding due to topography or snow.

We used the online exposure age calculator v3.0 (Balco et al., 2008) to calculate the theoretical ^{10}Be concentration of samples free of inheritance. We used the online erosion rate calculator v3.0 (Balco et al., 2008) to perform sensitivity analyses regarding the influence of (i) the simplified approach of averaging the catchments' elevations for the scaling of the production rate instead of considering every pixel of the catchment individually which would represent the entire catchment more accurately, (ii) the proportion of non-quartz-contributing areas, (iii) topographic shielding, and (iv) the intensity of snow shielding during interstadials/interglacials over the time averaging window on the calculated denudation rates.

The program uses a ^{10}Be half-life of $1.387 \pm 0.0012 \text{ Myr}$ (Chmeleff et al., 2010; Korschinek et al., 2010) and the production rate was corrected for latitude and altitude after the scaling scheme of Stone (2000). We assumed a density of 2.1 g cm^{-3} and a sample thickness of 0 cm. We supplied the program with the coordinates of the basin's centroid. We determined topographic shielding by using the ArcGIS geoprocessing tool developed by Li (2013). We calculated snow shielding S_{snow} using monthly snow depths according to Gosse and Phillips (2001):

$$S_{\text{snow}} = \frac{1}{12} \sum_i^{12} e^{-\left(\frac{z_{\text{snow},i} \cdot \rho_{\text{snow},i}}{\Lambda_{f,e}}\right)} \quad (5-7)$$

where $z_{\text{snow},i}$ is the monthly snow height (cm) above land surface, $\rho_{\text{snow},i}$ is the average monthly snow density, and $\Lambda_{f,e}$ is the attenuation length for absorption and moderation of epithermal neutron flux (g cm^{-2}). We used

the contemporary mean monthly snow height recorded at the meteorological station at Iskorasfjellet (591 m amsl, SN97710; Seklima, 2020) averaged over the period of November 2014 to October 2020 (longest available record at Iskorasfjellet). In the sensitivity analysis, we adjusted this thickness up to an increase of 100%, and tested snow densities of up to 0.48 g cm^{-3} (Onuchin and Burenina, 1996). We applied an attenuation length of 150 g cm^{-2} . The attenuation length for high-energy neutrons is thought to decrease up to 140 g cm^{-2} at the Earth's poles (Cerling and Craig, 1994) and snow contains considerably more hydrogen, which is a highly efficient moderator of neutrons, than other surfaces such as solid rocks (Zweck et al., 2013).

5.3 Results

5.3.1 $^{239+240}\text{Pu}$ in soils

All soils were mineral soils, with a median organic matter content of 1.9% (approximated as percentage by mass of material lost due to dry-ashing in the fine earth fraction). The mean (\pm standard deviation) ratio of $^{240}\text{Pu}/^{239}\text{Pu}$ of all incremental samples at both reference and sampling sites was 0.193 (± 0.011). This is congruent with an average global fallout ratio of 0.18 in the Northern Hemisphere (Kelley et al., 1999), indicating the absence of Pu derived from the 1986 Chernobyl incident. Therefore, the key assumption of the FRN method, a homogeneous fallout distribution, was fulfilled (Mabit et al., 2013; Meusburger et al., 2018). We can thus interpret the Pu data as describing soil redistribution during the last ~60 years.

Pu depth profiles at the references sites

The Pu depth profiles of the ten reference sites showed the general trend of decreasing Pu inventory with depth (Extended Data Fig. 5-1). With the exception of reference site 2 (Extended Data Fig. 5-1b), the inventory maximum was located in the uppermost soil increment of 0-3 cm. Thereafter, the inventory decreases exponentially with depth. Reference site 9 is an exception to this exponential decrease (Extended Data Fig. 5-1c), as it showed approximately equal inventories in the four layers below the inventory maximum in the top layer. The increment of 12-15 cm constitutes the deepest increment in which Pu could be detected. The mean depth with Pu activity across all reference sites was $10.5 (\pm 3.6) \text{ cm}$. At reference site 2, most Pu was found in the second increment of 3-6 cm. Since almost all Pu depth profiles showed a stringent exponential decrease, we assumed the loss of Pu due to vertical mixing unlikely at the reference sites.

The total inventory over all reference sites varied from 14.3 to 346.0 Bq m⁻². Based on the Grubbs test, at the 0.05 significance level, the highest value of 346.0 Bq m⁻² of reference site 5 is a significant outlier. Accordingly, we removed reference site 5 from the dataset and used only the mean over the remaining nine reference sites to calculate soil distribution rates (Fig. 5-3). The mean total inventory over the remaining nine reference sites was 46.1 (± 33.7) Bq m⁻².

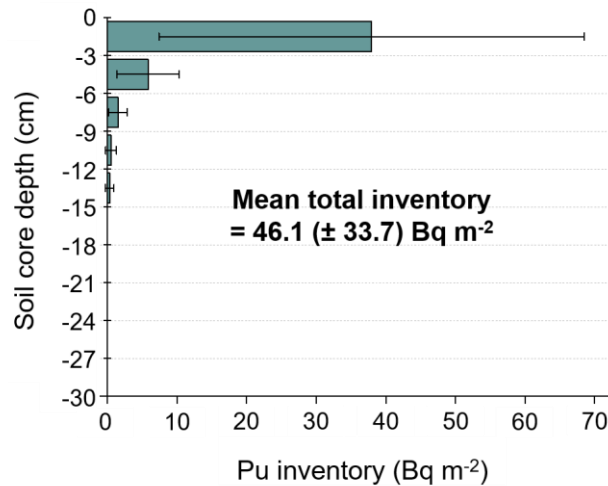


Fig. 5-3: Mean reference depth profile. Of the ten reference site samples measured, only nine were used to calculate the mean, as reference site 5 was found to be an outlier.

Pu inventory at the sampling sites

The total Pu inventory among all sampling sites ranged from 12.5 to 2223.0 Bq m⁻². The maximum soil depth at which we found Pu activity was 21 cm. Contrary to expectation, the total Pu inventory decreases with increasing depth with Pu activity (Fig. 5-4). Nearly half of all sites ($N = 39$) had total inventories greater and depths with Pu activity less than the respective mean values of the reference sites (gray box in Fig. 5-4). This quadrant should not exist under normal FRN transport conditions. Under typical conditions, sites are located in the lower, left ('erosion quadrant') and in the upper, right quadrant ('deposition quadrant'). For sites that experience erosion, both the total inventory and the depth with Pu activity normally decrease concomitantly. In our dataset, the mean total inventory for these erosion sites ($N = 25$) located in the lower, left quadrant was 31.5 (± 9.4) Bq m⁻². For sites that experience deposition, both the total inventory and the depth with Pu simultaneously increase. In our dataset, these depositional sites ($N = 7$) in the upper, right quadrant showed a mean total inventory of 58.4 (± 10.5) Bq m⁻². Another scenario is represented by sites

that experience erosion, indicated by a reduced total inventory (in our dataset: $N = 12$; mean total inventory = $29.5 (\pm 8.9) \text{ Bq m}^{-2}$), but whose depth with Pu activity is greater than the mean of the reference profiles because Pu is transported vertically downward due to mixing (lower, right ‘erosion and cryoturbation quadrant’ in Fig. 5-4). As the Gaskabohki catchment is underlain by sporadic permafrost, cryoturbation is a plausible explanation for this mixing behavior. However, bioturbation might also have been a (further) cause. We note here that we approximated the depth with Pu activity at the reference sites with 12 cm, although the actual mean value was determined to be 10.5 cm. However, as the first increment measured at the sampling sites was 12 cm, a comparison between reference and sampling sites was only possible at a depth of 12 or more cm.

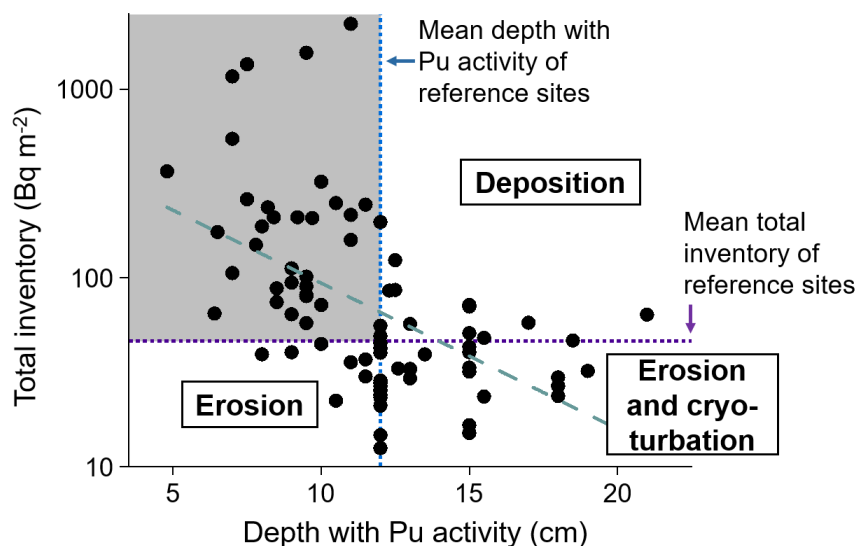


Fig. 5-4: Unusual distribution of total Pu inventories over depth with Pu activity of the sampling sites. Total inventory linearly decreases with depth with Pu activity (linear regression fit: dashed green line, $R^2 = 0.28$). Sites with a total inventory lower than the mean of the reference sites (dotted purple line) are thought to be erosion sites. In contrast, sites with a total inventory higher than the mean of the reference sites are considered depositional sites. While erosion decreases the depth with Pu activity (compared to the mean depth with Pu activity of the reference sites, dotted blue line; ‘erosion quadrant’), deposition leads to an increase in the depth with Pu activity (‘deposition quadrant’). Sites with a total inventory lower than the mean of the reference sites, but with a greater depth with Pu activity, could be erosion sites that experienced cryoturbation (‘erosion and cryoturbation quadrant’). The gray box indicates the sites where high to extremely high total inventories were present at short depths with Pu activity. Here probably an exceptionally high amount of Pu was deposited, but only in connection with very small amounts of material (sediment/soil). Note: Even though the actual mean of the depth with Pu activity of the reference sites was determined to be 10.5 cm, we approximated this value to be 12 cm because this corresponds to the first increment measured at the sampling sites.

Accordingly, the Pu depth profile within the upper 12 cm was not resolved in the sampling sites and thus it was only possible to test whether further Pu was present in the increments larger than 12 cm.

Sites in the gray box were characterized by short total soil core lengths, with 37 of 39 sites having total soil core lengths less than or equal to 12 cm. Since we did not subdivide the upper 12 cm into further increments, the Pu depth profile for this upper section was not resolved. Therefore, if the total soil core length was less than or equal to 12 cm, the total soil core length and the depth with Pu activity could not be distinguished from each other. There are three possible explanations for the occurrence of the numerous sites in the gray box in Fig. 5-4: (i) The total soil core lengths/depths with Pu activity were even much shorter at the time of Pu fallout distribution than at the time of sampling. Material from erosion sites was deposited there, resulting in an increase in both total inventory and depth with Pu activity (total soil core length). (ii) Total soil core lengths/depths with Pu activity were longer at the time of Pu fallout distribution than at the time of sampling. Initially, these lengths were reduced due to erosion. Thereafter, preferential deposition of 'pure Pu' must have occurred there. (iii) Total soil core lengths/depths with Pu activity were already as short at Pu fallout distribution as at sampling. These lengths did not change (significantly) due to erosion or deposition processes. Only 'pure Pu' was preferentially deposited there. By a deposition of 'pure Pu' we mean a deposition by which the total inventory at the sampling site was significantly increased, but 'no' (hardly any) material mass increase took place. In the discussion, we attempt to address the occurrence of this 'pure Pu' in our study area.

We regard the first explanation as implausible because the in some cases extremely high Pu total inventories ($> 1000 \text{ Bq m}^{-2}$) cannot be achieved even assuming extremely fast deposition rates, given the short total soil core lengths/depths with Pu activity. Placing the mean total Pu inventory of the reference sites in the first 3 cm of erosion sites and assuming that no material is initially present at the sites of interest (total soil core length = 0 cm), not even a material transport resulting in a soil thickness of 12 cm (which corresponds to the longest recorded total soil core length at 37 of the 39 sites of interest) would yield such high total inventories. In this scenario, the maximum total inventory would be 184.4 Bq m^{-2} ($4 \times 46.1 \text{ Bq m}^{-2}$). Assuming that all Pu was concentrated in the uppermost cm in erosion sites, a total inventory of 553.2 Bq m^{-2} ($12 \times 46.1 \text{ Bq m}^{-2}$) could be achieved with a deposition of 12 cm. Nevertheless, this does not explain the values that are four times as large in some cases.

Furthermore, we think that the second explanation is also not very likely, since the soil transport behavior at these sites probably did not change that drastically from erosion to deposition within the rather short observation window of about 60 years. We consider the third explanation to be the most likely, as the soil transport processes are most likely rather slow overall in the low-relief area we studied.

Current erosion rates using $^{239+240}\text{Pu}$

Because of the disproportionately large number of sites with extremely high total inventories (gray box, Fig. 5-4), the mean total inventory across all sampling sites was greater than the mean across the reference sites. Accordingly, the mass balance for the basin was not correct, i.e., the assumption of a net material loss was disregarded. Therefore, the dataset did not allow us to calculate a catchment-wide average erosion rate. We calculated site-based erosion rates using the total inventories of sites in the 'erosion quadrant' and 'erosion and cryoturbation quadrant' (Fig. 5-4).

The highest erosion rate was found at site 71 of the 'erosion quadrant' and determined to be $852 \text{ t km}^{-2} \text{ yr}^{-1}$ or 406 mm kyr^{-1} , based on a bulk dry density of 2.1 g cm^{-3} , which corresponds to the mean over all sample sites. Site 71 is situated in the upper part of the Gaskabohki headwater catchment, near the main channel (Fig. 5-5a). The mean erosion rate over all sites with presumably no cryoturbation ('erosion quadrant') was $175 (\pm 118) \text{ mm kyr}^{-1}$. The mean erosion rate of the sites that experienced cryoturbation ('erosion and cryoturbation quadrant') was slightly higher with $204 (\pm 107) \text{ mm kyr}^{-1}$. In contrast to the erosion sites that showed no signs of cryoturbation, the erosion sites with cryoturbation are located exclusively in the outer areas of the catchment (Fig. 5-5a), as evidenced by a higher mean elevation of 547 m amsl of the latter compared to the former at 516 m amsl.

Because the erosion sites where presumably no cryoturbation occurred had depths with Pu activity of 12 cm or less, preventing their Pu depth profiles from being resolved, we tested the change in erosion rates when the entire Pu inventory was concentrated in the upper 6 cm. Based on the mean Pu depth profile of the reference sites (Fig. 5-3), 95% of the total Pu inventory was located in the upper 6 cm at sites that were assumed to be free of cryoturbation. In contrast, the default setting in MODERN distributes the entire Pu inventory evenly over the depth with Pu activity, generally underestimating erosion rates. Applying the scenario oriented to the reference Pu depth profile (total Pu inventory in the upper 6 cm), the mean erosion rate of sites in the 'erosion quadrant' increases by 175% to $307 (\pm 244)$

mm kyr⁻¹. A deviation of similar magnitude would be obtained if we had not omitted reference site 5 from the dataset. If the erosion sites were compared with the mean of all reference sites, incl. site 5, the average erosion rate would be 330 (\pm 78) mm kyr⁻¹.

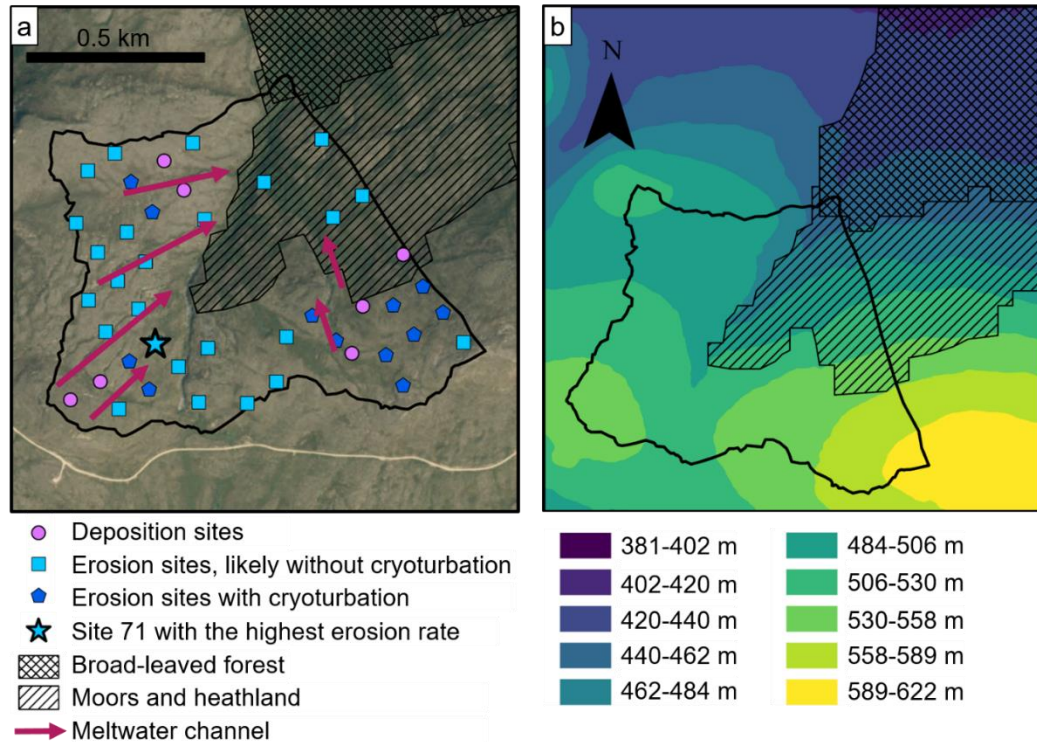
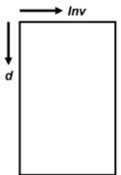

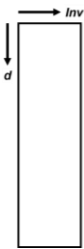



Fig. 5-5: Locations of erosion and deposition sites derived from ²³⁹⁺²⁴⁰Pu inventories and topography in the Gaskabohki headwater catchment. While the upper part of catchment is sparsely vegetated, the downstream area is dominated by moors and heathland (CLC, 2018). (a) Blue and pink colors indicate erosion and deposition sites, respectively. These sites are mainly located in the sparsely vegetated part of the catchment. The blue star denotes the highest recorded erosion rate in the catchment at site 71. A square and a pentagon represent sites that were presumably not cryoturbated and sites that were cryoturbated, respectively. Red arrows show melt water channels (NGU, 2022b). (b) Topography in the Gaskabohki catchment. Colors indicate the altitude in m above mean sea level (amsl).

Finally, the mean value of erosion rate across all erosion sites ($N = 37$), regardless of cryoturbation, was determined to be 184 (\pm 114) mm kyr⁻¹. Assuming no preferential erosion did occur in the watershed, this mean erosion rate could be considered the maximum erosion rate for the entire watershed. An overview of the different erosion rates due to cryoturbation are shown in Tab. 5-1.

Tab. 5-1: Overview of calculated current erosion rates derived from $^{239+240}\text{Pu}$ inventories using MODERN. The differences are due to the absence or presence of cryoturbation, resulting in different depths with Pu activity, and the settings used in MODERN. Listed are mean values and standard deviations. These erosion rates were derived from erosion sites only, while deposition sites were not considered. Therefore, these mean erosion rates should be treated as maximum values for the entire Gaskabohki watershed. For a better understanding of the different settings used in MODERN, a schematic depiction of the assumed Pu inventory distribution *Inv* over the depth with Pu activity *d* is included. Here, a total Pu inventory of the same size (same area) over all four cases was chosen for better comparison. In the fourth case, the depth averaged over cases 1 and 3 was visualized. We used a density of 2.1 g cm^{-3} .

	Sites with presumably no cryoturbation ('erosion quadrant') – default setting in MODERN	Sites with presumably no cryoturbation ('erosion quadrant') – all Pu located in upper 6 cm	Sites with cryoturbation ('erosion and cryoturbation quadrant') – default setting in MODERN	All erosion sites ('erosion quadrant' and 'erosion and cryoturbation quadrant') – default setting in MODERN
Mean erosion rate (mm kyr ⁻¹)	175 ± 118	307 ± 244	204 ± 107	184 ± 114
Mean erosion rate (t km ⁻² yr ⁻¹)	367 ± 248	645 ± 512	427 ± 225	387 ± 239
Schematic depiction of the assumed Pu inventory distribution <i>Inv</i> over the depth with Pu activity <i>d</i>				

All available parameters (fine earth fraction, dry bulk density, total soil core length, slope, SPI, TPI, and excess green index) were found to be not significant predictors at a significance level of 0.05 for erosion rate when all erosion sites ($N = 37$) were considered or for soil distribution rate when both erosion and deposition sites ($N = 44$) were considered.

5.3.2 In situ ^{10}Be in stream sediments

The in situ ^{10}Be concentrations of our samples range from 1.4×10^5 atoms g^{-1} in the large Karasjohka 1 basin to 3.7×10^5 atoms g^{-1} in the most upstream area of the Gaskabohki headwater catchment (Tab. 5-2). If the last glacial period had been erosional, the cosmogenic inventory would have been reset and the ^{10}Be concentration at the surface would reflect accumulation since the end of the last glaciation. Considering the deglaciation age of Iskorasfjellet of about 11 kyr BP and assuming a postglacial erosion rate of 0, a concentration of less than 4.5×10^4 atoms g^{-1} would be required for our samples to be free of inheritance (calculated using the exposure age online calculator v3.0; Balco et al., 2008). Taking postglacial erosion into account, the theoretical ^{10}Be concentration for samples without inheritance would be even lower, such as 2.5×10^4 atoms g^{-1} for a postglacial erosion rate of 100 mm kyr^{-1} . As the concentrations we measured are almost an order of magnitude higher than these reference values, we conclude that all of our samples contain inherited in situ ^{10}Be from previous glacial cycles. This is consistent with the assumption that the Fennoscandian ice sheets were cold-based and non-erosive (Kaitanen, 1969; Kleman et al., 1997; Kleman et al., 2008; Ebert et al., 2015).

Tab. 5-2: Sampling site information, ^{10}Be productions rates, and ^{10}Be concentrations. (a) A sea-level, high-latitude production rate of 4.12 ± 0.11 atoms $\text{g}^{-1} \text{yr}^{-1}$ (Stroeven et al., 2015) was used. It was scaled for altitude using the scaling factors proposed by Stone (2000), including a 2.6% muon contribution. (b) The $^{10}\text{Be}/^9\text{Be}$ ratios were measured at the Dresden Accelerator Mass Spectrometry (DREAMS) facility. Results were quantified versus the in-house standard SMD-Be-12 ($^{10}\text{Be}/^9\text{Be} = 1.704 \pm 0.030 \times 10^{-12}$; Akhmadaliev et al., 2013).

Sample ID	Latitude (°N)	Longitude (°E)	Mean catchment elevation (m amsl)	^{10}Be production rate ^(a) (atoms $\text{g}^{-1} \text{yr}^{-1}$)	^{10}Be concentration ^(b) (10^5 atoms g^{-1})
Gaskabohki 1	69.30423	25.29935	525	6.92	3.7
Gaskabohki 2	69.30461	25.30013	521	6.89	2.8
Gaskabohki 4-1	69.30595	25.30503	518	6.87	2.8
Gaskabohki 4-2					2.6
Guovzilbohki	69.31371	25.28749	464	6.55	2.2
Bahkiljohka	69.37173	25.33931	367	5.98	1.9
Karasjohka 1	69.29780	24.52258	348	5.87	1.4
Karasjohka 2	69.260702	24.856162	362	5.95	1.5

The ^{10}Be concentration across the catchments decreases with increasing catchment area (Fig. 5-6). The concentration at the most upstream sampling site of the Gaskabohki headwater catchment, Ga1, is markedly higher than at the two sampling sites further downstream, Ga2 and Ga4, and deviates the most from the power law fit across all catchments (Fig. 5-6). Sampling site Ga1 and its corresponding drainage area upslope is situated on the Iskorasfjellet ridge (Fig. 5-1c). The difference in concentration between the different catchments and the particularly high value of site Ga1 could be due to a variable erosive force from the last glaciation, with the erosive force being lowest along the Iskorasfjellet ridge. However, we consider it more likely that the differences in concentration are due to varying degrees of fluvial erosion since deglaciation.

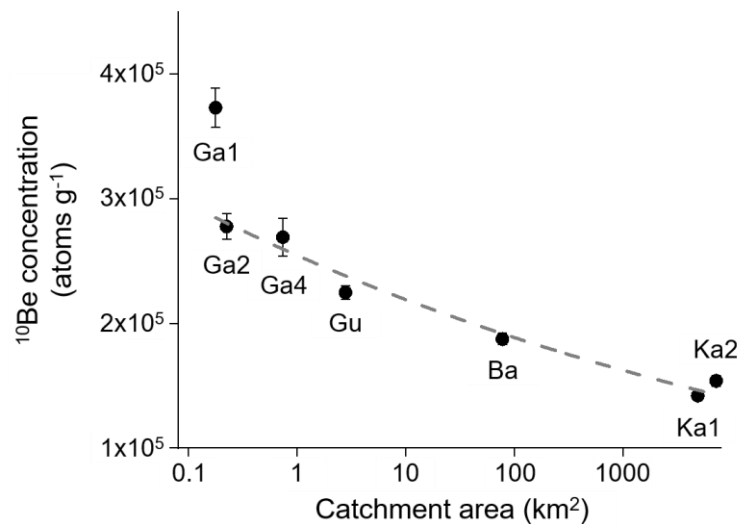


Fig. 5-6: In situ ^{10}Be concentration decreases with increasing catchment area. The relation of ^{10}Be concentration and catchment area is best fitted by a power law function ($y = Ax^B$, gray dashed line; $A = 2.5 \times 10^5$, $B = -0.065$, $R^2 = 0.90$). Error bars indicate the uncertainty in the ^{10}Be concentration in the quartz sample (uncertainty in the isotope ratio measurement, uncertainty in the number of atoms in the process blanks, and uncertainty in the mass of Be added as carrier). The concentration of the Gaskabohki catchment (Ga4) represents the mean of two separate measurements from two sediment samples taken only a few meters apart (Tab. 5-2). The difference in ^{10}Be concentration between the two samples was within measurement uncertainty limits, suggesting that the sources (soils and tills) for the collected sediment grains at the Gaskabohki catchment may have similar ^{10}Be inventories, at least over a relatively narrow spatial area. Ga: Gaskabohki with Ga4 at the outlet of the catchment and Ga1 and Ga2 upstream of Ga4; Gu: Guovzilbohki; Ba: Bahkiljohka; Ka1: Karasjohka 1; Ka2: Karasjohka 2.

While the two larger catchments, Karasjohka 1 and Karasjohka 2, have comparatively well developed river systems with a main channel width of

about 200-300 m (Fig. 5-1a), the three smaller catchments connected to Iskorasfjellet – Gaskabohki, Guovzilbohki, and Bahkiljohka – show only smaller streams with the main channel width not exceeding a few meters. We therefore suggest that the substantially lower ^{10}Be concentrations in the two larger catchments probably resulted from greater post-glacial erosion, including erosional processes such as incision and bank erosion. This is also reflected in higher SPI values, which scale with catchment area and indicate a higher fluvial erosive power, in these catchments. The smaller watersheds with their first to third order streams are much more limited in incision and bank erosion. This influence of fluvial erosion is particularly pronounced in our study because, due to the lack of steep slopes on the low-relief Finnmarksvidda, the sediments we collected at the outlets of the catchments most likely did not originate uniformly from all corners of the catchment, but rather represented the erosional behavior in the closer vicinity of the river system.

Indications of no glacial erosion at Iskoras

We consider glacial erosion as an unlikely driver of the widely varying ^{10}Be concentrations in the basins in our study, because we presume that no erosion occurred during glacial periods when ice sheets were frozen to their beds. This is manifested in a thick Quaternary deposits cover (maximum thickness > 50 m, and average thickness estimated to ~6 m) over most of the Finnmarksvidda, consisting of till beds, interstadial and interglacial deposits, and soils (paleosols) dating back to at least marine isotope stage (MIS) 9 or 11 (> 300 kyr BP; Olsen et al., 2013). Furthermore, the drainage systems of all our studied catchments have an overall rectangular rather than parallel pattern, which is an indicator for weak ice sheet erosion (Ebert et al., 2015).

However, the larger Karasjohka 1 und Karasjohka 2 basins appear to have been affected by glacial erosion, at least to some extent, as indicated by glacially streamlined features (drumlins, eskers, elongated lakes) located in the west of our studied area (Fig. 5-7). This area falls into the deglaciation fan 24 introduced by Kleman et al. (1997). This fan includes landforms that were created in a wet-based marginal zone and fossilized by inward transgression of the ice margin during the decay phase (Kleman et al., 1997). Further, small patches of bare bedrock, potentially indicating glacial scouring, are present in the larger Karasjohka 1 und Karasjohka 2 basins. The Karasjohka 1 basin shows the highest areal proportion of bare bedrock with 0.5%. In contrast, in the smaller catchments associated with Iskorasfjellet – Gaskabohki, Guovzilbohki, and Bahkiljohka – bare bedrock

is completely absent (NGU, 2022b). The Guovzilbohki and Bahkiljohka catchments show some eskers, which follow pre-glacial fracture-guided valleys (NGU, 2022b, 2022a). Finally, while the three smaller catchments lack moraines, the two larger catchments, Karasjohka 1 and Karasjohka 2, show many ablation ($N \sim 250$) and some end moraines ($N \sim 90$; NGU, 2022b).

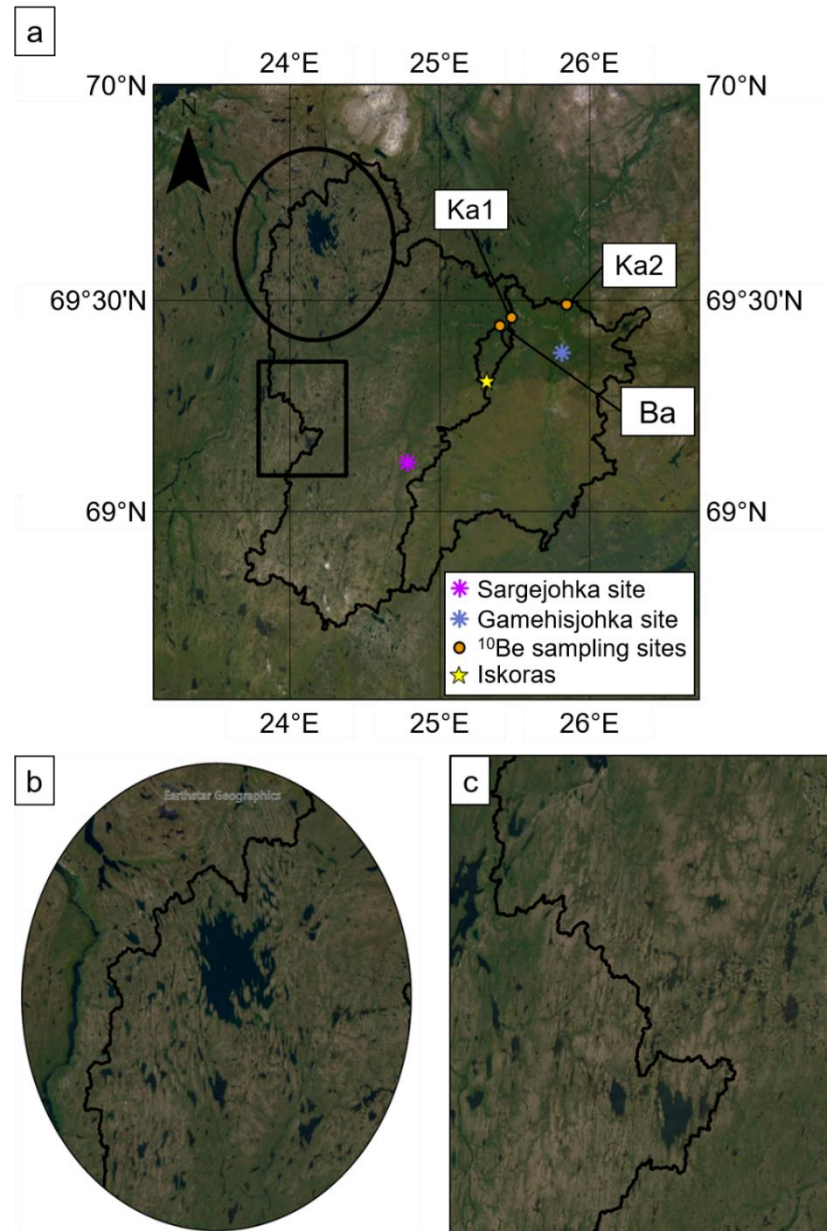


Fig. 5-7: Glacially streamlined areas are found in the western part of the Karasjohka 1 and Karasjohka 2 catchments. The orientation of the streamlined structures (drumlins, eskers, elongated lakes) are south-north-oriented, matching the deglaciation fan 24 of Kleman et al. (1997). (a) The areal proportion of glacially streamlining is highest for the Karasjohka 1 basin. The Bahkiljohka basin, which encloses the Gaskabohki and Guovzilbohki basins on the Iskorasfjellet ridge (yellow star), is not impacted by glacial streamlin-

ing. (b) and (c) Zoom on two glacially streamlined areas. Ka1: Karasjohka 1; Ka2: Karasjohka 2; Ba: Bahkiljohka. The background map is from 'Earthstar Geographics' (ESRI, 2022).

Although the Karasjohka 1 and Karasjohka 2 basins experienced some erosion in their western parts due to the retreat of the Fennoscandian ice sheet during the last deglaciation, consistent with the deglaciation fan 24 of Kleman et al. (1997), these catchments remained unaltered for most of the time during the last Weichselian glaciation (Kleman et al., 1997). They thus represent areas where the Fennoscandian ice sheet was frozen to its bed.

Affirming that the surface of the Gaskabohki basin, in particular, was not glacially eroded during the last stadials is of primary importance, as this was a major assumption for calculating long-term erosion rates derived from ^{10}Be (see below). Adequate determination of the long-term erosion rate was an important prerequisite for achieving the objective of our study – to compare this long-term erosion rate with a current (post-1960) erosion rate derived from $^{239+240}\text{Pu}$ for this small headwater catchment. Through field examinations, we determined that the Gaskabohki basin most likely did not experience glacial erosion because we found (i) the Gaskabohki stream in a v-shaped valley, (ii) the boulders in the v-shaped valley having an angular shape, which were most likely deposited there by short-distance transport, (iii) no glacially-scoured bare bedrock, (iv) tor-like features (Extended Data Fig. 5-2).

Tab. 5-3: The larger Karasjohka 1 (Ka1) and Karasjohka (Ka2) catchments are more likely to have experienced some glacial erosion than the three smaller catchments associated with Iskorasfjellet, Gaskabohki (Ga), Guovzilbohki (Gu), and Bahkiljohka (Ba). Indicators were adapted from Ebert et al. (2015): Indicators for non-erosion (+1) are a dendritic drainage pattern, presence of weathering remnants, presence of tors (or tor-like features), and non-streamlined features. Indicators for glacial erosion (-1) are a parallel drainage pattern, absence of weathering remnants, absence of tors, and streamlined features. No data is denoted with a value of 0.

Indicators	Ga	Gu	Ba	Ka1	Ka2
Drainage pattern	+1	+1	+1	+1	+1
Weathering remnants	+1	+1	+1	+1	+1
Tors	+1	0	0	0	0
Streamlining	+1	+1	+1	-1	-1
Sum of indicators	+4	+3	+3	+1	+1

In summary, we propose that all catchments we studied represent post-glacial landscapes that retain relict non-glacial features, such as tors and saprolites, rather than landscapes that were (strongly) influenced by glacial erosion, as evidenced by a positive sum of non-erosion/glacial erosion indicators for all catchments (Tab. 5-3).

Scenarios of reconstructed glacial history

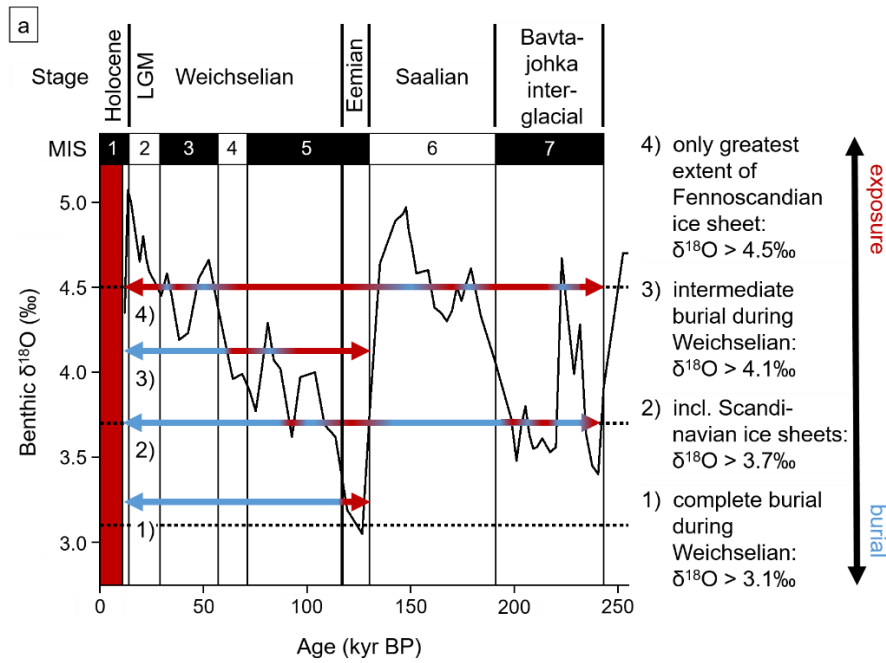
Assuming that the decreasing ^{10}Be concentration with catchment size (Fig. 5-6) reflects denudation during interglacials/interstadials, the very high ^{10}Be concentration of the smallest catchment, Ga1, located on the Iskorasfjellet ridge can be interpreted as a first-order approximation of inheritance. Based on the assumption that neither glacial nor interglacial erosion occurred along the ridge, the ^{10}Be concentration of the Ga1 catchment reflects accumulation during interglacials/interstadials and continuous decay.

Because we presume that both no glacial and no interglacial erosion occurred in the Ga1 catchment, we set the respective erosion rates in equation (5-2) equal to zero, thereby simplifying the equation to:

$$N_{\text{complex}} = \frac{P}{\lambda} (1 - e^{-\lambda T_{\text{exposure}}}) e^{-\lambda T_{\text{burial}}} \quad (5-8)$$

where T_{exposure} and T_{burial} are the cumulative exposure and burial times (yr), respectively.

Finmarksvidda is thought to have been covered both by Fennoscandian ice sheets and mountain-centered Scandinavian ice sheets (Olsen, 1988; Olsen et al., 2013). The respective ice sheet configurations are characterized by different benthic ^{18}O limits (Kleman et al., 1997; Kleman et al., 2008) of the DSDP 607 marine benthic foraminifer oxygen isotope records of global ice volume (Ruddiman et al., 1989; Raymo et al., 1989; Lisiecki and Raymo, 2005). While the northern Swedish mountains ice sheets occurred at $^{18}\text{O} > 3.7\text{‰}$ (scenario 2), the greatest extent of the Fennoscandian ice sheets was not reached until $^{18}\text{O} > 4.5\text{‰}$ (scenario 4; Kleman et al., 1997; Kleman et al., 2008). Using these constraints on ice sheet extent history, we were able to determine different cumulative exposure and burial times during the last glacial cycle(s) (Fig. 5-8). We note that such a partitioning of the DSDP 607 record could be prone to error for periods beyond the last glacial cycle, since there has been good temporal and spatial control of ice sheet extent only for the last glacial cycle (Kleman et al., 1997; Fabel et al., 2002; Kleman et al., 2008).



Scenario number	Description	since Eemian interglacial (since MIS 5 = 130 kyr)		since Bajtajohka interglacial (since MIS 7 = 243 kyr)	
		$\Sigma T_{\text{exposure}}$ (kyr)	ΣT_{burial} (kyr)	$\Sigma T_{\text{exposure}}$ (kyr)	ΣT_{burial} (kyr)
1	complete burial during Weichselian: $\delta^{18}\text{O} > 3.1\text{‰}$	23	107		
2	buried under Scandinavian ice sheets: $\delta^{18}\text{O} > 3.7\text{‰}$	41	89	71	172
3	intermediate burial during Weichselian: $\delta^{18}\text{O} > 4.1\text{‰}$	82	48		
4	only buried under greatest extent of Fennoscandian ice sheet: $\delta^{18}\text{O} > 4.5\text{‰}$	103	27	181	62

Fig. 5-8: Different scenarios of complex exposure and burial history at Iskorasfjellet. (a) DSDP 607 marine benthic foraminifer oxygen isotope record for the last 250 kyr (Ruddiman et al., 1989; Raymo et al., 1989; Lisiecki and Raymo, 2005). The four scenarios are differentiated by a certain ^{18}O threshold (see main text). The exposure time increases from scenario 1 to scenario 4. Red indicates exposure and blue indicates burial. Also included are the marine isotopes stages (MIS) and the corresponding names of the glacial and interglacial periods. We extracted the MIS boundaries from Lisiecki and Raymo (2005) and Lisiecki (2022). (b) The table shows the cumulative exposure and burial times for each scenario. The left bold column shows the cumulative times since the Eemian interglacial, i.e., since MIS 5, for all scenarios. The right bold column shows the cumulative times since the Bajtajohka interglacial, i.e., since MIS 7, for scenarios 2 and 4.

During the last glacial cycle, starting from the Eemian interglacial at 130 kyr BP (since MIS 5), the cumulative exposure times were 41 and 103 kyr in

scenario 2 and 4, respectively. Correspondingly, the cumulative burial times were 89 and 27 kyr in scenario 2 and 4, respectively. Because the limit of $^{18}\text{O} > 3.7\text{‰}$ was set for the ice sheets of the northern Swedish mountains (Kleman et al., 1997; Kleman et al., 2008) and Finnmarksvidda is believed to have also been covered by ice sheets of the Caledonian mountain range in Norway (Olsen, 1988; Olsen et al., 2013), we tested two additional scenarios. Scenario 1 represents an extreme case of burial, in which we assumed that the Iskorasfjellet ridge was covered by ice sheets during the entire last glacial period (Weichselian), resulting in a cumulative exposure time of only 23 kyr during the Eemian and Holocene, and a cumulative burial time of 107 kyr (Fig. 5-8). We also tested an intermediate burial scenario (scenario 3) in which the Iskorasfjellet ridge is covered only by ice sheets at $^{18}\text{O} > 4.1\text{‰}$, resulting in a cumulative exposure and burial time of 41 and 89 kyr, respectively (Fig. 5-8).

Assuming that no erosion occurred at site Ga1, we iteratively solved equation (5-8) using the different cumulative exposure and burial times of the different scenarios shown in Fig. 5-8. First, we examined the reconstructed glacial history scenarios up to the Eemian interglacial (130 kyr BP). In scenario 1 (complete burial during Weichselian stage), the theoretical accumulated ^{10}Be concentration at site Ga1 was determined to be substantially lower than the measured concentration (difference between theoretical and measured ^{10}Be concentration, $\Delta_{\text{conc.}} = 2.2 \times 10^5 \text{ atoms g}^{-1}$), indicating that the exposure time would not have been long enough to accumulate as much ^{10}Be as was found at site Ga1. We found the smallest difference between theoretical and measured concentration for the considered period in scenario 2 (Scandinavian ice sheet configuration; $\Delta_{\text{conc.}} = 1.0 \times 10^5 \text{ atoms g}^{-1}$). Scenarios 3 and 4 resulted in too high theoretical concentration ($\Delta_{\text{conc.}} = 1.7$ and $3.1 \times 10^5 \text{ atoms g}^{-1}$, respectively), indicating that actual exposure time must have been markedly shorter.

We also tested equation (5-8) over additional glacial cycles, up to MIS 11 (424 kyr BP). The best result, i.e., the smallest difference between theoretical and measured concentration ($\Delta_{\text{conc.}} = 7.1 \times 10^4 \text{ atoms g}^{-1}$), was obtained for scenario 2 when integrating over two glacial periods, the Weichselian and Saalian glaciations, starting from the Bvatajohka interglacial at 243 kyr BP (MIS 7), indicating that the accumulation of ^{10}Be in our study area must have already occurred in the Bvatajohka interglacial. This is consistent with a stratigraphic record northeast of Iskorasfjellet: The stratigraphy at the Gamehisjohka study site (Fig. 5-7) revealed that a layer of fluvial sediments from MIS 7 lies directly on top of bedrock (Olsen, 1988;

Olsen et al., 1996), suggesting that the erosive power of the previous ice sheet during MIS 8 was strong enough to remove deposits from earlier glacials and interglacials, possibly resetting the cosmogenic inventory. However, the stratigraphic record at the Sargejohka study site southwest of Iskorasfjellet contains a paleosol that most likely dates back to MIS 11 (Olsen, 1988; Olsen et al., 1996). Interestingly, the difference between theoretical and measured concentration in scenario 2 over two glacial periods was further reduced when snow shielding was considered, with the extreme snow shielding case yielding the smallest difference ($\Delta_{\text{conc.}} = 2.7 \times 10^4 \text{ atoms g}^{-1}$; see section 'Sensitivity analyses').

Long-term denudation rates using in situ ^{10}Be

We assumed that the inheritance concentration of the smallest Ga1 catchment at the Iskorasfjellet ridge results from long-term accumulation in a landscape with an intermittent glacial cover and zero erosion. Therefore, we attributed the lower concentrations in the larger catchments in our study area to interglacial erosion. As we assumed that all ice sheets were frozen to their beds, we set glacial erosion in all catchments to zero. We also assumed that the interglacial denudation rate D_S was the same during all considered interglacial periods, which allowed us to simplify equation (5-2) to:

$$N_{\text{complex}} = \frac{P}{\lambda + \mu D_S} \left(1 - e^{-(\lambda + \mu D_S) T_{\text{exposure}}} \right) e^{-\lambda T_{\text{burial}}} \quad (5-9)$$

We calculated long-term catchment-wide average interglacial denudation rates based on equation (5-9) under the assumption of zero glacial erosion and using the complex exposure and burial history of scenario 2, dating back to the Bajtjohka interglacial, MIS 7, i.e., setting T_{exposure} and T_{burial} equal to 71 and 172 kyr, respectively.

The calculated denudation rates ranged from 11 mm kyr^{-1} in the Gaskabohki headwater catchment to 25 mm kyr^{-1} in the larger Karasjohka 1 catchment. The denudation rates of all studied catchments are presented in Tab. 5-4. As anticipated from the relation between ^{10}Be concentration and catchment area (Fig. 5-6), the interglacial denudation rate increases with catchment area, reflecting stronger fluvial erosion in the larger catchments, as discussed above. We did not attempt to calculate a denudation rate for the Ga2 sampling site, which is located further upstream of the Ga4 site (which represents the entire catchment also studied in the Pu analysis), because the fluvial network of Ga2 is comparatively poorly developed and therefore reporting a spatially averaged denudation rate would be presumable.

Tab. 5-4: Calculated long-term interglacial catchment-wide average denudation rates. The denudation rates represent a long-term average over all interstadials/interglacials up to the Bajtajohka interglacial, MIS 7, considering an exposure and burial time of 71 and 172 kyr, respectively (refer to scenario 2 in Fig. 5-8). The values in parentheses denote the potential interglacial denudation rates in case the ^{10}Be concentration at the Ga1 site underestimates the inheritance. Accordingly, our calculated interglacial denudation rates should be considered minimum rates. We used a density of 2.1 g cm^{-3} . Ga4: Gaskabohki catchment at the outlet, corresponding to the grid sampled for the Pu analysis; Gu: Guovzilbohki; Ba: Bahkiljohka; Ka1: Karasjohka 1; Ka2: Karasjohka 2.

	Ga4	Gu	Ba	Ka1	Ka2
Interglacial denudation rate (mm kyr^{-1})	11 (-14)	14 (-17)	17 (-20)	25 (-27)	22 (-25)
Interglacial denudation rate ($\text{t km}^{-2} \text{ yr}^{-1}$)	23 (-30)	30 (-36)	35 (-42)	51 (-57)	47 (-53)

We consider the error in the calculated denudation rates due to our assumptions regarding inheritance and reconstructed glacial history to be larger than the error resulting from analytical processing, measurement and production rate scaling. The largest errors result from our key assumptions that the Ga1 site did not experience glacial or interglacial erosion and thus the ^{10}Be concentration at this site is representative of the region's inheritance concentration, and that all catchments did not experience glacial erosion. We explore the implications of a false inheritance assumption in Section 5.4.4.

Sensitivity analyses

While the three smaller catchments associated with Iskorasfjellet are not strongly affected by our chosen elevation averaging approach, the two larger catchments, Karasjohka 1 and Karasjohka 2, show markedly higher denudation rates (by $\sim 5\%$ on average) when examining 100 individual points and their elevations than when considering the elevation averaged over the catchment (Extended Data Fig. 5-3a). This suggests that the non-linear scaling of the ^{10}Be production rate as a function of elevation has a greater influence in the two larger catchments than in the smaller ones. This is likely explained by the difference in altitude being higher in the larger catchments than in the smaller catchments.

When excluding areas from the catchment that do not contain quartz minerals and thereby changing the mean elevation and thus the production rate of the catchment, the three largest catchments, Karasjohka 1, Karasjohka 2, and Bahkiljohka, show increased denudation rates (by up to

5%). The geology of the two headwater catchments, Gaskabohki and Guovzilbohki, consists only of quartz-bearing rock types; hence, the denudation rates of these catchments are not affected by this adjustment (Extended Data Fig. 5-3b). Because denudation of the surface in our study area is primarily related to Quaternary deposits, bedrock geology only plays a subordinate role in identifying areas that contribute quartz grains to the outlet of the catchment. Rather, the mineral composition of the deposited tills should be used as an indicator for this analysis. These data are not available. However, since the average transport length of coarse-grained till clasts based on stone counting and roundness analyses was reported to be about 5-7 km for the northeastern area around Iskorasfjellet (Olsen et al., 1996), we assume that the bedrock geology at least offers an understanding of quartz distribution in the study area. Furthermore, the influence by topographic shielding is negligible for all catchments, as expected for catchments located on the low-relief Finnmarksvidda (Extended Data Fig. 5-3c).

Presuming that current snow heights are also representative of the interstadials and interglacials of the last 243 kyr, and we use a moderate snow density of 0.32 g cm^{-3} , denudation rates decrease by $\sim 3\%$. If snow density remained the same but snow heights increased by 50%, denudation rates would already decrease by about $\sim 5\%$. In an extreme case of 100% increased snow height and a maximum snow density of 0.48 g cm^{-3} , denudation rates would drop by as much as $\sim 10\%$ (Extended Data Fig. 5-3d).

We conclude that the denudation rate of the Gaskabohki headwater catchment, which serves as the long-term, pre-industrial erosion rate for comparison with the current erosion rate determined via $^{239+240}\text{Pu}$, is not significantly affected by the elevation averaging approach for the production rate calculation, nor by consideration of non-quartz geologies or topographic shielding. It would be reduced only by snow shielding, by 3% when considering contemporary snow shielding and by a maximum of 10% when considering an extreme case of snow shielding. Therefore, we likely overestimate the denudation rate of the Gaskabohki catchment by about 3-10%.

The effects on the denudation rates of the Guovzilbohki and Bahkiljohka catchments are similar or only slightly less negative, respectively, than those of the Gaskabohki catchment. Finally, for the denudations rates of the Karasjohka 1 and Karasjohka 2 basins, we propose that the positive effect of both the elevation averaging approach for the production rate cal-

culuation and the consideration of non-quartz geologies is offset by the negative effect of snow shielding. Overall, however, the effects considered above will not constitute the largest error, but our key assumptions of no glacial erosion for all catchments and, in addition, no erosion during interglacial periods for the smallest Ga1 catchment.

5.4 Discussion

5.4.1 Current erosion rates using $^{239+240}\text{Pu}$

Current site-based erosion rates determined from $^{239+240}\text{Pu}$ inventories range from 367 to 645 t km² yr⁻¹ (175 to 307 mm kyr⁻¹), depending on the calculation procedure. Accordingly, the Gaskabohki catchment contains actively eroding sites, mainly located in the sparsely vegetated upslope area. These erosion rates cannot be interpreted as catchment-wide average erosion rates because we could not calculate a soil distribution rate for all the sites that we sampled in a grid scheme because we had to remove the ‘gray box’ sites (Fig. 5-4) from the dataset. Because most of these ‘gray box’ sites are located in the lower part of the catchment near the outlet, we cannot assess how much of the material eroded in the upper part of the catchment is deposited in the lower part and how much is transported out of the catchment.

Our results show that at least the upper part of the catchment has not yet geomorphologically stabilized since deglaciation about 11 kyr BP. This is in agreement with $^{239+240}\text{Pu}$ -derived erosion rates of 260-520 t km⁻² yr⁻¹ reported by Portes et al. (2018) for a young moraine (11.8 kyr) in the Central Rocky Mountains, USA. Average soil production rates for young soils (> 1-10 kyr) in alpine areas range from 119 to 248 t km⁻² yr⁻¹ (Alewell et al., 2015), which, when applied to our results, would imply that erosion rates exceed soil production rates in the Gaskabohki catchment. This is consistent with the relatively short mean soil core length over all sampling sites (14 cm). We therefore assume that active erosion continuously rejuvenates the soils. Since erosion rates have been found to generally decrease substantially over time as soils develop, eventually diminishing to near zero, presumably as a full vegetation cover develops (Portes et al., 2018), we propose that soil development in the sparsely vegetated area of the Gaskabohki catchment has not been sufficient to stop erosion to date.

Erosion rates of ice-cored moraines in a high-latitude permafrost environment on Svalbard, Norway, due to thermokarst, were about 1.5 times (400-940 t km⁻² yr⁻¹; Etzelmüller, 2000) as large as our maximum erosion rates

for the Gaskabohki catchment underlain by sporadic permafrost. In a response to the development of a thermokarst gully, a four orders of magnitude faster erosion rate of 3.5 m yr^{-1} was reported for a watershed in Alaska, USA, underlain by discontinuous permafrost, where soil erosion and ground-ice degradation were insignificant prior to initiation of the thermokarst (Toniolo et al., 2009). In the Gaskabohki watershed, the mean erosion rate determined at the sites that experienced cryoturbation is 17% higher than the mean erosion rate at the sites that were presumably not affected by cryoturbation when both rates were calculated using the default setting in MODERN, i.e., assuming that the Pu inventory was the same over the depth with Pu activity. This suggests that freeze-thaw processes could enhance sediment erosion, but not as intensively as through the pulse disturbances in the above studies. Further studies in alpine areas by Burga et al. (2004), Zollinger et al. (2015) and Zollinger et al. (2017) have shown that vegetation is generally scarce at sites affected by permafrost and that surface disturbance processes such as cryoturbation and permafrost creep appear to prevent the development of a denser vegetation cover, thereby destabilizing the soil. Zollinger et al. (2015), also using $^{239+240}\text{Pu}$ as a soil erosion tracer, reported that permafrost soils are more likely to show erosion, while non-permafrost soils accumulate material.

However, since no surface subsidence due to excess ice melting was simulated for the area in the years 2000, 2050, and 2100 (Lee et al., 2014), and we did not detect any pulse disturbances such as thermokarst in the Gaskabohki catchment, we believe that the major erosional process is rainfall and runoff erosivity, most intensified by snowmelt-generated runoff peaks. At the hillslope compartment, such as at the hillslope of the Gaskabohki headwater catchment, diffuse overland flow across the slope surface governs sheet erosion (Tananaev and Lotsari, 2022). Rills formed by rainfall runoff are primarily fluvial landforms largely unaffected by frozen ground (Tananaev and Lotsari, 2022). Since 25 of 37 soils at 'true' erosion sites (lower two quadrants in Fig. 5-4) have most likely not experienced cryoturbation over the past ~60 years, the importance of permafrost as one of the potential drivers of erosion has diminished. Drillings at the hilltop of Iskorasfjellet in the summers of 2007 and 2008 corroborate this assumption, as they showed that the active layer was more than 10 m and 7 m deep, respectively (Christiansen et al., 2010). Instead, potentially high snowmelt-generated runoff peaks, combined with soils that are not yet stabilized due to a sparse vegetation cover in the upstream area, could explain the comparatively high erosion rates in the Gaskabohki catchment, as the area west of the main stream channel has a comparatively well-

developed system of meltwater channels (Fig. 5-5a). Beylich (2009) emphasized the importance of snowmelt-generated runoff peaks for fluvial suspended sediment transport in low-relief Arctic areas, as he found for a catchment (18 km²) northeast of our study area in northernmost Finnish Lapland that 87% of the mean annual total mechanical denudation occurred during the annual snowmelt-generated peak runoff from 2002 to 2007. Rainfall-generated runoff peaks gain importance for mechanical denudation in steeper, less vegetated catchments (Beylich, 2009).

5.4.2 Increased adsorption of Pu by fine earth fraction

We found that about half of the sites are characterized by high, sometimes very high, Pu inventories that cannot be explained by plausible sediment transfer behavior ('gray box' sites in Fig. 5-4). We proposed that 'pure Pu', i.e., highly concentrated Pu associated with no or little mass transport, was deposited at these sites.

In a linear regression analysis with the 'gray box' sites, the parameters fine earth fraction and bulk density were not found to be significant predictors at the 0.05 significance level, but they showed Pearson correlation coefficients of 0.28 and -0.26, respectively. Accordingly, it appears that the Pu inventory increases with decreasing particle size. This trend is also evident when the 'gray box' sites are compared to the 'true' erosion and deposition sites that exhibit plausible sediment transfer behavior and are characterized by distinctly lower total Pu inventories (Fig. 5-9a). 'Gray box' sites show a higher fine earth fraction and a lower bulk density than the 'true' erosion and deposition sites (Fig. 5-9b and c). In agreement with our findings, Xu et al. (2017) reported that finer soil particles bind more Pu, and attributed this mainly to the larger specific surface area of finer soil particles.

The soils of the 'gray box' sites most likely already had a larger fine earth fraction during Pu fallout about 60 years ago than the soils of the 'true' erosion and deposition sites. Varying proportions of fine earth fraction between the two types of sites can be explained by the fact that they are located in areas with different properties. While the 'true' erosion and deposition sites are mainly located in the upper, sparsely vegetated part of the catchment, the 'gray box' sites are more likely to be found in the lower part of the catchment, which is covered with moors and heaths (Fig. 5-5). This difference in vegetation and topography is also reflected in a higher excess green index and a lower elevation of the 'gray box' sites, respectively, com-

pared to the 'true' erosion and deposition sites (Fig. 5-9e and f). Preferential transport of fine earth particles enriched with high levels of Pu down the hillslope in the catchment may intensify the accumulation of fine earth particles in the lower part of the catchment. In contrast to the transport of very coarse-grained material in steep, alpine catchments, a slow transport of fine-grained material occurs in catchments with lower gradients (Olsen et al., 2013). Since vegetation is known to trap eroded sediment from upslope (Sanchez and Puigdefabregas, 1994; Chappell et al., 1999; Rey, 2004), the more abundant vegetation in the downslope area of the Gaskabohki catchment could be responsible for the enhanced accumulation of the fine earth particles in the soils of the 'gray box' sites. Chappell et al. (1999) also found a general increase in the proportion of fine silt in the soil downslope.

Although the fine earth fraction, along with the presence of minerals oxides, are recognized as supporting factors for the occurrence of Pu in the soil, the organic matter content is considered the most important factor (Chawla et al., 2010; Meusburger et al., 2016; Alewell et al., 2017; Loba et al., 2022). The strong affinity of Pu for organic matter can be explained by the fact that in strongly acidic or anoxic soils organic compounds reduce Pu(V) and Pu(VI) to immobilized Pu(III), which is then often present as an organic complex (Nelson and Lovett, 1978; Choppin, 2006; Alewell et al., 2017). The higher oxidation states of Pu, Pu(V) and Pu(VI), are about two to three orders of magnitude more soluble than the lower oxidation states, Pu(III) and Pu(IV) (Nelson and Lovett, 1978). We cannot observe this in our dataset, as the Pearson correlation coefficient in the linear regression analysis of total Pu inventory as a function of organic matter content for the 'gray box' sites is close to 0, and no marked difference in organic matter content between 'gray box' and 'true' erosion and deposition sites is apparent (Fig. 5-9d). Nevertheless, soil pH may have been lower in the heath area downslope than in the sparsely vegetated area upslope, which could have led to the reduction of the higher oxidation states of Pu to the lower ones and resulted in increased immobilization and accumulation of Pu in the 'gray box' sites. Unfortunately, because we did not determine soil pH, we were unable to test this possibility.

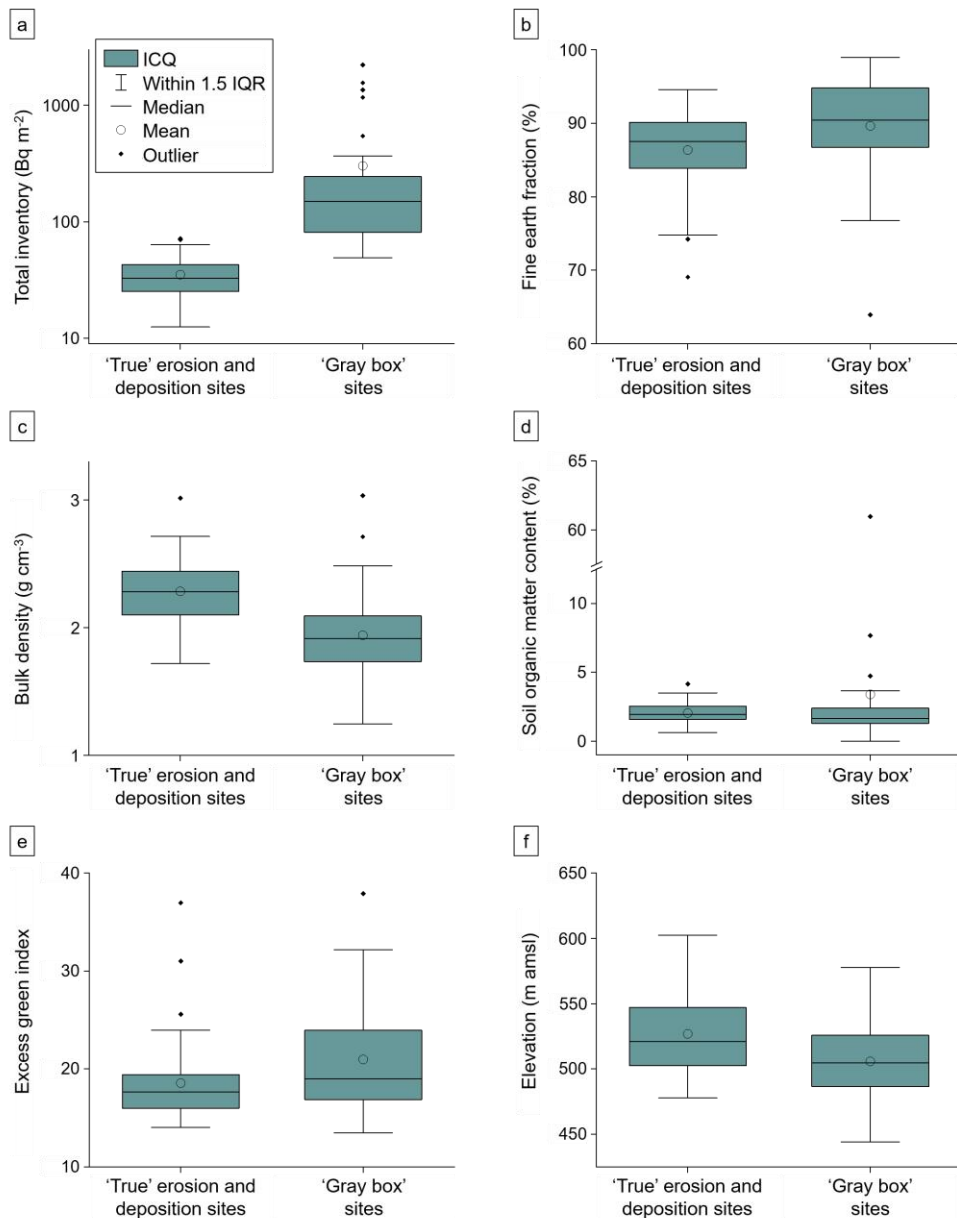


Fig. 5-9: Comparison of Pu total inventory, and soil and topographic properties between ‘gray box’ sites and ‘true’ erosion and deposition sites in the Gaskabohki catchment. The descriptions ‘gray box’ sites and ‘true’ erosion and depositions sites refer to the occurrence of these sites in the upper left quadrant and in the remaining three quadrants, respectively, in Fig. 5-4. As the description implies, we assume a plausible sediment transport behavior from erosional to depositional sites for the ‘true’ erosion and deposition sites, since they do not show a higher Pu total inventory than the mean value over the reference sites at a lower depth with Pu activity when compared to the reference sites (see Fig. 5-4). In contrast, the ‘gray box’ sites have higher, in some cases markedly higher, Pu inventories at a lower depth with Pu activity when compared to the reference sites. ‘Gray box’ sites show a higher (a) Pu total inventory and (b) fine earth fraction than the ‘true’ erosion and deposition sites. (c) ‘Gray box’ sites show a lower bulk density than the ‘true’ erosion and deposition sites. (d) The two types of sites show a similar organic matter content. (e) The higher excess green index and (f) the lower elevation at the ‘gray box’ sites indicate that these sites are located mainly in the lower part of the Gaskabohki

catchment, which is characterized by moors and heathland. In contrast, the 'true' erosion and deposition sites are located mainly in the upper part, which is characterized by a sparse vegetation (Fig. 5-5a). Boxes indicate 0.25 and 0.75 quantiles (i.e., interquartile range (IQR)), whiskers indicate the range within 1.5 times the IQR, and circles and black diamonds show the arithmetic means and outliers, respectively.

Another explanation for the very high Pu inventories in the downstream area of the Gaskabohki watershed could be the presence of snow during the winter months. When Pu was deposited onto the snowpack during fallout, it was not brought into the soil until the snow melted. On the Finnmarksvidda, the mean annual number of days with dry snow is usually between 150 and 200, and the mean fraction of snow of the total precipitation sum is about 40% (Martin et al., 2019; Seklima, 2020). Therefore, we propose that due to the main wind directions to the south and north (Chekushin et al., 1998), snow from the hilltops could have been transported by wind drift northward into the lower part of the catchment, where it accumulated (Fig. 5-5b). When the snow melts, a particularly large amount of Pu is brought into the soil there. Furthermore, the water derived from snowmelt may not infiltrate the underlying soil directly, but leaves the catchment rapidly as surface runoff. This effect is especially pronounced when the soils are frozen (McNamara et al., 1997). The 'gray box' sites are primarily located in an area in the lower part of the watershed, east of the main river, that does not show meltwater channels, suggesting that there, compared to the rest of the watershed, which is pervaded with many meltwater channels (Fig. 5-5a), water may increasingly infiltrate into the ground after snowmelt instead of going directly to runoff. Usually, only the FRN ^{137}Cs , originating mainly from the Chernobyl accident, is thought to be susceptible to a patchy spatial distribution in colder regions such as the Swiss Alps due to snowmelt, as the fallout from the Chernobyl accident occurred when the mountains were still snow-covered (Alewell et al., 2014; Loba et al., 2022).

The FRN $^{239+240}\text{Pu}$ is generally considered a suitable soil erosion tracer due to its rapid adsorption in the topsoil (Loba et al., 2022). However, our study revealed that even within a small catchment ($< 1 \text{ km}^2$), the accumulation of Pu in soil after fallout can be very heterogeneous, potentially due to (i) different oxidation-reduction conditions in areas of varying vegetation extent, (ii) preferential transport of fine particles with supposedly extremely high Pu concentrations downslope, and/or (iii) a spatially heterogeneous snow accumulation and meltwater runoff; rendering about half of the sampled sites unsuitable for the investigation of soil distribution rates. Accordingly, we propose that the Pu inventory in soils at about half of the sites was influenced more by chemical or hydrological processes than by actual

soil erosion processes after adsorption to the soil. Moreover, we suggest that future studies use a smaller first increment at the sampling sites, as our first increment of 12 cm did not allow us to more closely examine the Pu depth profile relative to other parameters such as the fine earth fraction. Finally, soil pH should also be recorded so that potentially elevated Pu inventories might be explained by changes in soil pH.

5.4.3 Long-term denudation rates using in situ ^{10}Be

Long-term catchment-wide average interglacial denudation rates determined from in situ ^{10}Be concentrations range from 23 to 51 t km² yr⁻¹ (11 to 25 mm kyr⁻¹) in the studied catchments, assuming no glacial erosion. Other ^{10}Be -derived catchment-wide average denudation rates in the Arctic exist for the large rivers Mackenzie and Lena, which were determined to be about five times higher than our highest rate (Wittmann et al., 2020). Wittmann et al. (2020) suggested that the sediments from the Lena River contained material fractions from both cold-based and warm-based glaciers. Our long-term rates are about two to five times as high as contemporary rates determined from suspended sediment yield data of rivers on the Siberian (tributaries of the Lena) and Canadian Shield (tributaries in the Grenville Province; Summerfield and Hulton, 1994; Millot et al., 2002; West et al., 2005). Tributaries in the Slave Province on the Canadian Shield and a smaller catchment (18 km²) in northernmost Finnish Lapland on the Fennoscandian Shield are characterized by very low contemporary denudation rates of 3.2 and 0.25 t km² yr⁻¹, respectively (Millot et al., 2002; West et al., 2005; Beylich, 2009). Beylich (2009) argued that contemporary fluvial sediment transport in Arctic low-relief areas was limited by sediment availability. We explain the higher denudation rates determined for the catchments in our study area with the markedly longer averaging window, which most likely also included periods with higher erosion rates. Because our rates integrate multiple interglacial/interstadial periods, the catchments were likely highly susceptible to fluvial erosion shortly after each deglaciation due to low vegetation and unstable sediment structures (Ballantyne, 2002).

Although denudation rates in the catchments we studied were probably temporarily higher directly after deglaciation than present-day rates determined for catchments in Northern Hemisphere cratonic areas, they were probably not nearly as high as in postglacial landscapes characterized by substantially steeper slopes, such as in the western margin of the Jura Mountains in France. There, postglacial rivers incised fine-grained glaciolacustrine deposits, resulting in extremely high erosion rates between about 18 and 6 kyr BP, on the order of 2,500 t km⁻² yr⁻¹ (Campy et al.,

1998), two orders of magnitude greater than the rates we determined for the studied catchments on the low-relief Finnmarksvidda.

5.4.4 Uncertainties in determining interglacial denudation rates

As the interglacial denudation rates were calculated using the cumulative exposure and burial times according to the reconstructed glacial history based on the ^{10}Be concentration of the Ga1 site on the Iskorasfjellet ridge, which was assumed to be a first-order approximation of the inheritance concentration, the largest uncertainty results from an underestimation of the inheritance at that site. If we exercise the scenario that the very small Ga1 catchment along the ridge did experience interglacial erosion, then the actual inheritance concentration would be higher. Accordingly, the exposure time must have been longer to accumulate ^{10}Be over a longer period. Scenario 3 of complex exposure and burial history (Fig. 5-8), in which ice sheet cover was present only at $\delta^{18}\text{O} > 4.1\text{‰}$, allows for a longer cumulative exposure time than the applied scenario 2. In this scenario 3, the theoretical inheritance concentration would be 5.4×10^5 atoms g^{-1} , or 1.5 times the measured concentration of the Ga1 site, resulting from accumulation during an exposure time of 82 kyr and continuous decay over the last glacial cycle, beginning with MIS 5 at 130 kyr BP. In this scenario, rates would be higher by about 3 mm kyr^{-1} in all basins studied (Tab. 5-4), resulting in an increasing percentage error with decreasing basin size. Accordingly, the largest percentage error is associated with the denudation rate of the Gaskabohki catchment at about 24%. In conclusion, an underestimation of the inheritance along the Iskorasfjellet ridge would lead to a systematic underestimation of the erosion rates, therefore we consider our long-term interglacial erosion rates as minimum rates.

The assumption that all ice sheets were frozen to their beds, and thus that a glacial erosion rate of zero prevailed over the entire period considered, was central to our overall interpretation of long-term interglacial erosion rates. We believe that this assumption holds true at least for the smaller catchments associated with Iskoras (see section 'Indications of no glacial erosion at Iskoras'), because there we found no bare bedrock or stream-lined features, but a rectangular drainage pattern, a thick Quaternary deposits cover, and tor-like features. However, since we found some stream-lined features in the western part of our study area, we cannot reject glacial erosion in the two larger catchments, Ka1 and Ka2. This speculation could be corroborated by the fact that the second largest catchment, Ka1, has a slightly lower concentration than the largest catchment, Ka2, violating the

stringent decrease in concentration with increasing catchment size suggested by the power law fit in Fig. 5-6. For Ka1 is proportionally more strongly affected by the glacially streamlined area than the larger Ka2 catchment (Fig. 5-7). Thus, the lower concentration in the Ka1 catchment could be explained by limited glacial erosion. As this area falls within deglaciation fan 24 of Kleman et al. (1997), it is likely that the erosion occurred during the retreat of the Fennoscandian ice sheet during the last deglaciation.

5.4.5 Comparison of current and long-term erosion rates in the Gaskabohki catchment

Due to the highly heterogeneous spatial distribution of $^{239+240}\text{Pu}$ in the Gaskabohki catchment, which cannot be explained by soil transport behavior (alone), we could not calculate a catchment-wide average current (post-1960) erosion rate from all gridded sampling sites. Instead, we determined a mean erosion rate of $184 (\pm 114) \text{ mm kyr}^{-1}$ from all plausible ('true') erosion sites, which can be considered a maximum value for the entire watershed. Calculation of the long-term catchment-wide average denudation rate was based on assumptions about inheritance, which specified the reconstruction of the complex exposure and burial history of the landscape over several glacial periods. This long-term interglacial catchment-wide average denudation rate of 11 mm kyr^{-1} (with an uncertainty of about 24%) should be regarded a minimum due to possible underestimation of the inheritance concentration.

Consequently, we compare a maximum current erosion rate of $184 (\pm 114) \text{ mm kyr}^{-1}$ with a minimum long-term erosion rate of 11 mm kyr^{-1} . The discrepancy is exacerbated by the fact that Pu is preferentially adsorbed to the finest earth fractions, and Be was measured from the medium to coarse sand fraction (400-630 μm). Since transport of fine-grained material is preferred over transport of coarser-grained material in catchments with a comparatively low relief (Olsen et al., 2013), such as catchments on the Finnmarksvidda, the Pu-adsorbed material was probably transported faster than the denuded grains containing in situ ^{10}Be . However, because erosion rates derived from ^{10}Be account for total mass loss (chemical and detritus), i.e., total denudation, the physical erosion rate is overestimated. Dixon and Blanckenburg (2012) found that globally physical erosion accounts for about 50-90% of total denudation. For Swedish Lapland, it was reported that the chemical weathering rates are similar to those in milder climates (Darmody et al., 2000; Darmody et al., 2007; Dixon, 2013). Thus, if we also

assumed active chemical weathering for the Gaskabohki catchment, contributing 50% of the total denudation, the potential underestimation due to inheritance would be compensated.

Despite the caveats and uncertainties associated with both rates, we conclude that erosion in the Gaskabohki catchment has very likely increased over the past ~60 years relative to a long-term interglacial baseline because the difference between the two rates is about an order of magnitude. Possible causes for the increase in erosion in the Gaskabohki catchment could be an increase in rainfall erosivity and permafrost thaw-enhanced erosion. That precipitation erosivity may have increased in recent years can be attributed to increased precipitation, as shown by the 117% and 237% increase in monthly summer and winter precipitation sums, respectively, over the last six years alone (longest available record at Iskorasfjellet) compared to the climate normal (1961-1990). In the wider Arctic, total annual precipitation increased by 24% from 1971 to 2019 (AMAP, 2022). The rapidly thawing permafrost in the Gaskabohki catchment may also have contributed to increased erosion by deepening the active layer. However, as no pulse disturbances such as thermokarst leading to strong erosional events were detected in the watershed, permafrost thaw could also lead to a reduction in soil erosion. As the thickness of the active layer increases, the water storage capacity increases, resulting in reduced surface runoff and increased subsurface flow (Woo, 1983), thereby reducing soil erosion. Possibly, the shortening of the freezing season could also have led to an increase in soil erosion. Because there are no runoff data for the watershed, we cannot comment on the effects of a potential change in the intensity of rainfall- or snowmelt-generated runoff on erosion.

5.5 Conclusions

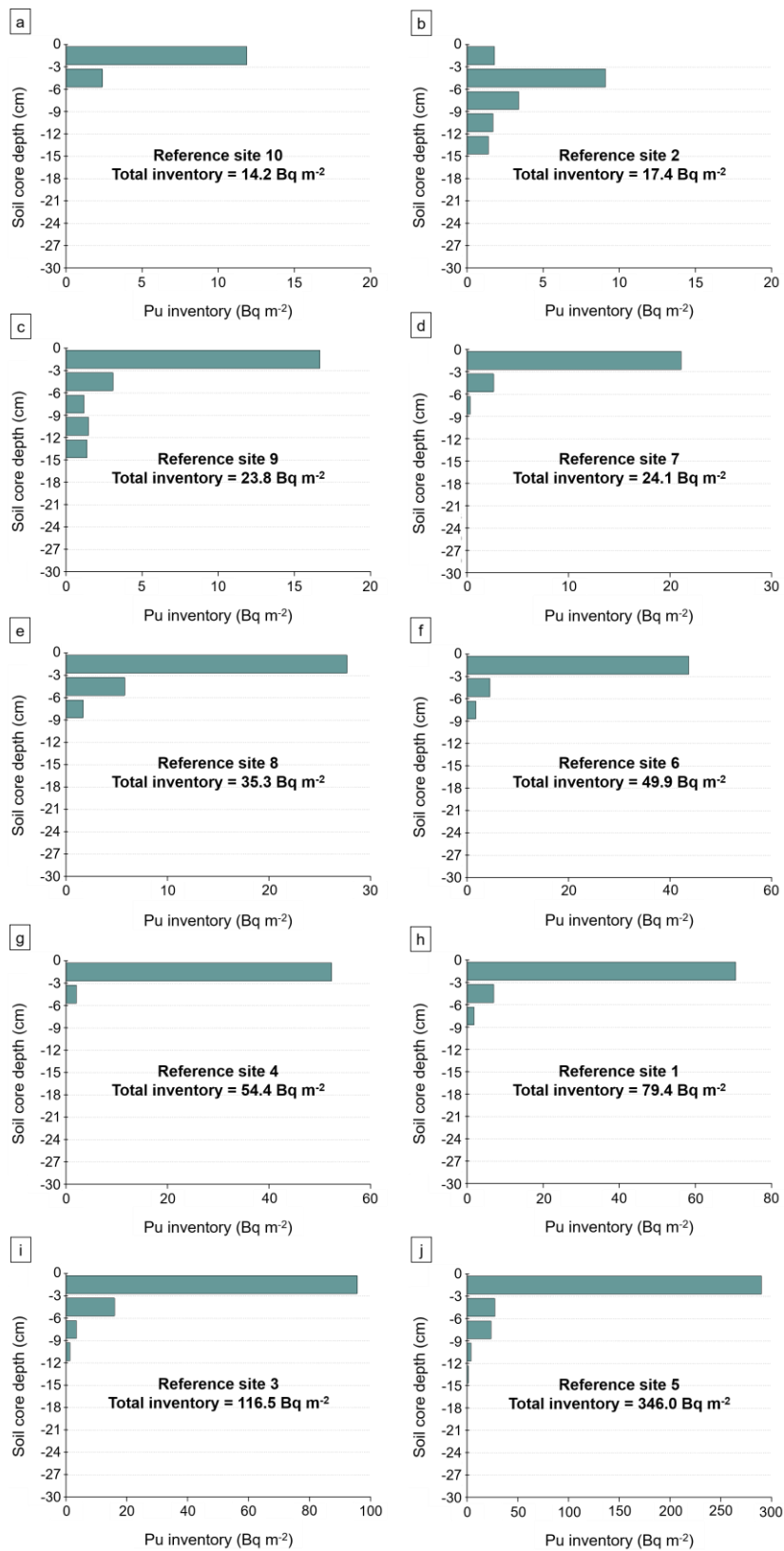
In the present study, we show that erosion in a subarctic headwater catchment on the Finnmarksvidda plateau in northern Norway has most likely increased over the past ~60 years. From $^{239+240}\text{Pu}$ inventories in soils at erosion sites ($N = 37$), we determined a mean maximum current (post-1960) erosion rate of $184 (\pm 114) \text{ mm kyr}^{-1}$, and from in situ ^{10}Be in stream sediments at the outlet of the catchment, a minimum interglacial denudation rate of 11 mm kyr^{-1} (with an uncertainty of about 24%), integrating over the last 243 kyr.

We have shown that the deployment of $^{239+240}\text{Pu}$ as a soil erosion tracer may not be appropriate for Arctic catchments similar to ours because the

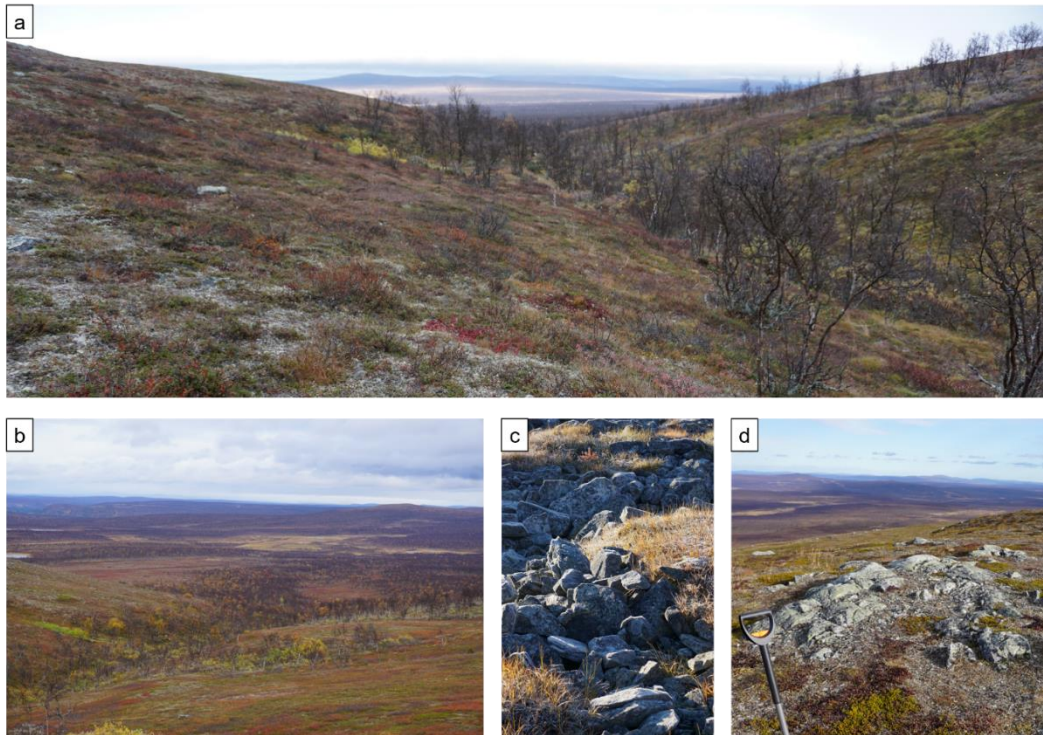
accumulation of Pu in soil after fallout can be very heterogeneous. We attributed the large discrepancies in Pu inventories among sampling sites to different oxidation-reduction conditions in areas with different vegetation extent, preferential transport of fine particles with presumably extremely high Pu concentrations downslope, and/or spatially heterogeneous snow accumulation and meltwater runoff. From the analysis of in situ ^{10}Be concentrations, we concluded that all studied catchments (0.2 to 7,255 km²) on the Finnmarksvidda reflected inheritance, confirming the general agreement on cold-based, non-erosive Fennoscandian ice sheets over the central sector of Fennoscandia (Kaitanen, 1969; Kleman et al., 1997; Kleman et al., 2008; Ebert et al., 2015; Stroeven et al., 2016).

We discussed that the soils of the current erosion sites, which are mainly located in an area with sparse vegetation, are not yet stabilized. We hypothesized that the comparatively high current erosion rates for a watershed located on the Fennoscandian Shield are probably due to increased rainfall erosivity due to on-going climate change combined with soils that are not yet stabilized due to a sparse vegetation cover. As climate change progresses, both vegetation extent and precipitation intensity are projected to increase in the Arctic (Meredith et al., 2019), with the former having a negative impact and the latter a positive impact on erosion rates. Currently, the upper part of the Gaskabohki catchment is sparsely vegetated and erosion is active. It is difficult to assess when (or even if) the soil stabilizing effect of an increased vegetation cover will dominate over an increased rainfall erosivity. Shelef et al. (2022) derived a threshold response of erosion rate to vegetation-related proxies from a sediment record of an Arctic lake in Alaska, suggesting that at a certain extent of vegetation, the erosion rate will decrease rather quickly. However, currently 78% of the Gaskabohki catchment and 23% of the entire study area, or 1,700 km², are characterized by a sparse vegetation cover (CLC, 2018), indicating that erosion is widespread on the Finnmarksvidda despite the low relief. As annual fluvial energy in the Arctic is currently shifting from skewed (snowmelt-dominated) to multimodal (snowmelt- and rainfall-dominated) distributions, Arctic material transfer regimes are fundamentally changing and increased precipitation in late summer could enhance terrestrial-aquatic connectivity for particulate material fluxes (Beel et al., 2021). Our finding of increased current erosion suggests that parts of the Fennoscandian Shield might have moved from a possibly supply-limited weathering regime to a kinetically limited one, potentially increasing terrestrial alkalinity generation, and thus CO₂ drawdown.

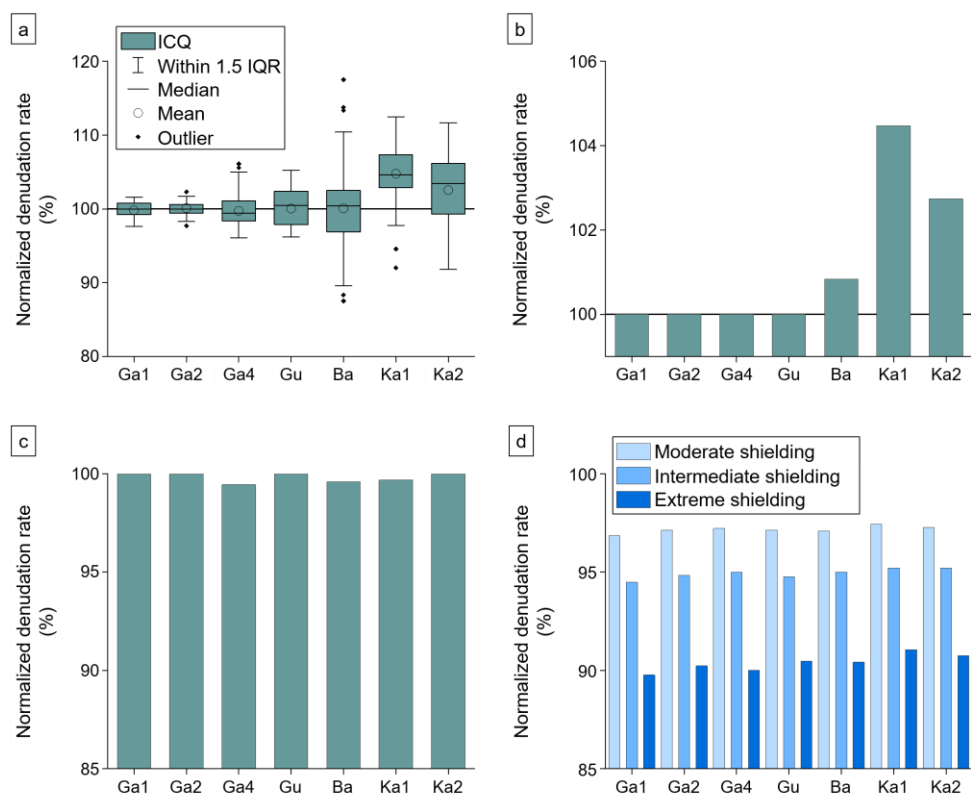
5.6 Supplementary material



Extended Data Fig. 5-1: Pu depth profiles of the reference sites. The graphs are sorted from the reference site with the lowest (a) to the site with the highest (j) total inventory.



Extended Data Fig. 5-2: Postglacial landscape with relict non-glacial features in the Gaskabohki catchment. (a) and (b) The Gaskabohki stream runs through a v-shaped valley. (c) Mainly angular boulders are found upstream in the main streambed. (d) A tor-like feature on the ridge of Iskorasfjellet: The longer side is oriented in a west-east orientation and has some striations in this direction. This striae could have resulted from an iceflow in this direction during the Early Weichselian, or possibly even during a Saalian ice flow stage (Olsen, 1988).



Extended Data Fig. 5-3: Relative changes in denudation rate by (a) using multiple point elevations within the catchment instead of using the mean, (b) excluding areas that do not contribute quartz grains, (c) applying topographic shielding, and (d) applying varying degrees of snow shielding. All values shown here were normalized to the mean denudation rates calculated using the mean elevations of the catchments and without applying any shielding corrections. A value of 100% means that none of the corrections applied in (a) to (d) caused a change in denudation rate and that the simplified averaging approach we used is acceptable. Ga: Gaskabohki with Ga4 at the outlet of the catchment and Ga1 and Ga2 upstream of Ga4; Gu: Guovzilbohki; Ba: Bahkiljohka; Ka1: Karasjohka 1; Ka2: Karasjohka 2. **(a)** We created 100 points randomly distributed in each watershed and calculated denudation rates for each of these points using the corresponding point elevations. Boxes indicate 0.25 and 0.75 quantiles (i.e., interquartile range (IQR)), whiskers indicate the range within 1.5 times the IQR, and circles and black diamonds show the arithmetic means and outliers, respectively. **(b)** We excluded the areas from each catchment that are underlain by metagabbro, ultramafic volcanic rock, albitite/scapolite, amphibolite gneiss, or amphibolite because those rock types do not contain quartz minerals. This leads to a new mean elevation of the catchments, which in turn affects production and denudation rates. **(c)** We applied a mean topographic shielding correction factor. **(d)** We applied varying degrees of snow shielding: (i) moderate shielding based on contemporary mean monthly snow heights and an assumed snow density of 0.32 g cm^{-3} , (ii) intermediate shielding based on snow heights 50% thicker than the contemporary ones and an assumed snow density of 0.32 g cm^{-3} , and (iii) extreme shielding based on snow heights 100% thicker than the contemporary ones and an assumed snow density of 0.48 g cm^{-3} .

6 Conclusions

In this conclusion, I will first outline the answers to the research questions I set in this thesis and highlight the key scientific advances. An overview of the chapter-specific results is provided in Fig. 6-1. Lastly, I will make suggestions for future work to close remaining knowledge gaps.

6.1 Answers to research questions

- 1) Is erosion rate a controlling factor on terrestrial alkalinity generation at the global scale?
 - If so, what are the dependencies between erosion rate and terrestrial alkalinity generation?

In Chapter 3, I showed that erosion rate is a first-order controlling factor on terrestrial alkalinity generation at the global scale. I demonstrated this by developing an empirically-based model from global (44°S to 51°N) riverine alkalinity data and ¹⁰Be-derived erosion rates. In addition to erosion rate, I included areal proportion of carbonate, MAT, catchment area, and soil thickness as covariates, demonstrating their first-order influence on alkalinity generation. I found that a non-linear relation characterizes erosion rate and terrestrial alkalinity generation, with alkalinity best modeled by a second-order polynomial of erosion rate. I identified a regime of '*efficient erosion rate*' at slow to intermediate erosion rates that also represents the optimum of the alkalinity-erosion rate function and is thus associated with the highest alkalinity generation.

This represents the first global assessment of controlling factors on alkalinity generation based on actual measurements of erosion rates, confirming that erosion rate is a driver of alkalinity generation globally. This has previously only been proven regionally. However, the compilation lacked erosion rates from high latitude systems, which prevented extrapolation to the entire land surface area. The extrapolation was also limited because the training data on catchment area and soil thickness were confined and certain combinations of different covariates were under-represented.

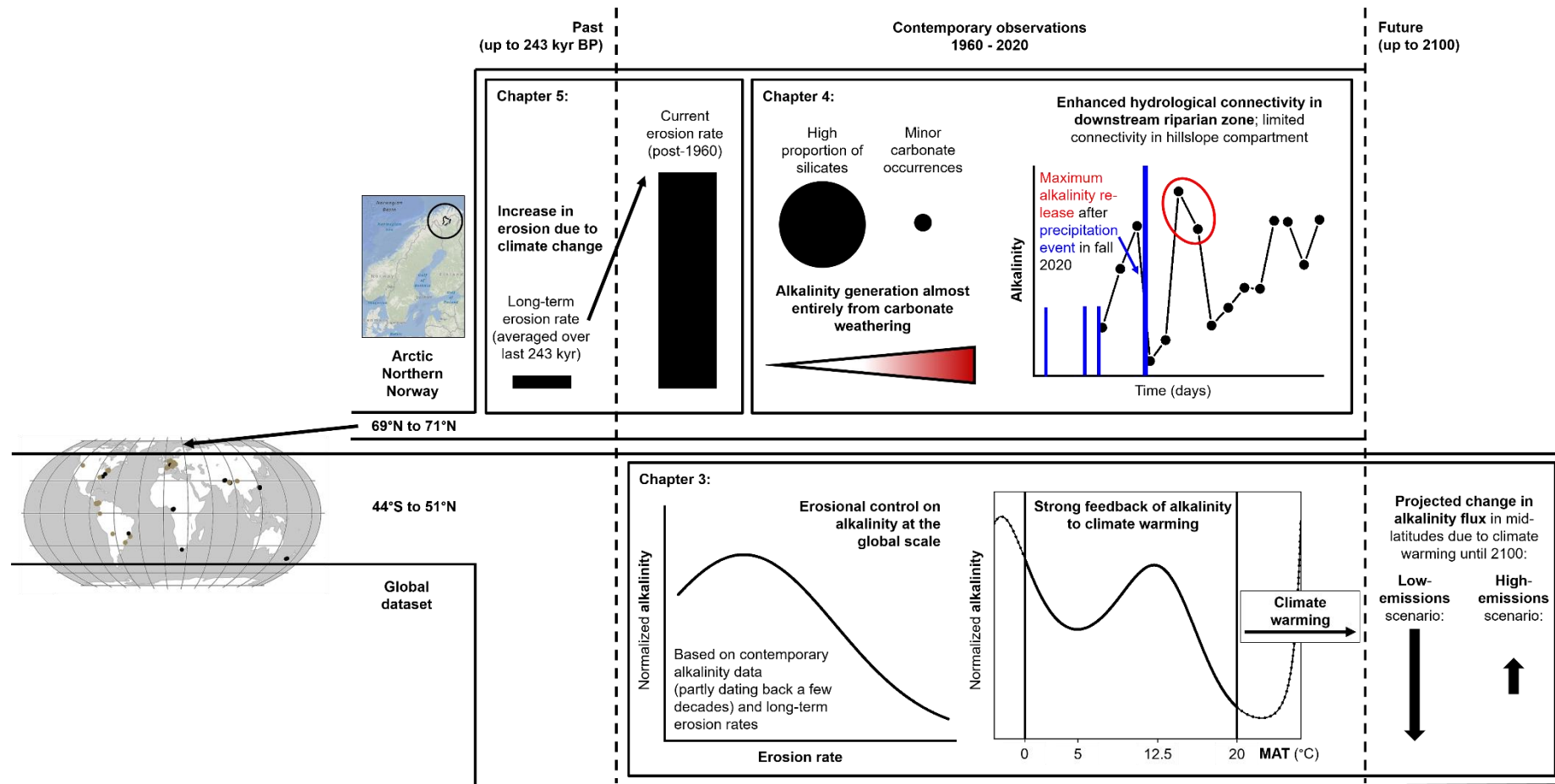


Fig. 6-1: Overview of the chapter-specific results of this thesis, sorted by latitude and time scale. While the results of Chapter 3 were derived from a global compilation, the results of Chapters 4 and 5 displayed in this figure relate to an Arctic headwater catchment on the Finnmarksvidda, Northern Norway.

Furthermore, I was able to separate climatic (MAT) from erosional influences and provided evidence that the weathering flux to the ocean will be significantly altered by climate warming as early as the end of this century. Thereby, both direction and accentuation of the change in alkalinity fluxes strongly depend on the evolution of climate, exemplified by projected emissions scenarios, resulting in either a strengthening or a weakening of the weathering-liberated alkalinity flux, and thus of the oceanic CO₂ buffer.

- 2) What is the influence of environmental forcing on alkalinity release in a small Arctic headwater catchment in a degrading permafrost landscape during fall? In particular:
- Is the primary pathway for alkalinity generation the weathering of silicate minerals?
 - How is alkalinity release hydrologically controlled in this hillside catchment underlain by sporadic permafrost?

In Chapter 4, I answered these questions by analyzing AT and DIC concentrations, stable isotope signatures of DIC and H₂O, and dissolved cation and anion loads from water samples collected in the Gaskabohki headwater catchment on the Finnmarksvidda in Northern Norway in the fall of 2020. Although the catchment is mainly underlain by silicates as the alkalinity-bearing lithology, I identified the weathering of minor carbonate occurrences as the primary pathway for alkalinity generation. Moreover, I identified two key catchment units – a downstream carbonate-enriched riparian zone and a silicate-dominated hillslope – that showed different degrees of hydrological connectivity. In addition to its advantageous lithological properties, I found that the riparian zone, if undisturbed, controlled the alkalinity release of the entire catchment due to its enhanced hydrological connectivity. I suggested that increased soil moisture and shallower water tables near the stream enabled both the transport of weathering agent, in the form of soil respired CO₂, to the weatherable material and the transport of weathered products from the groundwater to the stream. In contrast, weathering load contribution from the hillslope was most likely limited by insufficient contact time of weathering agent and weatherable material. Finally, I showed that the riparian zone responded more quickly and intensely to a precipitation event than the hillslope. However, immediately after the precipitation event, the control of the riparian zone on alkalinity release was temporarily reduced as the AT signal was diluted by surface runoff.

With the study presented in Chapter 4, I added observational data on alkalinity to the generally sparse record for small Arctic catchments. By discussing the release of alkalinity following a rainfall event, which is projected to increase substantially with on-going climate change in the Arctic (Meredith et al., 2019), I have contributed to a better process understanding of inorganic carbon dynamics in the Arctic. However, as I only sampled a narrow time window during one season, I was unable to examine changes in alkalinity concentration and flux over a longer period, preventing me from determining if only the transport rate changed or if the actual weathering rate changed as well.

- 3) Has the erosion rate in a small Arctic headwater catchment in a degrading permafrost landscape increased in the last few decades due to contemporary climate change?

In Chapter 5, despite the uncertainties associated with both rates, I argued that the erosion rate in the Gaskabohki catchment has most likely increased due to contemporary climate change, as I determined the difference between a post-1960 current erosion rate derived from $^{239+240}\text{Pu}$ and a long-term denudation rate derived from in situ ^{10}Be to be about an order of magnitude. I suggested that the elevated erosion is likely due to a combination of increased rainfall erosivity and the presence of erodible soils that are not yet stabilized due to a sparse vegetation cover. However, rapidly thawing permafrost could also have been a (further) cause.

This study represents one of the first quantifications of a change in erosion attributable to current climate change over several decades in a small Arctic catchment characterized by gradual degradation of sporadic permafrost. The calculated long-term denudation rates derived from ^{10}Be in stream sediments represent the first Arctic rates for intermediate- and small-sized catchments and extend the few records of long-term catchment-wide average denudation rates in Arctic watersheds. In contrast to the erosion rates of more than 500 mm kyr^{-1} of alpine catchments with a similar MAT in the study in Chapter 3, the erosion rates I determined for catchments on the Fennoscandian Shield are distinctly lower, underlining again the urgent need for Arctic catchment-wide average erosion rates. By providing these rates, I was able to begin to fill the data gap identified in Chapter 3.

As climate change progresses, both vegetation extent and precipitation intensity are projected to increase in the Arctic (Meredith et al.,

2019), with the former having a negative impact and the latter a positive impact on erosion rates. It remains unclear when (or even if) the soil stabilizing effect of an increased vegetation cover will dominate over an increased rainfall erosivity. Lastly, the increased erosion rate due to climate change that I found does suggest that alkalinity generation may have already changed or may still respond with a change in the future. However, I could not verify the former because there were no ancillary records of alkalinity since 1960.

6.2 Outlook

The study in Chapter 3 revealed that alkalinity generation from weathering of carbonates reacts strongly to a change in MAT. It demonstrated that mid-latitude alkalinity fluxes to the ocean will be significantly altered by the end of this century due to climate warming. However, as the study did not include data from the Arctic, but climate warming is strongest there, the possibly largest change in alkalinity flux was not quantified. As high-latitude catchments in North America and Asia contain substantial amounts of carbonate rock outcrop, a potential increase in alkalinity flux contributions due to increasing temperatures from these regions could constitute a sudden negative feedback to anthropogenic CO₂ emissions, and might greatly affect the global budget. I therefore advocate an extension of the dataset encompassing both alkalinity concentrations and ¹⁰Be-derived long-term erosion rates. I suggest that data points in the Arctic be added to the dataset primarily in such a way that ¹⁰Be-derived erosion rates are determined for catchments for which alkalinity datasets already exist, ideally encompassing several decades. Determining erosion rates using ¹⁰Be is more laborious and costly than determining alkalinity concentrations, but weathering may have already responded to fast-advancing climate change in the Arctic, such that a climate change biased situation might be examined if alkalinity were sampled. In addition, this dataset would benefit from an inclusion of catchments characterized by thick saprolites and catchments with both high MAT and high areal carbonate proportion (> 40%).

By showing in Chapter 4 that weathering of minor carbonate occurrences is the major source of alkalinity generation in a small silicate-dominated catchment on the Finnmarksvidda in Northern Norway, I have demonstrated that the vast Fennoscandian Shield may respond to climate change with a more rapid feedback of alkalinity generation from accessory carbonates than would be expected for an area that is underlain primarily by the slower-responding silicate minerals. However, since I also found that

the ratio of sulfuric acid- to carbonic acid-induced weathering of carbonate minerals increased with catchment size, indicating that carbonate weathering in the studied region not only consumes CO₂ but also releases CO₂, albeit to a lesser extent, my findings for the small Gaskabohki catchment may not be easily transferable to the Fennoscandian Shield. Accordingly, I argue for further studies of alkalinity generation and release in other areas of the Fennoscandian Shield with different catchment characteristics such as land cover, permafrost extent, and catchment size at different times of the year, ideally over a longer observation window of several years. As cause attribution in alkalinity flux change, i.e., resolving the sum signal into its individual components of change in weathering and change in discharge, remains a pivotal knowledge gap, studies that address the separation of weathering and transport rates are urgently needed. Thus, I advocate studies, including those in smaller watersheds, to continuously monitor both alkalinity concentrations and discharge so that changes in these parameters can be linked to climate change-induced increases in temperature, precipitation, vegetation expansion, erosion, and permafrost thaw.

Although the magnitude of the difference between the post-1960 current erosion rate and the long-term interglacial erosion rate in the study in Chapter 5 allowed me to conclude with a high degree of confidence that erosion in the Gaskabohki catchment has increased due to climate change in the Arctic over the last ~60 years, a method other than ²³⁹⁺²⁴⁰Pu should be used in future studies examining current erosion behavior in small catchments. For I have shown that the accumulation of Pu in soil after fallout can be spatially very heterogeneous in Arctic catchments similar to ours. Regular measurements of stream sediment discharge are labor-intensive but probably less error-prone than FRN-based methods in the Arctic. One knowledge gap that has emerged from the study of Chapter 5 is the clarification of the influence of potential factors acting on current erosion, such as precipitation, vegetation, and permafrost, their interdependencies, and the time scales on which they exert their effects on erosion. Finally, another important knowledge gap is whether increased erosion has already been followed by a change in alkalinity generation, which is critical for predicting future changes in the carbon cycle.

Acronyms

AIC	Akaike information criterion
AMS	Accelerator mass spectrometry
amsl	Above mean sea level
AT	Total alkalinity
AWI	Alfred Wegener Institute
BIC	Bayesian information criterion
BOD	Biological oxygen demand
CACW	Carbonic acid induced carbonate weathering
CASW	Carbonic acid induced silicate weathering
CF-irmMS	Continuous-flow isotope-ratio-monitoring mass spectrometry
CRDS	Cavity ring-down spectroscopy
CRM	Certified reference material
CZ	Critical zone
DEM	Digital elevation model
DIC	Dissolved inorganic carbon
DREAMS	Dresden Accelerator Mass Spectrometry
DSDP	Deep sea drilling project
ESI	Electrospray ionization
EVI	Enhanced vegetation index
ExGI	Excess green index
FRN	Fallout radionuclide
GAM	Generalized additive model
GLM	Generalized linear model
GMWL	Global meteoric water line
GNIP	Global Network of Isotopes in Precipitation
HZDR	Helmholtz-Zentrum Dresden-Rossendorf
IBC	Ion Beam Centre

IC	Ion chromatography
ICP-MS	Inductively coupled plasma mass spectrometry
ICP-OES	Inductively coupled plasma optical emission spectrometry
IOW	Leibniz Institute for Baltic Sea Research Warnemünde
IQR	Interquartile range
M	Model
MAP	Mean annual precipitation
MAT	Mean annual air temperature
MIS	Marine isotope stage
MODERN	Modelling Deposition and Erosion rates with RadioNuclides
MS	Mass spectrometry
NCACW	Non-carbon based acid induced carbonate weathering
PET	Poleward energy transport
POLMAR	Helmholtz Graduate School for Polar and Marine Research
RCP	Representative concentration pathway
RMWL	Regional meteoric water line
RSS	Residual sum of squares
SLHL	Sea-level high-latitude
SPI	Stream power index
SSP	Shared socio-economic pathway
TPI	Topographic position index

Bibliography

- Aas, W., Eckhardt, S., Fiebig, M., Solberg, S., Platt, S. M., Yttri, K. E., and Zwaafink, C.: Monitoring of long-range transported air pollutants in Norway: NILU report 13/2021, Norwegian Environment Agency, M-2072, 2021.
- Akhmadaliev, S., Heller, R., Hanf, D., Rugel, G., and Merchel, S.: The new 6MV AMS-facility DREAMS at Dresden, Nuclear Instruments and Methods in Physics Research Section B: Beam Interactions with Materials and Atoms, 294, 5–10, doi:10.1016/j.nimb.2012.01.053, 2013.
- Alewell, C., Egli, M., and Meusbürger, K.: An attempt to estimate tolerable soil erosion rates by matching soil formation with denudation in Alpine grasslands, *J Soils Sediments*, 15, 1383–1399, doi:10.1007/s11368-014-0920-6, 2015.
- Alewell, C., Meusbürger, K., Juretzko, G., Mabit, L., and Ketterer, M. E.: Suitability of $^{239+240}\text{Pu}$ and ^{137}Cs as tracers for soil erosion assessment in mountain grasslands, *Chemosphere*, 103, 274–280, doi:10.1016/j.chemosphere.2013.12.016, 2014.
- Alewell, C., Pitois, A., Meusbürger, K., Ketterer, M., and Mabit, L.: $^{239+240}\text{Pu}$ from “contaminant” to soil erosion tracer: Where do we stand?, *Earth-Science Reviews*, 172, 107–123, doi:10.1016/j.earsci-rev.2017.07.009, 2017.
- AMAP: AMAP Arctic Climate Change Update 2021: Key Trends and Impacts, Arctic Monitoring and Assessment Programme (AMAP), Tromsø, Norway, 2022.
- Amiotte Suchet, P. and Probst, J.-L.: Modelling of atmospheric CO_2 consumption by chemical weathering of rocks: Application to the Garonne, Congo and Amazon basins, *Chemical Geology*, 107, 205–210, doi:10.1016/0009-2541(93)90174-H, 1993.
- Amiotte Suchet, P. and Probst, J.-L.: A global model for present-day atmospheric/soil CO_2 consumption by chemical erosion of continental rocks (GEM- CO_2), *Tellus B*, 47, 273–280, 1995.
- Amiotte Suchet, P., Probst, J.-L., and Ludwig, W.: Worldwide distribution of continental rock lithology: Implications for the atmospheric/soil CO_2 uptake by continental weathering and alkalinity river transport to the oceans, *Global Biogeochem. Cycles*, 17, n/a-n/a, doi:10.1029/2002GB001891, 2003.
- Amundson, R., Stern, L., Baisden, T., and Wang, Y.: The isotopic composition of soil and soil-respired CO_2 , *Geoderma*, 82, 83–114, doi:10.1016/S0016-7061(97)00098-0, 1998.

- Anderson, S. P., Blanckenburg, F. von, and White, A. F.: Physical and Chemical Controls on the Critical Zone, *Elements*, 3, 315–319, doi:10.2113/gselements.3.5.315, 2007.
- Anderson, S. P., Dietrich, W. E., and Brimhall, G. H.: Weathering profiles, mass-balance analysis, and rates of solute loss: Linkages between weathering and erosion in a small, steep catchment, *Geological Society of America Bulletin*, 114, 1143–1158, doi:10.1130/0016-7606(2002)114%3C1143:WPMBAA%3E2.0.CO;2, 2002.
- Anisimov, O.: Permafrost, in: *Encyclopedia of the Arctic*, Nuttall, M. (Ed.), Routledge, New York, 1611–1613, 2005.
- Arata, L., Meusburger, K., Frenkel, E., A'Campo-Neuen, A., Iurian, A.-R., Ketterer, M. E., Mabit, L., and Alewell, C.: Modelling Deposition and Erosion rates with RadioNuclides (MODERN) - Part 1: A new conversion model to derive soil redistribution rates from inventories of fallout radionuclides, *Journal of environmental radioactivity*, 162-163, 45–55, doi:10.1016/j.jenvrad.2016.05.008, 2016.
- Arino, O., Ramos Perez, J. J., Kalogirou, V., Bontemps, S., Defourny, P., and van Bogaert, E.: *Global Land Cover Map for 2009 (GlobCover 2009)*, 2012.
- Balco, G., Stone, J. O., Lifton, N. A., and Dunai, T. J.: A complete and easily accessible means of calculating surface exposure ages or erosion rates from ^{10}Be and ^{26}Al measurements, *Quaternary Geochronology*, 3, 174–195, doi:10.1016/j.quageo.2007.12.001, 2008.
- Ballantyne, C. K.: Paraglacial geomorphology, *Quaternary Science Reviews*, 21, 1935–2017, doi:10.1016/S0277-3791(02)00005-7, 2002.
- Beaulieu, E., Godd eris, Y., Donnadieu, Y., Labat, D., and Roelandt, C.: High sensitivity of the continental-weathering carbon dioxide sink to future climate change, *Nature Clim Change*, 2, 346–349, doi:10.1038/nclimate1419, 2012.
- Beel, C. R., Heslop, J. K., Orwin, J. F., Pope, M. A., Schevers, A. J., Hung, J. K. Y., Lafreni re, M. J., and Lamoureux, S. F.: Emerging dominance of summer rainfall driving High Arctic terrestrial-aquatic connectivity, *Nature communications*, 12, 1448, doi:10.1038/s41467-021-21759-3, 2021.
- Berger, T. W., T urtscher, S., Berger, P., and Lindebner, L.: A slight recovery of soils from Acid Rain over the last three decades is not reflected in the macro nutrition of beech (*Fagus sylvatica*) at 97 forest stands of the Vienna Woods, *Environmental pollution (Barking, Essex 1987)*, 216, 624–635, doi:10.1016/j.envpol.2016.06.024, 2016.

- Berner, E. K. and Berner, R. A.: The global water cycle: Geochemistry and environment, Prentice-Hall, Englewood Cliffs, 397 pp., 1987.
- Berner, E. K. and Berner, R. A.: Global environment: Water, air, and geochemical cycles, 2. ed., Princeton Univ. Press, Princeton, N.J u. a., 444 pp., 2012.
- Berner, E. K., Berner, R. A., and Moulton, K. L.: Plants and Mineral Weathering: Present and Past, in: Treatise on Geochemistry, Drever, J. I. (Ed.), Elsevier, 169–188, 2003.
- Berner, R. A., Lasaga, A. C., and Garrels, R. M.: The carbonate-silicate geochemical cycle and its effect on atmospheric carbon dioxide over the past 100 million years, *American Journal of Science*, 283, 641–683, doi:10.2475/ajs.283.7.641, 1983.
- Beylich, A. A.: Chemical and mechanical fluvial denudation in cold environments: Comparison of denudation rates from three catchments in sub-Arctic Eastern Iceland, sub-Arctic Finnish Lapland and Arctic Swedish Lapland, *Jokull*, 59, 19–32, 2009.
- Binnie, S. A., Dunai, T. J., Voronina, E., Goral, T., Heinze, S., and Dewald, A.: Separation of Be and Al for AMS using single-step column chromatography, *Nuclear Instruments and Methods in Physics Research Section B: Beam Interactions with Materials and Atoms*, 361, 397–401, doi:10.1016/j.nimb.2015.03.069, 2015.
- Biskaborn, B. K., Smith, S. L., Noetzli, J., Matthes, H., Vieira, G., Streltsov, D. A., Schoeneich, P., Romanovsky, V. E., Lewkowicz, A. G., Abramov, A., Allard, M., Boike, J., Cable, W. L., Christiansen, H. H., Delaloye, R., Diekmann, B., Drozdov, D., Etzelmüller, B., Grosse, G., Guglielmin, M., Ingeman-Nielsen, T., Isaksen, K., Ishikawa, M., Johansson, M., Johannsson, H., Joo, A., Kaverin, D., Kholodov, A., Konstantinov, P., Kröger, T., Lambiel, C., Lanckman, J.-P., Luo, D., Malkova, G., Meiklejohn, I., Moskalenko, N., Oliva, M., Phillips, M., Ramos, M., Sannel, A. B. K., Sergeev, D., Seybold, C., Skryabin, P., Vasiliev, A., Wu, Q., Yoshikawa, K., Zheleznyak, M., and Lantuit, H.: Permafrost is warming at a global scale, *Nature communications*, 10, 264, doi:10.1038/s41467-018-08240-4, 2019.
- Blanckenburg, F. von: The control mechanisms of erosion and weathering at basin scale from cosmogenic nuclides in river sediment, *Earth and Planetary Science Letters*, 237, 462–479, doi:10.1016/j.epsl.2005.06.030, 2005.
- Blanckenburg, F. von, Bouchez, J., and Wittmann, H.: Earth surface erosion and weathering from the ^{10}Be (meteoric)/ ^9Be ratio, *Earth and*

- Planetary Science Letters, 351-352, 295–305,
doi:10.1016/j.epsl.2012.07.022, 2012.
- Blum, J. D., Gazis, C. A., Jacobson, A. D., and Page Chamberlain, C.: Carbonate versus silicate weathering in the Raikhot watershed within the High Himalayan Crystalline Series, *Geology*, 26, 411,
doi:10.1130/0091-7613(1998)026%3C0411:CVSWIT%3E2.3.CO;2, 1998.
- Blume, T. and van Meerveld, H. J.: From hillslope to stream: methods to investigate subsurface connectivity, *WIREs Water*, 2, 177–198,
doi:10.1002/wat2.1071, 2015.
- Bond-Lamberty, B. and Thomson, A.: Temperature-associated increases in the global soil respiration record, *Nature*, 464, 579–582,
doi:10.1038/nature08930, 2010.
- Borrelli, P., Robinson, D. A., Panagos, P., Lugato, E., Yang, J. E., Alewell, C., Wuepper, D., Montanarella, L., and Ballabio, C.: Land use and climate change impacts on global soil erosion by water (2015-2070), *Proceedings of the National Academy of Sciences of the United States of America*, 117, 21994–22001,
doi:10.1073/pnas.2001403117, 2020.
- Böttcher, M. E.: The Stable Isotopic Geochemistry of the Sulfur and Carbon Cycles in a Modern Karst Environment, *Isotopes in environmental and health studies*, 35, 39–61, doi:10.1080/10256019908234078, 1999.
- Böttcher, M. E. and Schmiedinger, I.: The impact of temperature on the water isotope ($2\text{H}/1\text{H}$, $17\text{O}/16\text{O}$, $18\text{O}/16\text{O}$) fractionation upon transport through a low-density polyethylene membrane, *Isotopes in environmental and health studies*, 57, 183–192,
doi:10.1080/10256016.2020.1845668, 2021.
- Braathen, A. and Davidsen, B.: Structure and stratigraphy of the Palaeoproterozoic Karasjok Greenstone Belt, north Norway - regional implications, *Norsk Geologisk Tidsskrift*, 80, 33–50,
doi:10.1080/002919600750042663, 2000.
- Bracken, L. J., Wainwright, J., Ali, G. A., Tetzlaff, D., Smith, M. W., Reaney, S. M., and Roy, A. G.: Concepts of hydrological connectivity: Research approaches, pathways and future agendas, *Earth-Science Reviews*, 119, 17–34, doi:10.1016/j.earscirev.2013.02.001, 2013.
- Brand, W. A. and Coplen, T. B.: Stable isotope deltas: tiny, yet robust signatures in nature, *Isotopes in environmental and health studies*, 48, 393–409, doi:10.1080/10256016.2012.666977, 2012.

- Brook, G. A., Folkoff, M. E., and Box, E. O.: A world model of soil carbon dioxide, *Earth Surf. Process. Landforms*, 8, 79–88, doi:10.1002/esp.3290080108, 1983.
- Brooks, S. T., Jabour, J., van den Hoff, J., and Bergstrom, D. M.: Our footprint on Antarctica competes with nature for rare ice-free land, *Nat Sustain*, 2, 185–190, doi:10.1038/s41893-019-0237-y, 2019.
- Brown, E. T., Stallard, R. F., Larsen, M. C., Raisbeck, G. M., and Yiou, F.: Denudation rates determined from the accumulation of in situ-produced ^{10}Be in the Luquillo experimental forest, Puerto Rico, *Earth and Planetary Science Letters*, 129, 193–202, doi:10.1016/0012-821X(94)00249-X, 1995.
- Brown, J., Ferrians Jr., O. J., Heginbottom, J. A., and Melnikov, E. S.: Circum-Arctic map of permafrost and ground-ice conditions, 1997.
- Bufe, A., Hovius, N., Emberson, R., Rugenstein, J. K. C., Galy, A., Hasenrueck-Gudipati, H. J., and Chang, J.-M.: Co-variation of silicate, carbonate and sulfide weathering drives CO_2 release with erosion, *Nat. Geosci.*, 14, 211–216, doi:10.1038/s41561-021-00714-3, 2021.
- Burga, C. A., Frauenfelder, R., Ruffet, J., Hoelzle, M., and Käab, A.: Vegetation on Alpine rock glacier surfaces: a contribution to abundance and dynamics on extreme plant habitats, *Flora - Morphology, Distribution, Functional Ecology of Plants*, 199, 505–515, doi:10.1078/0367-2530-00179, 2004.
- Calmels, D., Gaillardet, J., Brenot, A., and France-Lanord, C.: Sustained sulfide oxidation by physical erosion processes in the Mackenzie River basin: Climatic perspectives, *Geology*, 35, 1003, doi:10.1130/G24132A.1, 2007.
- Calmels, D., Gaillardet, J., and François, L.: Sensitivity of carbonate weathering to soil CO_2 production by biological activity along a temperate climate transect, *Chemical Geology*, 390, 74–86, doi:10.1016/j.chemgeo.2014.10.010, 2014.
- Campeau, A., Wallin, M. B., Giesler, R., Löfgren, S., Mörtz, C.-M., Schiff, S., Venkiteswaran, J. J., and Bishop, K.: Multiple sources and sinks of dissolved inorganic carbon across Swedish streams, refocusing the lens of stable C isotopes, *Scientific reports*, 7, 9158, doi:10.1038/s41598-017-09049-9, 2017.
- Camporese, M., Penna, D., Borga, M., and Paniconi, C.: A field and modeling study of nonlinear storage-discharge dynamics for an Alpine headwater catchment, *Water Resour. Res.*, 50, 806–822, doi:10.1002/2013WR013604, 2014.

- Campy, M., Buoncristiani, J. F., and Bichet, V.: Sediment yield from glacio-lacustrine calcareous deposits during the postglacial period in the Combe d'Ain (Jura, France), *Earth Surf. Process. Landforms*, 23, 429–444, doi:10.1002/(SICI)1096-9837(199805)23:5%3C429:AID-ESP858%3E3.0.CO;2-7, 1998.
- Cerling, T. E. and Craig, H.: Geomorphology and in-situ cosmogenic isotopes, *Annu. Rev. Earth Planet. Sci.*, 22, 273–317, doi:10.1146/annurev.ea.22.050194.001421, 1994.
- Cerling, T. E., Solomon, D., Quade, J., and Bowman, J. R.: On the isotopic composition of carbon in soil carbon dioxide, *Geochimica et Cosmochimica Acta*, 55, 3403–3405, doi:10.1016/0016-7037(91)90498-T, 1991.
- Chappell, A., Valentin, C., Warren, A., Noon, P., Charlton, M., and d'Herbes, J.: Testing the validity of upslope migration in banded vegetation from south-west Niger, *CATENA*, 37, 217–229, doi:10.1016/S0341-8162(98)00074-5, 1999.
- Chawla, F., Steinmann, P., Pfeifer, H.-R., and Froidevaux, P.: Atmospheric deposition and migration of artificial radionuclides in Alpine soils (Val Piora, Switzerland) compared to the distribution of selected major and trace elements, *The Science of the total environment*, 408, 3292–3302, doi:10.1016/j.scitotenv.2010.03.012, 2010.
- Chekushin, V. A., Bogatyrev, I. V., Caritat, P. de, Niskavaara, H., and Reimann, C.: Annual atmospheric deposition of 16 elements in eight catchments of the central Barents region, *Science of The Total Environment*, 220, 95–114, doi:10.1016/S0048-9697(98)00247-2, 1998.
- Chen, S.-A., Michaelides, K., Richards, D. A., and Singer, M. B.: Exploring exogenous controls on short- versus long-term erosion rates globally, *Earth Surf. Dynam.*, 10, 1055–1078, doi:10.5194/esurf-10-1055-2022, 2022.
- Chiaradia, E. A., Arata, L., and Meusbürger, K.: modeRn: an R package to convert FRN (Fallout Radio-1301 Nuclides) inventories into soil erosion/deposition rates, *modern.umweltgeo.unibas.ch*, 2016.
- Chmeleff, J., Blanckenburg, F. von, Kossert, K., and Jakob, D.: Determination of the ^{10}Be half-life by multicollector ICP-MS and liquid scintillation counting, *Nuclear Instruments and Methods in Physics Research Section B: Beam Interactions with Materials and Atoms*, 268, 192–199, doi:10.1016/j.nimb.2009.09.012, 2010.
- Choppin, G. R.: Actinide speciation in aquatic systems, *Marine Chemistry*, 99, 83–92, doi:10.1016/j.marchem.2005.03.011, 2006.

- Christiansen, H. H., Etzelmüller, B., Isaksen, K., Juliussen, H., Farbro, H., Humlum, O., Johansson, M., Ingeman-Nielsen, T., Kristensen, L., Hjort, J., Holmlund, P., Sannel, A. B. K., Sigsgaard, C., Åkerman, H. J., Foged, N., Blikra, L. H., Pernosky, M. A., and Ødegård, R. S.: The thermal state of permafrost in the nordic area during the international polar year 2007-2009, *Permafrost Periglac. Process.*, 21, 156–181, doi:10.1002/ppp.687, 2010.
- CLC: CORINE Land Cover: CLC2018, © European Union, Copernicus Land Monitoring Service 2018, European Environment Agency (EEA), 2018.
- Coch, C., Ramage, J. L., Lamoureux, S. F., Meyer, H., Knoblauch, C., and Lantuit, H.: Spatial Variability of Dissolved Organic Carbon, Solutes, and Suspended Sediment in Disturbed Low Arctic Coastal Watersheds, *J. Geophys. Res. Biogeosci.*, 125, doi:10.1029/2019JG005505, 2020.
- Codilean, A. T., Munack, H., Cohen, T. J., Saktura, W. M., Gray, A., and Mudd, S. M.: OCTOPUS: an open cosmogenic isotope and luminescence database, *Earth Syst. Sci. Data*, 10, 2123–2139, doi:10.5194/essd-10-2123-2018, 2018.
- Collins, S., Swinton, S., Anderson, C. W., Benson, B. J., Brunt, J., Gragson, T., Grimm, N., Grove, M., Henshaw, D. L., Knapp, A., Kofinas, G., Magnuson, J., McDowel, W., Melack, J. M., Moore, J. C., Ogden, L., Porter, J. H., Reichman, O. J., Robertson, G. P., and Whitmer, A. C.: Integrated Science for Society and the Environment: A strategic research initiative, U.S. Long Term Ecol. Res. Network, Albuquerque, USA, 2007.
- Conrad, O., Bechtel, B., Bock, M., Dietrich, H., Fischer, E., Gerlitz, L., Wehberg, J., Wichmann, V., and Böhner, J.: System for Automated Geoscientific Analyses (SAGA) v. 2.1.4, *Geosci. Model Dev.*, 8, 1991–2007, doi:10.5194/gmd-8-1991-2015, 2015.
- Corbett, L. B., Bierman, P. R., and Rood, D. H.: An approach for optimizing in situ cosmogenic ^{10}Be sample preparation, *Quaternary Geochronology*, 33, 24–34, doi:10.1016/j.quageo.2016.02.001, 2016.
- Darmody, R. G., Thorn, C. E., and Dixon, J. C.: Pyrite-enhanced chemical weathering in Karkevagge, Swedish Lapland, *Geological Society of America Bulletin*, 119, 1477–1485, doi:10.1130/B26228.1, 2007.
- Darmody, R. G., Thorn, C. E., Dixon, J. C., and Schlyter, P.: Soils and Landscapes of Kärkevagge, Swedish Lapland, *Soil Sci. Soc. Am. J.*, 64, 1455–1466, doi:10.2136/sssaj2000.6441455x, 2000.

- Davidson, G. R.: The stable isotopic composition and measurement of carbon in soil CO₂, *Geochimica et Cosmochimica Acta*, 59, 2485–2489, doi:10.1016/0016-7037(95)00143-3, 1995.
- Deines, P., Langmuir, D., and Harmon, R. S.: Stable carbon isotope ratios and the existence of a gas phase in the evolution of carbonate ground waters, *Geochimica et Cosmochimica Acta*, 38, 1147–1164, doi:10.1016/0016-7037(74)90010-6, 1974.
- Derakhshan-Babaei, F., Nosrati, K., Tikhomirov, D., Christl, M., Sadough, H., and Egli, M.: Relating the spatial variability of chemical weathering and erosion to geological and topographical zones, *Geomorphology*, 363, 107235, doi:10.1016/j.geomorph.2020.107235, 2020.
- Dickson, A. G.: An exact definition of total alkalinity and a procedure for the estimation of alkalinity and total inorganic carbon from titration data, *Deep Sea Research Part A. Oceanographic Research Papers*, 28, 609–623, doi:10.1016/0198-0149(81)90121-7, 1981.
- Didan, K., Munoz, A. B., Solano, R., and Huete, A.: MOD13Q1 v006: MODIS/Terra Vegetation Indices 16-Day L3 Global 720 250 m SIN Grid, Land Processes Distributed Active Archive Center (LP DAAC), <https://lpdaac.usgs.gov/>, 2015.
- Dingman, S. L.: Hydrology of the Glenn Creek watershed, Tanana River Basin, central Alaska: Res. Rep. 297, Cold Regions Research and Engineering Laboratory, Hanover, New Hampshire, USA, 1971.
- Dixon, J. C.: 13.11 Response of Periglacial Geomorphic Processes to Global Change, in: *Treatise on Geomorphology*, Shroder, J. F. (Ed.), Elsevier, 176–189, 2013.
- Dixon, J. L. and Blanckenburg, F. von: Soils as pacemakers and limiters of global silicate weathering, *Comptes Rendus Geoscience*, 344, 597–609, doi:10.1016/j.crite.2012.10.012, 2012.
- Dornblaser, M. M. and Striegl, R. G.: Switching predominance of organic versus inorganic carbon exports from an intermediate-size subarctic watershed, *Geophys. Res. Lett.*, 42, 386–394, doi:10.1002/2014GL062349, 2015.
- Drake, T. W., Tank, S. E., Zhulidov, A. V., Holmes, R. M., Gurtovaya, T., and Spencer, R. G. M.: Increasing Alkalinity Export from Large Russian Arctic Rivers, *Environmental science & technology*, 52, 8302–8308, doi:10.1021/acs.est.8b01051, 2018.
- Dreybrodt, W.: *Processes in Karst Systems: Physics, Chemistry, and Geology*, Springer Series in Physical Environment, 4, Springer, Berlin, Heidelberg, 288184 pp., 1988.

- Ebert, K., Hall, A. M., Kleman, J., and Andersson, J.: Unequal ice-sheet erosional impacts across low-relief shield terrain in northern Fennoscandia, *Geomorphology*, 233, 64–74, doi:10.1016/j.geomorph.2014.09.024, 2015.
- Erlanger, E. D., Rugenstein, J. K. C., Bufe, A., Picotti, V., and Willett, S. D.: Controls on Physical and Chemical Denudation in a Mixed Carbonate-Siliciclastic Orogen, *JGR Earth Surface*, 126, doi:10.1029/2021JF006064, 2021.
- Eroglu, A. E., McLeod, C. W., Leonard, K. S., and McCubbin, D.: Determination of plutonium in seawater using co-precipitation and inductively coupled plasma mass spectrometry with ultrasonic nebulisation, *Spectrochimica Acta Part B: Atomic Spectroscopy*, 53, 1221–1233, doi:10.1016/S0584-8547(98)00179-7, 1998.
- ESRI: ArcGIS pro, ESRI, Redlands, USA, 2022.
- Etzelmüller, B.: Quantification of thermo-erosion in pro-glacial areas - examples from Svalbard, *zfg*, 44, 343–361, doi:10.1127/zfg/44/2000/343, 2000.
- Eyring, V., Bony, S., Meehl, G. A., Senior, C. A., Stevens, B., Stouffer, R. J., and Taylor, K. E.: Overview of the Coupled Model Intercomparison Project Phase 6 (CMIP6) experimental design and organization, *Geosci. Model Dev.*, 9, 1937–1958, doi:10.5194/gmd-9-1937-2016, 2016.
- Fabel, D. and Harbor, J.: The use of in-situ produced cosmogenic radionuclides in glaciology and glacial geomorphology, *Ann. Glaciol.*, 28, 103–110, doi:10.3189/172756499781821968, 1999.
- Fabel, D., Stroeven, A. P., Harbor, J., Kleman, J., Elmore, D., and Fink, D.: Landscape preservation under Fennoscandian ice sheets determined from in situ produced ^{10}Be and ^{26}Al , *Earth and Planetary Science Letters*, 201, 397–406, doi:10.1016/S0012-821X(02)00714-8, 2002.
- Fahrmeir, L., Kneib, T., Lang, S., and Marx, B.: *Regression: Models, methods and applications*, Springer, Berlin, Heidelberg, 698 pp., 2013.
- Fekete, B. M., Vörösmarty, C. J., and Grabs, W.: High-resolution fields of global runoff combining observed river discharge and simulated water balances, *Global Biogeochem. Cycles*, 16, 15-1-15-10, doi:10.1029/1999GB001254, 2002.
- Ferrier, K. L. and Kirchner, J. W.: Effects of physical erosion on chemical denudation rates: A numerical modeling study of soil-mantled hillslopes, *Earth and Planetary Science Letters*, 272, 591–599, doi:10.1016/j.epsl.2008.05.024, 2008.

- Fick, S. E. and Hijmans, R. J.: WorldClim 2: new 1-km spatial resolution climate surfaces for global land areas, *Int. J. Climatol*, 37, 4302–4315, doi:10.1002/joc.5086, 2017.
- Flato, G. M. and Boer, G. J.: Warming asymmetry in climate change simulations, *Geophys. Res. Lett.*, 28, 195–198, doi:10.1029/2000GL012121, 2001.
- Frey, K. E. and McClelland, J. W.: Impacts of permafrost degradation on arctic river biogeochemistry, *Hydrol. Process.*, 23, 169–182, doi:10.1002/hyp.7196, 2009.
- Fritz, P., Drimmie, R. J., Frapce, S. K., and O'Shea, K.: The isotopic composition of precipitation and groundwater in Canada, IAEA, International Atomic Energy Agency (IAEA), 1987.
- Gabet, E. J.: A theoretical model coupling chemical weathering and physical erosion in landslide-dominated landscapes, *Earth and Planetary Science Letters*, 264, 259–265, doi:10.1016/j.epsl.2007.09.028, 2007.
- Gabet, E. J. and Mudd, S. M.: A theoretical model coupling chemical weathering rates with denudation rates, *Geology*, 37, 151–154, doi:10.1130/G25270A.1, 2009.
- Gaillardet, J., Calmels, D., Romero-Mujalli, G., Zakharova, E., and Hartmann, J.: Global climate control on carbonate weathering intensity, *Chemical Geology*, 527, 118762, doi:10.1016/j.chemgeo.2018.05.009, 2019.
- Gaillardet, J., Dupré, B., Louvat, P., and Allègre, C. J.: Global silicate weathering and CO₂ consumption rates deduced from the chemistry of large rivers, *Chemical Geology*, 159, 3–30, doi:10.1016/S0009-2541(99)00031-5, 1999.
- Garrels, R. M. and Berner, R. A.: The Global Carbonate-Silicate Sedimentary System — Some Feedback Relations, in: *Biom mineralization and Biological Metal Accumulation*, Westbroek, P., Jong, E. W. de (Eds.), Springer Netherlands, Dordrecht, 73–87, 1983.
- Gislason, S. R., Oelkers, E. H., Eiriksdottir, E. S., Kardjilov, M. I., Gisladottir, G., Sigfusson, B., Snorrason, A., Elefsen, S., Hardardottir, J., Torssander, P., and Oskarsson, N.: Direct evidence of the feedback between climate and weathering, *Earth and Planetary Science Letters*, 277, 213–222, doi:10.1016/j.epsl.2008.10.018, 2009.
- Goddéris, Y., Williams, J. Z., Schott, J., Pollard, D., and Brantley, S. L.: Time evolution of the mineralogical composition of Mississippi Valley loess over the last 10kyr: Climate and geochemical modeling, *Geochimica et Cosmochimica Acta*, 74, 6357–6374, doi:10.1016/j.gca.2010.08.023, 2010.

- Goll, D. S., Moosdorf, N., Hartmann, J., and Brovkin, V.: Climate-driven changes in chemical weathering and associated phosphorus release since 1850: Implications for the land carbon balance, *Geophys. Res. Lett.*, 41, 3553–3558, doi:10.1002/2014GL059471, 2014.
- González-Pinzón, R., Ward, A. S., Hatch, C. E., Wlostowski, A. N., Singha, K., Gooseff, M. N., Haggerty, R., Harvey, J. W., Cirpka, O. A., and Brock, J. T.: A field comparison of multiple techniques to quantify groundwater–surface-water interactions, *Freshwater Science*, 34, 139–160, doi:10.1086/679738, 2015.
- Gosse, J. C. and Phillips, F. M.: Terrestrial in situ cosmogenic nuclides: theory and application, *Quaternary Science Reviews*, 20, 1475–1560, doi:10.1016/S0277-3791(00)00171-2, 2001.
- GRDC: Major River Basins of the World / Global Runoff Data Centre, GRDC: 2nd, rev. ext. ed, Federal Institute of Hydrology (BfG), Koblenz, Germany, 2020.
- Grosse, G., Harden, J., Turetsky, M., McGuire, A. D., Camill, P., Tarnocai, C., Frohling, S., Schuur, E. A. G., Jorgenson, T., Marchenko, S., Romanovsky, V., Wickland, K. P., French, N., Waldrop, M., Bourgeau-Chavez, L., and Striegl, R. G.: Vulnerability of high-latitude soil organic carbon in North America to disturbance, *J. Geophys. Res.*, 116, doi:10.1029/2010JG001507, 2011.
- Günther, F., Overduin, P. P., Yakshina, I. A., Opel, T., Baranskaya, A. V., and Grigoriev, M. N.: Observing Muostakh disappear: permafrost thaw subsidence and erosion of a ground-ice-rich island in response to arctic summer warming and sea ice reduction, *The Cryosphere*, 9, 151–178, doi:10.5194/tc-9-151-2015, 2015.
- Gwiazda, R. H. and Broecker, W. S.: The separate and combined effects of temperature, soil p CO₂ and organic acidity on silicate weathering in the soil environment: Formulation of a model and results, *Global Biogeochem. Cycles*, 8, 141–155, doi:10.1029/94GB00491, 1994.
- Haine, T. W., Curry, B., Gerdes, R., Hansen, E., Karcher, M., Lee, C., Rudels, B., Spreen, G., Steur, L. de, Stewart, K. D., and Woodgate, R.: Arctic freshwater export: Status, mechanisms, and prospects, *Global and Planetary Change*, 125, 13–35, doi:10.1016/j.gloplacha.2014.11.013, 2015.
- Hartmann, J.: Bicarbonate-fluxes and CO₂-consumption by chemical weathering on the Japanese Archipelago — Application of a multi-lithological model framework, *Chemical Geology*, 265, 237–271, doi:10.1016/j.chemgeo.2009.03.024, 2009.

- Hartmann, J., Jansen, N., Dürr, H. H., Kempe, S., and Köhler, P.: Global CO₂-consumption by chemical weathering: What is the contribution of highly active weathering regions?, *Global and Planetary Change*, 69, 185–194, doi:10.1016/j.gloplacha.2009.07.007, 2009.
- Hartmann, J., Lauerwald, R., and Moosdorf, N.: GLORICH - Global river chemistry database, supplement to: Hartmann, Jens; Lauerwald, Ronny; Moosdorf, Nils (2014): A Brief Overview of the GLObal River Chemistry Database, GLORICH. *Procedia Earth and Planetary Science*, 10, 23-27, 2019.
- Hartmann, J. and Moosdorf, N.: The new global lithological map database GLiM: A representation of rock properties at the Earth surface, *Geochem. Geophys. Geosyst.*, 13, doi:10.1029/2012GC004370, 2012.
- Hartmann, J., Moosdorf, N., Lauerwald, R., Hinderer, M., and West, A. J.: Global chemical weathering and associated P-release — The role of lithology, temperature and soil properties, *Chemical Geology*, 363, 145–163, doi:10.1016/j.chemgeo.2013.10.025, 2014.
- Heimsath, A. M., Chadwick, O. A., Roering, J. J., and Levick, S. R.: Quantifying erosional equilibrium across a slowly eroding, soil mantled landscape, *Earth Surf. Process. Landforms*, 45, 499–510, doi:10.1002/esp.4725, 2020.
- Heimsath, A. M., Dietrich, W. E., Nishiizumi, K., and Finkel, R. C.: The soil production function and landscape equilibrium, *Nature*, 388, 358–361, doi:10.1038/41056, 1997.
- Heimsath, A. M., Dietrich, W. E., Nishiizumi, K., and Finkel, R. C.: Stochastic processes of soil production and transport: erosion rates, topographic variation and cosmogenic nuclides in the Oregon Coast Range, *Earth Surf. Process. Landforms*, 26, 531–552, doi:10.1002/esp.209, 2001.
- Hill, T. and Neal, C.: Spatial and temporal variation in pH, alkalinity and conductivity in surface runoff and groundwater for the Upper River Severn catchment, *Hydrol. Earth Syst. Sci.*, 1, 697–715, doi:10.5194/hess-1-697-1997, 1997.
- Hoefs, J.: Contribution to the isotopic geochemistry of carbon in magmatic rocks, Goettingen Univ., Goettingen, Germany, 1973.
- Holmes, R. M., McClelland, J. W., Peterson, B. J., Tank, S. E., Bulygina, E., Eglinton, T. I., Gordeev, V. V., Gurtovaya, T. Y., Raymond, P. A., Repeta, D. J., Staples, R., Striegl, R. G., Zhulidov, A. V., and Zimov, S. A.: Seasonal and Annual Fluxes of Nutrients and Organic Matter from Large Rivers to the Arctic Ocean and Surrounding Seas, *Estuaries and Coasts*, 35, 369–382, doi:10.1007/s12237-011-9386-6, 2012.

- Hovius, N. and Blanckenburg, F. von: Constraining the denudational response to faulting, in: *Tectonic faults: Agents of change on a dynamic Earth*, Handy, M., Hirth, D., Hovius, N. (Eds.), MIT Press, Cambridge, USA, 231–272, 2007.
- Huete, A., Didan, K., Miura, T., Rodriguez, E., Gao, X., and Ferreira, L.: Overview of the radiometric and biophysical performance of the MODIS vegetation indices, *Remote Sensing of Environment*, 83, 195–213, doi:10.1016/S0034-4257(02)00096-2, 2002.
- Hunt, A. L., Larsen, J., Bierman, P. R., and Petrucci, G. A.: Investigation of factors that affect the sensitivity of accelerator mass spectrometry for cosmogenic ^{10}Be and ^{26}Al isotope analysis, *Analytical chemistry*, 80, 1656–1663, doi:10.1021/ac701742p, 2008.
- Hunt, A. L., Petrucci, G. A., Bierman, P. R., and Finkel, R. C.: Metal matrices to optimize ion beam currents for accelerator mass spectrometry, *Nuclear Instruments and Methods in Physics Research Section B: Beam Interactions with Materials and Atoms*, 243, 216–222, doi:10.1016/j.nimb.2005.07.220, 2006.
- International Atomic Energy Agency: Global Network of Isotopes in Precipitation, The GNIP Database, <https://nucleus.iaea.org/wiser>.
- IPCC: Climate Change 2013, in: *The Physical Science Basis. Contribution of Working Group I to the Fifth Assessment Report of the Intergovernmental Panel on Climate Change*, Stocker, T. F., Qin, D., Plattner, G.-K., Tignor, M., Allen, S. K., Boschung, J., Nauels, A., Xia, Y., Bex, V., Midgley, P. M. (Eds.), Cambridge University Press, Cambridge, United Kingdom and New York, NY, USA, 2013.
- IPCC: Climate Change 2021: The Physical Science Basis: Contribution of Working Group I to the Sixth Assessment Report of the Intergovernmental Panel on Climate Change, Cambridge University Press, Cambridge, United Kingdom and New York, NY, USA, 2021.
- Isaksen, K., Lutz, J., Sørensen, A. M., Godøy, Ø., Ferrighi, L., Eastwood, S., and Aaboe, S.: Advances in operational permafrost monitoring on Svalbard and in Norway, *Environ. Res. Lett.*, 17, 95012, doi:10.1088/1748-9326/ac8e1c, 2022.
- Jacobson, A. D. and Blum, J. D.: Relationship between mechanical erosion and atmospheric CO_2 consumption in the New Zealand Southern Alps, *Geology*, 31, 865, doi:10.1130/G19662.1, 2003.
- Jacobson, A. D., Blum, J. D., Chamberlain, C., Craw, D., and Koons, P. O.: Climatic and tectonic controls on chemical weathering in the New Zealand Southern Alps, *Geochimica et Cosmochimica Acta*, 67, 29–46, doi:10.1016/S0016-7037(02)01053-0, 2003.

- Jacobson, A. D., Blum, J. D., Chamberlain, C., Poage, M. A., and Sloan, V. F.: Ca/Sr and Sr isotope systematics of a Himalayan glacial chronosequence: carbonate versus silicate weathering rates as a function of landscape surface age, *Geochimica et Cosmochimica Acta*, 66, 13–27, doi:10.1016/S0016-7037(01)00755-4, 2002.
- Jacobson, A. D., Grace Andrews, M., Lehn, G. O., and Holmden, C.: Silicate versus carbonate weathering in Iceland: New insights from Ca isotopes, *Earth and Planetary Science Letters*, 416, 132–142, doi:10.1016/j.epsl.2015.01.030, 2015.
- Jansen, J. D., Knudsen, M. F., Andersen, J. L., Heyman, J., and Egholm, D. L.: Erosion rates in Fennoscandia during the past million years, *Quaternary Science Reviews*, 207, 37–48, doi:10.1016/j.quascirev.2019.01.010, 2019.
- Jiang, L.-Q., Carter, B. R., Feely, R. A., Lauvset, S. K., and Olsen, A.: Surface ocean pH and buffer capacity: past, present and future, *Scientific reports*, 9, 18624, doi:10.1038/s41598-019-55039-4, 2019.
- Johnsson, H. and Lundin, L.-C.: Surface runoff and soil water percolation as affected by snow and soil frost, *Journal of Hydrology*, 122, 141–159, doi:10.1016/0022-1694(91)90177-J, 1991.
- Jones, B. M., Arp, C. D., Jorgenson, M. T., Hinkel, K. M., Schmutz, J. A., and Flint, P. L.: Increase in the rate and uniformity of coastline erosion in Arctic Alaska, *Geophys. Res. Lett.*, 36, n/a-n/a, doi:10.1029/2008GL036205, 2009.
- Jones, J. B. and Mulholland, P. J.: Influence of drainage basin topography and elevation on carbon dioxide and methane supersaturation of stream water, *Biogeochemistry*, 40, 57–72, doi:10.1023/A:1005914121280, 1998.
- Kaitanen, V.: A geographical study of the morphogenesis of Northern Lapland, *Fennia*, 99, 1969.
- Karjalainen, O., Aalto, J., Luoto, M., Westermann, S., Romanovsky, V. E., Nelson, F. E., Eitzelmüller, B., and Hjort, J.: Circumpolar raster grids of permafrost extent and geohazard potential for near-future climate scenarios, supplement to: Hjort, Jan; Karjalainen, Olli; Aalto, Juha; Westermann, Sebastian; Romanovsky, Vladimir E; Nelson, Frederick E; Eitzelmüller, Bernd; Luoto, Miska (2018): Degrading permafrost puts Arctic infrastructure at risk by mid-century. *Nature Communications*, 9(1), 5147, 2018.
- Kasting, J. F. and Catling, D.: Evolution of a Habitable Planet, *Annu. Rev. Astron. Astrophys.*, 41, 429–463, doi:10.1146/annurev.astro.41.071601.170049, 2003.

- Kelley, J. M., Bond, L. A., and Beasley, T. M.: Global distribution of Pu isotopes and ^{237}Np , *Science of The Total Environment*, 237-238, 483–500, doi:10.1016/S0048-9697(99)00160-6, 1999.
- Kempe, S.: Long-term records of CO₂ pressure fluctuations in fresh waters, *Mitt. Geol-Paläont. Inst. Univ. Hamburg; SCOPE/UNEP Sonderband*, 52, 91–332, 1982.
- Ketterer, M. E., Hafer, K. M., Jones, V. J., and Appleby, P. G.: Rapid dating of recent sediments in Loch Ness: inductively coupled plasma mass spectrometric measurements of global fallout plutonium, *Science of The Total Environment*, 322, 221–229, doi:10.1016/j.scitotenv.2003.09.016, 2004.
- Ketterer, M. E., Watson, B. R., Matisoff, G., and Wilsont, C. G.: Rapid dating of recent aquatic sediments using Pu activities and $^{240}\text{Pu}/^{239}\text{Pu}$ as determined by quadrupole inductively coupled plasma mass spectrometry, *Environmental science & technology*, 36, 1307–1311, doi:10.1021/es010826g, 2002.
- Kirchner, J. W., Finkel, R. C., Riebe, C. S., Granger, D. E., Clayton, J. L., King, J. G., and Megahan, W. F.: Mountain erosion over 10 yr, 10 k.y., and 10 m.y. time scales, *Geology*, 29, 591, doi:10.1130/0091-7613(2001)029%3C0591:MEOYKY%3E2.0.CO;2, 2001.
- Kirkby, M. J.: A Model for Variations in Gelifluction Rates with Temperature and Topography: Implications for Global Change, *Geografiska Annaler: Series A, Physical Geography*, 77, 269–278, doi:10.1080/04353676.1995.11880447, 1995.
- Kjellman, S. E., Axelsson, P. E., Etzelmüller, B., Westermann, S., and Sannel, A. B. K.: Holocene development of subarctic permafrost peatlands in Finnmark, northern Norway, *The Holocene*, 28, 1855–1869, doi:10.1177/0959683618798126, 2018.
- Kleman, J., Hättestrand, C., Borgström, I., and Stroeven, A.: Fennoscandian palaeoglaciology reconstructed using a glacial geological inversion model, *J. Glaciol.*, 43, 283–299, doi:10.3189/S0022143000003233, 1997.
- Kleman, J., Stroeven, A. P., and Lundqvist, J.: Patterns of Quaternary ice sheet erosion and deposition in Fennoscandia and a theoretical framework for explanation, *Geomorphology*, 97, 73–90, doi:10.1016/j.geomorph.2007.02.049, 2008.
- Kohl, C. and Nishiizumi, K.: Chemical isolation of quartz for measurement of in-situ -produced cosmogenic nuclides, *Geochimica et Cosmochimica Acta*, 56, 3583–3587, doi:10.1016/0016-7037(92)90401-4, 1992.

- Korschinek, G., Bergmaier, A., Faestermann, T., Gerstmann, U. C., Knie, K., Rugel, G., Wallner, A., Dillmann, I., Dollinger, G., Gostomski, C. L. von, Kossert, K., Maiti, M., Poutivtsev, M., and Remmert, A.: A new value for the half-life of ^{10}Be by Heavy-Ion Elastic Recoil Detection and liquid scintillation counting, *Nuclear Instruments and Methods in Physics Research Section B: Beam Interactions with Materials and Atoms*, 268, 187–191, doi:10.1016/j.nimb.2009.09.020, 2010.
- Krasting, J. P. et al.: NOAA-GFDL GFDL-ESM4 model output prepared for CMIP6 CMIP, Earth System Grid Federation, 2018.
- Lag, J.: Soil Map Norway - Jordbunnskart, Norges Landbrukshogskole, <https://esdac.jrc.ec.eu-1396.ropa.eu/content/soil-map-norway-jordbunnskart>, 1983.
- Lal, D.: Cosmic ray labeling of erosion surfaces: in situ nuclide production rates and erosion models, *Earth and Planetary Science Letters*, 104, 424–439, doi:10.1016/0012-821X(91)90220-C, 1991.
- Lamoureux, S. F., Lafrenière, M. J., and Favaro, E. A.: Erosion dynamics following localized permafrost slope disturbances, *Geophys. Res. Lett.*, 41, 5499–5505, doi:10.1002/2014GL060677, 2014.
- Land, L. S.: The isotopic and trace element geochemistry of dolomite: the state of the art, in: *Concepts and Models of Dolomitization*, Zenger, D. H., Dunham, J. B., Ethington, R. L. (Eds.), SEPM (Society for Sedimentary Geology), 87–110, 1980.
- Lange, S. and Büchner, M.: ISIMIP3b bias-adjusted atmospheric climate input data (v1.1), ISIMIP Repository, 2021.
- Larrinaga, A. and Brotons, L.: Greenness Indices from a Low-Cost UAV Imagery as Tools for Monitoring Post-Fire Forest Recovery, *Drones*, 3, 6, doi:10.3390/drones3010006, 2019.
- Lasaga, A. C.: Chemical kinetics of water-rock interactions, *J. Geophys. Res.*, 89, 4009–4025, doi:10.1029/JB089iB06p04009, 1984.
- Lechuga-Crespo, J. L., Sánchez-Pérez, J. M., Sauvage, S., Hartmann, J., Amiotte Suchet, P., Probst, J. L., and Ruiz-Romera, E.: A model for evaluating continental chemical weathering from riverine transports of dissolved major elements at a global scale, *Global and Planetary Change*, 192, 103226, doi:10.1016/j.gloplacha.2020.103226, 2020.
- Lee, H., Swenson, S. C., Slater, A. G., and Lawrence, D. M.: Effects of excess ground ice on projections of permafrost in a warming climate, *Environ. Res. Lett.*, 9, 124006, doi:10.1088/1748-9326/9/12/124006, 2014.
- Lehn, G. O., Jacobson, A. D., Douglas, T. A., McClelland, J. W., Barker, A. J., and Khosh, M. S.: Constraining seasonal active layer dynamics

- and chemical weathering reactions occurring in North Slope Alaskan watersheds with major ion and isotope ($\delta^{34}\text{S}_{\text{SO}_4}$, $\delta^{13}\text{C}_{\text{DIC}}$, $^{87}\text{Sr}/^{86}\text{Sr}$, $\delta^{44}/^{40}\text{Ca}$, and $\delta^{44}/^{42}\text{Ca}$) measurements, *Geochimica et Cosmochimica Acta*, 217, 399–420, doi:10.1016/j.gca.2017.07.042, 2017.
- Li, S., Xia, X., Tan, X., and Zhang, Q.: Effects of catchment and riparian landscape setting on water chemistry and seasonal evolution of water quality in the upper Han River basin, China, *PloS one*, 8, e53163, doi:10.1371/journal.pone.0053163, 2013.
- Li, S.-L., Calmels, D., Han, G., Gaillardet, J., and Liu, C.-Q.: Sulfuric acid as an agent of carbonate weathering constrained by $\delta^{13}\text{C}_{\text{DIC}}$: Examples from Southwest China, *Earth and Planetary Science Letters*, 270, 189–199, doi:10.1016/j.epsl.2008.02.039, 2008.
- Li, S.-L., Liu, C.-Q., Li, J., Lang, Y.-C., Ding, H., and Li, L.: Geochemistry of dissolved inorganic carbon and carbonate weathering in a small typical karstic catchment of Southwest China: Isotopic and chemical constraints, *Chemical Geology*, 277, 301–309, doi:10.1016/j.chemgeo.2010.08.013, 2010.
- Li, X., Wang, N., Ding, Y., Hawkings, J. R., Yde, J. C., Raiswell, R., Liu, J., Zhang, S., Kang, S., Wang, R., Liu, Q., Liu, S., Bol, R., You, X., and Li, G.: Globally elevated chemical weathering rates beneath glaciers, *Nature communications*, 13, 407, doi:10.1038/s41467-022-28032-1, 2022.
- Li, Y.: Determining topographic shielding from digital elevation models for cosmogenic nuclide analysis: a GIS approach and field validation, *J. Mt. Sci.*, 10, 355–362, doi:10.1007/s11629-013-2564-1, 2013.
- Lisiecki, L. E.: Ages of MIS boundaries, https://lorraine-lisiecki.com/LR04_MISboundaries.txt, 2022.
- Lisiecki, L. E. and Raymo, M. E.: A Pliocene-Pleistocene stack of 57 globally distributed benthic $\delta^{18}\text{O}$ records, *Paleoceanography*, 20, 1–17, doi:10.1029/2004PA001071, 2005.
- Liu, J. and Han, G.: Effects of chemical weathering and CO_2 outgassing on $\delta^{13}\text{C}_{\text{DIC}}$ signals in a karst watershed, *Journal of Hydrology*, 589, 125192, doi:10.1016/j.jhydrol.2020.125192, 2020.
- Liu, Z., Deng, Z., Davis, S. J., Giron, C., and Ciais, P.: Monitoring global carbon emissions in 2021, *Nat Rev Earth Environ*, 3, 217–219, doi:10.1038/s43017-022-00285-w, 2022.
- Liu, Z., Macpherson, G. L., Groves, C., Martin, J. B., Yuan, D., and Zeng, S.: Large and active CO_2 uptake by coupled carbonate weathering,

- Earth-Science Reviews, 182, 42–49, doi:10.1016/j.earsci-rev.2018.05.007, 2018.
- Loba, A., Waroszewski, J., Sykuła, M., Kabala, C., and Egli, M.: Meteoric ^{10}Be , ^{137}Cs and $^{239+240}\text{Pu}$ as Tracers of Long- and Medium-Term Soil Erosion—A Review, *Minerals*, 12, 359, doi:10.3390/min12030359, 2022.
- Ludwig, W., Amiotte-Suchet, P., Munhoven, G., and Probst, J.-L.: Atmospheric CO_2 consumption by continental erosion: present-day controls and implications for the last glacial maximum, *Global and Planetary Change*, 16-17, 107–120, doi:10.1016/S0921-8181(98)00016-2, 1998.
- Lutsko, N. J. and Popp, M.: The Influence of Meridional Gradients in Insolation and Longwave Optical Depth on the Climate of a Gray Radiation GCM, *J. Climate*, 31, 7803–7822, doi:10.1175/JCLI-D-18-0103.1, 2018.
- Lyons, W. B.: Chemical weathering in high-sediment-yielding watersheds, New Zealand, *J. Geophys. Res.*, 110, doi:10.1029/2003JF000088, 2005.
- Mabit, L., Meusburger, K., Fulajtar, E., and Alewell, C.: The usefulness of ^{137}Cs as a tracer for soil erosion assessment: A critical reply to Parsons and Foster (2011), *Earth-Science Reviews*, 127, 300–307, doi:10.1016/j.earsci-rev.2013.05.008, 2013.
- Macpherson, G. L., Roberts, J. A., Blair, J. M., Townsend, M. A., Fowle, D. A., and Beisner, K. R.: Increasing shallow groundwater CO_2 and limestone weathering, Konza Prairie, USA, *Geochimica et Cosmochimica Acta*, 72, 5581–5599, doi:10.1016/j.gca.2008.09.004, 2008.
- Macpherson, G. L., Sullivan, P. L., Stotler, R. L., and Norwood, B. S.: Increasing groundwater CO_2 in a mid-continent tallgrass prairie: Controlling factors, *E3S Web Conf.*, 98, 6008, doi:10.1051/e3sconf/20199806008, 2019.
- Maher, K.: The dependence of chemical weathering rates on fluid residence time, *Earth and Planetary Science Letters*, 294, 101–110, doi:10.1016/j.epsl.2010.03.010, 2010.
- Martin, L. C. P., Nitzbon, J., Aas, K. S., Etzelmüller, B., Kristiansen, H., and Westermann, S.: Stability Conditions of Peat Plateaus and Palsas in Northern Norway, *JGR Earth Surface*, 124, 705–719, doi:10.1029/2018JF004945, 2019.
- Marx, A., Conrad, M., Aizinger, V., Prechtel, A., van Geldern, R., and Barth, J. A. C.: Groundwater data improve modelling of headwater stream CO_2 outgassing with a stable DIC isotope approach, *Biogeosciences*, 15, 3093–3106, doi:10.5194/bg-15-3093-2018, 2018.

- Marx, A., Dusek, J., Jankovec, J., Sanda, M., Vogel, T., van Geldern, R., Hartmann, J., and Barth, J. A. C.: A review of CO₂ and associated carbon dynamics in headwater streams: A global perspective, *Rev. Geophys.*, 55, 560–585, doi:10.1002/2016RG000547, 2017a.
- Marx, A., Hintze, S., Sanda, M., Jankovec, J., Oulehle, F., Dusek, J., Vitvar, T., Vogel, T., van Geldern, R., and Barth, J. A. C.: Acid rain footprint three decades after peak deposition: Long-term recovery from pollutant sulphate in the Uhlirská catchment (Czech Republic), *The Science of the total environment*, 598, 1037–1049, doi:10.1016/j.scitotenv.2017.04.109, 2017b.
- McClelland, J. W., Holmes, R. M., Peterson, B. J., Amon, R., Brabets, T., Cooper, L., Gibson, J., Gordeev, V. V., Guay, C., Milburn, D., Staples, R., Raymond, P. A., Shiklomanov, I., Striegl, R., Zhulidov, A., Gurtovaya, T., and Zimov, S.: Development of a Pan-Arctic Database for River Chemistry, *Eos Trans. AGU*, 89, 217–218, doi:10.1029/2008EO240001, 2008.
- McGivney, E., Gustafsson, J. P., Belyazid, S., Zetterberg, T., and Löfgren, S.: Assessing the impact of acid rain and forest harvest intensity with the HD-MINTEQ model – soil chemistry of three Swedish conifer sites from 1880 to 2080, *SOIL*, 5, 63–77, doi:10.5194/soil-5-63-2019, 2019.
- McGlynn, B. L. and McDonnell, J. J.: Quantifying the relative contributions of riparian and hillslope zones to catchment runoff, *Water Resour. Res.*, 39, doi:10.1029/2003WR002091, 2003a.
- McGlynn, B. L. and McDonnell, J. J.: Role of discrete landscape units in controlling catchment dissolved organic carbon dynamics, *Water Resour. Res.*, 39, doi:10.1029/2002WR001525, 2003b.
- McGlynn, B. L. and Seibert, J.: Distributed assessment of contributing area and riparian buffering along stream networks, *Water Resour. Res.*, 39, doi:10.1029/2002WR001521, 2003.
- McGuire, A. D., Anderson, L. G., Christensen, T. R., Dallimore, S., Guo, L., Hayes, D. J., Heimann, M., Lorenson, T. D., Macdonald, R. W., and Roulet, N.: Sensitivity of the carbon cycle in the Arctic to climate change, *Ecological Monographs*, 79, 523–555, doi:10.1890/08-2025.1, 2009.
- McGuire, K. J. and McDonnell, J. J.: Hydrological connectivity of hillslopes and streams: Characteristic time scales and nonlinearities, *Water Resour. Res.*, 46, doi:10.1029/2010WR009341, 2010.

- McNamara, J. P., Kane, D. L., and Hinzman, L. D.: Hydrograph separations in an arctic watershed using mixing model and graphical techniques, *Water Resour. Res.*, 33, 1707–1719, doi:10.1029/97WR01033, 1997.
- Merchel, S., Akhmadaliev, S., Pavetich, S., and Rugel, G.: Ungeduldige Forscher träumen mit DREAMS: Bestimmung langlebiger Radionuklide mit Beschleunigermassenspektrometrie, *GIT Labor-Fachzeitschrift*, 56, 88–90, 2012.
- Merchel, S., Arnold, M., Aumaître, G., Benedetti, L., Boulès, D. L., Braucher, R., Alfimov, V., Freeman, S., Steier, P., and Wallner, A.: Towards more precise ^{10}Be and ^{36}Cl data from measurements at the 10–14 level: Influence of sample preparation, *Nuclear Instruments and Methods in Physics Research Section B: Beam Interactions with Materials and Atoms*, 266, 4921–4926, doi:10.1016/j.nimb.2008.07.031, 2008.
- Merchel, S., Gärtner, A., Beutner, S., Bookhagen, B., and Chabilan, A.: Attempts to understand potential deficiencies in chemical procedures for AMS: Cleaning and dissolving quartz for ^{10}Be and ^{26}Al analysis, *Nuclear Instruments and Methods in Physics Research Section B: Beam Interactions with Materials and Atoms*, 455, 293–299, doi:10.1016/j.nimb.2019.02.007, 2019.
- Merchel, S. and Herpers, U.: An Update on Radiochemical Separation Techniques for the Determination of Long-Lived Radionuclides via Accelerator Mass Spectrometry, *Radiochimica Acta*, 84, 215–220, doi:10.1524/ract.1999.84.4.215, 1999.
- Meredith, M., Sommerkorn, M., Cassotta, S., Derksen, D., Ekaykin, A., Hollowed, A., Kofinas, G., Mackintosh, A., Melbourne-Thomas, J., Muelbert, M. M. C., Ottersen, G., Pritchard, H., and Schuur, E. A. G.: Polar Regions, in: *IPCC Special Report on the Ocean and Cryosphere in a Changing Climate*, Pörtner, H.-O., Roberts, D. C., Masson-Delmotte, V., Zhai, P., Tignor, M., Poloczanska, E., Mintenbeck, K., Alegría, A., Nicolai, M., Okem, A., Petzold, J., Rama, B., Weyer, N. M. (Eds.), Cambridge University Press, Cambridge, UK and New York, NY, USA, 203–320, 2019.
- Merlis, T. M. and Henry, M.: Simple Estimates of Polar Amplification in Moist Diffusive Energy Balance Models, *J. Climate*, 31, 5811–5824, doi:10.1175/JCLI-D-17-0578.1, 2018.
- Meusburger, K., Mabit, L., Ketterer, M., Park, J.-H., Sandor, T., Porto, P., and Alewell, C.: A multi-radionuclide approach to evaluate the suitability

- ity of $(^{239}+^{240})\text{Pu}$ as soil erosion tracer, *The Science of the total environment*, 566-567, 1489–1499, doi:10.1016/j.scitotenv.2016.06.035, 2016.
- Meusburger, K., Porto, P., Mabit, L., La Spada, C., Arata, L., and Alewell, C.: Excess Lead-210 and Plutonium-239+240: Two suitable radiogenic soil erosion tracers for mountain grassland sites, *Environmental research*, 160, 195–202, doi:10.1016/j.envres.2017.09.020, 2018.
- Meybeck, M.: Concentration des eaux fluviales en éléments majeurs et apports en solution aux océans, *Revue de géologie dynamique et de géographie physique Paris*, 21, 215–246, 1979.
- Meybeck, M.: Composition chimique des ruisseaux non pollués en France. Chemical composition of headwater streams in France, *sgeol*, 39, 3–77, doi:10.3406/sgeol.1986.1719, 1986.
- Meybeck, M.: Global chemical weathering of surficial rocks estimated from river dissolved loads, *American Journal of Science*, 287, 401–428, doi:10.2475/ajs.287.5.401, 1987.
- Meyboom, P.: Groundwater Studies in the Assiboine River Drainage Basin: Part II: Hydrologic Characteristics of Phreatophytic Vegetation in South-Central Saskatchewan, Geological Survey of Canada, Ottawa, Canada, 1967.
- Michaelis, J.: Carbonate rock dissolution under intermediate system conditions, in: *Progress in Hydrogeochemistry: Organics - Carbonate Systems - Silicate Systems - Microbiology - Models*, Matthes, G., Frimmel, F., Hirsch, P., Schulz, H. D., Usdowski, H.-E. (Eds.), Springer Berlin Heidelberg, Berlin, Heidelberg, 167–174, 1992.
- Michaelis, J., Usdowski, E., and Menschel, G.: Partitioning of ^{13}C and ^{12}C on the degassing of CO_2 and the precipitation of calcite; Rayleigh-type fractionation and a kinetic model, *American Journal of Science*, 285, 318–327, doi:10.2475/ajs.285.4.318, 1985.
- Millero, F. J.: The thermodynamics of the carbonate system in seawater, *Geochimica et Cosmochimica Acta*, 43, 1651–1661, doi:10.1016/0016-7037(79)90184-4, 1979.
- Millot, R., Gaillardet, J., Dupré, B., and Allègre, C. J.: The global control of silicate weathering rates and the coupling with physical erosion: new insights from rivers of the Canadian Shield, *Earth and Planetary Science Letters*, 196, 83–98, doi:10.1016/S0012-821X(01)00599-4, 2002.
- Mintrop, L.: *VINDTA: Versatile INSTRUMENT for the Determination of Titration Alkalinity*, Marianda, 2016.

- Moore, J., Jacobson, A. D., Holmden, C., and Craw, D.: Tracking the relationship between mountain uplift, silicate weathering, and long-term CO₂ consumption with Ca isotopes: Southern Alps, New Zealand, *Chemical Geology*, 341, 110–127, doi:10.1016/j.chemgeo.2013.01.005, 2013.
- Moosdorf, N., Hartmann, J., and Lauerwald, R.: Changes in dissolved silica mobilization into river systems draining North America until the period 2081–2100, *Journal of Geochemical Exploration*, 110, 31–39, doi:10.1016/j.gexplo.2010.09.001, 2011.
- Moss, A. J., Walker, P. H., and Hutka, J.: Movement of loose, sandy detritus by shallow water flows: An experimental study, *Sedimentary Geology*, 25, 43–66, doi:10.1016/0037-0738(80)90053-6, 1980.
- Muller, S. W. and Geological Survey: Permafrost: or permanently frozen ground and related engineering problems, Special report, Strategic engineering study, Army map service, U. S. Army, 1945.
- Mulligan, M., van Soesbergen, A., and Sáenz, L.: GOODD, a global dataset of more than 38,000 georeferenced dams, *Scientific data*, 7, 31, doi:10.1038/s41597-020-0362-5, 2020.
- Muramatsu, Y., Hamilton, T., Uchida, S., Tagami, K., Yoshida, S., and Robison, W.: Measurement of ²⁴⁰Pu/²³⁹Pu isotopic ratios in soils from the Marshall Islands using ICP-MS, *Science of The Total Environment*, 278, 151–159, doi:10.1016/S0048-9697(01)00644-1, 2001.
- Musso, A., Ketterer, M. E., Greinwald, K., Geitner, C., and Egli, M.: Rapid decrease of soil erosion rates with soil formation and vegetation development in periglacial areas, *Earth Surf. Process. Landforms*, 45, 2824–2839, doi:10.1002/esp.4932, 2020.
- Myrabø, S.: Temporal and spatial scale of response area and groundwater variation in Till, *Hydrol. Process.*, 11, 1861–1880, doi:10.1002/(SICI)1099-1085(199711)11:14%3C1861:AID-HYP535%3E3.0.CO;2-P, 1997.
- Natali, S. M., Holdren, J. P., Rogers, B. M., Treharne, R., Duffy, P. B., Pomerance, R., and MacDonald, E.: Permafrost carbon feedbacks threaten global climate goals, *Proceedings of the National Academy of Sciences of the United States of America*, 118, doi:10.1073/pnas.2100163118, 2021.
- Nearing, M. A., Pruski, F. F., and O'Neal, M. R.: Expected climate change impacts on soil erosion rates: A review, *Journal of Soil and Water Conservation*, 59, 43–50, 2004.
- Nelson, D. and Lovett, M.: Oxidation state of plutonium in the Irish Sea, *Nature*, 276, 599–601, doi:10.1038/276599a0, 1978.

- Nezat, C. A., Lyons, W. B., and Welch, K. A.: Chemical weathering in streams of a polar desert (Taylor Valley, Antarctica), *Geological Society of America Bulletin*, 113, 1401–1408, doi:10.1130/0016-7606(2001)113%3C1401:CWISOA%3E2.0.CO;2, 2001.
- NGU: Berggrunn Data N250, Geological Survey of Norway, <https://www.ngu.no/en/topic/datasets>, 2022a.
- NGU: Sediments, Geological Survey of Norway, <https://www.ngu.no/en/topic/datasets>, 2022b.
- Nilsen, K. S.: Karasjok: Berggrunnskart: Karasjok; 20331; 1:50 000; sort/hvitt, Norges geologiske undersøkelse, <https://aps.ngu.no/>, 1986.
- Norwegian Mapping Authority: Norge i bilder, www.norgebilder.no, 2022.
- Obu, J., Westermann, S., Kääh, A., and Bartsch, A.: Ground Temperature Map, 2000-2016, Northern Hemisphere Permafrost, 2018.
- Ochs, M. and Ivy-Ochs, S.: The chemical behavior of Be, Al, Fe, Ca and Mg during AMS target preparation from terrestrial silicates modeled with chemical speciation calculations, *Nuclear Instruments and Methods in Physics Research Section B: Beam Interactions with Materials and Atoms*, 123, 235–240, doi:10.1016/S0168-583X(96)00680-5, 1997.
- O'Leary, M. H.: Carbon Isotopes in Photosynthesis, *BioScience*, 38, 328–336, doi:10.2307/1310735, 1988.
- Olefeldt, D., Goswami, S., Grosse, G., Hayes, D., Hugelius, G., Kuhry, P., McGuire, A. D., Romanovsky, V. E., Sannel, A. B. K., Schuur, E. A. G., and Turetsky, M. R.: Circumpolar distribution and carbon storage of thermokarst landscapes, *Nature communications*, 7, 13043, doi:10.1038/ncomms13043, 2016.
- Oliva, P., Dupré, B., Martin, F., and Viers, J.: The role of trace minerals in chemical weathering in a high-elevation granitic watershed (Estibère, France): chemical and mineralogical evidence, *Geochimica et Cosmochimica Acta*, 68, 2223–2243, doi:10.1016/j.gca.2003.10.043, 2004.
- Oliver, L., Harris, N., Bickle, M., Chapman, H., Dise, N., and Horstwood, M.: Silicate weathering rates decoupled from the $^{87}\text{Sr}/^{86}\text{Sr}$ ratio of the dissolved load during Himalayan erosion, *Chemical Geology*, 201, 119–139, doi:10.1016/S0009-2541(03)00236-5, 2003.
- Olsen, L.: Stadials and interstadials during the Weichsel glackiation on Finnmarksvidda, northern Norway, *Boreas*, 17, 517–539, doi:10.1111/j.1502-3885.1988.tb00566.x, 1988.
- Olsen, L., Fredin, O., and Olesen, O.: Quaternary Geology of Norway, Geological Survey of Norway Special Publication 13, 2013.

- Olsen, L., Mejdahl, V., and Selvik, S. F.: Middle and Late Pleistocene stratigraphy, chronology and glacial history in Finnmark, North Norway, *NGU Bulletin*, 429, 1–111, 1996.
- O'Nions, R. K., Morton, R. D., and Batey, R.: Geological investigations in the Bamble sector of the Fennoscandian Shield South Norway: I. The geology of eastern Bamble, Universitetsforlaget, Oslo, Norway, 1970.
- Onuchin, A. A. and Burenina, T. A.: Climatic and Geographic Patterns in Snow Density Dynamics, Northern Eurasia, *Arctic and Alpine Research*, 28, 99, doi:10.2307/1552091, 1996.
- Osborne, E., Richter-Menge, J., and Jeffries, M.: Arctic report card 2018, Arctic Program, <https://www.arctic.noaa.gov/Report-Card>, 2018.
- Osterkamp, T. E., Jorgenson, M. T., Schuur, E. A. G., Shur, Y. L., Kanevskiy, M. Z., Vogel, J. G., and Tumskey, V. E.: Physical and ecological changes associated with warming permafrost and thermokarst in Interior Alaska, *Permafrost Periglac. Process.*, 20, 235–256, doi:10.1002/ppp.656, 2009.
- Petrone, K. C., Hinzman, L. D., Shibata, H., Jones, J. B., and Boone, R. D.: The influence of fire and permafrost on sub-arctic stream chemistry during storms, *Hydrol. Process.*, 21, 423–434, doi:10.1002/hyp.6247, 2007.
- Pierrot, D. E., Wallace, D., and Lewis, E.: CO2SYS, Carbon Dioxide Information Analysis Center, 2011.
- Pokrovsky, O. S., Manasypov, R. M., Loiko, S., Shirokova, L. S., Krickov, I. A., Pokrovsky, B. G., Kolesnichenko, L. G., Kopysov, S. G., Zemtsov, V. A., Kulizhsky, S. P., Vorobyev, S. N., and Kirpotin, S. N.: Permafrost coverage, watershed area and season control of dissolved carbon and major elements in western Siberian rivers, *Biogeosciences*, 12, 6301–6320, doi:10.5194/bg-12-6301-2015, 2015.
- Polsenaere, P. and Abril, G.: Modelling CO₂ degassing from small acidic rivers using water pCO₂, DIC and δ¹³C-DIC data, *Geochimica et Cosmochimica Acta*, 91, 220–239, doi:10.1016/j.gca.2012.05.030, 2012.
- Porter, C., Morin, P., Howat, I., Noh, M.-J., Bates, B., Peterman, K., Keeseey, S., Schlenk, M., Gardiner, J., Tomko, K., Willis, M., Kelleher, C., Cloutier, M., Husby, E., Foga, S., Nakamura, H., Platson, M., Wethington, M., JR., Williamson, C., Bauer, G., Enos, J., Arnold, G., Kramer, W., Becker, P., Doshi, A., D'Souza, C., Cummins, P., Laurier, F., and Bojesen, M.: ArcticDEM: V1, Harvard Dataverse, 2018.
- Portes, R., Dahms, D., Brandová, D., Raab, G., Christl, M., Kühn, P., Ketterer, M., and Egli, M.: Evolution of soil erosion rates in alpine soils of

- the Central Rocky Mountains using fallout Pu and $\delta^{13}\text{C}$, *Earth and Planetary Science Letters*, 496, 257–269, doi:10.1016/j.epsl.2018.06.002, 2018.
- Previdi, M., Smith, K. L., and Polvani, L. M.: Arctic amplification of climate change: a review of underlying mechanisms, *Environ. Res. Lett.*, 16, 93003, doi:10.1088/1748-9326/ac1c29, 2021.
- Purkamo, L., Ahn, C. M. E. von, Jilbert, T., Muniruzzaman, M., Bange, H. W., Jenner, A.-K., Böttcher, M. E., and Virtasalo, J. J.: Impact of submarine groundwater discharge on biogeochemistry and microbial communities in pockmarks, *Geochimica et Cosmochimica Acta*, 334, 14–44, doi:10.1016/j.gca.2022.06.040, 2022.
- QGIS.org: QGIS Geographic Information System, QGIS Association, <http://www.qgis.org>, 2022.
- R Core Team: R, R Foundation for Statistical Computing, Vienna, Austria, 2020.
- Rantanen, M., Karpechko, A. Y., Lipponen, A., Nordling, K., Hyvärinen, O., Ruosteenoja, K., Vihma, T., and Laaksonen, A.: The Arctic has warmed nearly four times faster than the globe since 1979, *Commun Earth Environ*, 3, doi:10.1038/s43247-022-00498-3, 2022.
- Rawlins, M. A., Steele, M., Holland, M. M., Adam, J. C., Cherry, J. E., Francis, J. A., Groisman, P. Y., Hinzman, L. D., Huntington, T. G., Kane, D. L., Kimball, J. S., Kwok, R., Lammers, R. B., Lee, C. M., Lettenmaier, D. P., McDonald, K. C., Podest, E., Pundsack, J. W., Rudels, B., Serreze, M. C., Shiklomanov, A., Skagseth, Ø., Troy, T. J., Vörösmarty, C. J., Wensnahan, M., Wood, E. F., Woodgate, R., Yang, D., Zhang, K., and Zhang, T.: Analysis of the Arctic System for Freshwater Cycle Intensification: Observations and Expectations, *J. Climate*, 23, 5715–5737, doi:10.1175/2010JCLI3421.1, 2010.
- Raymo, M. E., Ruddiman, W. F., Backman, J., Clement, B. M., and Martinson, D. G.: Late Pliocene variation in northern hemisphere ice sheets and North Atlantic deep water circulation, *Paleoceanography*, 4, 413–446, doi:10.1029/PA004i004p00413, 1989.
- Raymond, P. A. and Hamilton, S. K.: Anthropogenic influences on riverine fluxes of dissolved inorganic carbon to the oceans, *Limnol Oceanogr Letters*, 3, 143–155, doi:10.1002/lol2.10069, 2018.
- Raymond, P. A., Oh, N.-H., Turner, R. E., and Broussard, W.: Anthropogenically enhanced fluxes of water and carbon from the Mississippi River, *Nature*, 451, 449–452, doi:10.1038/nature06505, 2008.

- Rey, F.: Effectiveness of vegetation barriers for marly sediment trapping, *Earth Surf. Process. Landforms*, 29, 1161–1169, doi:10.1002/esp.1108, 2004.
- Riebe, C. S., Kirchner, J. W., and Finkel, R. C.: Erosional and climatic effects on long-term chemical weathering rates in granitic landscapes spanning diverse climate regimes, *Earth and Planetary Science Letters*, 224, 547–562, doi:10.1016/j.epsl.2004.05.019, 2004.
- Riley, S. J., DeGloria, S. D., and Elliot, R.: A terrain ruggedness index that quantifies topographic heterogeneity, *Intermountain Journal of Sciences*, 5, 23–27, 1999.
- Roering, J. J., Almond, P., Tonkin, P., and McKean, J.: Soil transport driven by biological processes over millennial time scales, *Geology*, 30, 1115, doi:10.1130/0091-7613(2002)030%3C1115:STDBBP%3E2.0.CO;2, 2002.
- Roering, J. J., Marshall, J., Booth, A. M., Mort, M., and Jin, Q.: Evidence for biotic controls on topography and soil production, *Earth and Planetary Science Letters*, 298, 183–190, doi:10.1016/j.epsl.2010.07.040, 2010.
- Rohrweber, A.-C.: Optimized analysis of Pu-239 and Pu-240 in geological samples via ICP–MS/MS for use as a tracer for soil erosion rates, Master Thesis, University of Hamburg, Hamburg, Germany, 2022.
- Romero-Mujalli, G., Hartmann, J., and Börker, J.: Temperature and CO₂ dependency of global carbonate weathering fluxes – Implications for future carbonate weathering research, *Chemical Geology*, 527, 118874, doi:10.1016/j.chemgeo.2018.08.010, 2019a.
- Romero-Mujalli, G., Hartmann, J., Börker, J., Gaillardet, J., and Calmels, D.: Ecosystem controlled soil-rock pCO₂ and carbonate weathering – Constraints by temperature and soil water content, *Chemical Geology*, 527, 118634, doi:10.1016/j.chemgeo.2018.01.030, 2019b.
- Rouault, E., Warmerdam, F., Schwehr, K., Kiselev, A., Butler, H., Łoskot, M., Szekeres, T., Tourigny, E., Landa, M., Miara, I., Elliston, B., Kumar, C., Plesea, L., Morissette, D., Jolma, A., and Dawson, N.: GDAL, Zenodo, 2022.
- Rowland, J. C., Jones, C. E., Altmann, G., Bryan, R., Crosby, B. T., Hinzman, L. D., Kane, D. L., Lawrence, D. M., Mancino, A., Marsh, P., McNamara, J. P., Romanovsky, V. E., Toniolo, H., Travis, B. J., Trochim, E., Wilson, C. J., and Geernaert, G. L.: Arctic Landscapes in Transition: Responses to Thawing Permafrost, *Eos Trans. AGU*, 91, 229–230, doi:10.1029/2010eo260001, 2010.

- Ruddiman, W. F., Raymo, M. E., Martinson, D. G., Clement, B. M., and Backman, J.: Pleistocene evolution: Northern hemisphere ice sheets and North Atlantic Ocean, *Paleoceanography*, 4, 353–412, doi:10.1029/PA004i004p00353, 1989.
- Rugel, G., Pavetich, S., Akhmadaliev, S., Enamorado Baez, S. M., Scharf, A., Ziegenrucker, R., and Merchel, S.: The first four years of the AMS-facility DREAMS: Status and developments for more accurate radionuclide data, *Nuclear Instruments and Methods in Physics Research Section B: Beam Interactions with Materials and Atoms*, 370, 94–100, doi:10.1016/j.nimb.2016.01.012, 2016.
- Sanchez, G. and Puigdefabregas, J.: Interactions of plant growth and sediment movement on slopes in a semi-arid environment, *Geomorphology*, 9, 243–260, doi:10.1016/0169-555X(94)90066-3, 1994.
- Sandström, B. and Tullborg, E.-L.: Episodic fluid migration in the Fennoscandian Shield recorded by stable isotopes, rare earth elements and fluid inclusions in fracture minerals at Forsmark, Sweden, *Chemical Geology*, 266, 126–142, doi:10.1016/j.chemgeo.2009.04.019, 2009.
- Schaefer, K. W. and Usdowski, E.: Models for the dissolution of carbonate rocks and the carbon-13/carbon-12 evolution of carbonate groundwaters, *Zeitschrift fuer Wasser- und Abwasser-Forschung*, 20, 69–81, 1987.
- Schaefer, K. W. and Usdowski, E.: Application of stable carbon and sulfur isotope models to the development of ground water in a limestone-dolomite-anhydrite-gypsum area, in: *Progress in Hydrogeochemistry: Organics - Carbonate Systems - Silicate Systems - Microbiology - Models*, Matthes, G., Frimmel, F., Hirsch, P., Schulz, H. D., Usdowski, H.-E. (Eds.), Springer Berlin Heidelberg, Berlin, Heidelberg, 157–163, 1992.
- Schoonejans, J., Vanacker, V., Opfergelt, S., Ameijeiras-Mariño, Y., and Christl, M.: Kinetically limited weathering at low denudation rates in semiarid climatic conditions, *JGR Earth Surface*, 121, 336–350, doi:10.1002/2015JF003626, 2016.
- Schroeder, E. D.: Water Resources, in: *Encyclopedia of physical science and technology*, 3. ed., Meyers, R. A. (Ed.), Academic Press, San Diego, 721–751, 2002.
- Schuur, E. A. G., McGuire, A. D., Schädel, C., Grosse, G., Harden, J. W., Hayes, D. J., Hugelius, G., Koven, C. D., Kuhry, P., Lawrence, D. M., Natali, S. M., Olefeldt, D., Romanovsky, V. E., Schaefer, K., Turetsky,

- M. R., Treat, C. C., and Vonk, J. E.: Climate change and the permafrost carbon feedback, *Nature*, 520, 171–179, doi:10.1038/nature14338, 2015.
- Seibert, J., Grabs, T., Köhler, S., Laudon, H., Winterdahl, M., and Bishop, K.: Linking soil- and stream-water chemistry based on a Riparian Flow-Concentration Integration Model, *Hydrol. Earth Syst. Sci.*, 13, 2287–2297, doi:10.5194/hess-13-2287-2009, 2009.
- Seklima: Observations and weather statistics, Norsk Klimaservicesenter, <https://seklima.met.no/observations/>, 2020.
- Shadwick, E. H., Thomas, H., Gratton, Y., Leong, D., Moore, S. A., Papyriakou, T., and Prowe, A.: Export of Pacific carbon through the Arctic Archipelago to the North Atlantic, *Continental Shelf Research*, 31, 806–816, doi:10.1016/j.csr.2011.01.014, 2011.
- Shadwick, E. H., Trull, T. W., Thomas, H., and Gibson, J. A. E.: Vulnerability of polar oceans to anthropogenic acidification: comparison of arctic and antarctic seasonal cycles, *Scientific reports*, 3, 2339, doi:10.1038/srep02339, 2013.
- Shangguan, W., Hengl, T., Mendes de Jesus, J., Yuan, H., and Dai, Y.: Mapping the global depth to bedrock for land surface modeling, *J. Adv. Model. Earth Syst.*, 9, 65–88, doi:10.1002/2016MS000686, 2017.
- Shelef, E., Griffore, M., Mark, S., Coleman, T., Wondolowski, N., Lasher, G. E., and Abbott, M.: Sensitivity of Erosion-Rate in Permafrost Landscapes to Changing Climatic and Environmental Conditions Based on Lake Sediments From Northwestern Alaska, *Earth's Future*, 10, doi:10.1029/2022EF002779, 2022.
- Shin, W. J., Chung, G. S., Lee, D., and Lee, K. S.: Dissolved inorganic carbon export from carbonate and silicate catchments estimated from carbonate chemistry and $\delta^{13}\text{C}_{\text{DIC}}$, *Hydrol. Earth Syst. Sci.*, 15, 2551–2560, doi:10.5194/hess-15-2551-2011, 2011.
- Singh, H. A., Garuba, O. A., and Rasch, P. J.: How Asymmetries Between Arctic and Antarctic Climate Sensitivity Are Modified by the Ocean, *Geophys. Res. Lett.*, 45, doi:10.1029/2018GL079023, 2018.
- Sklar, L. and Dietrich, W. E.: River longitudinal profiles and bedrock incision models: Stream power and the influence of sediment supply, in: *Rivers Over Rock: Fluvial Processes in Bedrock Channels*, Tinkler, J., Wohl, E. (Eds.), Geophysical Monograph Series, American Geophysical Union, Washington, D. C., 237–260, 1998.
- Sollid, J. L., Andersen, S., Hamre, N., Kjeldsen, O., Salvigsen, O., Sturød, S., Tveitå, T., and Wilhelmsen, A.: Deglaciation of Finnmark,

- North Norway, *Norsk Geografisk Tidsskrift - Norwegian Journal of Geography*, 27, 233–325, doi:10.1080/00291951.1973.9728306, 1973.
- Speetjens, N. J., Hugelius, G., Gumbrecht, T., Lantuit, H., Berghuijs, W., Pika, P., Poste, A., and Vonk, J.: The Pan-Arctic Catchment Database (ARCADE), 2022.
- Stacke, T. and Hagemann, S.: HydroPy (v1.0): a new global hydrology model written in Python, *Geosci. Model Dev.*, 14, 7795–7816, doi:10.5194/gmd-14-7795-2021, 2021.
- Stallard, R. F.: Tectonic, Environmental, and Human Aspects of Weathering and Erosion: A Global Review using a Steady-State Perspective, *Annu. Rev. Earth Planet. Sci.*, 23, 11–39, doi:10.1146/annurev.ea.23.050195.000303, 1995.
- Stallard, R. F. and Edmond, J. M.: Geochemistry of the Amazon: 2. The influence of geology and weathering environment on the dissolved load, *J. Geophys. Res.*, 88, 9671–9688, doi:10.1029/JC088iC14p09671, 1983.
- Stallard, R. F. and Edmond, J. M.: Geochemistry of the Amazon: 3. Weathering chemistry and limits to dissolved inputs, *J. Geophys. Res.*, 92, 8293, doi:10.1029/JC092iC08p08293, 1987.
- Stone, J. O.: Air pressure and cosmogenic isotope production, *J. Geophys. Res.*, 105, 23753–23759, doi:10.1029/2000JB900181, 2000.
- Stone, L. E., Fang, X., Haynes, K. M., Helbig, M., Pomeroy, J. W., Sontag, O., and Quinton, W. L.: Modelling the effects of permafrost loss on discharge from a wetland-dominated, discontinuous permafrost basin, *Hydrol. Process.*, 33, 2607–2626, doi:10.1002/hyp.13546, 2019.
- Striegl, R. G., Aiken, G. R., Dornblaser, M. M., Raymond, P. A., and Wickland, K. P.: A decrease in discharge-normalized DOC export by the Yukon River during summer through autumn, *Geophys. Res. Lett.*, 32, doi:10.1029/2005GL024413, 2005.
- Stroeven, A. P., Hättestrand, C., Kleman, J., Heyman, J., Fabel, D., Fredin, O., Goodfellow, B. W., Harbor, J. M., Jansen, J. D., Olsen, L., Caffee, M. W., Fink, D., Lundqvist, J., Rosqvist, G. C., Strömberg, B., and Jansson, K. N.: Deglaciation of Fennoscandia, *Quaternary Science Reviews*, 147, 91–121, doi:10.1016/j.quascirev.2015.09.016, 2016.
- Stroeven, A. P., Heyman, J., Fabel, D., Björck, S., Caffee, M. W., Fredin, O., and Harbor, J. M.: A new Scandinavian reference ^{10}Be production rate, *Quaternary Geochronology*, 29, 104–115, doi:10.1016/j.quageo.2015.06.011, 2015.

- Stumm, W. and Morgan, J. J.: Aquatic chemistry an introduction chemical equilibria in natural water: 2nd ed., A Wiley-Interscience Publication, Wiley, New York, 780 pp., 1981.
- Summerfield, M. A. and Hulton, N. J.: Natural controls of fluvial denudation rates in major world drainage basins, *J. Geophys. Res.*, 99, 13871–13883, doi:10.1029/94JB00715, 1994.
- Tananaev, N. and Lotsari, E.: Defrosting northern catchments: Fluvial effects of permafrost degradation, *Earth-Science Reviews*, 228, 103996, doi:10.1016/j.earscirev.2022.103996, 2022.
- Tank, S. E., Frey, K. E., Striegl, R. G., Raymond, P. A., Holmes, R. M., McClelland, J. W., and Peterson, B. J.: Landscape-level controls on dissolved carbon flux from diverse catchments of the circumboreal, *Global Biogeochem. Cycles*, 26, doi:10.1029/2012GB004299, 2012.
- Tank, S. E., Striegl, R. G., McClelland, J. W., and Kokelj, S. V.: Multi-decadal increases in dissolved organic carbon and alkalinity flux from the Mackenzie drainage basin to the Arctic Ocean, *Environ. Res. Lett.*, 11, 54015, doi:10.1088/1748-9326/11/5/054015, 2016.
- Tanneberger, F., Tegetmeyer, C., Busse, S., Barthelmes, A., and 55 others: The peatland map of Europe, *Mires and Peat*, 19, 1–17, 2017.
- Toniolo, H., Kodial, P., Hinzman, L. D., and Yoshikawa, K.: Spatio-temporal evolution of a thermokarst in Interior Alaska, *Cold Regions Science and Technology*, 56, 39–49, doi:10.1016/j.coldregions.2008.09.007, 2009.
- Torres, M. A., West, A. J., Clark, K. E., Paris, G., Bouchez, J., Ponton, C., Feakins, S. J., Galy, V., and Adkins, J. F.: The acid and alkalinity budgets of weathering in the Andes–Amazon system: Insights into the erosional control of global biogeochemical cycles, *Earth and Planetary Science Letters*, 450, 381–391, doi:10.1016/j.epsl.2016.06.012, 2016.
- Trolier, M., White, J. W. C., Tans, P. P., Masarie, K. A., and Gemery, P. A.: Monitoring the isotopic composition of atmospheric CO₂ Measurements from the NOAA Global Air Sampling Network, *J. Geophys. Res.*, 101, 25897–25916, doi:10.1029/96JD02363, 1996.
- Vidon, P.: Towards a better understanding of riparian zone water table response to precipitation: surface water infiltration, hillslope contribution or pressure wave processes?, *Hydrol. Process.*, 26, 3207–3215, doi:10.1002/hyp.8258, 2012.
- Waldbauer, J. R. and Chamberlain, C. P.: Influence of uplift, weathering and base cation supply on past and future CO₂ levels., in: *A history of atmospheric CO₂ and its effects on plants, animals, and ecosystems*, Baldwin, I. T., Caldwell, M. M., Heldmaier, G., Jackson, R. B., Lange,

- O. L., Mooney, H. A., Schulze, E.-D., Sommer, U., Ehleringer, J. R., Dearing, M. D., Cerling, T. E. (Eds.), *Ecological Studies, Analysis and Synthesis*, 177, Springer Verlag, New York, NY, 2005.
- Walker, J. C. G., Hays, P. B., and Kasting, J. F.: A negative feedback mechanism for the long-term stabilization of Earth's surface temperature, *J. Geophys. Res.*, 86, 9776, doi:10.1029/JC086iC10p09776, 1981.
- Walvoord, M. A. and Striegl, R. G.: Increased groundwater to stream discharge from permafrost thawing in the Yukon River basin: Potential impacts on lateral export of carbon and nitrogen, *Geophys. Res. Lett.*, 34, doi:10.1029/2007GL030216, 2007.
- Warner, D. L., Bond-Lamberty, B., Jian, J., Stell, E., and Vargas, R.: Spatial Predictions and Associated Uncertainty of Annual Soil Respiration at the Global Scale, *Global Biogeochem. Cycles*, 33, 1733–1745, doi:10.1029/2019GB006264, 2019.
- Watts, J. D., Natali, S., and Minions, C.: Soil Respiration Maps for the ABoVE Domain, 2016-2017, 2022.
- Watts, J. D., Natali, S. M., Minions, C., Risk, D., Arndt, K., Zona, D., Euskirchen, E. S., Rocha, A. V., Sonnentag, O., Helbig, M., Kalhori, A., Oechel, W., Ikawa, H., Ueyama, M., Suzuki, R., Kobayashi, H., Celis, G., Schuur, E. A. G., Humphreys, E., Kim, Y., Lee, B.-Y., Goetz, S., Madani, N., Schiferl, L. D., Commane, R., Kimball, J. S., Liu, Z., Torn, M. S., Potter, S., Wang, J. A., Jorgenson, M. T., Xiao, J., Li, X., and Edgar, C.: Soil respiration strongly offsets carbon uptake in Alaska and Northwest Canada, *Environ. Res. Lett.*, 16, 84051, doi:10.1088/1748-9326/ac1222, 2021.
- Wegner, C., Bennett, K. E., Vernal, A. de, Forwick, M., Fritz, M., Heikkilä, M., Łacka, M., Lantuit, H., Laska, M., Moskalik, M., O'Regan, M., Pawłowska, J., Promińska, A., Rachold, V., Vonk, J. E., and Werner, K.: Variability in transport of terrigenous material on the shelves and the deep Arctic Ocean during the Holocene, *Polar Research*, 34, doi:10.3402/polar.v%v.24964, 2015.
- Weiler, M., McDonnell, J. J., Tromp-van Meerveld, I., and Uchida, T.: Subsurface Stormflow, in: *Encyclopedia of Hydrological Sciences*, Anderson, M. G., McDonnell, J. J. (Eds.), John Wiley & Sons, Ltd, Chichester, UK, 2006.
- West, A. J., Galy, A., and Bickle, M.: Tectonic and climatic controls on silicate weathering, *Earth and Planetary Science Letters*, 235, 211–228, 2005.

- White, A. F. and Blum, A. E.: Effects of climate on chemical weathering in watersheds, *Geochimica et Cosmochimica Acta*, 59, 1729–1747, doi:10.1016/0016-7037(95)00078-E, 1995.
- White, A. F. and Brantley, S. L.: The effect of time on the weathering of silicate minerals: why do weathering rates differ in the laboratory and field?, *Chemical Geology*, 202, 479–506, doi:10.1016/j.chemgeo.2003.03.001, 2003.
- White, A. F., Bullen, T. D., Vivit, D. V., Schulz, M. S., and Clow, D. W.: The role of disseminated calcite in the chemical weathering of granitoid rocks, *Geochimica et Cosmochimica Acta*, 63, 1939–1953, doi:10.1016/S0016-7037(99)00082-4, 1999.
- White, A. F., Schulz, M. S., Lowenstern, J. B., Vivit, D. V., and Bullen, T. D.: The ubiquitous nature of accessory calcite in granitoid rocks: Implications for weathering, solute evolution, and petrogenesis, *Geochimica et Cosmochimica Acta*, 69, 1455–1471, doi:10.1016/j.gca.2004.09.012, 2005.
- Willenbring, J. K., Codilean, A. T., and McElroy, B.: Earth is (mostly) flat: Apportionment of the flux of continental sediment over millennial time scales, *Geology*, 41, 343–346, doi:10.1130/G33918.1, 2013.
- Winde, V., Böttcher, M. E., Escher, P., Böning, P., Beck, M., Liebezeit, G., and Schneider, B.: Tidal and spatial variations of DI13C and aquatic chemistry in a temperate tidal basin during winter time, *Journal of Marine Systems*, 129, 396–404, doi:10.1016/j.jmarsys.2013.08.005, 2014.
- Winnick, M. J., Carroll, R. W. H., Williams, K. H., Maxwell, R. M., Dong, W., and Maher, K.: Snowmelt controls on concentration-discharge relationships and the balance of oxidative and acid-base weathering fluxes in an alpine catchment, *East River, Colorado, Water Resour. Res.*, 53, 2507–2523, doi:10.1002/2016WR019724, 2017.
- Wittmann, H., Oelze, M., Gaillardet, J., Garzanti, E., and Blanckenburg, F. von: A global rate of denudation from cosmogenic nuclides in the Earth's largest rivers, *Earth-Science Reviews*, 204, 103147, doi:10.1016/j.earscirev.2020.103147, 2020.
- Woo, M.: Hydrology of a Drainage Basin in the Canadian High Arctic, *Annals of the Association of American Geographers*, 73, 577–596, doi:10.1111/j.1467-8306.1983.tb01860.x, 1983.
- Wood, S. N.: Fast stable restricted maximum likelihood and marginal likelihood estimation of semiparametric generalized linear models, *Journal of the Royal Statistical Society: Series B (Statistical Methodology)*, 73, 3–36, doi:10.1111/j.1467-9868.2010.00749.x, 2011.

- Xu, Y., Pan, S., Wu, M., Zhang, K., and Hao, Y.: Association of Plutonium isotopes with natural soil particles of different size and comparison with ^{137}Cs , *The Science of the total environment*, 581-582, 541–549, doi:10.1016/j.scitotenv.2016.12.162, 2017.
- Xu, Y., Qiao, J., Pan, S., Hou, X., Roos, P., and Cao, L.: Plutonium as a tracer for soil erosion assessment in northeast China, *The Science of the total environment*, 511, 176–185, doi:10.1016/j.scitotenv.2014.12.006, 2015.
- Yuanrong, S., Ruihong, Y., Mingyang, T., Xiankun, Y., Lishan, R., Haizhu, H., Zhuangzhuang, Z., and Xixi, L.: Major ion chemistry in the headwater region of the Yellow River: impact of land covers, *Environ Earth Sci*, 80, doi:10.1007/s12665-021-09692-6, 2021.
- Zeebe, R. E. and Westbroek, P.: A simple model for the CaCO_3 saturation state of the ocean: The “Strangelove,” the “Neritan,” and the “Cretan” Ocean, *Geochem. Geophys. Geosyst.*, 4, doi:10.1029/2003GC000538, 2003.
- Zeng, S., Kaufmann, G., and Liu, Z.: Natural and Anthropogenic Driving Forces of Carbonate Weathering and the Related Carbon Sink Flux: A Model Comparison Study at Global Scale, *Global Biogeochem. Cycles*, 36, doi:10.1029/2021GB007096, 2022.
- Zeng, S., Liu, Z., and Kaufmann, G.: Sensitivity of the global carbonate weathering carbon-sink flux to climate and land-use changes, *Nature communications*, 10, 5749, doi:10.1038/s41467-019-13772-4, 2019.
- Zhang, J., Quay, P. D., and Wilbur, D. O.: Carbon isotope fractionation during gas-water exchange and dissolution of CO_2 , *Geochimica et Cosmochimica Acta*, 59, 107–114, doi:10.1016/0016-7037(95)91550-D, 1995.
- Zhang, X., He, J., Zhang, J., Polyakov, I., Gerdes, R., Inoue, J., and Wu, P.: Enhanced poleward moisture transport and amplified northern high-latitude wetting trend, *Nature Clim Change*, 3, 47–51, doi:10.1038/nclimate1631, 2013.
- Zolkos, S., Tank, S. E., Striegl, R. G., Kokelj, S. V., Kokoszka, J., Estop-Aragonés, C., and Olefeldt, D.: Thermokarst amplifies fluvial inorganic carbon cycling and export across watershed scales on the Peel Plateau, Canada, *Biogeosciences*, 17, 5163–5182, doi:10.5194/bg-17-5163-2020, 2020.
- Zollinger, B., Alewell, C., Kneisel, C., Brandová, D., Petrillo, M., Plötze, M., Christl, M., and Egli, M.: Soil formation and weathering in a permafrost environment of the Swiss Alps: a multi-parameter and non-

steady-state approach, *Earth Surf. Process. Landforms*, 42, 814–835, doi:10.1002/esp.4040, 2017.

Zollinger, B., Alewell, C., Kneisel, C., Meusburger, K., Brandová, D., Kubik, P., Schaller, M., Ketterer, M., and Egli, M.: The effect of permafrost on time-split soil erosion using radionuclides (^{137}Cs , $^{239} + ^{240}\text{Pu}$, meteoric ^{10}Be) and stable isotopes ($\delta^{13}\text{C}$) in the eastern Swiss Alps, *J Soils Sediments*, 15, 1400–1419, doi:10.1007/s11368-014-0881-9, 2015.

Zweck, C., Zreda, M., and Desilets, D.: Snow shielding factors for cosmogenic nuclide dating inferred from Monte Carlo neutron transport simulations, *Earth and Planetary Science Letters*, 379, 64–71, doi:10.1016/j.epsl.2013.07.023, 2013.

Acknowledgements

Reflecting back on the adventurous and challenging last three years of my PhD, I am very thankful for all the support I received during this time. I started the journey as a geochemistry greenhorn (“What does ‘DIC’ stand for?”) and feel I have now truly arrived at my nerdy ^{10}Be erosion rate/weathering-liberated alkalinity niche. I would like to thank my one supervisor, Helmuth Thomas, for giving me the opportunity to change my field of work to geochemistry and introducing me to the interesting world of alkalinity in a changing climate. Thank you for giving me ownership of my research and scientific guidance. I especially thank you for the times when you still saw the forest for the trees when I had already started to examine the leaf structure. I wish to thank my other supervisor, Hugues Lantuit, for his great supervision, despite distance and Covid. Thank you for the scientific-constructive meetings and the many entertaining meetings. When Covid started and all field campaign plans fell through, you sought an alternative in Norway with me, thank you! Many thanks to the additional members of my PhD committee, Thorsten Dittmar and John Gosse, who followed the progress of the project and contributed to the discussions. John, I especially thank you for the ‘erosion rate meeting week’ in Halifax at the beginning of my PhD, through which my project was steered in the right direction. I would like to thank Konstanze Stübner first for her help in processing the ^{10}Be samples and second for her scientific guidance in erosion rate interpretation. Thank you for having my back. Furthermore, I wish to thank Michael Böttcher and Peter Fiener for their valuable scientific input.

This PhD would not have been possible without receiving funding from the German Federal Ministry of Education and Research (BMBF) under “Make our Planet Great Again – German Research Initiative”. I am grateful for this funding, which allowed me to conduct fieldwork and attend conferences. I wish to thank both the Helmholtz-Zentrum Hereon and the Alfred Wegener Institute (AWI) for hosting me, and helping me with travel arrangements and logistical coordination of field campaigns. I would also like to thank the Ion Beam Centre at the Helmholtz-Zentrum Dresden-Rossendorf (HZDR) for the hospitality during my numerous research visits and providing the infrastructure for ^{10}Be sample preparation and AMS measurements.

Through the POLMAR graduate school, I was able to participate in interesting courses that helped me grow professionally and personally. Thank you so much, Claudia Hanfland and Claudia Sprengel. Your work does make a big difference!

I would like to thank all the members of my KCK working group at Hereon for their support. I would like to thank especially Mona Norbistrath for her support and friendship. Thank you for always keeping an open ear for me. I would also like to give a special thanks to Kathleen Hobus and Catharina Petrauskas for their assistance in the lab. I wish to thank all the members of the COPER group at AWI. Even though Covid made a lot of things difficult, the online meetings with you that took place regularly as a result made me feel (virtually) at home also in Potsdam. I wish to thank KCK's neighboring department, KUA, for their assistance with ICP-MS measurements, providing laboratory infrastructure, and pleasant hallway conversations. Moreover, I would like to thank all members of the FWIR group at HZDR for their hospitality during my research stays in Dresden and their assistance, together with the DREAMS operator team, with AMS-measurements. Additionally, I wish to thank Peggy Bartsch for measuring alkalinity, Iris Schmiedinger for measuring stable isotopes, Antje Eulenburg for measuring cation and anion concentrations, Michael Ketterer for measuring $^{239+240}\text{Pu}$, and Linda Baldewein for helping in data stewardship. I wish to thank Sebastian Westermann for providing information on logistics and permit acquisition and sharing his experience with fieldwork in the area of Iskoras in northern Norway.

Last, but not least, I wish to thank my friends and family. This thesis would literally not have been possible without you! Special thanks to Laura Luitjens and Maike Ostermann, who climbed down with me even the most daring slopes to the rivers to be sampled in Austria, Switzerland and Italy. Thank you Philipp Knobloch for wearing the super cute GPS cap when nobody else would. Special thanks go to my parents, Heidrun and Christoph Treblin. Without you, I would not be where I am today. Thanks for always supporting me! Very special thanks goes to my sister, Mascha Treblin, and her partner, Lukas Detjen. Thank you for marching with me through the Norwegian Arctic tundra for three weeks and tirelessly supporting me in sample acquisition, food preparation and transport. Thank you, Mascha and Mama, for accompanying me for the sampling in the Black Forest. You made sure that I got all the intended water samples in the end, despite non-stop rain and wild-eyed bulls. Finally, I wish to thank my husband, Sebastian Lehmann, with all my heart. Besides the technical support through your knowledge in statistics and R , you gave me the greatest moral support I could imagine. I could always rely on you.

Eidesstaatliche Erklärung

Hiermit versichere ich, dass ich die vorliegende Arbeit selbstständig angefertigt und keine anderen als die angegebenen Quellen und Hilfsmittel verwendet habe. Zusätzlich erkläre ich, dass diese Dissertation weder in ihrer Gesamtheit noch in Teilen einer anderen wissenschaftlichen Hochschule zur Begutachtung in einem Promotionsverfahren vorliegt oder vorgelegt hat. Außerdem versichere ich, dass die allgemeinen Prinzipien wissenschaftlicher Arbeit und Veröffentlichung, wie sie in den Leitlinien guter wissenschaftlicher Praxis der Carl von Ossietzky Universität Oldenburg festgelegt sind, von mir befolgt wurden.

Oldenburg, Dezember 2022
